INFORMATION TO USERS

This material was produced from a microfilm copy of the original document. While the most advanced technological means to photograph and reproduce this document have been used, the quality is heavily dependent upon the quality of the original submitted.

The following explanation of techniques is provided to help you understand markings or patterns which may appear on this reproduction.

1. The sign or "target" for pages apparently lacking from the document photographed is "Missing Page(s)". If it was possible to obtain the missing page(s) or section, they are spliced into the film along with adjacent pages. This may have necessitated cutting thru an image and duplicating adjacent pages to insure you complete continuity.

2. When an image on the film is obliterated with a large round black mark, it is an indication that the photographer suspected that the copy may have moved during exposure and thus cause a blurred image. You will find a good image of the page in the adjacent frame.

3. When a map, drawing or chart, etc., was part of the material being photographed the photographer followed a definite method in "sectioning" the material. It is customary to begin photoing at the upper left hand corner of a large sheet and to continue photoing from left to right in equal sections with a small overlap. If necessary, sectioning is continued again — beginning below the first row and continuing on until complete.

4. The majority of users indicate that the textual content is of greatest value, however, a somewhat higher quality reproduction could be made from "photographs" if essential to the understanding of the dissertation. Silver prints of "photographs" may be ordered at additional charge by writing the Order Department, giving the catalog number, title, author and specific pages you wish reproduced.

5. PLEASE NOTE: Some pages may have indistinct print. Filmed as received.

Xerox University Microfilms

300 North Zeeb Road
Ann Arbor, Michigan 48106

Downloaded from SHAREOK. Persistent Handle URL: https://hdl.handle.net/11244/4125

76-24,362

CHARLES, John Andrew, 1948-
THE USE OF THERMOGRAPHY IN FATIGUE STUDIES.

The University of Oklahoma, Ph.D., 1976
Engineering, mechanical

Xerox University Microfilms, Ann Arbor, Michigan 48106

THE UNIVERSITY OF OKLAHOMA

GRADUATE COLLEGE

THE USE OF THERMOGRAPHY IN FATIGUE STUDIES

A DISSERTATION

SUBMITTED TO THE GRADUATE FACULTY

in partial fulfillment of the requirements for the

degree of

DOCTOR OF PHILOSOPHY

BY

JOHN ANDREW CHARLES

Norman, Oklahoma

1976

THE USE OF THERMOGRAPHY IN FATIGUE STUDIES

APPROVED BY

John E. Francis

Franklin J. Appl

Charles W. Bert

[illegible]

William N. Huff

DISSERTATION COMMITTEE

ACKNOWLEDGMENTS

The author wishes to express his sincere appreciation to his major advisors, Dr. John E. Francis and Dr. Franklin J. Appl, for their guidance and support throughout this study. The assistance and cooperation of Drs. Tom J. Love, Charles W. Bert and William N. Huff, also members of the Doctoral Committee, are greatly appreciated as well.

The Tulsa Division, Rockwell International Corporation of Tulsa, Oklahoma is gratefully acknowledged for their contribution of the graphite-epoxy composite material used in this work. The computer time provided by the University of Oklahoma, Merrick Computer Center, is also appreciated.

The author would also like to thank his wife, Janet, for her continuing strength and encouragement during this endeavor.

TABLE OF CONTENTS

Page

LIST OF TABLES v

LIST OF FIGURES vi

Chapter

I. INTRODUCTION 1

II. THEORY 12

III. EXPERIMENTAL EQUIPMENT AND PROCEDURE 38

IV. EMISSIVITY MEASUREMENTS 49

V. EXPERIMENTAL RESULTS 59

VI. ANALYTICAL CONSIDERATIONS 166

VII. CONCLUSIONS 240

REFERENCES 247

APPENDICES 253

LIST OF TABLES

Table		Page
I.	"ThermIscope" System Parameters	41
II.	Thermal Emissivities of Materials	55
III.	Surface Coating Properties	56
IV.	Double-notched Steel Fatigue Tests	79

LIST OF FIGURES

Figure		Page
1.	Stages in the fatigue life of a specimen	16
2.	Energy dissipation in cyclic loading	22
3.	Plastic zones for plane stress conditions	26
4.	Plastic zones for plane strain conditions	26
5.	"ThermIscope" scanning infrared camera	39
6.	Tatnall-Krouse fatigue machine	39
7.	Experimental method for determining surface emissivities using the scanning infrared camera	51
8.	Single-notched steel fatigue specimen	61
9.	Thermogram of single-notched steel fatigue specimen at 3,400 cycles	61
10.	Temperature field maps of single-notched steel specimen	63
11.	Maximum temperature rise above ambient during test of single-notched steel specimen	67
12.	Tapered steel fatigue specimen	69
13.	Temperature field map of tapered steel specimen at 1,100 cycles	70
14.	Double-notched steel fatigue specimen	73
15.	Stress-strain curve for double-notched mild steel fatigue specimen material	76

Figure Page

16. Strain gage positions for double-notched steel fatigue specimens 78
17. Strain and stress distributions at notches for double-notched steel fatigue specimens . . . 80
18. Maximum temperature rise on specimen as a function of the number of fatigue cycles endured for the 1-6 series 87
19. Non-dimensional temperature rise as a function of fraction of fatigue life for the 1-6 series. . 89
20. Slope and change in slope of non-dimensional temperature rise curve for the 1-6 series 91
21. Maximum temperature rise on specimen as a function of the number of fatigue cycles endured for the 2-7 series 94
22. Non-dimensional temperature rise as a function of fraction of fatigue life for the 2-7 series . . 96
23. Slope and change in slope of non-dimensional temperature rise curve for the 2-7 series 97
24. Maximum temperature rise on specimen as a function of the number of fatigue cycles endured for the 5-0 series 99
25. Non-dimensional temperature rise as a function of fraction of fatigue life for the 5-0 series 100

Figure Page

26. Slope and change in slope of non-dimensional temperature rise curve for the 5-0 series . . . 101

27. Maximum temperature rise on specimen as a function of the number of fatigue cycles endured for the 3-8 series 103

28. Non-dimensional temperature rise as a function of fraction of fatigue life for the 3-8 series 104

29. Slope and change in slope of non-dimensional temperature rise curve for the 3-8 series . . . 105

30. Maximum temperature rise on specimen as a function of the number of fatigue cycles endured for the 4-9 series 107

31. Non-dimensional temperature rise as a function of fraction of fatigue life for the 4-9 series 108

32. Slope and change in slope of non-dimensional temperature rise curve for the 4-9 series . . . 109

33. Thermograms of specimen S-36 114

34. Temperature field maps of specimen S-36 115

35. Energy dissipation rates for specimen S-36 during fatigue test 123

36. Thermograms of specimen S-52 125

37. Temperature field maps of specimen S-52 126

Figure Page

38. Energy dissipation rates for specimen S-52 during fatigue test 135
39. Thermograms of specimen S-55 136
40. Temperature field maps of specimen S-55 138
41. Energy dissipation rates for specimen S-55 during fatigue test 145
42. Aluminum fatigue specimen 147
43. Thermogram of aluminum fatigue specimen at 30,000 cycles 147
44. Composite material fatigue specimens 151
45. Thermograms of graphite-epoxy specimen 152
46. Temperature field maps of graphite-epoxy specimen 154
47. Thermogram of notched fiberglass-epoxy specimen at 30,000 cycles 159
48. Temperature field map of notched fiberglass-epoxy specimen at 30,000 cycles 160
49. Temperature rise at U-notch root as a function of stress concentration factor, K_t, for fiberglass-epoxy specimens 161
50. Thermogram of slotted fiberglass-epoxy specimen at 150,000 cycles 163
51. Temperature field map of slotted fiberglass-epoxy specimen at 150,000 cycles 165

Figure Page

52. Temperature field about a point heat source near an isothermal boundary 169

53. Exact solution for a point source of heat moving in an infinite plane 172

54. Numerical model for heat transfer in rectangular fatigue specimens 178

55. Maximum temperature rise and gradient as a function of heat generation rate for rectangular fatigue specimens 182

56. Maximum temperature rise and gradient as a function of thermal conductivity for rectangular fatigue specimens 184

57. Maximum temperature rise and gradient as a function of specimen thickness for rectanuglar steel fatigue specimens 185

58. Maximum temperature rise and gradient as a function of thickness and heat generation rate when $Q \alpha b$ 187

59. Maximum temperature rise as a function of h_{vise} for rectangular fatigue specimens 189

60. Maximum temperature rise as a function of h_{crank} for rectangular fatigue specimens . . . 190

61. Maximum temperature rise as a function of the order of the heat transfer coefficient for rectangular fatigue specimens 192

Figure Page

62. Maximum temperature rise for constant generation rate at different positions in rectangular steel fatigue specimens 193

63. Temperature field map for numerical model of steel fatigue specimen 196

64. Temperature field map for numerical model of steel fatigue specimen near end of fatigue life 198

65. Geometry and nomenclature for enhancement study by blowing air 201

66. Temperature rise and gradient at generation point with enhancement 203

67. Effect of h_{add} on temperature gradient in aluminum 204

68. Results of transient numerical model for constant heat generation rate in rectangular fatigue specimens 209

69. Experimental data for temperature rise during initial stage of life 210

70. Comparison of numerical and experimental results for temperature rise with time for constant heat generation rate 211

71. Results of numerical model with time-variable heat generation rate 214

Figure Page

72. Comparison of experimental and numerical data for time-variable heat generation rate 215

73. Effect of numerous restarts on maximum temperature rise with time 217

74. Geometry and nomenclature for triangular specimen with uniform heat generation 220

75. Centerline temperature rise for triangular fatigue specimen by exact and numerical solutions 225

76. Geometry and nomenclature for triangular numerical model of fatigue specimen with uniform heat generation 227

77. Centerline temperature rise as a function of specific heat generation rate in triangular fatigue specimens 230

78. Centerline temperature rise as a function of thermal conductivity in triangular fatigue specimens 231

79. Numerical model results for tapered specimen with strong extra heat generation point superimposed on uniform generation 233

80. Numerical model results for tapered specimen with weak edge heat generation point superimposed on uniform generation 236

Figure Page

81. Stress-strain data in yield region of mild steel used for double-notched specimens 259

THE USE OF THERMOGRAPHY IN FATIGUE STUDIES

CHAPTER I

INTRODUCTION

It has long been recognized that failures can occur in materials under repeated stress application at stresses well below those required to produce failure of the material under static loading conditions. Even when the loading of the material does not reach the yield stress of the material for static conditions, repeated application will result in physical damage to the material and eventually the material fails completely. The failures which occur under repeated or cyclic stressing are called fatigue failures. Sometimes such failures are catastrophic, involving the loss of life and property. Perhaps the first concerted efforts toward fatigue research stemmed from the frequent failures of railroad axles which occurred while the axles were not being overloaded from a static standpoint[1]. The results of those studies form the basis for much of the fatigue data available today. One of the primary objectives of that early research was the establishment of fatigue-life curves for materials and commonly-used machine

parts. By properly using these curves, machine designers could make a rough estimate of the useful life of a given part, or design a part to withstand a specified number of repeated loadings. After that number of loadings, the part became suspect from a fatigue standpoint, and was simply replaced with a new part. Similar procedures are currently being applied to some fatigue problems in aircraft, which are subjected to considerable fatigue loading.

Such a policy for dealing with fatigue problems is probably the simplest to pursue, but often the replacement of a part is in fact unnecessary. In other cases, parts have been known to fail before their design life is reached. Indeed, it has been estimated that approximately 80 percent of all machine part failures are traceable to fatigue[2]. Thus, while the fatigue-life curve is still of primary importance to the designer, it provides only a rough estimate of the useful life of a part in service in a particular application. In order to make the most efficient use of materials, and in order to ensure the safety of machinery, there exists the need for a more accurate means of evaluating the condition of materials subjected to cyclic loading.

The most reliable way to avoid fatigue failures in machine parts subjected to cyclic loading is to periodically inspect the parts for signs of fatigue damage. This damage may take many forms, according to the material in question.

Various techniques have been developed and refined to accomplish the periodic inspections of materials. The earliest and simplest technique of inspection is visual. Depending on the care exercised during the inspection, fatigue cracks can be detected as early as within the first 15 percent of the life of the part[3]. Unfortunately, the accuracy of this method depends greatly on the skill of the inspector, and it is also possible to miss a fatigue crack entirely. This would obviously be the case for sub-surface fatigue cracks. Early findings of damage also depend on the careful preparation of the part of interest. Often this part is subjected to a dye penetrant in order to make the fatigue crack more easily visible. The use of a microscope during visual inspections enhances the sensitivity of the technique, but such an inspection can be lengthy if there are several areas to be inspected on each part. The main drawback of the visual inspection is that it is limited for all practical purposes to the detection of fatigue macrocracks on the surface of materials. Visual inspections can lead only to conjecture about regions likely to incur fatigue damage in the future.

Other inspection techniques are currently being used or are under study which can provide much more useful information than the visual inspection. Many of these techniques work in conjunction with visual inspections to enhance the dependability of the latter. Several methods

may be termed nondestructive techniques in that they do not affect the material being inspected. Some might also be classified as dynamic fatigue inspections, being related directly to the stress levels in the materials and requiring that the part be cycled while being inspected. Perhaps the oldest and most widely used form of nondestructive testing is radiography[4]. Basically, this technique depends on the absorption of X-rays in a material being irradiated. Where the material is flawed, or includes a void, the effective thickness of the material is changed and the intensity of the X-rays leaving the material is increased. In this manner, an image of the defect is formed and generally recorded on photographic film. Considerable experience is necessary to interpret the results of a radiograph, particularly in identifying the source of the indication and in judging how harmful the defect might be in service. The principal field of application of radiography is in the inspection of welds and castings, but it has been used in fatigue inspections. The primary difficulty in fatigue application is that radiography does not detect very thin flaws, unless such a flaw lies parallel to the direction of the X-rays. Unfortunately, fatigue cracks are "thin flaws" and therefore may be missed in a radiographic inspection. Another disadvantage of radiography is that the X-rays used in the inspection can pose a health hazard to the inspectors.

Another method of detecting discontinuities in materials is by magnetic inspection. These methods are used in conjunction with the visual inspection. Magnetic inspection methods depend upon establishing a uniform magnetic field around the material of interest by using a magnetic coil or by passing an electrical current through the material[5]. Any discontinuity in the material disturbs this magnetic field, and the disturbance can be detected using either magnetic powder or a pick-up coil. Two common examples of the magnetic powder techniques are Magnaflux and Magnaglow. Both of these techniques can detect fine surface and subsurface cracks. An example of the use of a pick-up coil is the Sperry rail tester used by railroads. In this case, an electrical current is passed through the rail while a pick-up coil monitors the induced current above the rail. Any disturbance in the induced current may indicate the presence of a defect, perhaps a fatigue crack. These magnetic methods have the advantage of being able to discern small flaws, but they depend eventually for their success on a visual inspection.

Another useful technique for fatigue damage inspection is ultrasonic testing[6]. In this technique, a beam of ultrasonic waves is transmitted through a material, and reflections from any defects are detected electrically. The method is capable of discerning small surface and sub-surface flaws, but locating the flaws within the material may

pose a considerable problem due to wave reflections within the part. This may be especially true for parts with complicated geometries.

The previous examples of fatigue damage detection techniques should be classified as "static" in that the inspection takes place with the part out of service and unstressed. A few damage detection techniques are "dynamic" in their nature. This permits them to be predictive to some extent. They in fact depend upon the stressing of the material for their success. One example of such a method is based on the detection of electrons being emitted from a material under stress. When a metal is irradiated by ultraviolet light, it emits electrons. If the material is stressed at the same time, electrons are emitted more easily. This increased emission of electrons is called "exoelectron emission"[7]. Results obtained on aluminum indicate that by monitoring the electron emission from a cyclically loaded part, and determining where on the part that emission is greatest, it is possible to predict the eventual fracture point on the specimen after less than one percent of the specimen's fatigue life. The primary disadvantage of the method is that it must be carried out in a high vacuum, which makes field use impractical.

A more widely researched method a fatigue investigation is acoustic emission[8]. In this technique, material undergoing cyclic loading emits acoustic or elastic waves

from regions incurring damage. As the damage increases, the acoustic emission increases. The generally accepted means of quantitizing acoustic emission data, which occur as a continuous signal in the material, is to count the number of times the signal level passes a predetermined level. The frequency of these "bursts" is then related to the damage occurring in the material. Research has shown that acoustic emission can detect the presence of very small flaws in a material well before such flaws become obvious to visual inspection. One drawback of the technique is the need to eliminate as much of the background noise due to external sources as possible. In this technique, as in ultrasonic testing, it may be difficult to accurately locate a flaw without visual inspection due to the complexity of the wave propagation and reflection problems in the material.

A relatively new and extremely promising technique for fatigue inspection is that of thermography using the scanning infrared camera. This technique can be intimately related to the operational stress levels in the part of interest, and is nondestructive in that the material being inspected is not affected by the inspection itself. "Thermography" is used herein to denote thermal imaging using the scanning infrared camera exclusively. Most thermal imaging techniques, including thermography, utilize the infrared emission from a body to discern its temperature.

For quite some time the use of infrared detectors for nondestructive testing has been widely accepted. Some of the pre-scanning infrared applications include the detection of weld defects, inspection of nuclear fuel elements, inspection for bond defects in rocket propellant and case assemblies, and others[9,10,11].

The advent of the scanning infrared camera opened the doors to many new research efforts in infrared imaging. The scanning infrared camera has been used successfully for some years as a research and diagnostic tool by the medical profession[12]. In other applications, thermography has been used to inspect food package seals, power plant systems, printed circuit boards, heated aircraft panels, and insulation on structures from residential homes to bulk storage tanks[13]. In one unusual application, thermography was used to locate contraband compartments hidden inside large tank trucks.

Materials research and inspection techniques using thermography are becoming ever more numerous. In static applications, it has been used as a nondestructive instrument locate flaws in critical parts of aircraft fuel systems, and to locate bond defects in honeycomb panels[14,15]. These applications require the use of an external heat source for the specimen, which is then scanned for abnormalities in its surface-temperature distribution. This approach may also prove successful in detecting small fatigue cracks

in a static sense through the flaw in the surface temperatures created by the thermal contact resistance across the crack. Another potentially useful static application of thermography in fatigue studies utilizes the increase in electrical resistivity within a material which occurs after only a few fatigue cycles[16]. A current of uniform density being passed through the slightly damaged specimen is disturbed by the changed resistivity, and local heating results in the damaged region of the material. When developed, this technique could lead to accurate early detection of areas likely to incur the greatest fatigue damage.

The thermographic techniques discussed above are not related to the operational stress levels in the materials and are static in nature. A different thrust in thermographic-fatigue research leads to the development of thermography as a dynamic fatigue testing technique[17-25]. In this application the source of heat is the energy dissipation within the material due to hysteresis effects. This energy dissipation is a direct function of the stress level in the material. Areas of high stress are accompanied by higher hysteresis losses than the surrounding material. There results on the surface of the specimen a non-uniform temperature distribution in which warm regions are indicative of areas of locally high stress. The first published work on this application of thermography was that of Attermo and Ostberg, who simply measured the temperature

rise ahead of a fatigue crack[17]. Further studies of this technique have been undertaken by Reifsnider et al.[18,19], Nevedunsky et al.[20], and Charles et al.[21-25]. The first two groups concentrated their efforts on composite materials. In their work, thermography was not the primary means of gaining thermal data, but rather was a secondary system used mainly for qualitative indications of the temperature distributions. However, the work does show the relationship of the thermal patterns generated on the material to the strain-energy density field in the material. The work of Charles et al. was undertaken using a variety of materials, and used the scanning infrared camera as the means of gaining quantitative thermal data. The potential for thermography as a nondestructive inspection and research tool was demonstrated using steel, aluminum, fiberglass-epoxy composite, and graphite-epoxy composite. The results indicated that thermography could provide early warning of areas likely to incur fatigue damage, monitor damage already present, and provide accurate surface-temperature maps of the specimens at any time during their lives.

The present work carries this basic research in the use of thermography in fatigue studies still further. Comprehensive data are presented for steel fatigue specimens, and additional data are added to that already reported for composite materials. The results include the prediction of damage-prone areas, the accurate monitoring

of progressing fatigue damage, mapping surface temperatures on specimens, and the determination of energy dissipation rates and total energy dissipation during a test. In addition, attempts are made to relate thermographic data to the size of the plastic zone ahead of the propagating fatigue cracks. Limitations of the technique and possibilities for further application are discussed in the light of information from analytical models.

CHAPTER II

THEORY

It is believed that fatigue damage accumulates as the result of cyclic plastic strains, and that these strains occur in all materials under any finite stresses[26]. Because of these plastic deformations in fatigue loading, energy is dissipated in the material during the loading. Most of this energy manifests itself as heat and is not recoverable as strain energy. Since the stress levels within a material are seldom uniform, areas of locally severe plastic deformation occur in the material. These are the areas which eventually become locations of macroscopic fatigue damage and lead to the ultimate failure of the material. During the energy dissipation, it is possible for the affected areas to become warmer than the surrounding regions due to the interaction of the heat generation and the heat-transfer mechanisms acting on the material. A knowledge of the temperature distribution throughout the material under stress may therefore lead one to some useful conclusions pertaining to the likelihood of significant fatigue damage at a given location. Such information may

also provide insights on the total energy required to produce a fatigue failure under a given cyclic loading condition. In fact, many useful conclusions can be drawn if a knowledge of the temperature distribution within a body undergoing fatigue loading is obtainable.

For most cases, a complete three-dimensional temperature distribution within a body would be difficult if not impossible to obtain using nondestructive techniques. However, with the scanning infrared camera, a high-resolution picture of the surface temperature distribution on the body is readily obtainable. A knowledge of the heat-transfer mechanisms acting in the body is necessary if the surface temperatures are to be related to possible fatigue damage occurring inside the body. For many practical cases, notably thin plates and shells, the heat-transfer problem poses no major obstacles. Thus, one can readily draw conclusions pertaining to the state of damage in a part by looking only at the thermographic data obtained with the scanning infrared camera. Furthermore, thermography in no way interferes with the surface being observed, making it truly nondestructive as a monitoring technique.

Fatigue Mechanisms

An understanding of the mechanisms of fatigue is helpful in trying to interpret the data obtained with the scanning infrared camera. Many factors affect the fatigue behavior of materials. Even the behavior of two seemingly

identical pieces of material can be quite different. Various materials display different behaviors under fatigue loading primarily because of their mechanical properties, their fracture characteristics, and their chemical and microstructural composition. For example, fatigue damage in metals usually occurs in the form of cracks which propagate in the material until failure[27]. On the other hand, composite materials display many kinds of fatigue damage simultaneously, including debonding, delamination, matrix cracking and others[28]. Specimens of a given material may yield very different results in fatigue tests due to the effects of the type of loading, mean stress level, notch configuration, surface condition, environment, and others[29]. It is beyond the scope of this study to attempt to deal with all these effects. Rather, consistency of geometry, loading and preparation of a given material will be maintained. Hostile environments of high temperature or corrosive atmosphere can seriously affect the fatigue behavior of many materials, with some materials exhibiting significant changes in behavior with temperature changes. In particular, composite materials may show a relatively high sensitivity to adverse environmental conditions due to changes in the matrix material. In the present work, discussion will be limited to environments at room temperature.

Indeed, the very phenomenon which makes the use of thermography in fatigue studies possible is the temperature

rise in the material which results from the plastic deformations. That temperature rise is usually no greater than about $50^{\circ}F$ to $80^{\circ}F$ for the studies conducted in this work, so it will be assumed that no significant changes in the material behavior stem from the thermal "feedback" of the material[30]. It is then possible to uncouple the heat-transfer and stress problems from one another, greatly simplifying the total problem.

Many theories exist which try to explain the mechanism of fatigue from a single viewpoint. Some are based on statistical theory, while others are extended from experimental results of pure fracture[31]. However, it appears that the entire life of a fatigue specimen cannot be adequately described by resorting to a single approach. A more likely method is to describe different stages of the fatigue life with different models, as is done in the theory of Yokobori[32]. In this sense, it is more appropriate to discuss the mechanisms of fatigue rather than only one mechanism. The discussion which follows will be limited to metallic materials.

It is convenient to break the fatigue life down into four or five stages, based on the damage present or occurring in the material at any time. These stages are illustrated in Fig. 1. During the first stage, comprising the nondimensional fraction N_1^* of the life of the specimen, work hardening occurs in the material. Some theories choose

Note: Lengths of stages shown are only approximate.

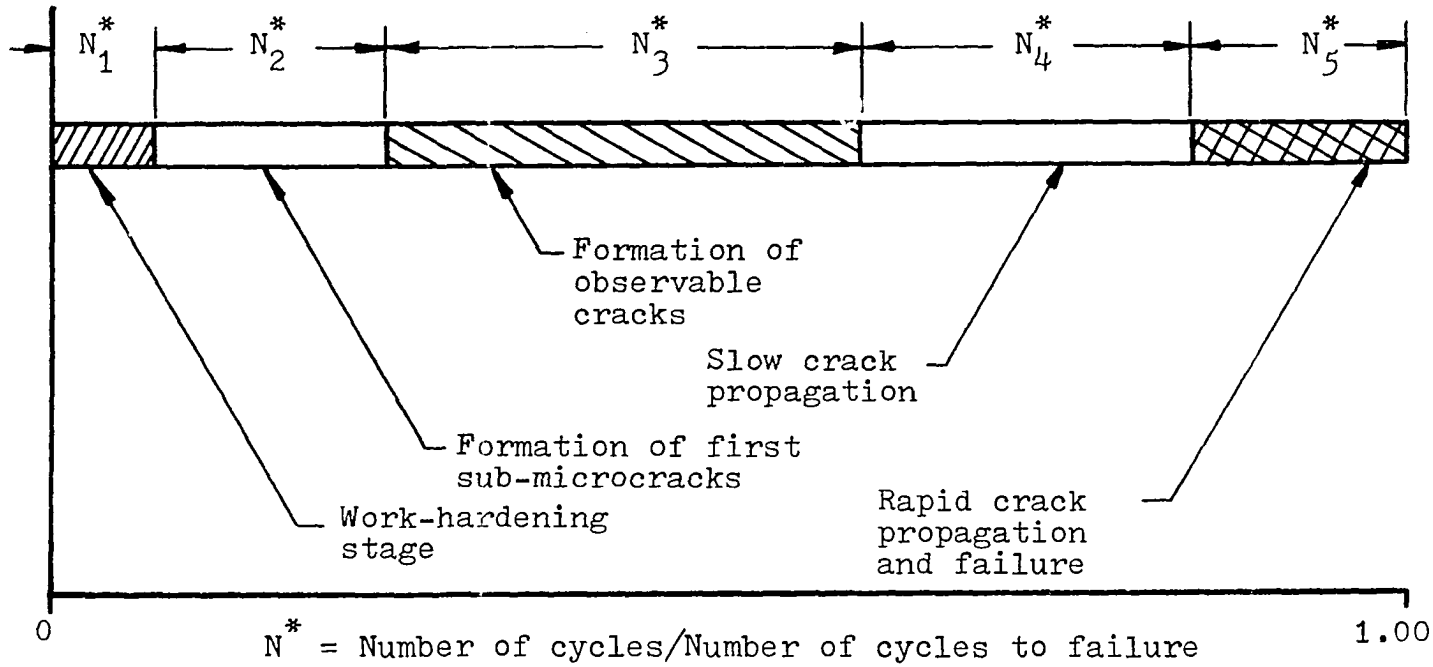

Figure 1. Stages in the fatigue life of a specimen.

to ignore the effects of work hardening[33], but it has been shown that such changes in the material do indeed take place[34]. In fact, the initial stage has many of the features of work hardening. There is an increase in hardness, yield point and electrical resistivity during this stage. X-ray methods have been used to show that crystal lattice strain also occurs during the early portions of the fatigue life[35]. It has also been observed that no microscopically observable cracks are formed during the work hardening process[36]. The work-hardening stage occupies a very small part of the fatigue life, perhaps only a few thousand cycles at most.

The second stage of the fatigue life occupies a period N_2^* and represents the time necessary for the formation of the first sub-microcracks. In fact, the mechanisms which account for the formation of these cracks are also operating during the first stage of the life. It is believed that these first sub-microcracks form at the ends of slip bands, which are composed of a cluster of fine slip lines[37]. Observations by Bullen et al.[38] have shown that slip lines appear under the microscope after the application of about a thousand cycles, using tension-compression tests of copper. This number of cycles seemed to be independent of cycling rate and stress amplitude. The fine slip lines were observed in broad bands located far apart. Upon further loading, these slip bands broadened, supposedly due to the greater mobility of atoms in the slip planes induced

by the additional stressing. Eventually, the slip bands broaden to the point where they may be called sub-microcracks, and serve as the sites for microscopic crack formation.

A further portion of the fatigue life, N_3^*, is required for the sub-microcracks to grow and link to form a "detectable" crack. It may be somewhat difficult to generalize this stage since the sensitivity of the crack detection instrument will determine when it ends. Nevertheless, during this stage, the broadened slip bands give rise to microcracks which eventually precipitate the fatigue failure. It is thought that the governing condition determining in which planes these cracks form is the maximum shear stress acting on the material[39]. However, in polycrystalline materials, cracks propagate with a zigzag path from one grain to another. This discrepancy has been explained by McClintock[40], who showed that in each grain of the material, the crack lies parallel to the slip plane experiencing the maximum shear stress, but that in polycrystals, the grains themselves are arranged randomly. Hence the apparent zigzag propagation of the crack.

In Yokobori's theory, a final stage, N_4^*, includes the propagation of the now-visible crack in the material to ultimate failure. He explains that the distinction between the third and fourth stages is actually one of convenience. In fact, the mechanisms acting in each of the

last two stages are the same. The length of the fourth stage is said to be quite short, but this conclusion must be accompanied by some statements concerning the type of loading being used in the fatigue test. If the test is load-controlled, then the last stage will indeed be short, since the stress on the reduced cross-section increases rapidly as the crack propagates. However, in deflection-controlled testing such as was used in this study, the load and therefore the stress on the material decreases as the crack propagates. This tends to slow the propagation of the crack, and extends greatly the length of the fourth stage of the fatigue life. It is common in this case to observe cracks visually at about 50 percent of the specimen life, leaving half the life to comprise the final stage.

From both visual and thermographic observations of deflection-controlled tests in this study, it is the author's opinion that there should be a fifth stage of N_5^* cycles added to the theory above. This stage will be discussed in some detail later, but basically it comprised about the final 20 to 30 percent of the fatigue lives of the steel specimens tested. Before this stage, in the fourth stage, a visible crack propagated slowly across the surface of the specimen. Toward the end of the tests, the propagation became more rapid, and was accompanied by a significant increase in the energy dissipation in the material. Perhaps in load-controlled tests the fourth and fifth stages are in fact one,

but in deflection-controlled tests they can be readily separated. For completeness, this distinction will be continued herein. The probable cause of the increased energy dissipation in the fifth stage is an increase in plastic deformation which occurs as fracture is imminent.

The most significant aspect of the fatigue process for the purpose of this study is the energy dissipation which occurs in cyclically loaded materials. It is in fact this energy dissipation which results in local temperature rises in materials and enables one to obtain useful information from scanning camera studies. Energy is dissipated in fatigue loading because of plastic deformations brought about by locally high stresses. The energy lost per unit volume per cycle is measured as the area inside the hysteresis loop, which traces the cyclic stress-strain behavior of the material[41]. Hysteresis loops can take various shapes and areas depending on the behavior of the material and the loading imposed. Even with a given material under a specified loading, the hysteresis loop changes markedly throughout the duration of a fatigue test. This change is usually associated with the local changes in the material which occur during the fatigue stages discussed previously. In addition, hysteresis loops pertain only to a point in the material, and hence neighboring points can display different loops at any time.

Several different hysteresis loops are shown in

Fig. 2. Figure 2(a) illustrates how a hysteresis loop becomes a straight line for purely elastic action. In practice, such behavior does not exist, so there is always an energy loss associated with fatigue loading[42]. Figure 2(b) shows a hysteresis loop for completely reversed loading past the elastic limit of the material. The loop shown actually changes shape as the test progresses. If the material cyclically hardens as the test proceeds, the width of the loop gradually decreases until a stable loop is achieved somewhere before the half-life of the material. If the material cyclically softens, the reverse is true and the loop gradually increases in area. Cyclic hardening is the phenomenon which occurs in the metals used in this study, so one would expect the energy dissipation to be large in the material initially, and subside to a steady value somewhat later. The development of the hysteresis loop for loading which is not completely reversed is not the same as that in Fig. 2(b). In cyclic loading where the specimen is subjected only to cyclic tension, there is a large initial plastic deformation as the material strain hardens if loaded past the elastic limit. The hysteresis loop then develops about an elastic line with its peak at the limiting value of the stress. This condition is illustrated in Fig. 2(c). The energy loss in this case is quite different from that in fully reversed loading where the material is yielded in each cycle in tension and compression.

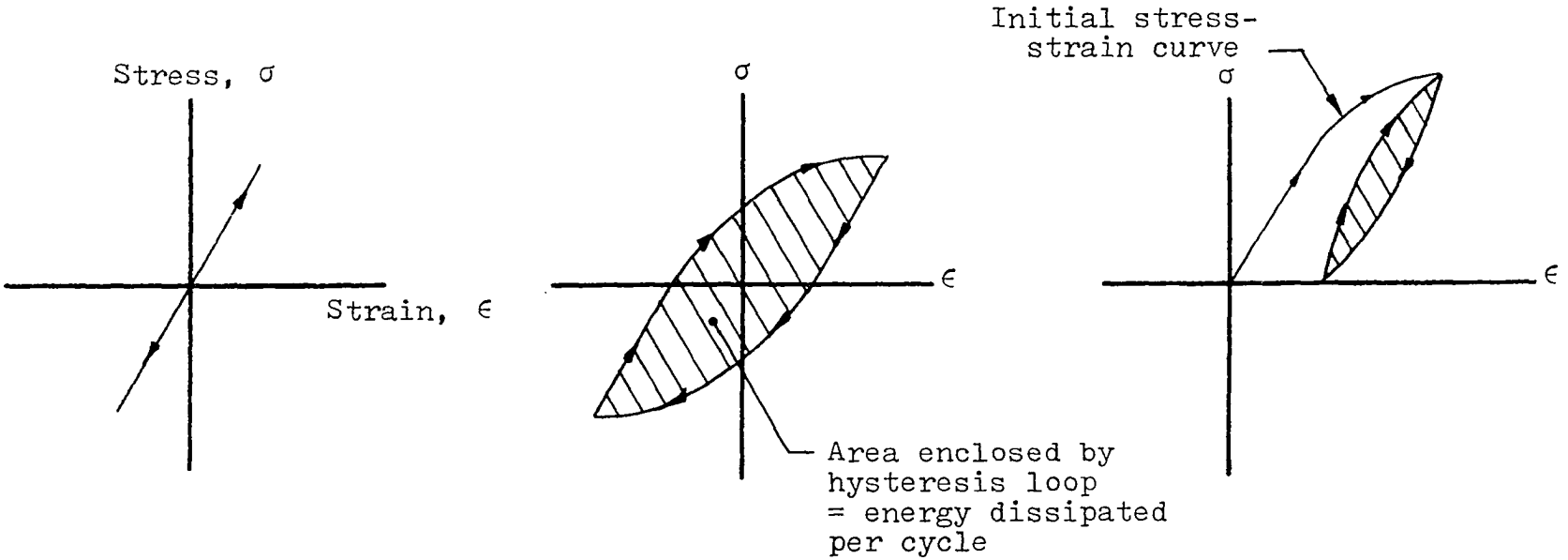

a. Fully elastic fatigue loading

b. Completely reversed fatigue loading beyond yield stress

c. Fatigue loading in tension only beyond initial yield stress

Figure 2. Energy dissipation in cyclic loading.

Energy approaches have been used by several authors as a basis of theories to predict crack propagation rates and fatigue lives[43-45]. The sum of all the areas under all the hysteresis loops for a material during a fatigue test is an indication of the total plastic strain energy, or fatigue toughness, used in failing the material. It is interesting that it may take 100 times the energy to fracture a material in fatigue than is necessary in static loading. Raju[43] used the energy of plastic deformation in a prediction of crack growth rates for materials whose static stress-strain curves could be expressed in a bi-linear representation. While his theory is comprehensive, he chose to neglect the work hardening in the material. As illustrated in Fig. 2(c), the work hardening of the material has a significant effect on the energy dissipated in the material. Nevertheless, Raju's work contains a lengthy discussion of the energy dissipation in the fatigue loading. He contended that there is a non-hysteretic component to the total energy dissipation which is a result of crack extension during each loading cycle. Obviously, this analysis should be limited to stages after the first stage of the fatigue life, since no cracks are formed in the very early life.

In his theory, as in most other fatigue theories, Raju assumes that there is a region about the stress concentrator or travelling crack in which plastic deformation

occurs. This region is called the plastic zone. It is also generally assumed that outside the plastic zone or enclave the material response is completely elastic, yielding no energy dissipation whatsoever. The problem then becomes one of determining the size of the plastic zone and the strain distribution within it in order to calculate the energy dissipation rate in the material. The plastic zone is of importance in the present study also, and a further discussion of the plastic zone and the energy generation within it is included in Chapter VI.

Considerable literature is available dealing with the plastic zone and energy considerations for monotonic fracture. Some of the literature deals explicitly with the temperature rise ahead of a running crack[44,45]. Many parallels can be drawn between the plastic zone for fatigue loading and monotonic fracture, even when the latter does not encounter work hardening at the crack tips, but the comparison of temperature rises is futile. As already noted, there is usually a much greater total energy dissipation in fatigue loading than in monotonic fracture, but it occurs over a much longer time. Hence the heat-transfer problem is substantially different in the two cases. However, many studies of plastic zone shapes and sizes have yielded similar results for the two cases. A classic reference in the study of plastic zones is a report on the yielding of steel sheets in tension by

D. S. Dugdale[46]. In this work, Dugdale analyzed the yielding of sheets containing stress concentrations, arriving at an expression for the length of the plastic zone as a function of the loading and the crack length. If the applied stress is T, and the initial yield stress of the material is Y, then Dugdale deduced that the length of the plastic zone, s, is given by

$$\frac{s}{a} = 2\sin^2\left(\frac{\pi T}{4Y}\right) , \qquad (2.1)$$

where a represents the length of the plastic zone and the crack. By yielding, ageing and etching several test pieces, Dugdale was able to measure directly the lengths of the plastic zones. The lengths compared well with his calculations. The shape of the plastic zones observed is shown in Fig. 3(a).

Work by Yokobori et al.[47,48] extended the results of Dugdale into the realm of fatigue loading. The major difference in the analysis of Yokobori compared to that of Dugdale is that the former included the effects of strain hardening in his analysis. This necessity was motivated by a discrepancy in the plastic zone sizes measured by Yokobori and those calculated from Dugdale's formula. Including the effect of work hardening in a region measuring c about the crack tip, Yokobori found

$$\frac{T}{2Y} = \cos^{-1}\left(\frac{L}{a}\right) - \frac{S}{Y}\left[\cos^{-1}\left(\frac{L+c}{a}\right) - \cos^{-1}\left(\frac{L}{a}\right)\right]. \qquad (2.2)$$

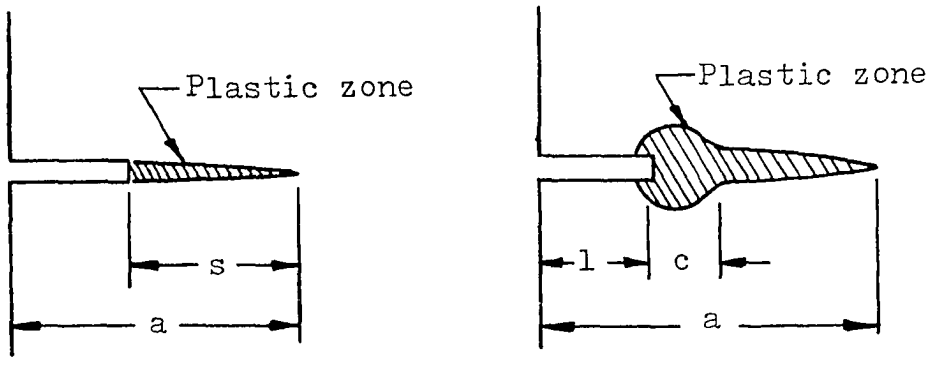

a. Dugdale's model b. Yokobori's model

Figure 3. Plastic zones for plane stress conditions.

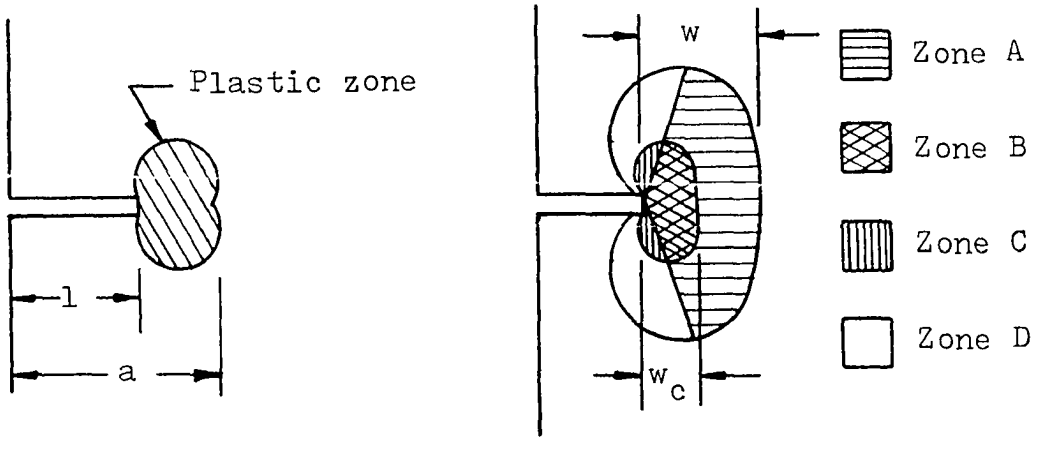

a. Yokobori's model b. Raju's model

Figure 4. Plastic zones for plane strain conditions.

In eq. (2.2), S represents the difference between the applied stress T and the initial yield stress Y, and L=a-s where a corresponds to that used by Dugdale. The geometry of this plastic zone is shown in Fig. 3(b).

The shape of the plastic zone in plane strain differs significantly from that in plane stress. Yokobori also analyzed the plastic zone for plane strain. In this case, the plastic zone is shaped more like a flattened circle than in the case of plane stress. This geometry makes it convenient to describe the size of the plastic zone by defining a radius of the plastic zone, R. It is generally believed that the radius of the plastic zone is linearly dependent on crack length[49]. The shape of the plastic zone for plane strain observed by Yokobori is shown in Fig. 4(a). Numerical results for this case are presented in graphical form in the reference.

By careful observation and comparison of his two models for plastic zones, Yokobori concluded that the plastic zone approximates that for plane strain early in the fatigue life of a material, or for short crack lengths. This is true based on tension-tension fatigue tests performed. For longer crack lengths or nearer the end of the tests, Yokobori found that the plastic zone began to look like that for plane stress. In this case, the region c of strain hardening appears to be a component similar to the plastic zone for plane strain. Superimposed on this

is a long tapered plastic zone of plane stress. The width of the tapered region was reported to be about twice the thickness of the specimen.

Most investigators deal only with the shape of the plastic zone and not with its internal structure. A notable exception is the work of Raju[43], who deals in depth with the structure of the plastic zone in plane strain. The model used by Raju is shown in Fig. 4(b). Raju subdivides the zone into four regions according to their contribution to the total energy dissipation. In zone A (see Fig. 4), plastic deformation occurs only when the crack tip extends at the maximum stress in each cycle. In zone D, normally included in the plastic zone, deformations are elastic due to elastic unloading which takes place during crack extension. Zones B and C then comprise the "cyclic plastic enclave". Zone B represents the area in which, because of crack growth, hysteresis losses increase with each loading cycle. In zone C, the opposite effect is seen, with hysteresis losses decreasing due to the movement of the crack tip away from that region. Thus Raju defines two dimensions for his plastic zone model. The total plastic zone width, w, is given as

$$w = K_{max}^2 / 9\tau_{oli}^2 \quad , \tag{2.3}$$

where K_{max} is the stress intensity factor corresponding to the maximum stress in each cycle, and τ_{oli} is the octahed-

ral shear stress at yield under monotonic loading. The cyclic plastic enclave is included in the plastic enclave, and its width w_c is given by

$$w_c = K_R^2 / 9 \bar{\tau}_{oli}^2 \quad . \tag{2.4}$$

In eq. (2.4), the stress intensity factor K_R is based on the stress range, and the octahedral shear stress is that which occurs at yield in the cyclic loading. It should be recalled that no work hardening is accounted for in this model, and a somewhat idealized model is used to determine the octahedral shear stress needed to pursue the approach further.

Raju proceeds to determine relationships for the energy losses per cycle based on the simplified material response noted, dividing the losses into hysteretic and non-hysteretic dissipation. An interesting conclusion is arrived at while considering the change in hysteresis losses in zones B and C due to crack extension. It is shown that the increase in loss that occurs in B is exactly balanced by the decrease that occurs in C. Thus, the hysteretic loss is seen to be independent of crack growth itself.

The plastic zone model of Raju is the most detailed of all considered from an energy standpoint, but all of the plastic zone models may lend insight to what is in fact a very complicated process. These models will be mentioned again in the light of the data obtained from thermography.

Heat Transfer Mechanisms

Once energy in the form of heat is released in the material being fatigued, the ability to measure any temperature rise locally on the surface of the material depends strongly on the heat transfer mechanisms operating in the material. Fortunately, the mechanisms of heat transfer are fairly well understood, at least from a macroscopic viewpoint. Closed-form solutions are available to a large number of practical problems[50], and numerical approaches to heat transfer are helpful in other cases[51]. The ability to uncouple the energy generation problem from the subsequent heat transfer problem makes the problem to be considered much simpler than if such an assumption could not be imposed.

The difficulty in the heat transfer problem stems from the fact that three heat transfer modes are operating on the material simultaneously. The region of generation of energy from plastic deformation loses heat by conduction within the material, convection from the surface of the material, and radiation from the surface to the surroundings of the material. Of these three mechanisms, perhaps the most important to understand here is radiative heat transfer. The heat conduction problem is well understood, although it may pose some difficulties when dealing with composite materials. The heat convection problem is likewise well understood, although difficulties may arise when trying to specify an accurate heat transfer coefficient between the

surface and the atmosphere. This is especially true when the fatigue specimen is not stationary or at least quasi-stationary. Nevertheless, the most difficult heat transfer mode to deal with herein is that of radiation, and it is the radiative heat transfer which allows one to visualize the surface temperature distributions on the materials being studied.

Several explanations of the physical mechanism of radiative heat transfer process have been proposed[52]. Sometimes the radiation of heat is assumed to be by an electromagnetic wave process, while at other times a photon theory seems to best describe observed phenomena. Generally, radiant heat energy is classified by its wavelength. The wavelength of all radiation depends on how it is produced. Thermal radiation is emitted by virtue of the temperature of a body. All bodies with a temperature greater than absolute zero emit thermal radiation according to their temperatures. Hence, the wavelength of the thermal radiation is governed by the temperature of the body. The wavelengths usually encompassed by thermal radiation fall between 0.1 and 100μ, where one micron, μ, is equal to 10^{-6} meters. This range is generally subdivided into visible, ultraviolet and infrared portions. The radiant energy of interest here occurs in the infrared portion of the spectrum, with wavelengths just longer than visible light.

The radiant heat transfer to and from a surface is

highly dependent on the radiative quality of the surface. An ideal radiator would be one which emits or absorbs all of the radiant energy available. Such a radiator is said to be a "blackbody". The fraction of the available radiant energy which is emitted by a body is its emissivity, with a blackbody having an emissivity of 1.00. This property of a material is most important to the present study. If a body is opaque and cannot transmit thermal radiation in its interior, it can be shown that in thermal equilibrium the portion of energy emitted plus the portion of energy reflected must equal one. Thus, if a body is radiatively black, it will not reflect any thermal radiation. If it is not a blackbody, then the radiation leaving the surface will be only partly that emitted due to the temperature of the body, and partly reflected incoming radiation. The importance of this phenomenon to the success of thermographic inspection of fatigue specimens will be discussed shortly.

A body at an absolute temperature T will emit thermal radiation over a broad band of wavelengths. The wavelength at which this emission is a maximum for a given temperature is given by Wien's displacement law, which states that the product of the absolute temperature and the wavelength, in microns, for the maximum emission is a constant.

$$\lambda_{max} T = 5215.6 \ \mu^{o}R \qquad (2.5)$$

Thus, as temperature increases, the wavelength for the maximum radiant emission decreases. In this study, the temperatures of interest fall generally between 70°F and about 120°F, the upper limit for temperatures with the scanning infrared camera used. Using Wien's displacement law, one finds that the wavelengths for the maximum radiant emission lie between 8.99 and 9.84 microns. These wavelengths will be recalled in the discussion of the scanning camera used for this study (see Chapter III).

The radiant heat transfer problem is also highly dependent on the relative positions of the emitting and absorbing surfaces. Since the thermal radiation travels in straight lines at the speed of light, the radiating surface must be able to "see" at least a portion of the absorbing surface before heat transfer can take place. This leads to the study of shape factors, or configuration factors, which describes the fraction of diffuse radiation leaving one surface which falls on another. A thorough discussion of shape factors can be found in most texts covering radiant heat transfer[53-55].

Infrared detectors, including those used in scanning infrared cameras, are able to receive thermal radiation and convert it into an electrical signal. This is accomplished by various means[56]. Regardless of the method used to convert the energy, the temperature of the body being studied can be determined from the signal. This is made

possible through the use of the Stefan-Boltzman law, which states that the total emission of radiation per unit surface area per unit time from a blackbody is proportional to the fourth power of the absolute temperature of the surface:

$$E_b(T) = \sigma T^4 . \qquad (2.6)$$

In eq. (2.6), E_b is the radiant blackbody emissive power, T is the absolute temperature of the body, and σ is a constant of proportionality, equal to 1.714 (10^{-9}) Btu/hr-ft^2-R^4 and called the Stefan-Boltzman constant. Thus, by studying the radiant emission from a surface, the surface temperature distribution can be determined. The advantage of the scanning infrared camera over a simple radiometer is that a large surface can be studied in a short time, as the scanning camera actually monitors thousands of points on the surface in each second through a scanning optics system. The result of this process is a visual image of the surface under study in which the various temperatures on the surface are seen as shades of gray. The resolution of this picture depends to a large extent on the number of points scanned on the surface. The emissivity of the surface becomes important when using a scanning infrared camera designed for use with blackbodies. Unless the emissivity of the surface is nearly one, the scanning infrared camera receives less radiant energy than is possible from the surface. In interpreting this energy as coming from a blackbody, the scanning

camera predicts a temperature of the surface that is less than the actual temperature. In itself, this may not be a critical shortcoming, since much information can often be gained from relative temperatures on a surface without resorting to quantitative analysis. However, it is possible to be unable to detect any surface temperature if the emissivity is too low. Another real problem arises in the possible reflections that may be seen on a surface with low emissivity. Unless the surface can be isolated from other sources of heat and infrared radiation, it becomes most difficult to determine whether detected radiation is due to the temperature of the surface or due to reflections from the surroundings. In this case, very few accurate conclusions can be drawn from the data obtained. Fortunately, it is often possible to change the emissivity of a surface by adding a thin surface coating, which can be assumed not to change the temperature distribution of the surface itself. This technique is used often in this work, and will be discussed further in Chapter IV.

The Combined Problem

It has been seen that heat is generated in materials undergoing fatigue loading due to hysteresis effects in the plastic zones in the areas of high stress levels. If one assumes the heat to be generated essentially at a point or points in the body, then the important question is whether or not the heat generation will be sufficient to produce

measurable local temperature rises on the surface of the material. The answer to this question depends on many factors. Of primary importance is the amount of heat released, which depends on the stress levels in the material, as discussed previously. It will obviously be easier to measure a temperature rise for stress levels above the initial yield stress than for levels below the yield point. Acting in conjunction with the generation are the three means of heat removal by conduction, convection and radiation. Usually, the most important of these is heat transfer by conduction. Materials with low thermal conductivities retain the heat locally quite well and make the detection of a temperature rise due to a small heat generation possible. Composite materials usually display a low thermal conductivity. Also a factor in conduction heat transfer is the cross-sectional area available through which the heat may be transferred. A thick member will be able to transfer more heat with a given temperature difference than a thin member. Thus, thermography promises to be more successful in dealing with plates than it does in dealing with large three-dimensional bodies.

The convection heat losses will not be a major consideration for most applications in the laboratory, but could present obstacles in field use. Once the heat reaches the surface of the specimen, it is convected to the atmosphere in proportion to the difference between the surface

temperature and the atmospheric temperature. Unless this temperature difference is large, the heat transfer by convection will not adversely affect the results to be gained by thermography. However, the presence of a non-uniform heat transfer coefficient can complicate attempts to model the combined problem analytically or numerically.

The importance of the radiant heat transfer has already been discussed at some length. In practice, it is the balance of generation, heat conduction, heat convection, and radiant heat transfer which determines the success of the method. Any temperature rises that are observed on the surface of the fatigue specimen are related to the damage occurring in the material. The conclusions which can be drawn from the thermographic data taken during fatigue tests can help aviod costly in-service failures, locate areas of likely fatigue damage, and lend insight to the fatigue process itself.

CHAPTER III

EXPERIMENTAL EQUIPMENT AND PROCEDURE

Temperature Measurement

The scanning infrared camera used in this study was the Model 700 "ThermIscope", manufactured by Texas Instruments and now distributed by Union Instrument Corporation. This instrument, pictured in Fig. 5, consists of four units; a scanner, a tripod, a recorder console and a camera. The scanner, at the left of Fig. 5, rests on a mobile tripod which allows adjustment of its vertical and horizontal position. The infrared detector and its associated optics system are housed in the scanner. Incoming thermal radiation is focused on the detector through a hexagonal rotating mirror (seen in Fig. 5 as the light area inside the front of the scanner) and converging optics. The detector itself is a compound of mercury, cadmium and telluride which must be cooled by liquid nitrogen when the scanner is operating. The detector is sensitive to thermal radiation in the 8 to 14μ wavelength band. This band encompasses the wavelengths at which blackbodies with temperatures between 70°F and 120°F emit the maximum thermal radiation according to Wien's displacement law, eq. (2.5). The time required for the

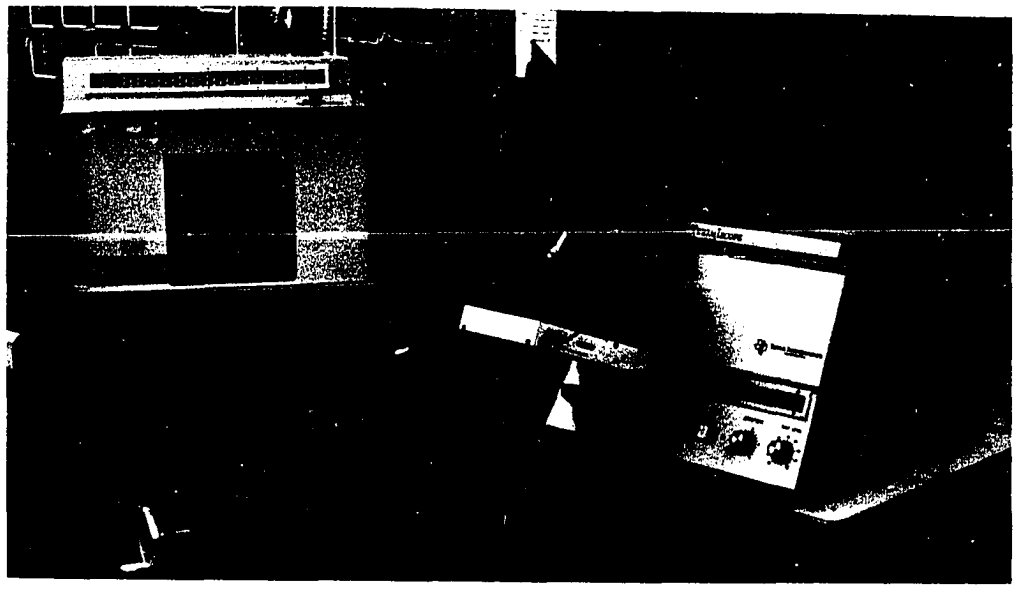

Figure 5. "ThermIscope" scanning infrared camera.

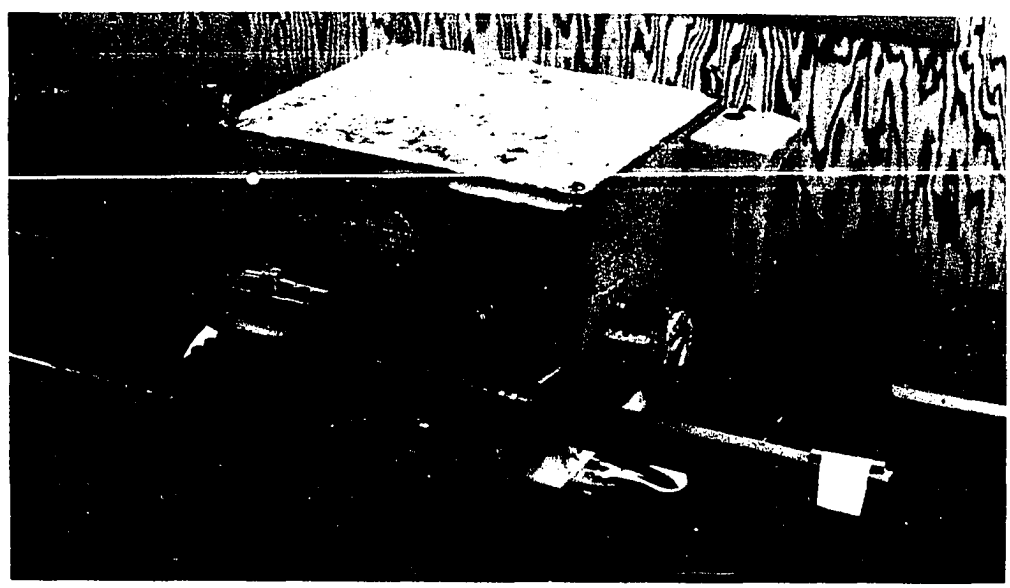

Figure 6. Tatnall-Krouse fatigue machine.

scanner to complete one scan of the viewing field is 4.5 seconds, with an additional 1.5 seconds required to recycle before the following scan commences. Although this scanning rate is somewhat slow, it produces an image of high thermal and spatial resolution. The signal from the scanner is processed in the recorder, which displays an image of the surface temperatures being scanned on a cathode-ray tube. The thermal sensitivity of the scanner is specified by the manufacturer to be 0.07°C (0.125°F), and the image on the cathode-ray tube is composed of 525 lines, each of which consists of 525 points. Thus the total image is composed of 275,000 elements. These and other important parameters of the ThermIscope are listed in Table I.

The image on the cathode-ray tube of the recorder is actually a black-and-white picture of the surface temperature distribution on the body being observed. The level of temperatures observed and the range about that level can be controlled from the recorder console. The limits of the temperatures that can be observed are 60 to 120°F, governed by the original intention that the ThermIscope be used in medical applications. The range is adjustable from 1 to 20°F continuously. An internally-generated reference scale is displayed on the cathode-ray tube along with the image from the scanner. This scale is designed to allow one to convert shades of gray to quantitative temperatures easily. It was found that this scale was slightly out of calibra-

Table I. "ThermIscope" System Parameters

Resolution:	275,000 elements/frame (525 lines x 525 elements/line) 0.00075 radian angular resolution 0.022 in. linear resolution (min.)
Thermal Sensitivity:	0.07°C (0.125°F)
Detector:	Mercury-Cadmium-Telluride (cooled by liquid nitrogen)
Spectral Range:	8 to 14 micrometers
Frame Time:	4.5 sec. (+ 1.5 sec. recycle)
Field of View:	33° by 33°
Focal Range:	4 inches to infinity
Display:	High-resolution, cathode-ray tube
Display Format:	3-in. by 2.75-in. image with reference scale
Camera:	Polaroid using Type 55 P/N film

tion during the present study, and that in fact the calibration error was not consistent from one run to the next. Therefore, it was necessary to include a reference source of temperature in each thermogram made. This allowed much more accurate determination of the temperatures in the field of view. The procedure for this calibration correction is outlined in Appendix A.

In order to closely analyze the images on the cathode-ray tube, a camera is provided with the ThermIscope. On the unit used in this study, the camera was a 4 by 5-inch Polaroid camera which used Type 55 P/N film to produce both a positive and a negative of the image. These photographs are termed "thermograms". In practice, more information is available from the negative than from the positive of the same image, probably due to the contrast limitations of the positive material. The negatives were therefore given the recommended photographic treatment for archival storage.

The negatives were analyzed to yield temperatures with the aid of a Gamma Scientific Instruments Microdensitometer and a Gamma Scientific Instruments Log Converter. The illuminator microscope of the densitiometer was fitted with an aperture of approximately 0.013 inches diameter. This small aperture allowed the determination of temperatures at points without having to average over a larger region. The density of the negative was compared to that

of the reference scale after the scale density was adjusted using the external reference source, which consisted simply of a heated 750-ohm resistor. The dissipation in the resistor was controlled with a potentiometer so that the reference temperature was always within the range of the temperatures being scanned by the ThermIscope. The temperature of the reference was monitored with a thermistor which was permanently attached to its surface. By using the reference scale generated internally in the recorder and the external calibration source, accurate temperatures at any points on the thermograms could be determined. To speed the data reduction process, digital computer programs were used which converted the densities determined with the densitometer into temperatures. One program was written to provide temperatures for up to four points on each thermogram analyzed. This was useful in determining the maximum temperatures on thermograms. Another program used densitometer readings taken on a grid system from one thermogram and produced temperatures on a correctly-scaled grid in the output. This program was used to produce the temperature field maps of various specimens to be presented later.

During some of the fatigue tests discussed in this study, temperatures at points of interest were monitored using thermistors taped to the bottom sides of the specimens. The thermistors were used with a Yellow Springs Instrument Co. Scanning Tele-thermometer and a Hewlett-

Packard 7100 strip-chart recorder. These measurements were of importance mainly during the first few cycles of the fatigue tests, where the slow scanning rate of the ThermIscope could not give complete information about the transient start-up temperature rise, and at the end of some of the tests when the maximum temperatures exceeded the range of the ThermIscope. For these reasons, thermistors were placed at notch roots and at the centerline of the specimens, where fracture finally occurred.

The difficulty presented by the slow scanning rate of the ThermIscope was apparent only at the start of each fatigue test. It has been suggested that a higher scanning rate would be desirable for this reason, but in order to attain a higher scanning rate, sacrifices would have been made in either thermal or spatial resolution, at least with the scanning infrared cameras available at the time this study was conducted[23]. Once the initial transient passed, the fatigue damage process, including crack propagation, proceeded slowly enough that the heat transfer problem became quasi-steady-state, and the scanning rate was no longer a problem. Far more important was the thermal and spatial resolution combination which led to high-quality thermograms, and the wavelength response of the ThermIscope detector, which was so well matched to the range of temperatures observed in the study. Thus, at the time this study was conducted, the ThermIscope was judged to be the best

choice of scanning infrared cameras for fatigue research.

Mechanical Testing

Specimens were cyclically loaded using the Tatnall-Krouse variable-speed plate-fatigue-testing machine shown in Fig. 6. This testing machine produces a deflection-controlled cyclic bending stress in the plate specimens. The deflection of the free end of the cantilevered specimen is adjustable continuously from 0 to 2.0 inches. The fixed end of the specimen may be adjusted vertically to produce different stress ratios, R, defined as the algebraic ratio of the minimum stress to the maximum stress in a cycle[57]. The frequency of the loading is adjustable from 750 to 2000 cycles per minute. The manufacturer recommends that the force to be applied by the connecting rod at the movable end of the specimen be limited to 150 pounds.

Visual observations of fatigue damage were conducted using a 20-power binocular microscope and a stroboscopic light source. The use of the strobe was necessary since the fatigue tests were not interrupted to make visual inspections. Using this system, fatigue cracks of lengths on the order of 0.01 inches could be readily discerned.

When determined experimentally, strain distributions were found using Micro-Measurements resistance strain gages of 120-ohm nominal resistance. These were used in conjunction with a Vishay Instruments Model 350AK Portable Strain Indicator and a Budd SB-1 Switch and Balance Unit.

Strain gages were also used to help determine the stress-strain curve for the steel used in many of the fatigue tests of this work. The tension tests were conducted in a Riehle testing machine and an Instron testing machine, with a dial-reading extensometer used to read large strains. The extensometer was readable to 0.001 inches.

Procedure

The specimens were prepared in various ways, based mainly on their material group. Some steel specimens were notched simply by cutting a rough slit with a band saw. Most were carefully milled to the required dimensions, and notches of uniform shape and depth were milled into their sides. Tapered specimens were milled to shape and then either drilled or notched as will be discussed in Chapter V. Fiberglass-epoxy specimens were milled with notches much like the steel was, and graphite-epoxy specimens were notched with a saw only.

The importance of the thermal emissivity of the surfaces of the fatigue specimens has already been discussed. Tabulated values[58] for the emissivity of steel, and most other metals in a clean condition, indicated that it would be necessary to enhance the emissivity of the metal specimens in order to obtain good results from the scanning infrared camera studies. This preliminary conclusion was borne out by emissivity tests performed with the ThermIscope, to be described in Chapter IV. Using these tests and some

simple tension tests, it was decided to coat the metal specimens with Krylon Ultra-flat Black spray paint, which brought the emissivity up to very nearly one. It was found that the emissivity of the composite materials was such that painting was unnecessary. This was fortunate in that the fatigue damage which occurred in the fiberglass-epoxy would have been completely obscured by the paint. Since good adhesion of the paint to the specimen was important, careful preparation was given each specimen before painting. The procedure used was much like that used in applying strain gages: the specimens were washed and then sanded lightly with increasingly finer emery cloth, until a smooth, clean surface resulted. Micro-Measurements M-Prep metal conditioner was used during the sanding, and neutralizer was used following the sanding. A final acetone rinse was applied just prior to spraying. Care was taken that each specimen received the same preparation. The specimens were sprayed with paint on the surface which would be observed with the scanning infrared camera, producing a coating with approximately a 0.002-inch thickness.

All the tests conducted in this study were cycled at a frequency of 1,800 cycles per minute, and the stress ratio was maintained at zero with the maximum stress on the top of the specimens always in tension. In order to scan the specimens, which were placed in a horizontal plane, a 45° front-surface mirror was attached to the front of the scanner

unit. This produced images of the specimens that were inverted compared to a normal view of the specimens. Once the tests were started, they were allowed to proceed to completion without interruption, with the exception of one particularly long test. Hence, all thermograms were made while the specimens were being fatigued, as were all visual inspections. The motion of the specimens was in and out of the plane of focus of the scanner, but was sufficiently small that the thermogram quality did not suffer. The detection of small cracks was probably inhibited by the manner in which the inspections were conducted, but this too was deemed insignificant. Indeed, it is possible that the layer of paint on the metal specimens was more detrimental to crack detection by visual inspection than was the decision not to interrupt the tests. When thermistor data were taken using the strip-chart recorder, the thermistor being recorded was changed from the notch root to the specimen centerline as the fatigue cracks propagated.

As already mentioned, thermogram negatives were photographically treated and stored carefully prior to densitometer analysis. The densitometer analysis, in conjunction with the reference scale calibration, yielded the results presented in Chapter V.

CHAPTER IV

EMISSIVITY MEASUREMENTS

Before one can accurately measure the temperature of a surface using the infrared radiation from the surface, the emissivity of the surface must be known. This is particularly true for studies with the scanning infrared camera, since these instruments are calibrated to yield the temperatures of blackbodies, and radiation coming from a gray body (with emissivity less than one) will be misinterpreted as coming from a surface of lower temperature than the actual surface. The emissivity of surfaces can display marked variations with both wavelength of the radiation and the angle from which the surface is viewed. The spectral character of the surface emissivity, or that variation with wavelength, is of importance since the scanning infrared camera has a band of wavelengths to which its detector will respond. The scanning infrared camera actually averages the incoming radiation over this band (8 to 14μ for the ThermIscope) to determine the temperature of the surface. Therefore, a good measure of the emissivity of a surface to be used with scanning infrared camera studies is an average emissivity over the wavelengths to which the instrument responds.

Lerner has proposed an experimental technique for measuring the emissivities of surfaces using the scanning infrared camera[59]. In a report dealing with the emissivity of human skin, he outlined a method whereby the reflectivity of a surface is measured with the thermograph and then used to yield the emissivity of the surface. The technique is an attractive one for use in thermographic studies because the emissivity yielded is one averaged over the wavelength band of the camera's detector response. The experimental procedure itself is quickly carried out, and the necessary calculations are done using widely-published tables of radiation functions. It was decided to use this technique to determine the emissivities of the fatigue specimens tested in this study.

The experimental arrangement used to measure the reflectivities of the specimens is illustrated in Fig. 7. Two different sources of infrared radiation were used. For cases where the reflectivity was expected to be high, a variable-temperature hohlraum was used. The temperature of the source was maintainable at any level up to 230°C (446°F), so it was possible to keep the apparent temperature of the reflection on the surface being scanned within the temperature range of the scanning infrared camera. When the reflectivity of the surface was expected to be very low, a higher temperature globar was used as the infrared source. In some cases, this was the only way a reflected image could

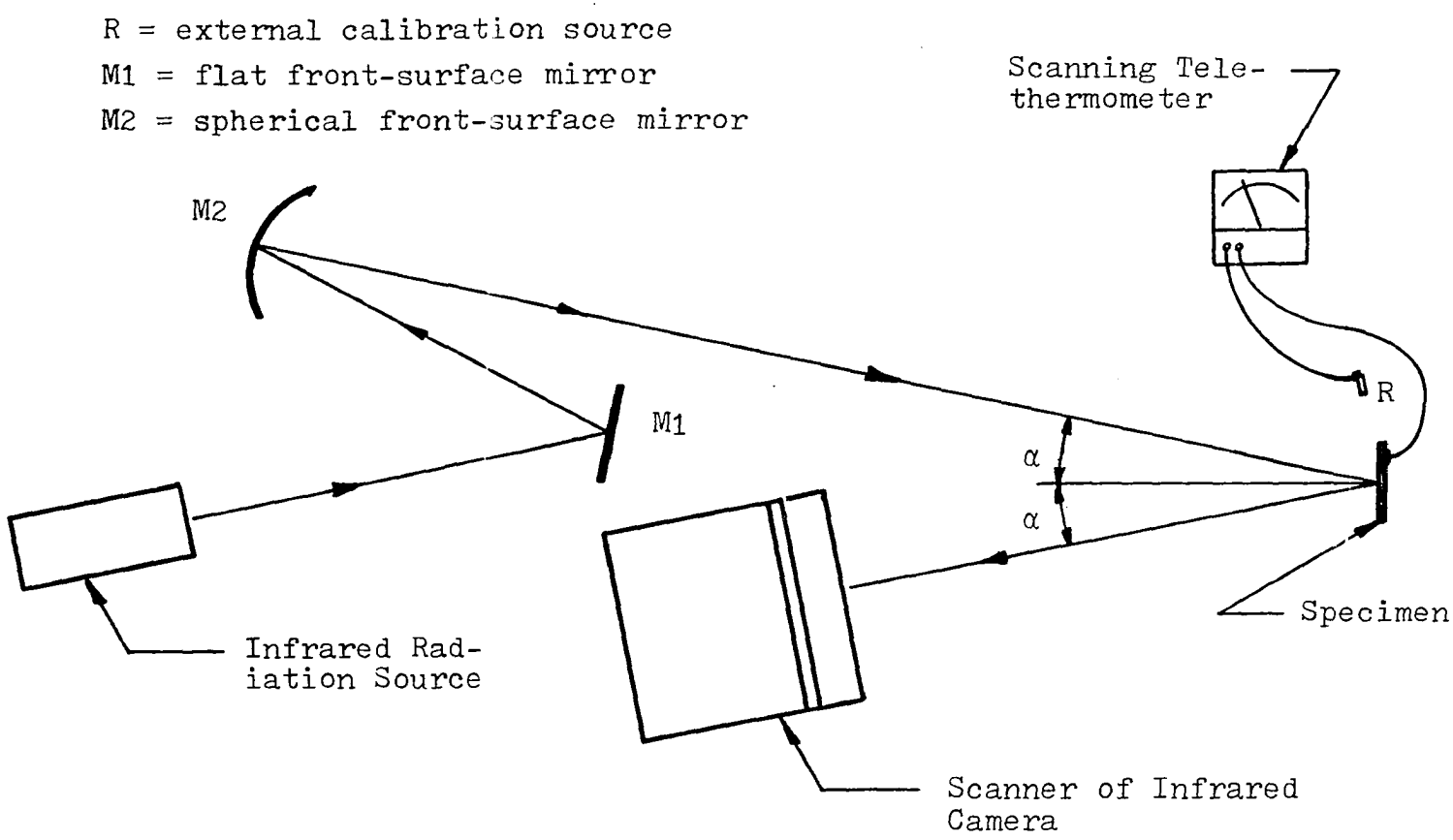

Figure 7. Experimental method for determining surface emissivities using the scanning infrared camera.

be produced on the surface of the specimens. The temperature of the globar was measured using an optical pyrometer, and was found to be about 2135°F. The emissivity of the globar at this temperature was taken to be 0.90, and the hohlraum was treated as a perfect blackbody. The radiation emitted from the infrared source was focused on the surface of each specimen with one flat mirror and one spherical mirror, both front-surface types. The scanning infrared camera was then used to observe the specimens and calculate the apparent temperatures of the images formed. Only the specular component of the reflected image was used. Care was taken with each specimen to ensure that the angles α shown in Fig. 7 were indeed equal and small as practical. The actual temperature of the specimen and the temperature of the reference source were monitored with the tele-thermometer. It was assumed that no heating of the specimen occurred during the exposure to the infrared source. In fact, the fiberglass-epoxy specimen did exhibit a temperature rise due to prolonged irradiation, but this was alleviated by shuttering the infrared source so that the specimen was irradiated only during one scan of the ThermIscope.

Lerner presented a method to determine the emissivity of the surface of the specimen, averaged over the 8 to 14μ wavelength band, using tabulated radiation functions[59]. Assuming that the body does not transmit any radiation, the average reflectivity is determined first, and then sub-

tracted from one to give the average emissivity, $\bar{\epsilon}$. Only the final result of the derivation by Lerner will be presented here. If ϵ_h is the emissivity of the infrared source, and λ_1 and λ_2 are the low and high wavelengths to which the scanning infrared camera responds, then the average reflectivity is given by

$$\bar{\rho} = \frac{\int_{\lambda_1}^{\lambda_2} I_{b,\lambda}(T_i)d\lambda - \int_{\lambda_1}^{\lambda_2} I_{b,\lambda}(T_s)d\lambda}{\epsilon_h \int_{\lambda_1}^{\lambda_2} I_{b,\lambda}(T_h)d\lambda \left[1 - \frac{\int_{\lambda_1}^{\lambda_2} I_{b,\lambda}(T_s)d\lambda}{\epsilon_h \int_{\lambda_1}^{\lambda_2} I_{b,\lambda}(T_h)d\lambda}\right]}, \quad (4.1)$$

where T_i, T_s and T_h are the temperatures of the image, specimen, and hohlraum respectively. The limits for each integral when using the ThermIscope are 8 to 14μ. These integrals are evaluated using tabulated radiation functions[52]. Then the average emissivity is $\bar{\epsilon} = 1 - \bar{\rho}$.

Using the technique outlined above, one can quickly determine the emissivities of any number of surfaces. All of the materials to be used as fatigue specimens were tested without any surface coatings using this technique. Then several commercially-available surface coatings were tested for their emissivities. The results of the tests on the raw

materials are presented in Table II, along with published values of emissivities where available. Note that the published values are not averaged over the range of wavelengths as the scanning camera data are, but rather are normal and total normal emissivities as noted. A few of the values listed specified no particular type of emissivity. The temperature of the body for the published data is given, and that for the scanning camera data was always room temperature, about 70°F. The published data represent only a small portion of the values in the literature, but note that the results using thermography are consistently too high.

The same technique was used to measure the emissivities of several surface coatings. The results of this study are presented in Table III. As can be seen in the table, the emissivities found for the paints are all rather high, especially compared to the published values for lacquers, which range from about 0.95 to 0.98. However, even if the actual values are erroneous, their relative blackness is certainly useful in determining the best choice for fatigue specimens. The proper choice of a surface coating for fatigue specimens is also a function of the adhesion of the paint to the surface. If the paint does not adhere well to the surface, even if slight yielding takes place, the coating may actually shield the surface from the view of the scanning infrared camera. A coating which adheres well to a metallic surface is a better choice for the

Table II. Thermal Emissivities of Materials

Material	Using Thermography		Published Values+		
	Finish	$\bar{\epsilon}$	Finish	e*	Temp.
Mild Steel (sheet)	As delivered	0.82	As rolled	0.66^{1}	70F
	Clean/sanded	0.83	Rough	0.94^{1}	100F
	Shiny oxide	0.80	Shiny oxide	0.82^{1}	75F
	Highly oxidized	0.98	Rough oxide	0.80^{1}	70F
			Oxidized	0.85^{3}	100F
			Oxidized	0.81^{2}	25C
			Cold rolled	0.80^{2}	93C
			Stained	0.65^{2}	25C
Aluminum (sheet)	Unprepared	0.61	Dull	0.18^{2}	70F
	Sanded	0.93	Oxidized	0.11^{1}	100F
	Polished	0.22	Heavy oxide	0.87^{2}	100C
			Polished	0.05^{2}	100F
Fiberglass -epoxy	Cleaned	0.98	Clean	0.88^{1}	300C
Graphite-epoxy	As received	>.99	-	-	-

*Superscript refers to type of emissivity reported:
1 = "Total Normal"
2 = "Total"
3 = Unspecified

+Source: References 52, 54, and 58.

Table III. Surface Coating Properties

Surface Coating*	$\bar{\epsilon}$**	σ_f(psi)	Amount of Flaking at 40 Ksi
Paints:			
Flat black enamel (T.G.&Y.)	0.995	36,800	Light
Flat black lacquer (Floquil RR10S)	0.997	36,160	Medium
3M Optical black	0.999+	37,700	Heavy
Flat black paint (Krylon)	0.997	38,400	Extremely light
Flat black paint ("Bar-B-Q")	0.998	34,800	Medium
Others:			
Metal Bluing Dye	0.995	28,800	Heavy
Black undercoating (Stresscoat)	0.993	38,080	Heavy
Chemical blackener (Hobby Black)	0.996	32,640++	Light

*On clean, sanded steel plate

**Accuracy to 3 places implied only as a relative measure

+Reported to be 0.93 in 8 to 14μ wavelength; ref. 60

++Flaking occurred as a fine dust rather than flakes

σ_f = stress at which first flaking was observed

purposes of this study than one that does not, even if the latter has a higher emissivity. To determine the relative quality of the adhesion of each of the surface coatings, tensile loads were used to strain the material while the coating was carefully observed for signs of flaking. The stress level at which flaking first was observed, and the amount of flaking present at a stress of 40,000 psi are also given in Table III. It should be noted that each sample coating was prepared in the same manner (using the procedure outlined previously) and on material from a single sheet of steel.

It appears from some published data that in both Table II and Table III the values obtained for the emissivities of the surfaces and the coatings are unrealistically high. This may be the result of errors in the temperatures measured or errors accumulated in the use of the tabulated radiation functions. However, an error of 20°C in measuring (or controlling) the hohlraum at 220°C would yield an emissivity of 0.995 rather than the value 0.997 given in Table III for Krylon paint. On the same specimen, an error of 10°F in measuring the image temperature leads to an emissivity of 0.987. Although the calculation of eq. (4.1) is thus more sensitive to an error in determining T_i, such a large error in measurement is not to be expected, and it would appear that there is something more basic wrong with this approach to emissivity determination.

Nevertheless, the results of this technique are useful in selecting which materials should be coated, and which coating is best suited to the demands of thermographic fatigue studies. On the basis of the results obtained here, it was decided that the metals used must be coated, but that the composite materials studied did not need a coating. Furthermore, taking into consideration the results of the adhesion tests, it was decided that Krylon flat black paint was the best choice for coating the metal specimens, even though it did not display the highest relative emissivity.

CHAPTER V

EXPERIMENTAL RESULTS

The fatigue tests comprising the experimental portion of this study were conducted using specimens of various materials made in several geometries. As noted in Chapter III, all tests were conducted with the same loading frequency (1,800 cycles/minute), and with the same stress ratio ($R = 0$). The results of these tests take several forms. Thermograms provide the source of the data, which can be presented as temperature rises during the tests, isotherm maps at any time, or heat generation rates at any time, among other possibilities. It is not practical to present here the results of all of the many fatigue tests conducted. Rather, important tests for each material will be selected for discussion to show clearly the potential for thermographic fatigue testing and to illustrate the technique for gaining various data for each case. The results will be arranged according to the material used, and chronologically within each material classification.

Fatigue Tests Using Steel

A large number of fatigue tests were conducted using

mild steel specimens. Many of the "preliminary" tests on steel were conducted to determine the possibilities of the method with this material and to discern just what type of results were obtainable.

One early fatigue test of interest was conducted using a mild steel specimen of the geometry shown in Fig. 8. This specimen was cycled in bending with a nominal stress of about 56,000 psi while being observed with the scanning infrared camera. The single notch in the specimen, which was produced by cutting with a band saw, provided a stress concentration where the fatigue crack would eventually form in the material. Hence, it was possible to observe that location carefully in order to correlate the thermographic findings to the visual inspections.

One thermogram taken during the fatigue test of the single-notched steel specimen is shown in Fig. 9. This thermogram was taken at 3,400 cycles, or about 4.7 percent of the life of the specimen (72,000 cycles). The room temperature for this test was constant at 69°F. As can be seen from the reference scale at the right of the figure, the range of temperatures covered in this thermogram is from 70°F to 75°F. At temperatures below 70°F or above 75°F, objects being scanned will be presented as all black or all white respectively. Recall that this instrument is calibrated for use with blackbodies, so reflected radiation from non-blackbodies can make them appear even if their tempera-

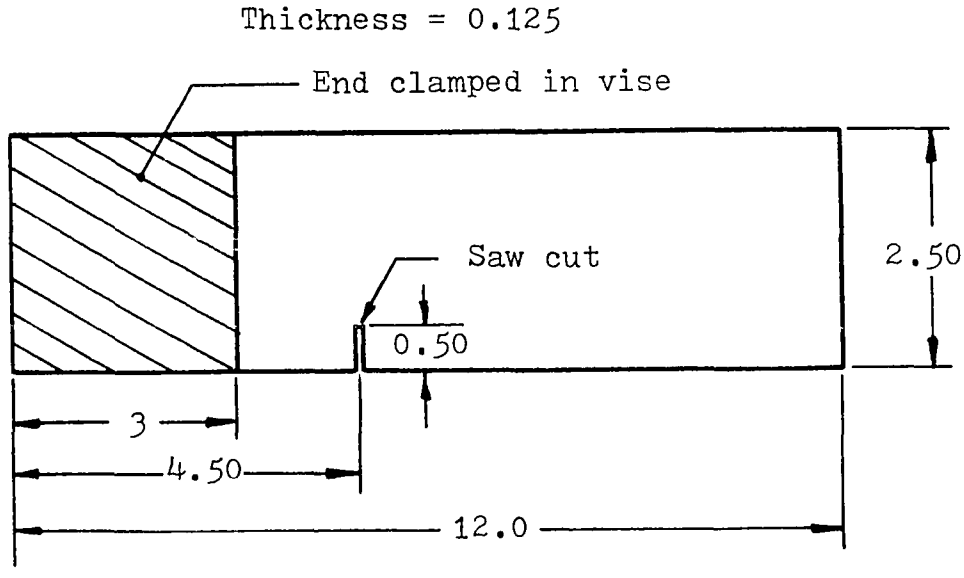

Figure 8. Single-notched steel fatigue specimen (Dimensions given in inches).

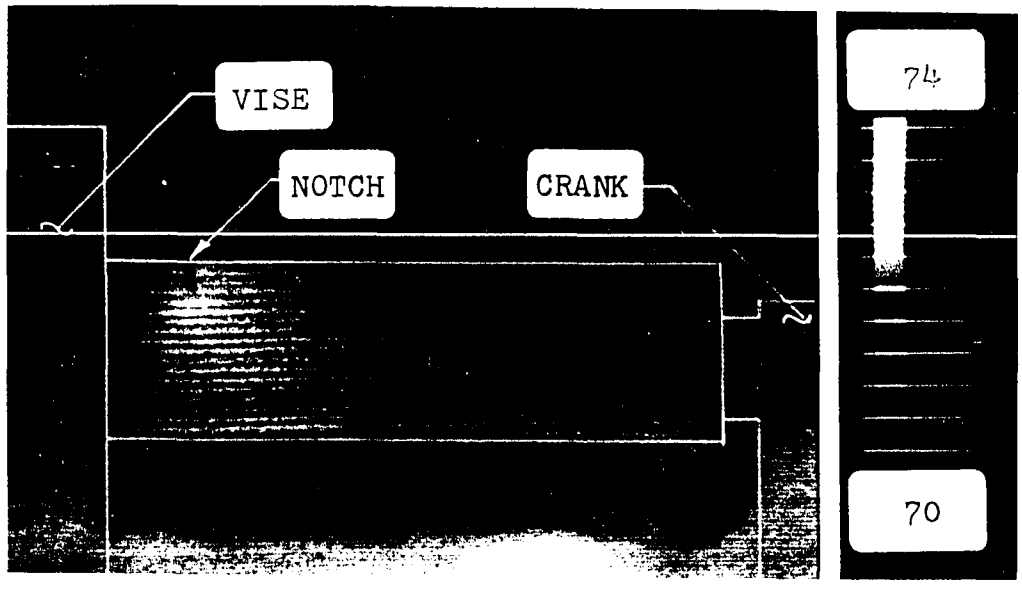

Figure 9. Thermogram of single-notched steel fatigue specimen at 3,400 cycles.

ture is below 70°F. The reference temperatures on the figure have been corrected to account for the slight miscalibration of the ThermIscope. The specimen and other prominent features have been outlined on Fig. 9 for clarity. The vise of the Tatnall-Krouse fatigue machine is at the left. The right end of the specimen is deflected during the test. The crank and frame of the testing machine appear white because they are reflecting infrared radiation from their smooth surfaces rather than because they are blackbodies at high temperatures. A slight temperature rise can be seen on the surface of the single-notched specimen, located at the tip of the notch. This is an early indication of the location of the eventual fatigue crack. The probable cause of the heat dissipation at this early phase of the fatigue life of the specimen is severe work hardening occurring around the notch root, and the initial slipping in the material which will lead to the formation of a crack.

Figure 10 shows a series of temperature field maps taken from three thermograms of this fatigue test. Figure 10(a) was taken from the thermogram of Fig. 9. Although information some distance from the notch root is hard to obtain, this figure clearly shows the temperature rise at the root of the notch to be 3.42°F above the ambient temperature. The temperature field map of Fig. 10(b) was taken from a thermogram of the specimen at 27,700 cycles. In this figure, the maximum temperature has increased to 8.1°F above room

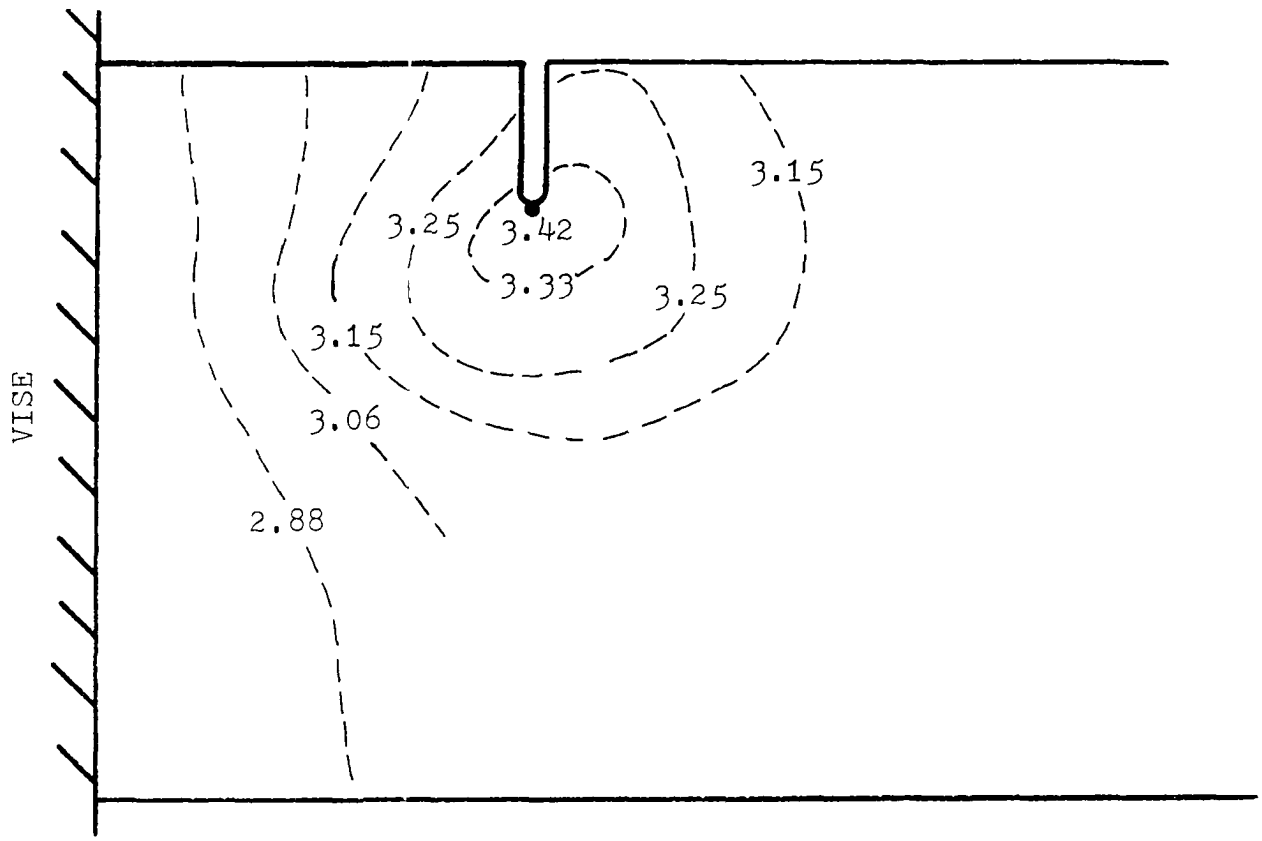

Figure 10(a). Temperature field map of single-notched steel specimen at 3,400 cycles (Temperatures in deg. F above ambient).

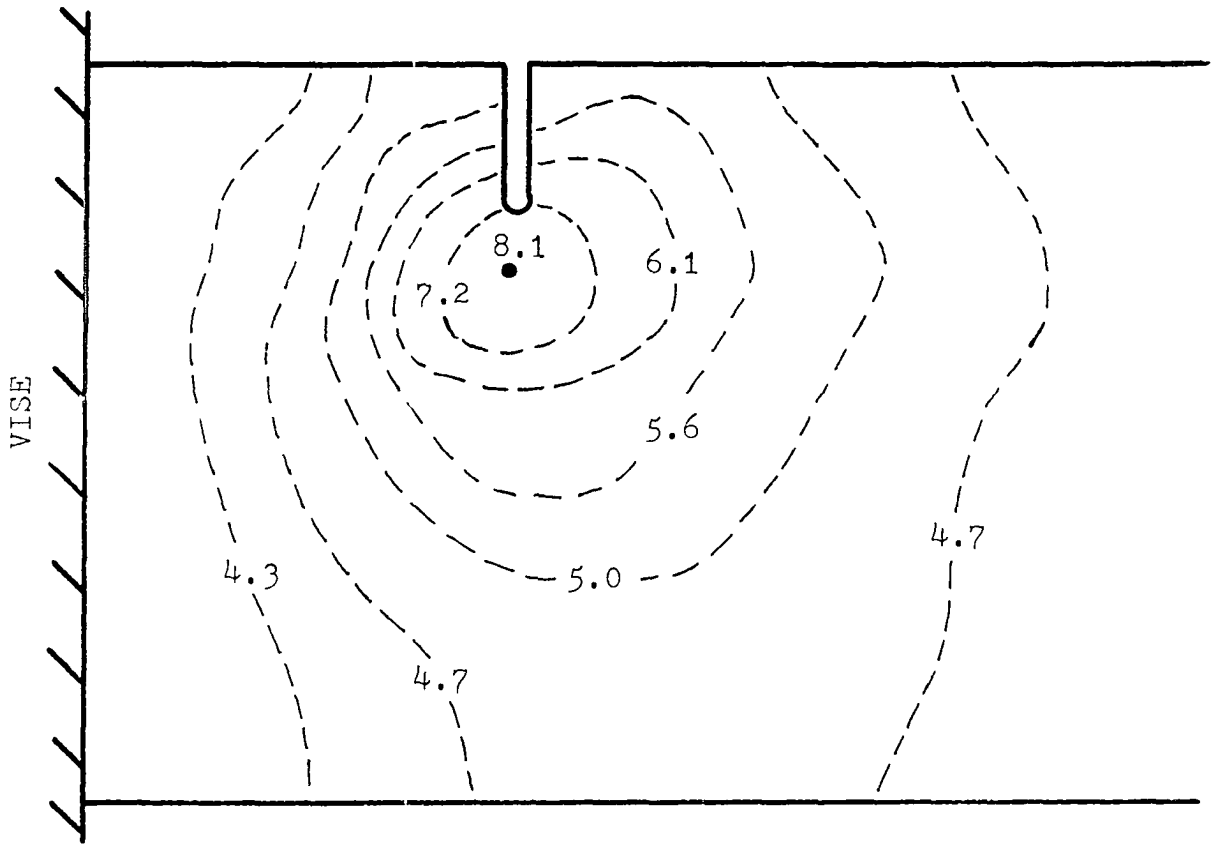

Figure 10(b). Temperature field map of single-notched steel specimen at 27,700 cycles (Temperatures in deg. F above ambient).

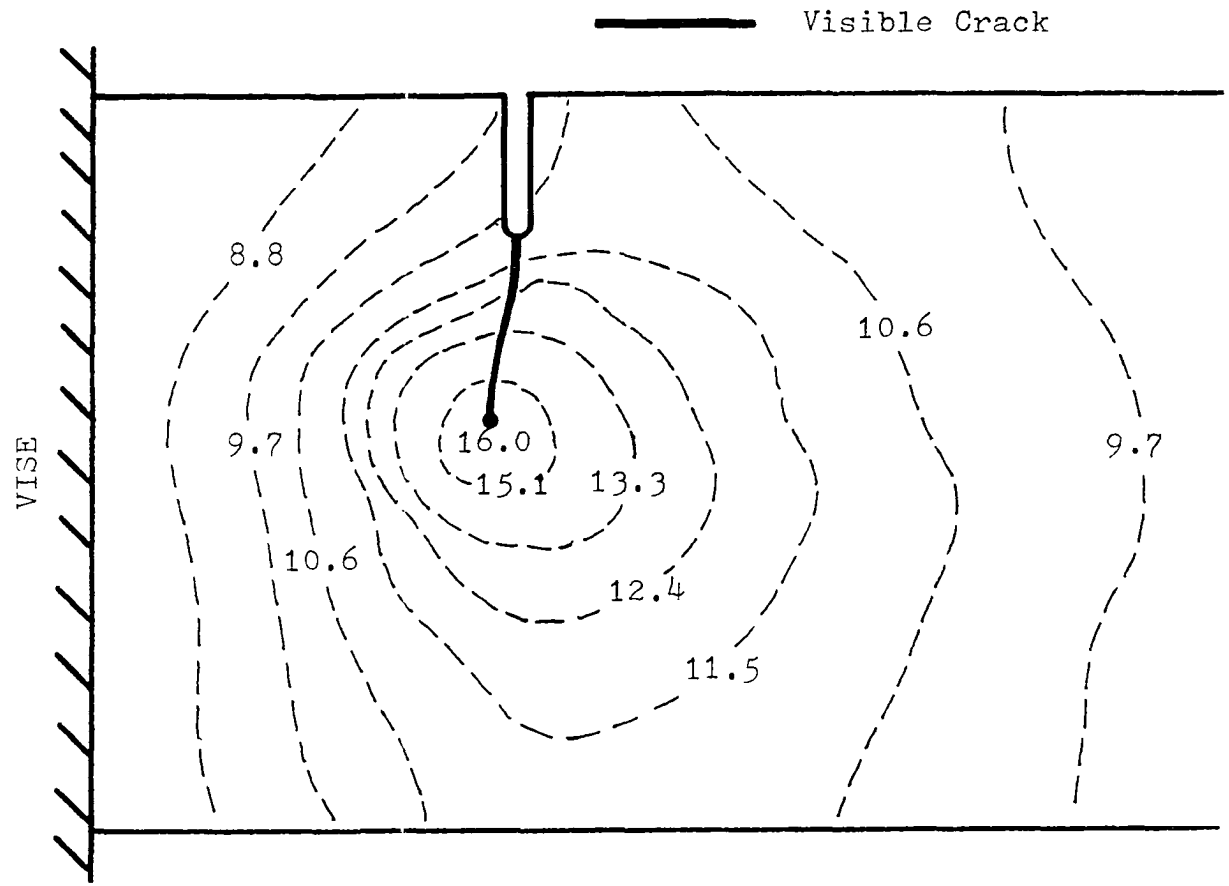

Figure 10(c). Temperature field map of single-notched steel specimen at 60,000 cycles (Temperatures in deg. F above ambient).

temperature, and the point at which it occurs has moved toward the centerline of the specimen. It is apparent that a fatigue crack is now propagating across the specimen, since the hottest point on the specimen can be taken to indicate the location of the tip of a crack. It is interesting that a visual observation just prior to the taking of the thermogram yielding Fig. 10(b) revealed no fatigue cracks. A visible crack was measured at the time of Fig. 10(c), which was taken at 60,000 cycles. As indicated, the hottest point on the thermogram corresponded to the tip of the propagating crack.

Figure 11 presents the maximum temperature rise on the single-notched specimen as a function of the number of fatigue cycles endured by the steel. Note that there is an initial period of rapid temperature rise followed by a longer one of gradual rise. At the end of the second period, the presence of the fatigue crack was indicated by Fig. 10(b), several thousand cycles before the crack was found visually. Thus, in this preliminary fatigue test on steel, a significant number of tentative conclusions were formed. First, there was considerable early warning of the eventual site of the formation of the fatigue crack (even though it was preordained where the failure would initiate by the presence of only one stress concentrator). The ability to accurately map the temperature field on the specimen was shown, and led to the detection of a fatigue crack prior to visible detection

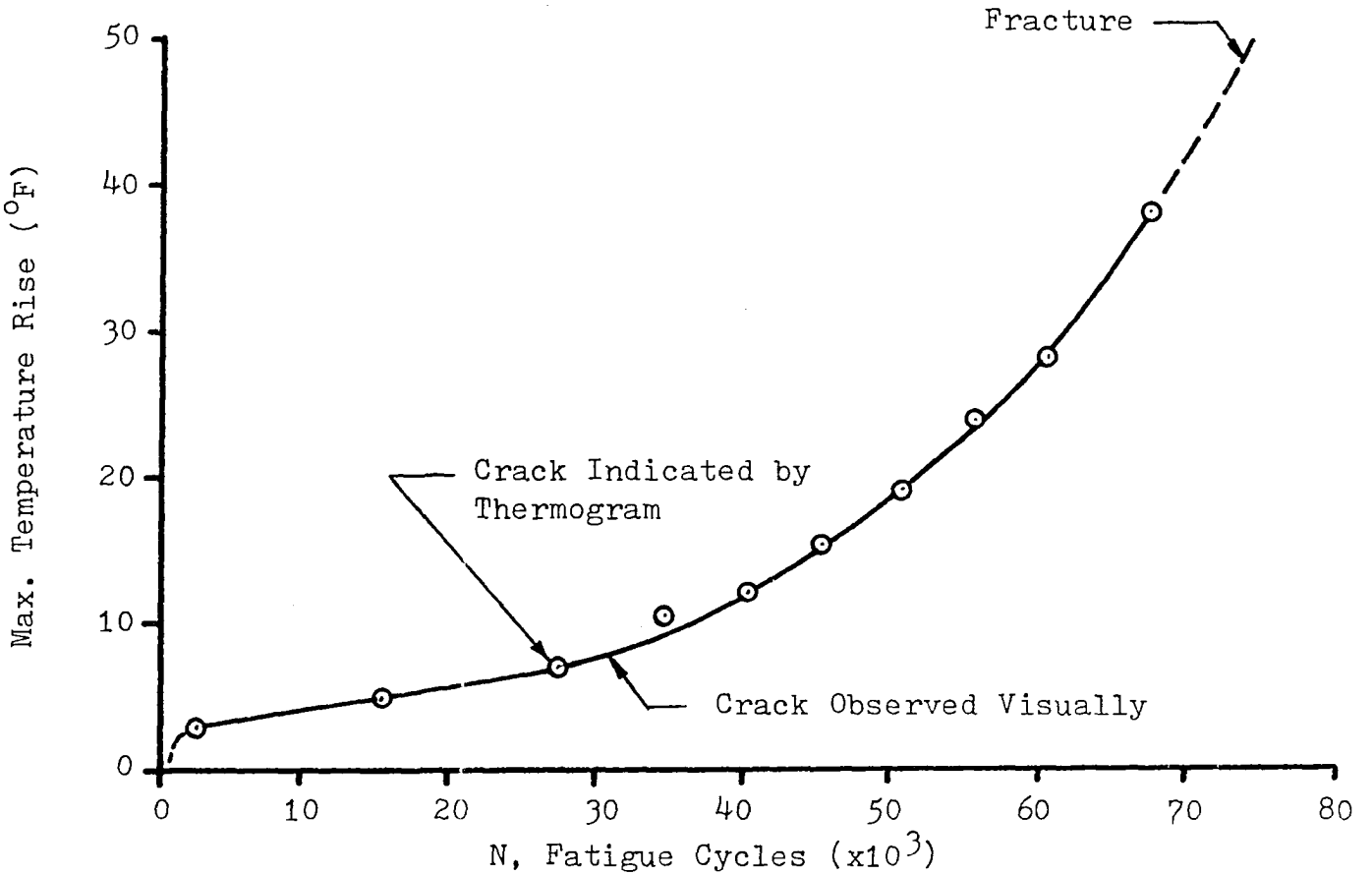

Figure 11. Maximum temperature rise above ambient during test of single-notched steel specimen.

of one. Of course, the stress level used was high, but the results were quite promising.

The possibilities of early prediction of likely areas for fatigue damage and early detection of fatigue damage were further investigated using a tapered steel specimen. This specimen is shown in Fig. 12. Without the presence of holes, the tapered section would result in a uniform bending stress on the top surface of the specimen during the fatigue test. Three holes were drilled on the centerline of the specimen within the tapered section. Each was sized to remove 20 percent of the area at its position along the centerline. Thus, three stress concentrators were introduced into the material, and the prediction of just where the fatigue damage would be greatest became difficult. The specimen was fatigued at a maximum nominal bending stress level of 50,000 psi on the top of the beam in the tapered section. Room temperature was again constant at 69°F throughout the test.

Figure 13 shows the temperature field map which was obtained from a thermogram taken at just 1,100 cycles into the fatigue test of the tapered steel specimen. No visible damage was present at any of the three holes. Only two of the holes are included in Fig. 13, since no measurable temperature rise occurred at the smallest hole near the crank. At the time of Fig. 13, temperature rises can be seen at both of the holes shown, with the maximum temperature rise at the

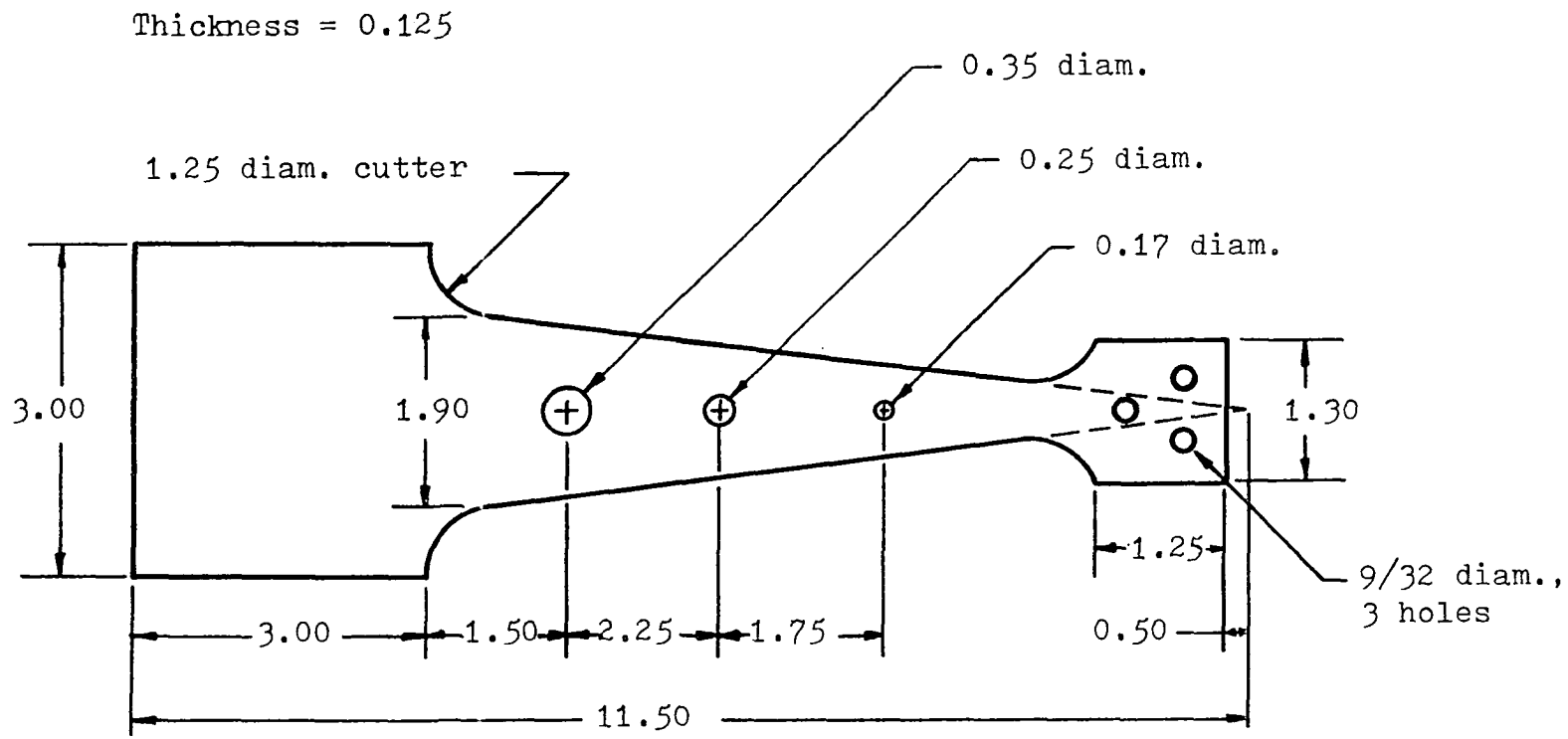

Figure 12. Tapered steel fatigue specimen (Dimensions in inches).

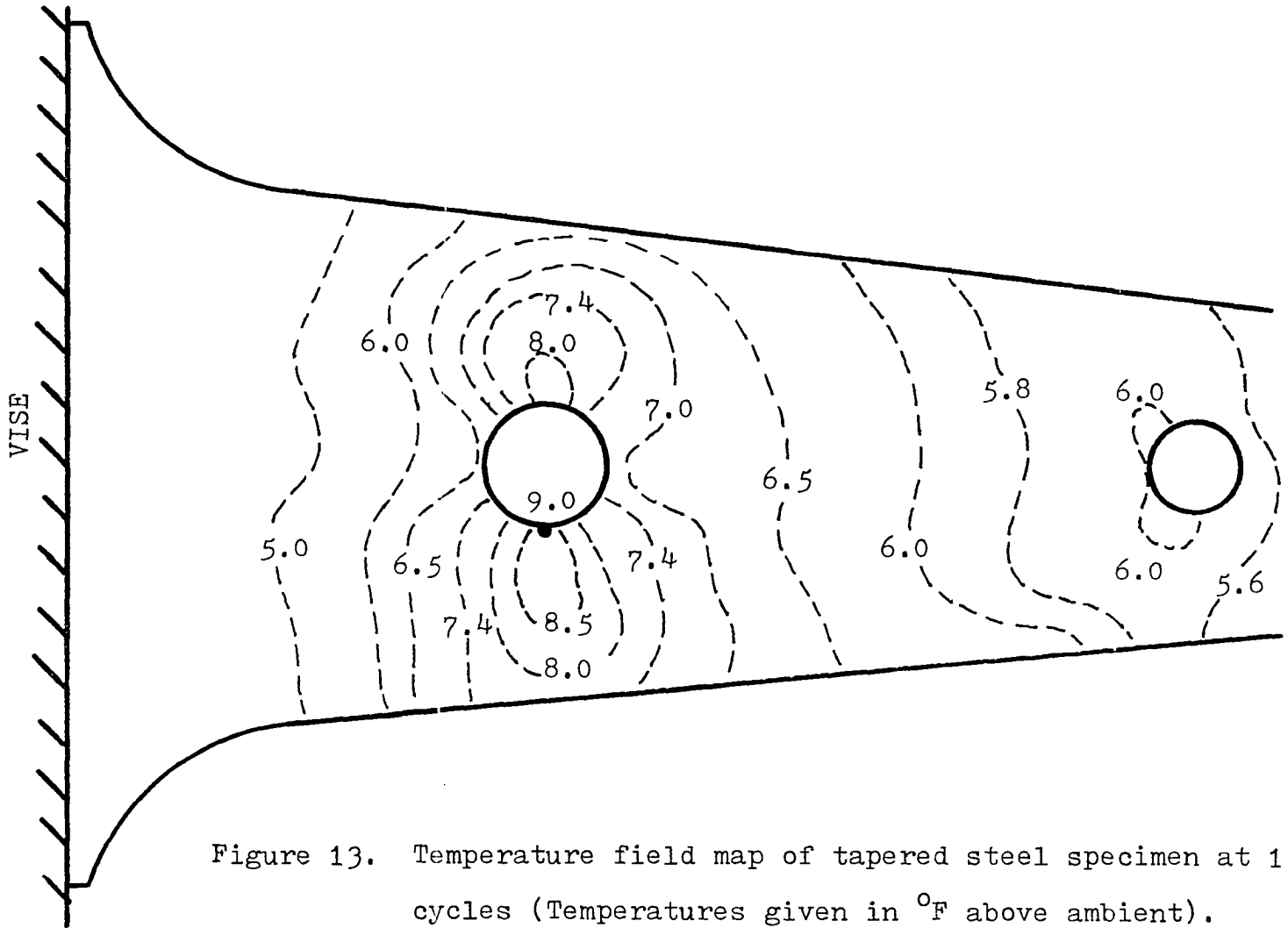

Figure 13. Temperature field map of tapered steel specimen at 1,100 cycles (Temperatures given in ^{o}F above ambient).

lower edge of the larger hole in the figure. The extent of the temperature rise indicates that the maximum fatigue damage (work hardening, slipping, etc.) is occurring at the lower edge of the largest hole in the specimen. The upper edge of the same hole is also the site of substantial damage processes, as indicated by its temperature rise. The middle hole in the specimen is also causing some fatigue damage to occur, but by its temperature rise, one concludes that the extent of the damage is less than that at the larger hole. By 10,000 cycles, the temperature rise at the largest hole had increased and dominated the temperature field image produced by the ThermIscope. The hottest point continued to be at the lower edge of the largest hole, but no visible damage was detected at 10,000 cycles. In fact, it was not until 30,000 cycles that a fatigue crack was finally detected, propagating from the lower edge of the largest hole in the specimen. Failure finally occurred at the section of the largest hole at 45,000 cycles.

The results of the test with the tapered steel specimen are important. The location of the eventual fatigue crack was predictable from the thermographic data at only 2.5 percent of the life of the specimen. It was not until some 67 percent of the specimen's life that any visible damage was detected. At that time, careful attention was being paid to the edge of the largest hole, or it might have been possible to have missed the damage even then. It might be

argued that the largest hole is indeed the most likely site for damage from a careful study of the stress concentrations in the specimen, but to predict on which side of the hole the eventual failure would begin would be difficult indeed. The thermographic results, however, readily gave the location where the fatigue crack eventually formed, and allowed the damage to be observed as early as possible by focusing attention on a particular area of the specimen.

The previously-desrcibed fatigue tests were conducted primarily to determine the potential of the use of thermography in fatigue studies and to gain experience in the technique. Careful controls on the materials used were not imposed, nor were the stress and strain distributions on the material investigated. However, a comprehensive series of 25 fatigue tests was performed on double-notched steel specimens. Here, the mechanical properties of the material were studied, and stress and strain distributions were obtained for each specimen. Careful controls were imposed so that each specimen received the same treatment prior to testing. This included the specimen machining, painting and storage. All specimens were cut from a single sheet of steel. The stress levels were maintained well below those of the previous two tests in order to gain more useful data from a designer's standpoint.

The specimen geometry for this double-notched steel series of fatigue tests is illustrated in Fig. 14. The

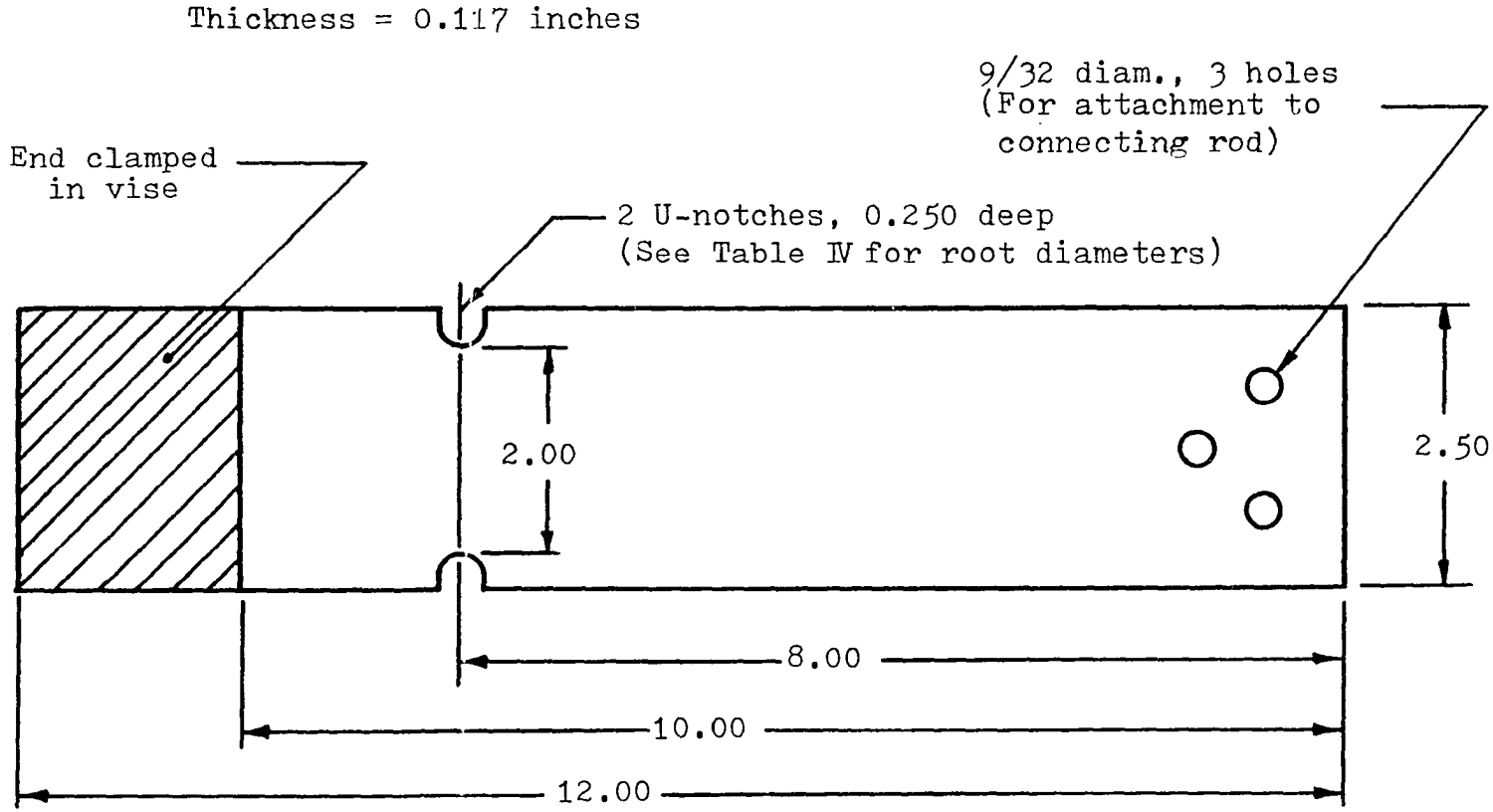

Figure 14. Double-notched steel fatigue specimen (Dimensions in inches).

notches milled into the sides of the specimens ranged in diameter from 0.094 inches to 0.500 inches; the notches on a given specimen were identical and exactly opposite one another. Regardless of the diameter used, the notch depth was maintained at 0.250 inches, leaving a reduced width of 2.00 inches on each specimen. The thickness of the sheet used for these specimens was 0.117 inches.

In order to determine the yield stress of the material and to obtain stress distributions on the fatigue specimens, a series of tensile tests was conducted using a Riehle testing machine. The material specification on the order from the supplier was for 1018 cold-rolled sheet. The data obtained on the Riehle testing machine did not agree well with the published properties of the specified steel. Nor did the resulting stress-strain curve display the upper and lower yield point behavior typical of mild steel. Furthermore, the modulus of elasticity determined from the tests was only 25 million psi, well below the expected value of 30 million psi. Further tests were conducted to determine if the difference in the values obtained and those expected for mild steel were the result of either machine miscalibration or operator error. These tests were carried out using the Riehle testing machine, an Instron tensile testing machine, and a cantilever beam of the material. Data were taken from strain gages and an extensometer during most of the tests. It was found that the data from these tests sup-

ported the results obtained initially, indicating that the material used was in fact not the 1018 cold-rolled steel specified by the supplier. A stress-strain curve, as determined experimentally, for the material is given in Fig. 15. This curve represents only the initial part of the curve, which is the region of interest for this study. The strain at failure was approximately 0.55 in./in., and the ultimate tensile stress for the material was nearly 43,500 psi. Complete data and a more detailed stress-strain curve for the material are given in Appendix B.

As can be seen from Fig. 15, the steel used for the double-notched fatigue specimens exhibited a low yield stress, and showed no definite yield point in any of the tension tests performed. Therefore, it is appropriate to express the yield stress of the material as the ASTM 0.2 percent offset yield stress, which was 26,000 psi. Another possible measure of the yield strength of the material is Johnson's apparent elastic limit, where the slope of the stress-strain curve is fifty percent less than the initial slope[61]. This occurred at a stress of 19,000 psi for the material.

The 25 specimens were fatigued in groups of five (each of the five having a different notch diameter) at five different stress levels. The strain and stress distributions on the specimens were determined using strain gages on the specimens and the stress-strain curve shown in Fig. 15. Gages were placed at three positions across the width of the

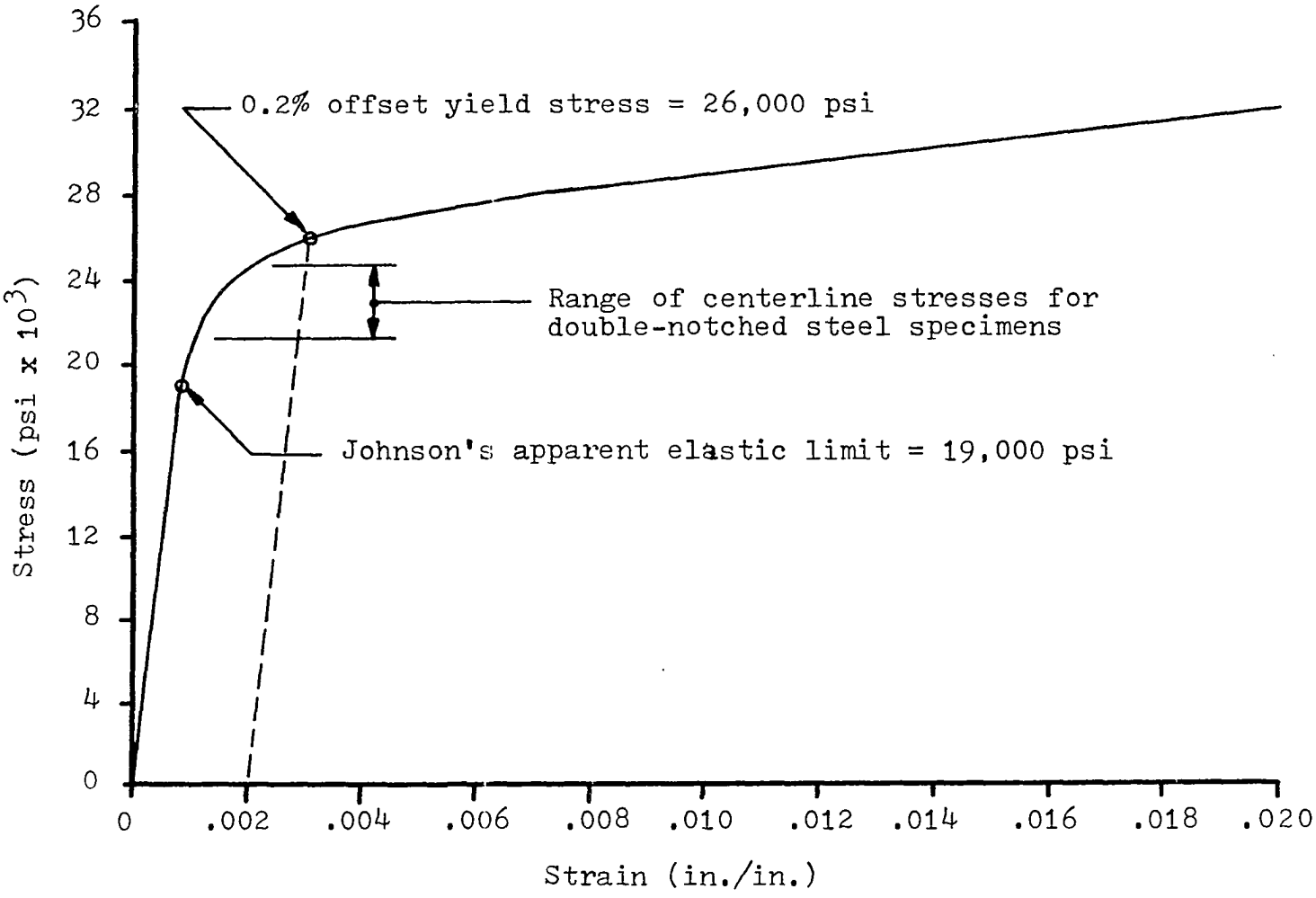

Figure 15. Stress-strain curve for double-notched mild steel fatigue specimen material.

specimen as shown in Fig. 16. The gage on the specimen centerline (CL) was used to determine the maximum centerline bending stress for each geometry at each level. The resulting range of centerline stresses which will be used to distinguish the stress level for each test is indicated on Fig. 15. The range of centerline stresses falls between Johnson's apparent elastic limit and the offset yield stress. This results in a somewhat narrow range of stresses, but does in fact represent a range of centerline strains from 1,160 μin./in. to 2,130 μin./in., a more reasonable difference.

Table IV gives the strain and stress levels for all of the tests in the double-notched steel series. In addition, the notch root diameters and the specimen numbers are given. As can be seen, the entire group of tests is broken down into five "series", each at a given centerline bending stress level. Within each series, there are five specimens with different notch root diameters as listed. The series number corresponds to the last digits in the specimen numbers used.

Figure 17, (a) through (e), gives the strain and stress distributions in each of the specimens, as determined from strain gage measurements. The locations indicated in Fig. 17 correspond to the positions shown for the gages in Fig. 16. Each of the graphs for Fig. 17 is for a given notch root diameter. For example, Fig. 17(a) is for a notch root diameter of 0.094 inches, etc. The use of Fig. 17 ena-

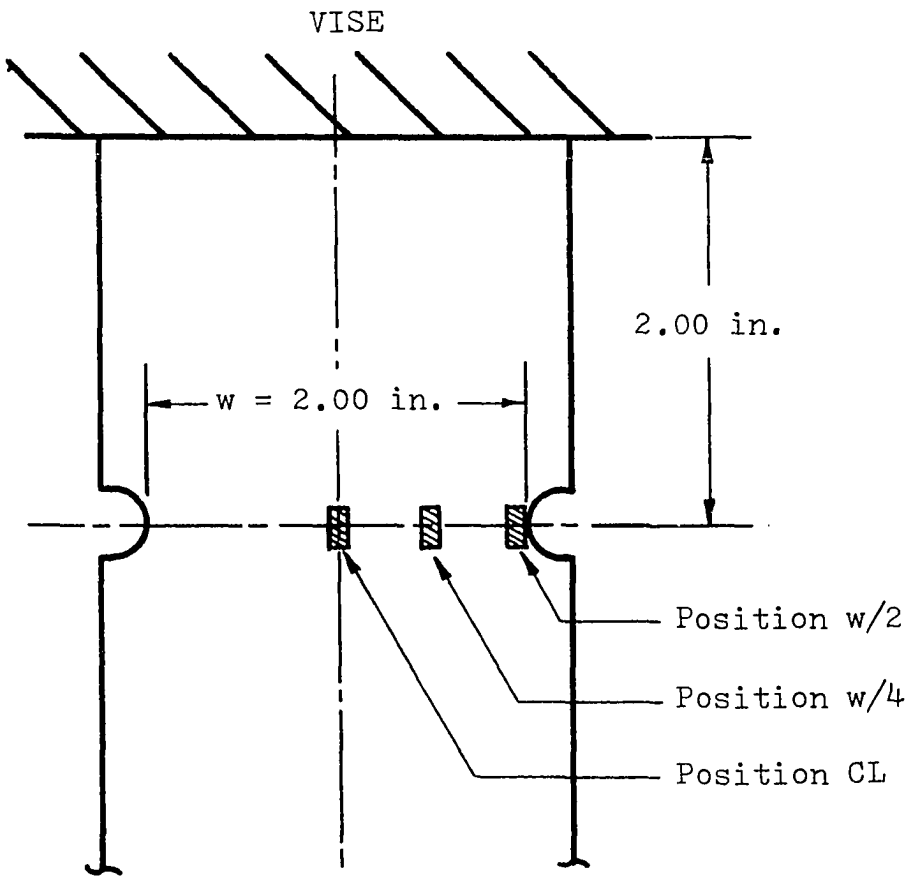

Figure 16. Strain gage positions for double-notched steel fatigue specimens.

Table IV. Double-notched Steel Fatigue Tests

Series	Specimen No.	D_{notch} (inches)	Max. Centerline Levels	
			Stress (psi)	Strain (μin./in.)
1-6	S-31	0.500	21,600	1160
	S-36	0.375		
	S-41	0.250		
	S-46	0.125		
	S-51	0.094		
2-7	S-32	0.500	22,700	1410
	S-37	0.375		
	S-42	0.250		
	S-47	0.125		
	S-52	0.094		
5-0	S-35	0.500	23,600	1660
	S-40	0.375		
	S-45	0.250		
	S-50	0.125		
	S-55	0.094		
3-8	S-33	0.500	24,300	1920
	S-38	0.375		
	S-43	0.250		
	S-48	0.125		
	S-53	0.094		
4-9	S-34	0.500	24,700	2130
	S-39	0.375		
	S-44	0.250		
	S-49	0.125		
	S-54	0.094		

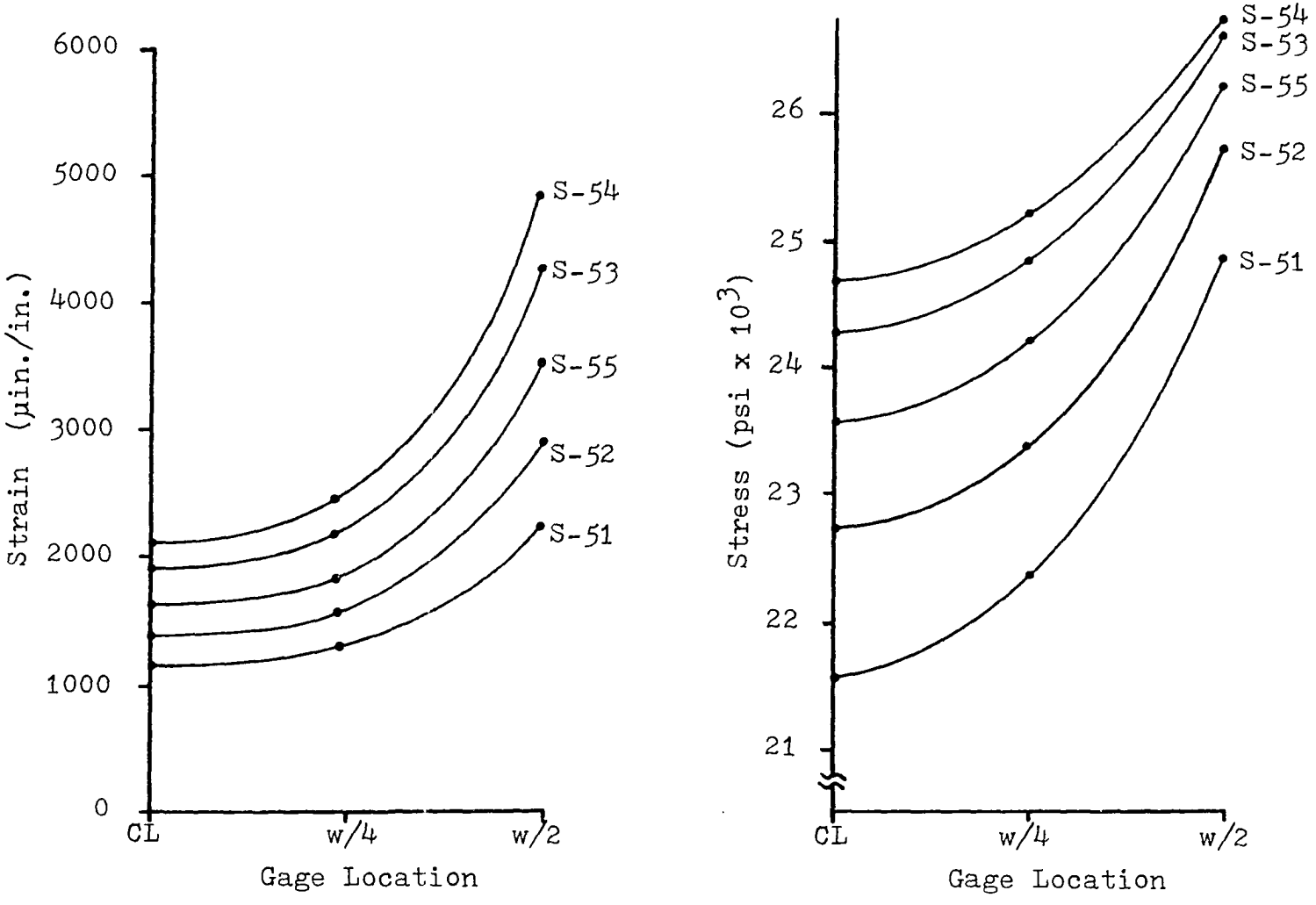

Figure 17(a). Strain and stress distributions at notches for double-notched steel fatigue specimens with D_{notch} = 0.094 in.

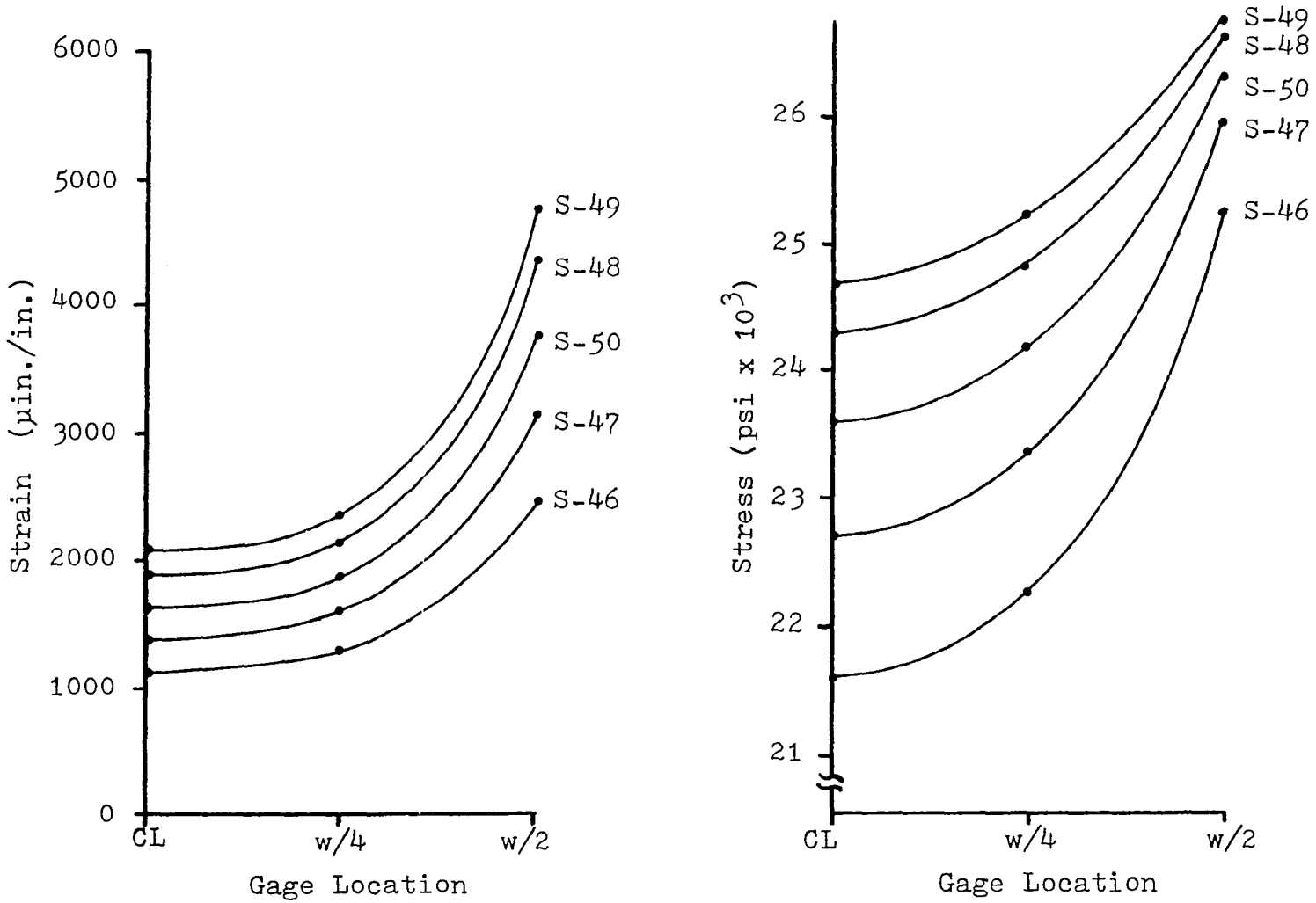

Figure 17(b). Strain and stress distributions at notches for double-notched steel fatigue specimens with D_{notch} = 0.125 in.

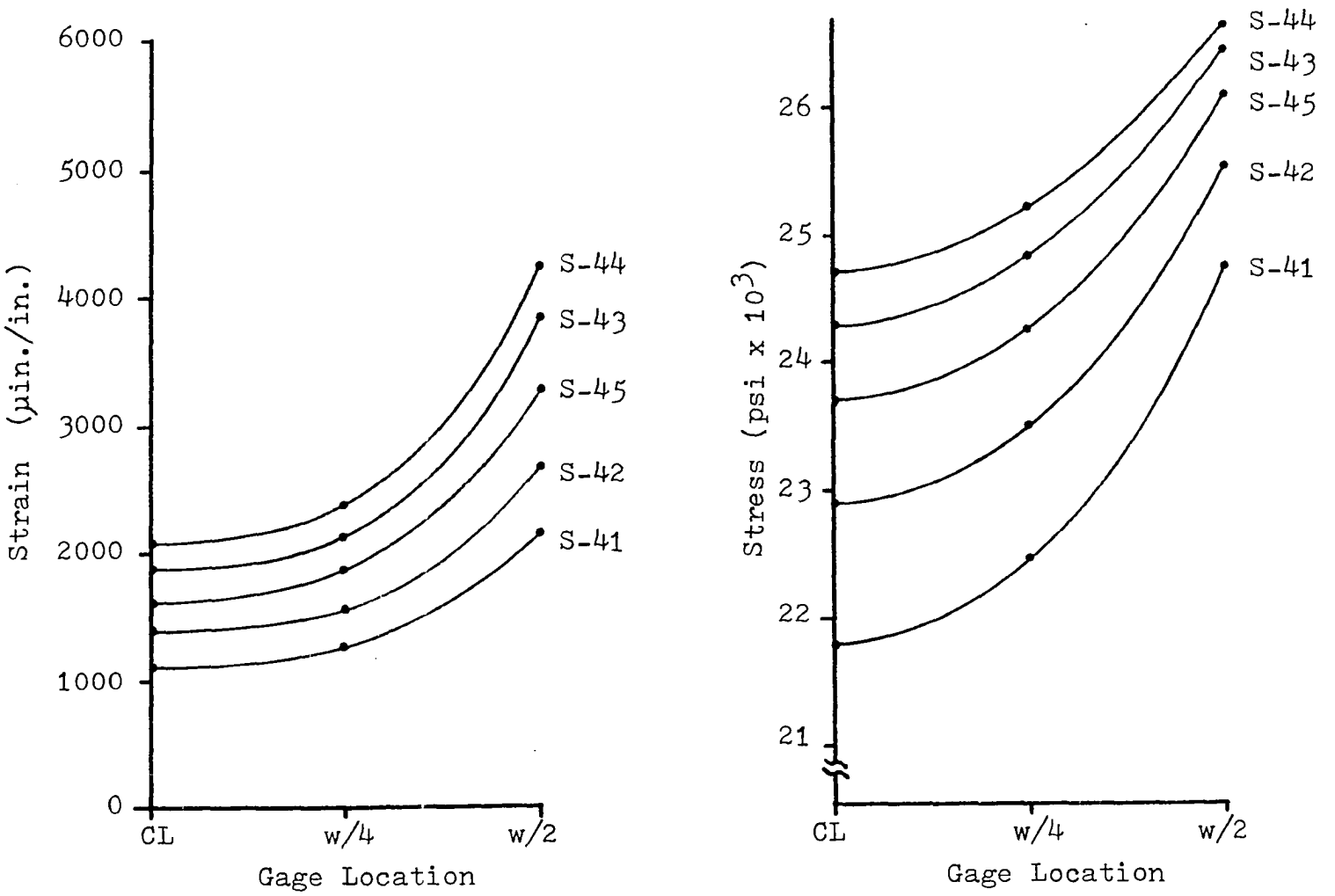

Figure 17(c). Strain and stress distributions at notches for double-notched steel fatigue specimens with D_{notch} = 0.250 in.

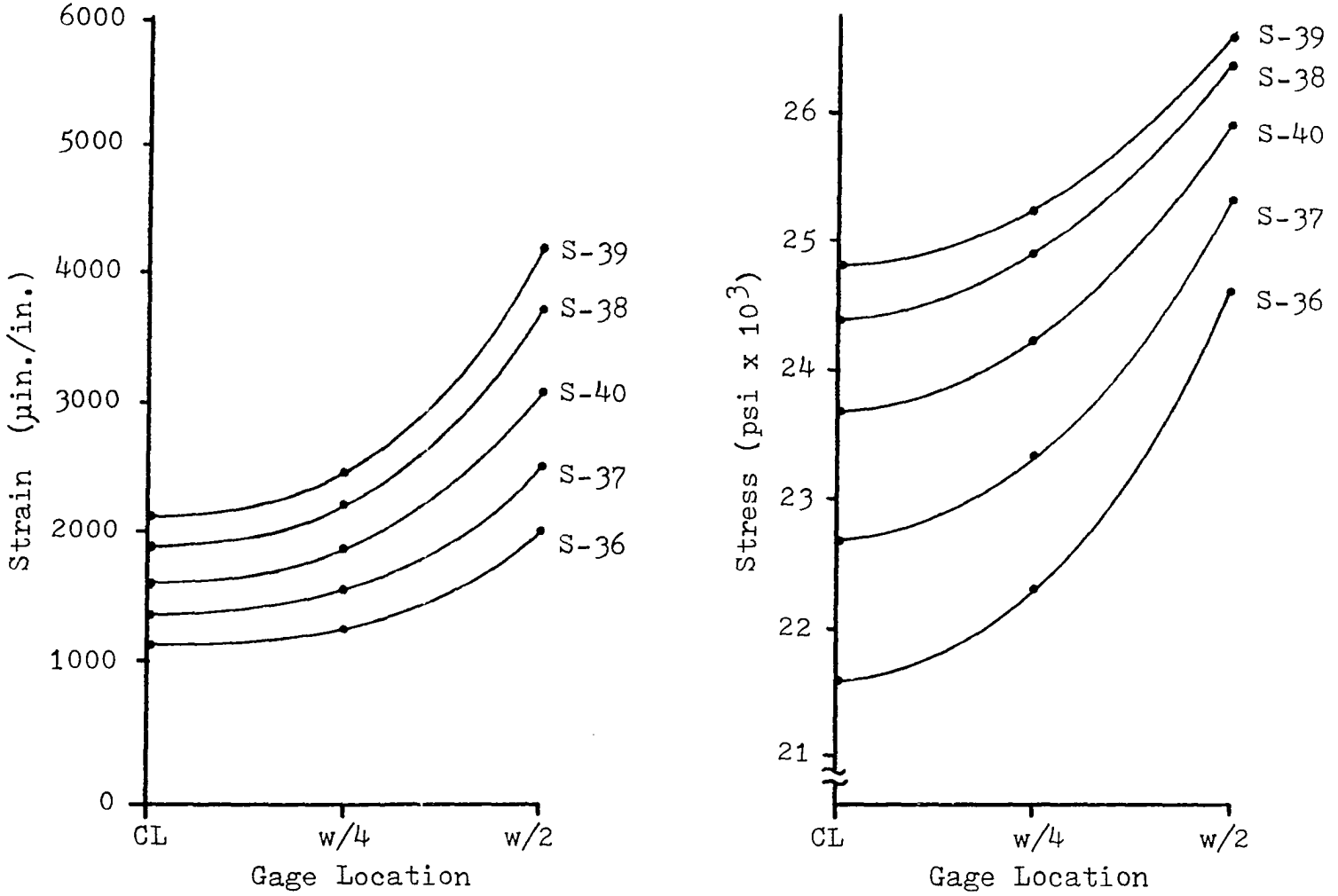

Figure 17(d). Strain and stress distributions at notches for double-notched steel fatigue specimens with D_{notch}= 0.375 in.

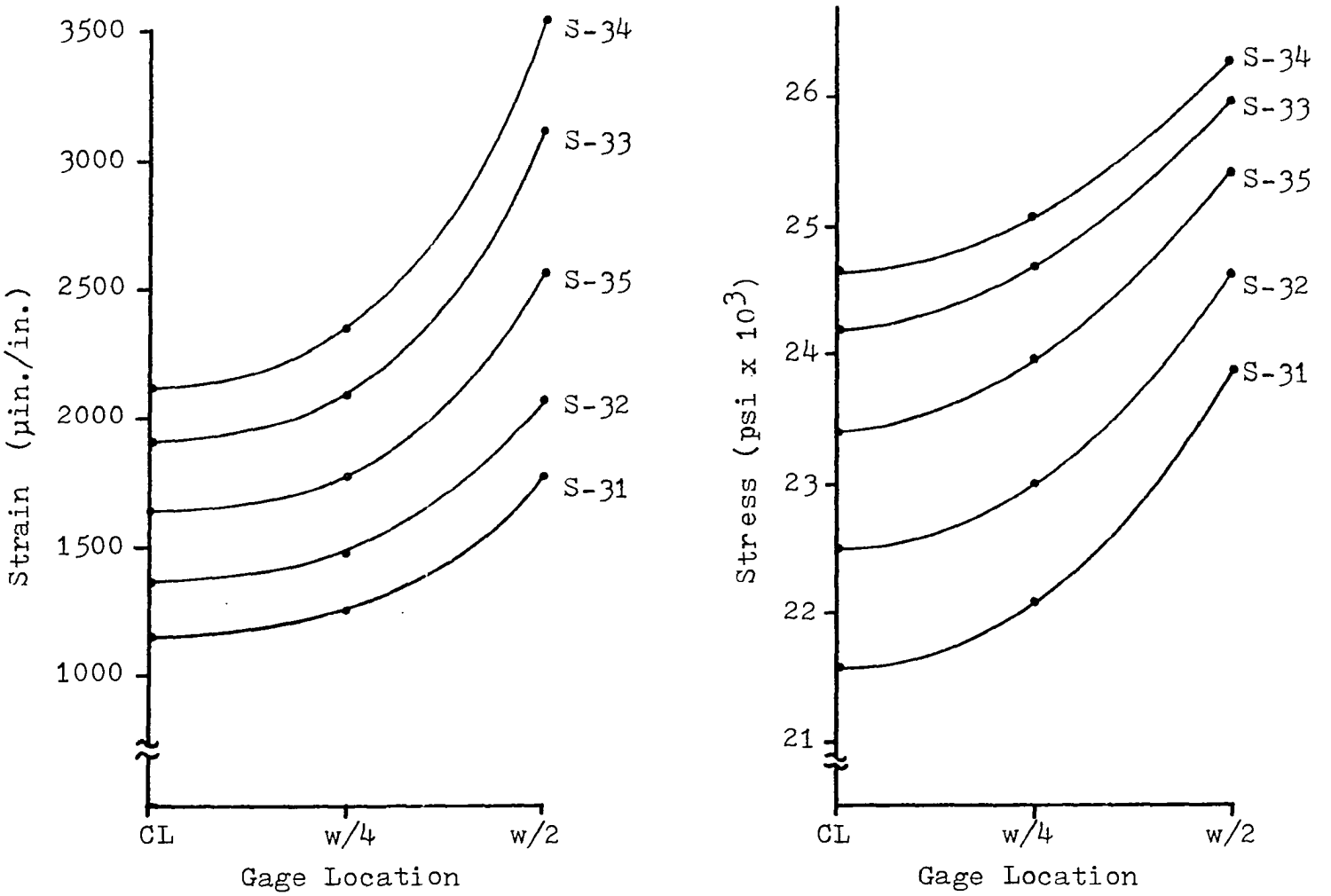

Figure 17(e). Strain and stress distributions at notches for double-notched steel fatigue specimens with D_{notch}= 0.500 in.

bles the reader to discern nominal stress or strain levels, average levels, and the extent of yielding based on any criteria needed.

The thermographic data obtained from these series of fatigue tests can be presented in several forms. For this work, it will be of interest to examine the maximum temperature rise on the surface of the specimen at any time, and to study the temperature field maps generated from a few select thermograms. The majority of the data presented comes from the thermograms, with strip-chart data used to provide information during the start-up period and at the end of some tests when the maximum temperatures exceeded the capabilities of the scanning infrared camera.

The early warning of impending fatigue damage discussed in relation to the previous tests of steel specimens was also apparent in these tests. In all cases, the temperatures at the roots of the two notches each showed a rise soon after the test of a specimen was started. In addition, the notch root which displayed the hotter temperature was always the notch root at which a fatigue crack was first observed microscopically. Thus, by determining where on the specimen the temperature rise was greatest, one could successfully predict where the first fatigue damage would become visible long before such an observation was made. Once the cracks had formed, their propagation across the specimen could easily be followed until the failure occurred. Several

other trends in the data obtained are common to all the tests of the double-notched steel specimens, and these will be brought out after examining the data from each series individually.

The relatively low centerline stress level of the 1-6 series of tests resulted in some long-life fatigue tests. The longest test of the double-notched steel specimens occurred in this series for specimen S-31, which lasted over 1.3 million cycles. Figure 18 gives the important results of the thermographic monitoring of the 1-6 series of tests. In this figure, the maximum temperature rise on the specimen, regardless of its location, is shown as a function of the number of fatigue cycles endured by the specimen. It can be seen that each of the tests in the series displays an initial temperature rise of a few degrees in a few thousand cycles. There follows then a long period in which the temperature of the warmest point on the specimen increases very slowly. During this period, the first visual observation of a fatigue crack was made, as indicated by the arrows on Fig. 18. Finally, the maximum temperature rise on the specimen surface begins to increase sharply and continues to do so until fracture occurs. The temperature rise just at the instant of fracture is, of course, the greatest rise obtained during each test. The difference in fatigue lives indicated in Fig. 18 can be attributed to the differences in notch root diameters. Each of the tests was at the same

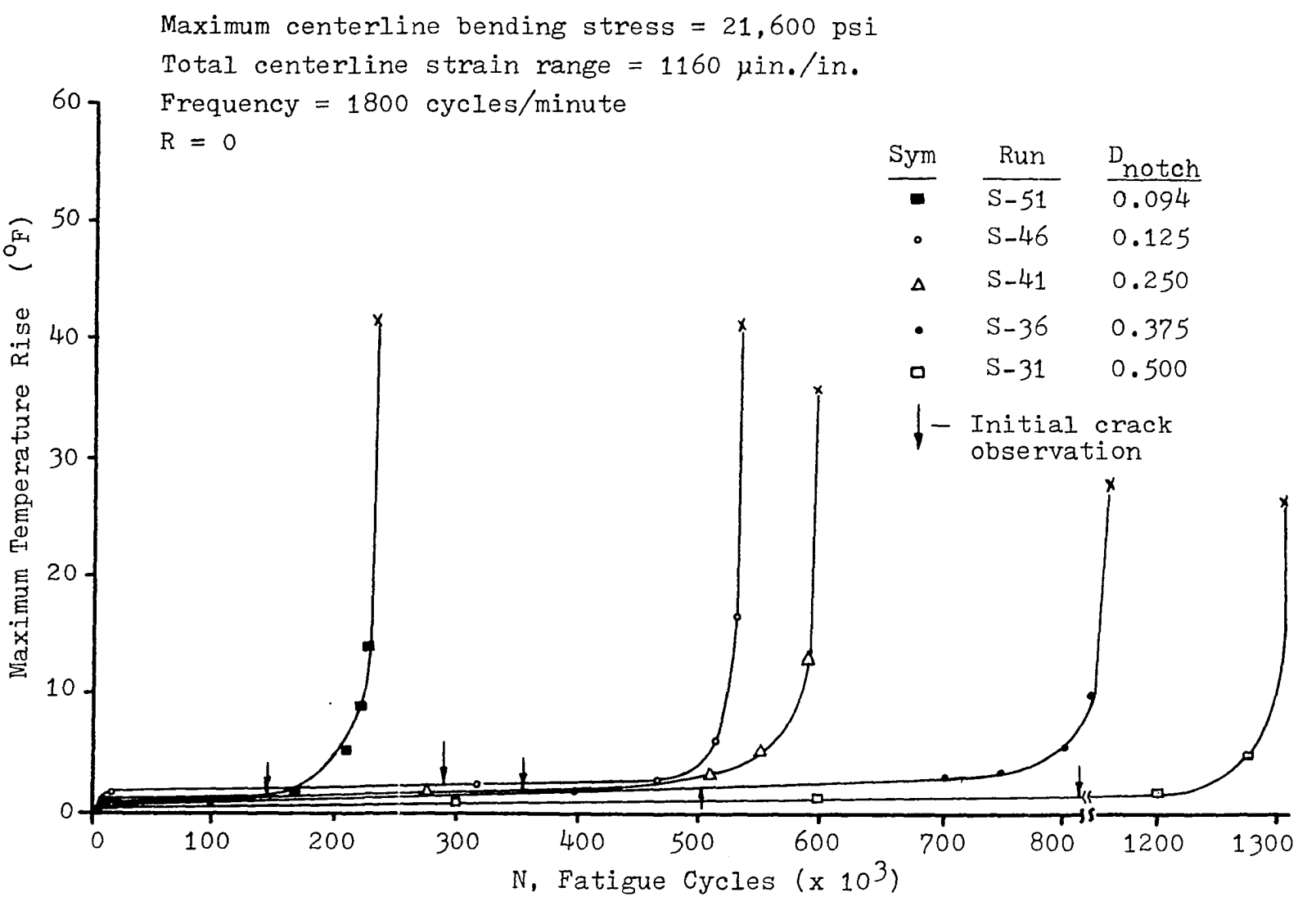

Figure 18. Maximum temperature rise on specimen as a function of the number of fatigue cycles endured for the 1-6 series.

stress level and frequency of loading. The effect of the different notch diameters is to introduce different stress concentrations in the specimens, leading to the formation of cracks at different times. Once a crack is present, the behavior of the different specimens should be essentially the same, as the notch no longer has an important effect.

The data presented in Fig. 18 can also be presented in a non-dimensional form, as shown in Fig. 19. In this case, the temperature rise on the specimen at any time is non-dimensionalized by the temperature rise on the material at failure, yielding the variable T^*. The number of cycles endured is given as N^*, the fraction of the fatigue life of the specimen. It is interesting that the data for each of the tests in the series fall on or near a common curve of T^* versus N^*. Hence, this one curve can be used to describe the thermal behavior of all the specimens in this series. The three phases of the lifetime based on thermographic observations can be clearly seen in Fig.19. The initial phase, or start-up phase, lasts only a few percent of the life of the specimen, and results in a non-dimensional temperature rise of about 0.06. The long phase which follows occupies another 70 percent of the life, and includes the average initial crack observation and the range of observations for all tests. At about 70 to 75 percent of the lives of the specimens, the last phase begins with a gradual increase in T^*. This increase becomes more and more rapid as the test

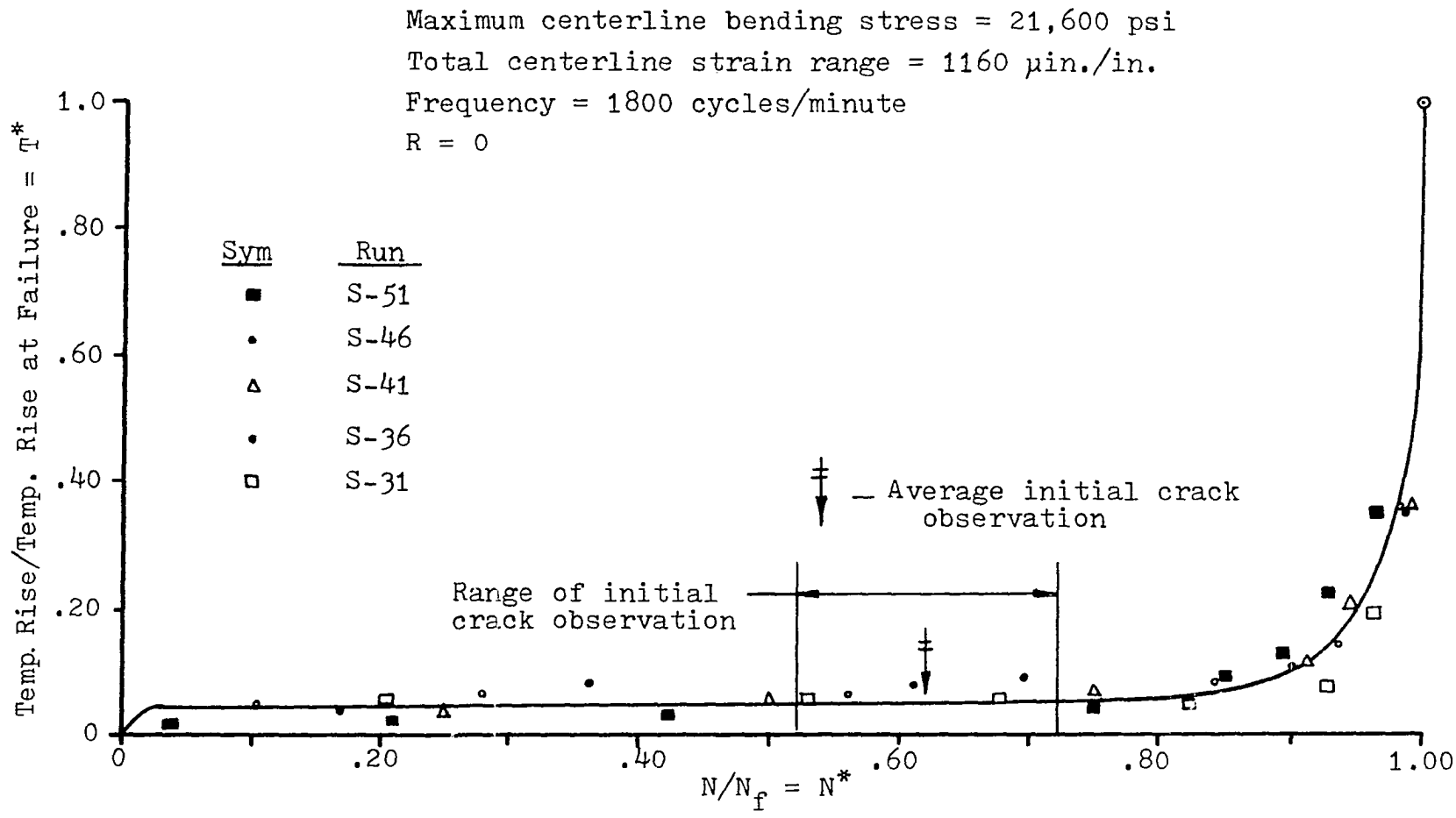

Figure 19. Non-dimensional temperature rise as a function of fraction of fatigue life for the 1-6 series.

progresses to failure.

The data in Fig. 20(a) and 20(b) make the three phases of the life even more obvious. Figure 20(a) gives the slope of the non-dimensional temperature-rise curve from Fig. 19 as a function of N^*. In the initial phase, the slope decreases from a large initial value to a constant one only slightly greater than zero. The long region of zero slope (note the break in the scale in Fig. 20(a)) corresponds to the second phase discussed in relation to Fig. 19. At the end of the lifetime, the slope of the curve shows the rapid upswing as failure approaches. Figure 20(b) gives the second derivative of T^* with respect to N^* as a function of N^*, or simply the change in the slope of the non-dimensional temperature-rise curve. This figure clearly indicates that the three phases discussed may be described by the sign of the non-dimensional second derivative. The first phase results in a negative second derivative. The second phase displays a zero second derivative, as the slope remains constant. Finally, the last phase is described by the period in which the second derivative is positive. It would appear, therefore, that the phase of the fatigue life in which a material is operating may be determined by finding the second derivative of the non-dimensionalized temperature rise, and comparing that to the results of this series of tests. In fact, since each specimen shows the same behavior, and since it is possible to appeal to just the sign of the

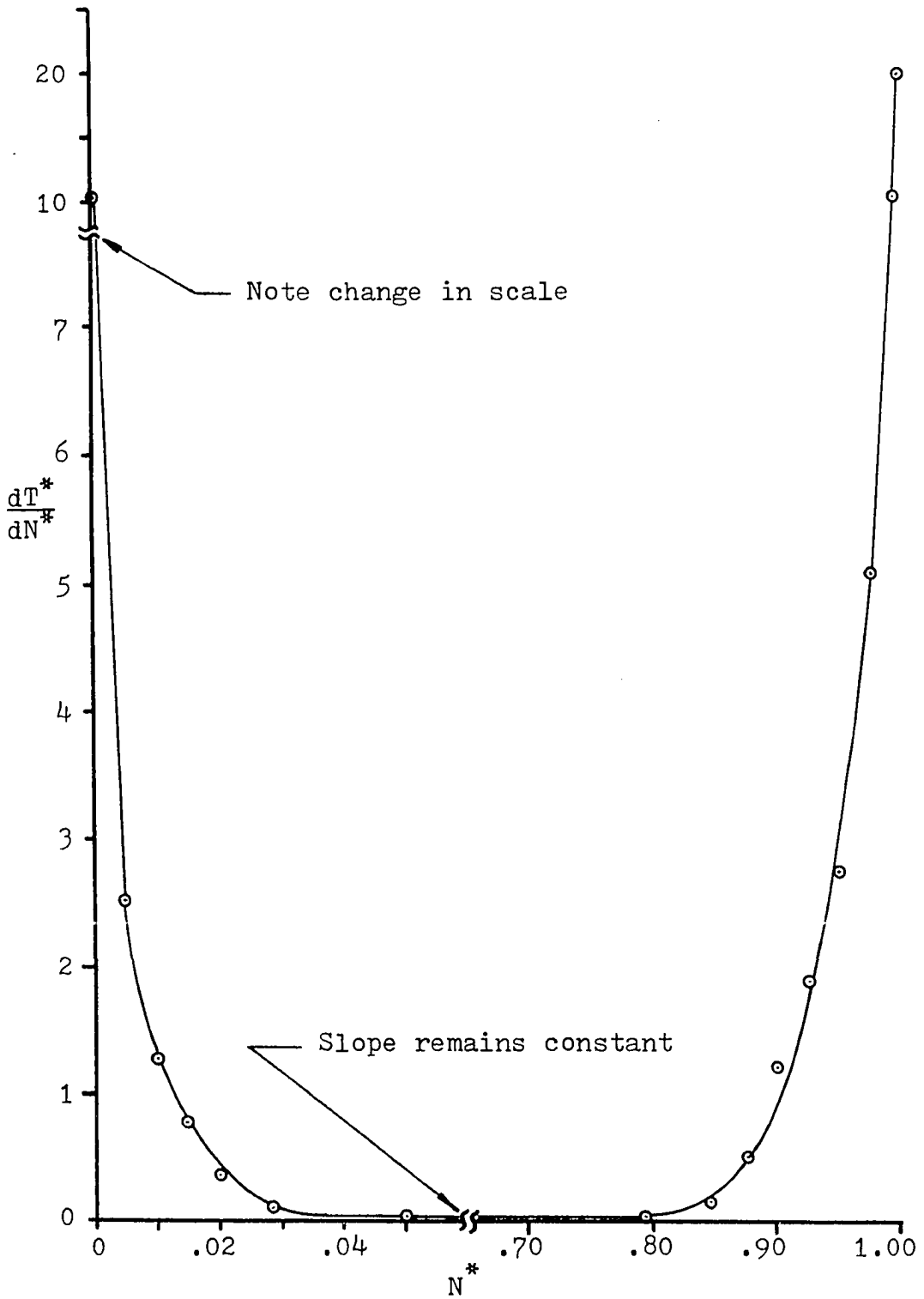

Figure 20(a). Slope of non-dimensional temperature-rise curve for the 1-6 series.

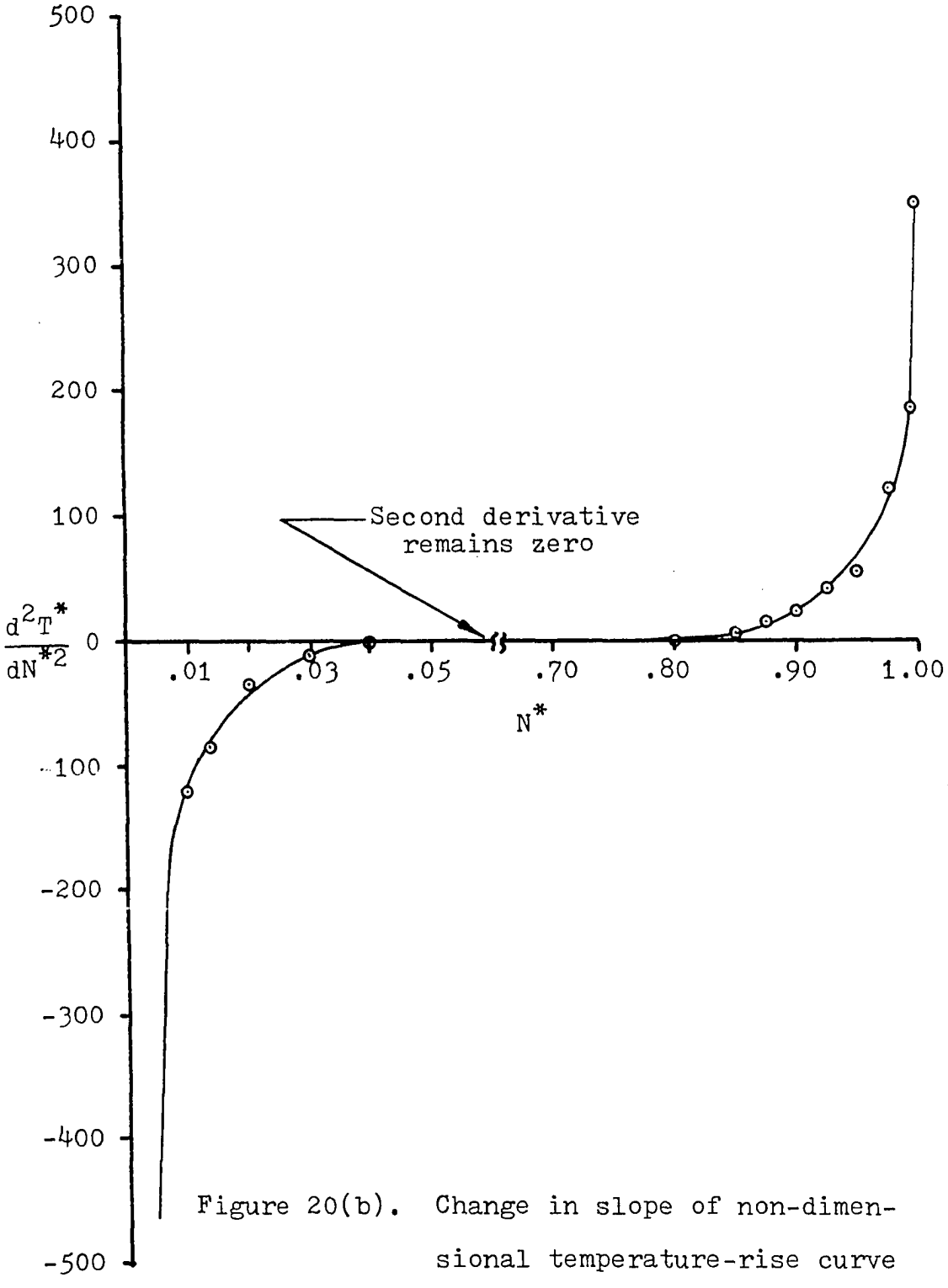

Figure 20(b). Change in slope of non-dimensional temperature-rise curve for the 1-6 series.

second derivative, the second derivatives do not need to be non-dimensionalized to determine the phase of the life in which a specimen is operating.

It appears from the data of this series that there is no change in the temperature rise on the material associated with the formation of a propagating crack. This result is in keeping with the theory that the fatigue process is one of gradually accumulating damage, and not a sudden departure from a stable structure. Hence, the temperature rise noted from the beginning of the tests is the indication that a crack is in the process of forming, and the only way of detecting the presence of a propagating crack is to follow the movement of the hottest point on the specimen, as was seen previously with the single-notched steel specimen.

The next series of tests to be discussed is the 2-7 series, which was run at a maximum centerline stress level of 22,700 psi. This level resulted in tests of shorter lives than those for the same notch diameters in the 1-6 series, as would be expected. Furthermore, the effect of the notch diameter on the life of the specimen is decreased compared to that of the previous series. However, the thermal data from the 2-7 series show behavior very similar to that observed in the 1-6 series. Figure 21 presents the temperature rises on the specimens as functions of the number of fatigue cycles endured by the material. These curves show substantially the same behavior as those for the previous

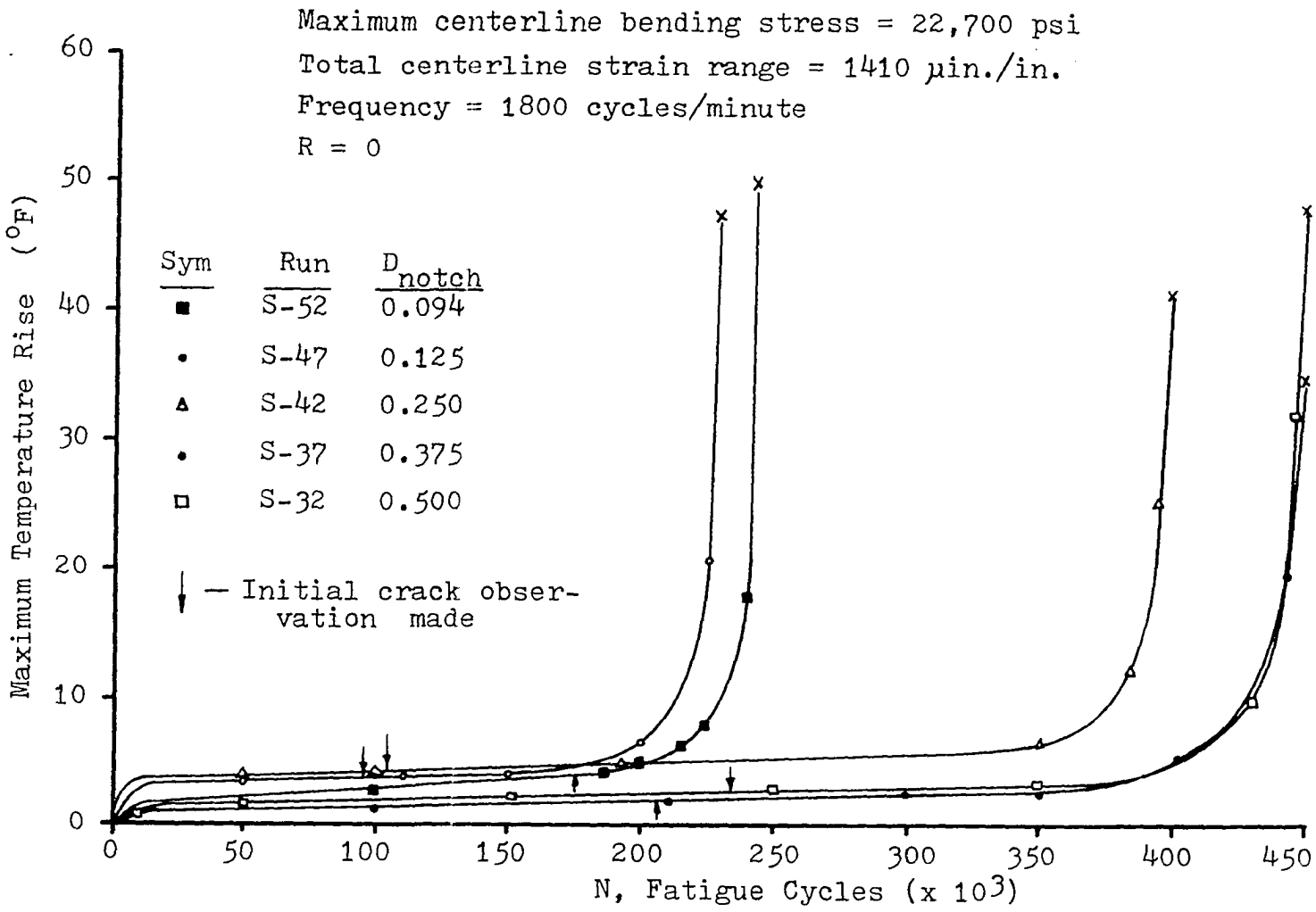

Figure 21. Maximum temperature rise on specimen as a function of the number of fatigue cycles endured for the 2-7 series.

series, with three distinct phases evident in each case. The data on Fig. 21 can be non-dimensionalized as were the data for the 1-6 series, yielding the curve in Fig. 22. Again, all the tests in the series can be reduced to one average curve of T^* versus N^*. In this series, the scatter in the data at the end of the tests is more pronounced than previously, but the resulting curve is still a good description of the behavior of the series. The slope of the curve in Fig. 22 and the change in the slope are given in Fig. 23(a) and (b) as functions of the non-dimensionalized fatigue cycles. As was the case in the 1-6 series, the three phases of the fatigue life can be readily discerned from these figures. The different behavior of the slope and the second derivative at the very end of the life can be attributed to the particular average curve selected from the non-dimensionalized data, and carries no real significance. In the case of the 2-7 series, the first phase lasted about 3 percent of the total lifetime, and the last phase began at about 70 percent, as indicated from the second derivative curve.

The remainder of these data for the double-notched fatigue specimens are given in Figures 24 through 32. For each of the three remaining stress levels, data are given on the maximum temperature rise, non-dimensional temperature rise, slope and change in slope as a function of either dimensional or non-dimensional fatigue cycles. Consistent

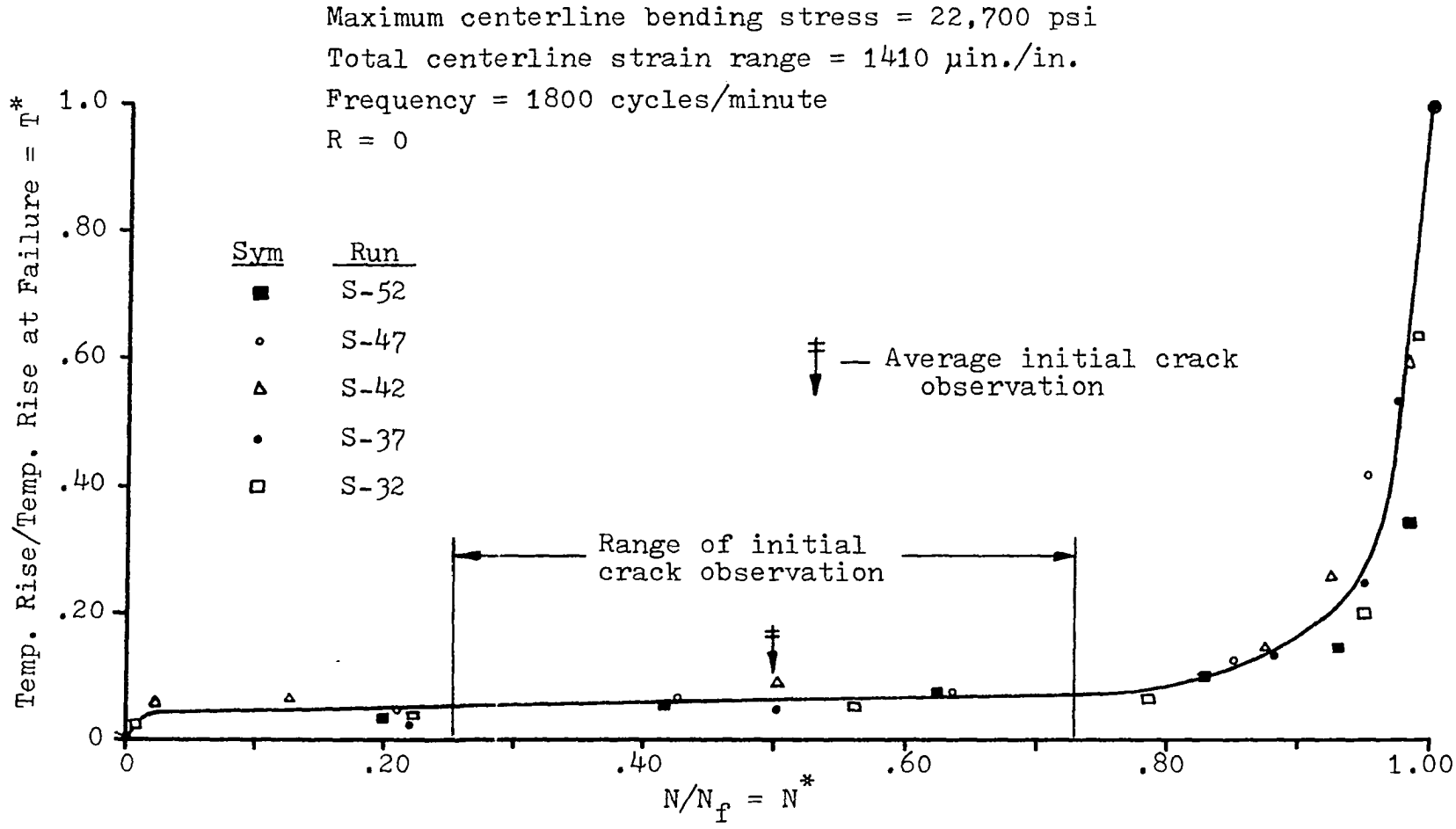

Figure 22. Non-dimensional temperature rise as a function of fraction of fatigue life for the 2-7 series.

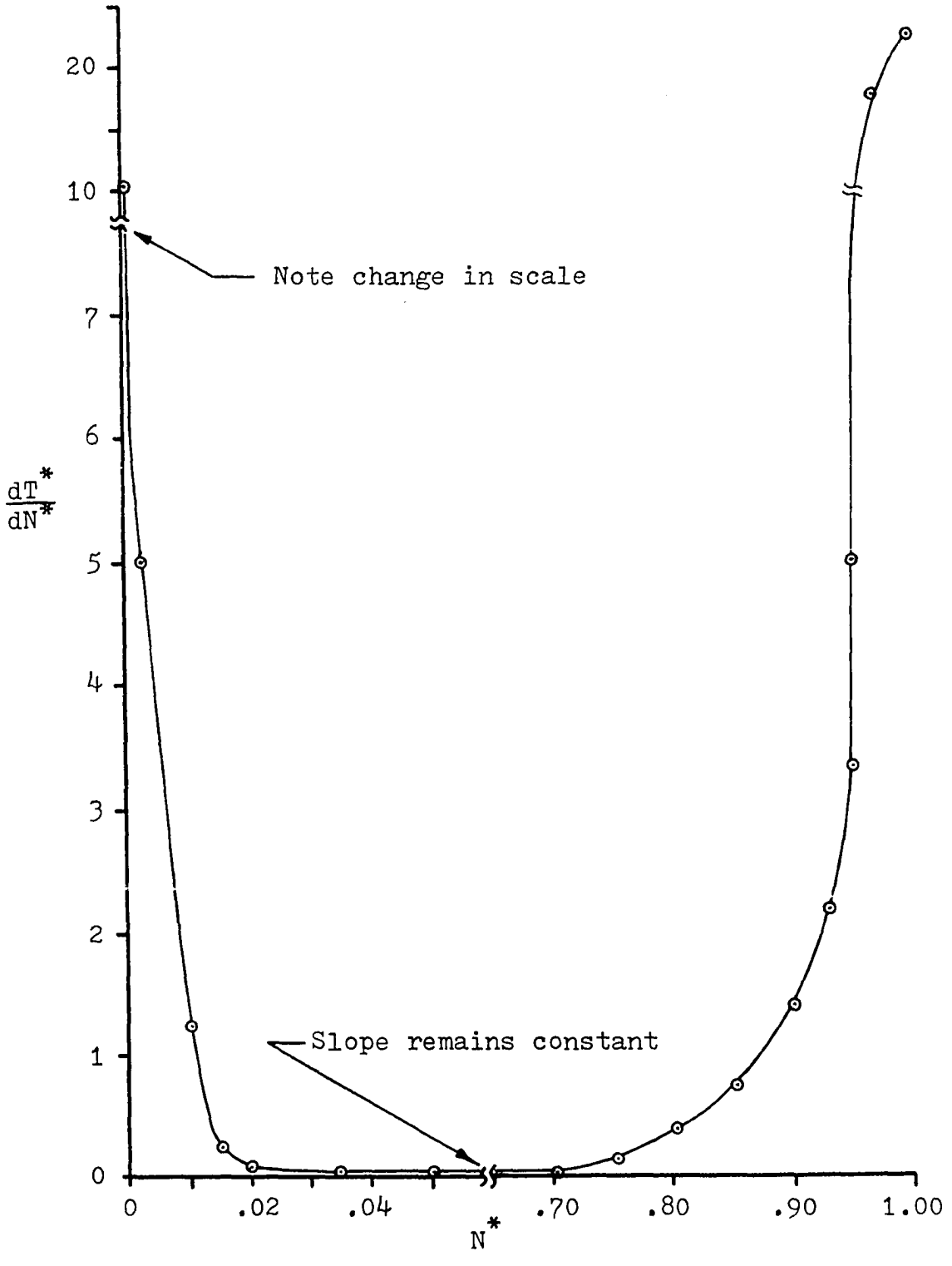

Figure 23(a). Slope of non-dimensional temperature-rise curve for the 2-7 series.

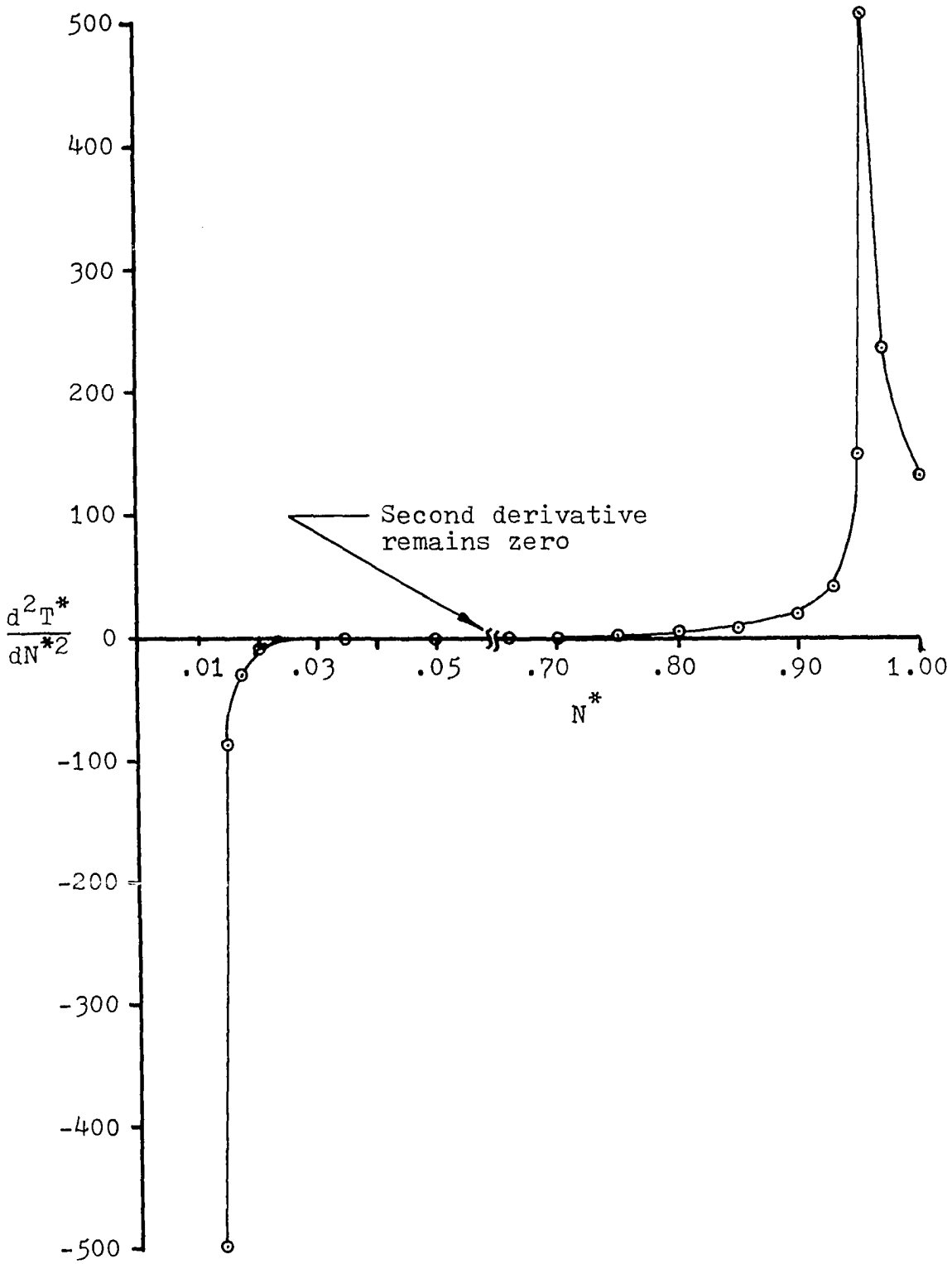

Figure 23(b). Change in slope of non-dimensional temperature-rise curve for the 2-7 series.

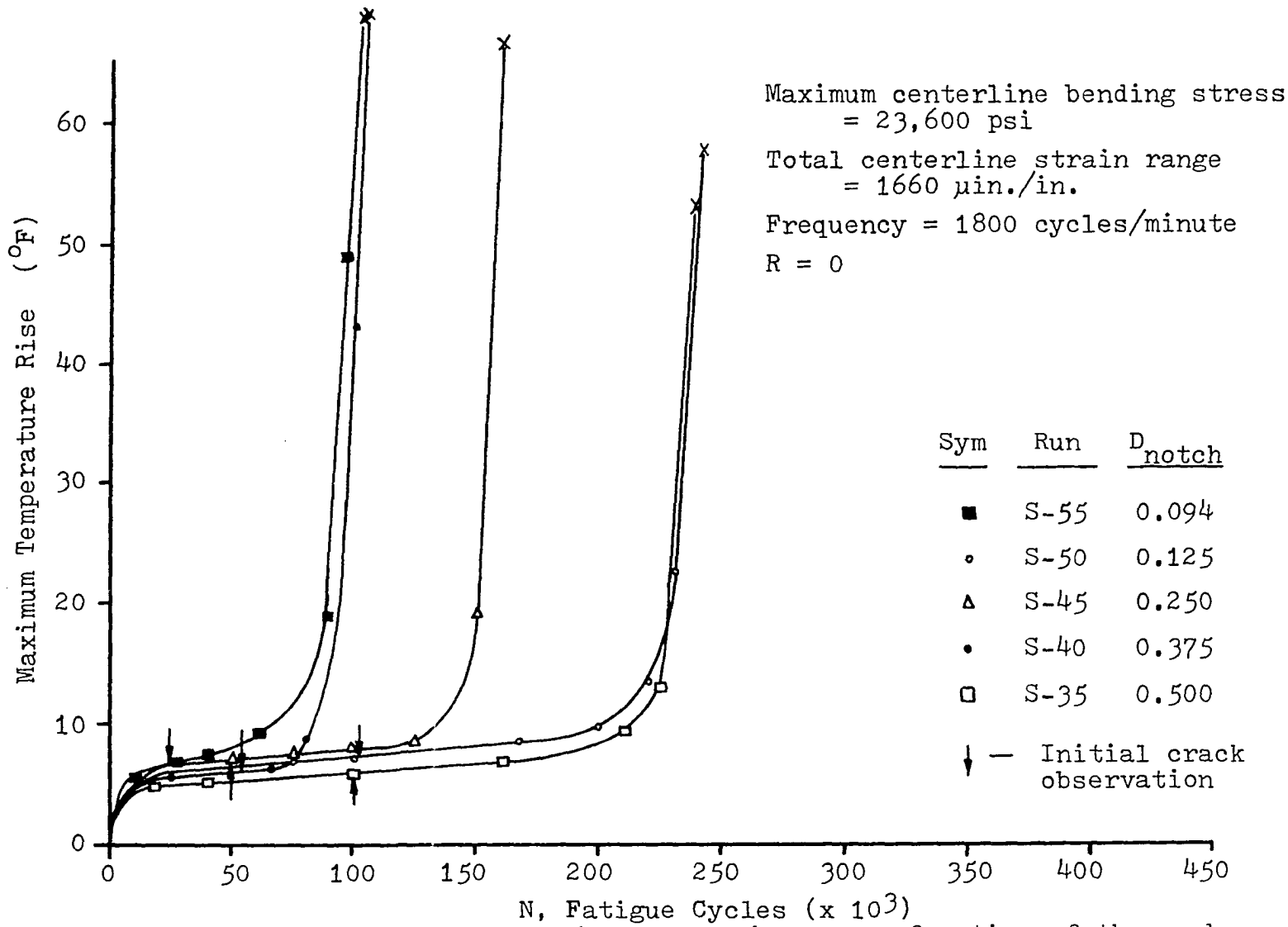

Figure 24. Maximum temperature rise on specimen as a function of the number of fatigue cycles endured for the 5-0 series.

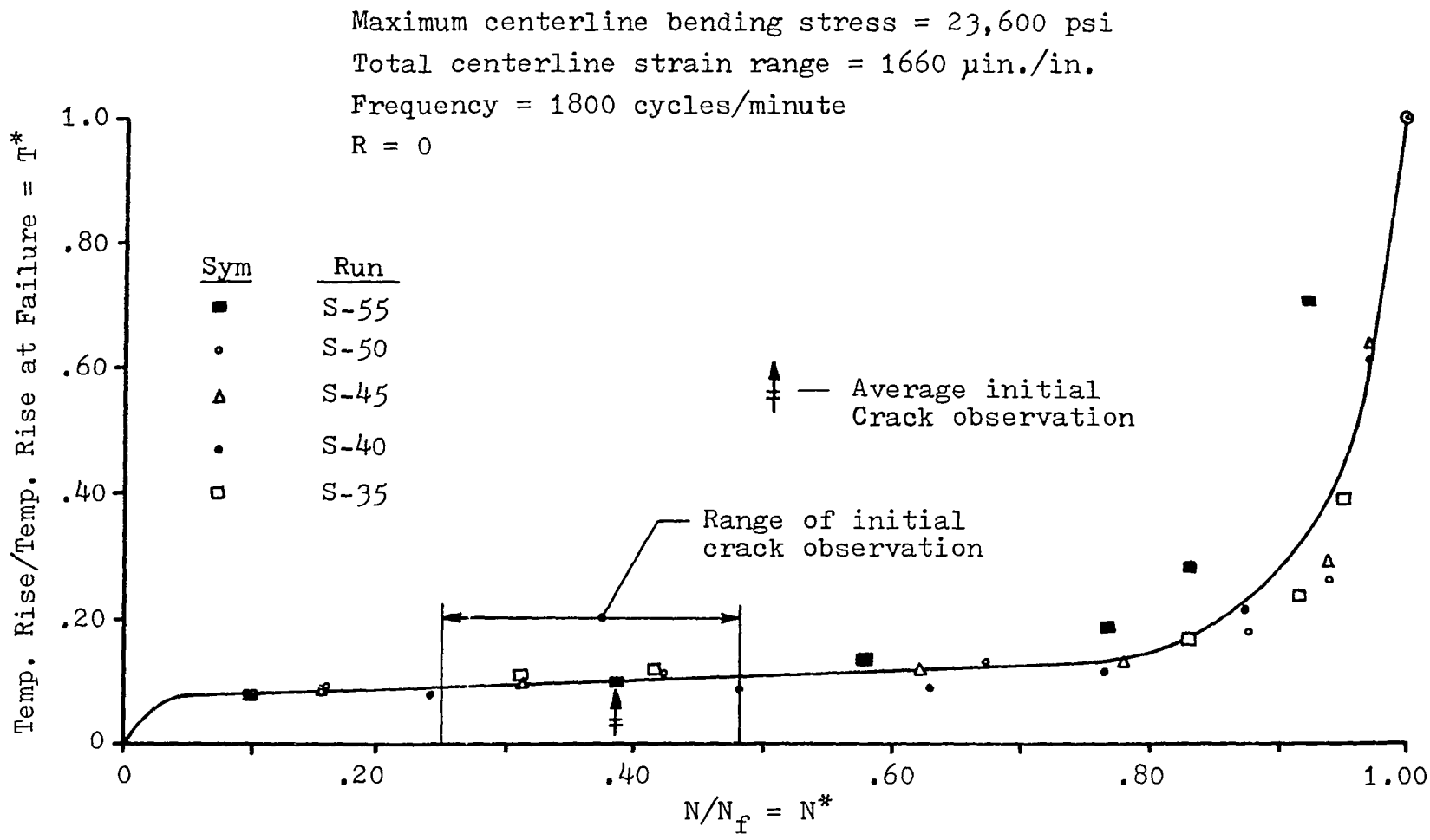

Figure 25. Non-dimensional temperature rise as a function of fraction of fatigue life for the 5-0 series.

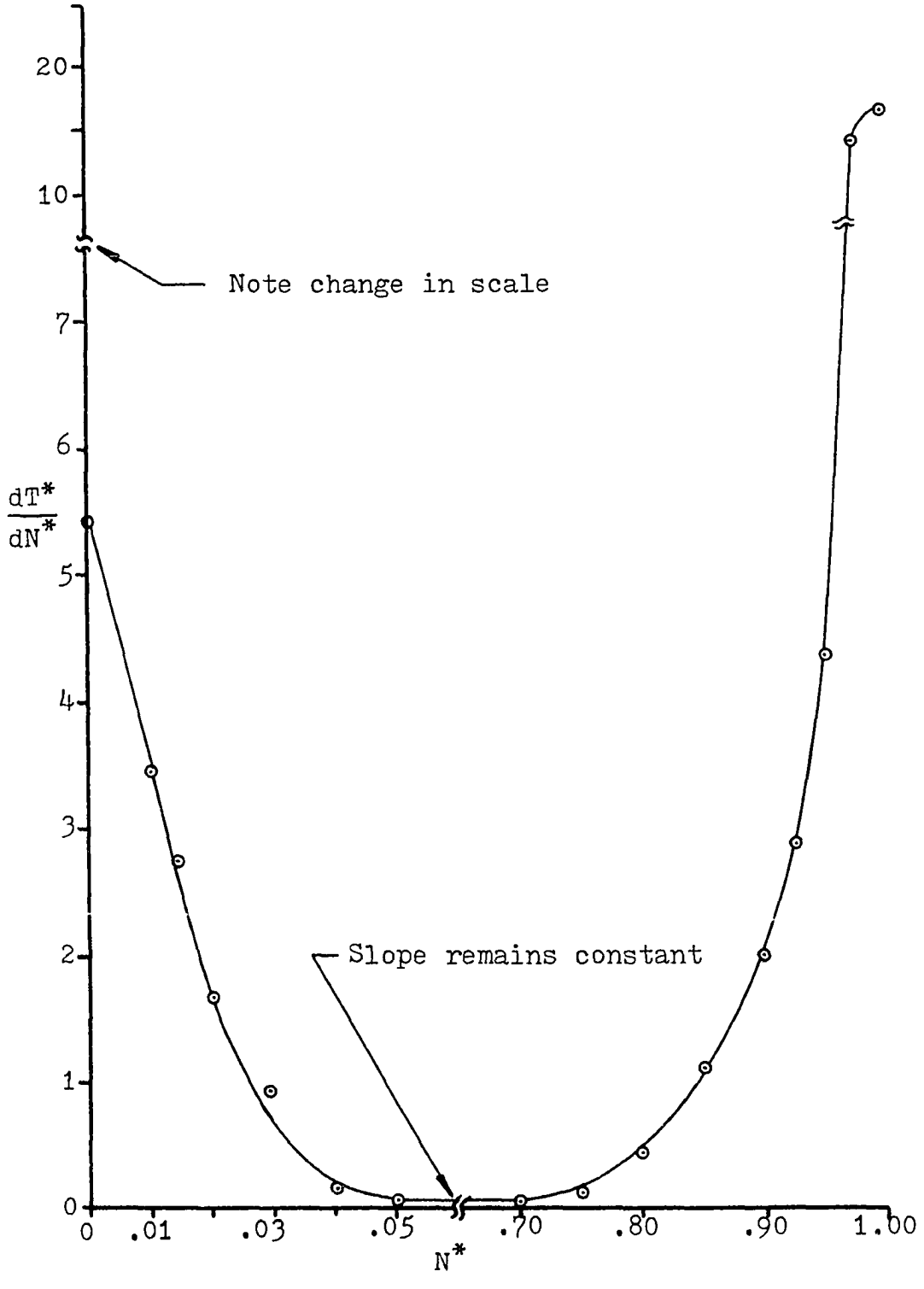

Figure 26(a). Slope of non-dimensional temperature-rise curve for the 5-0 series.

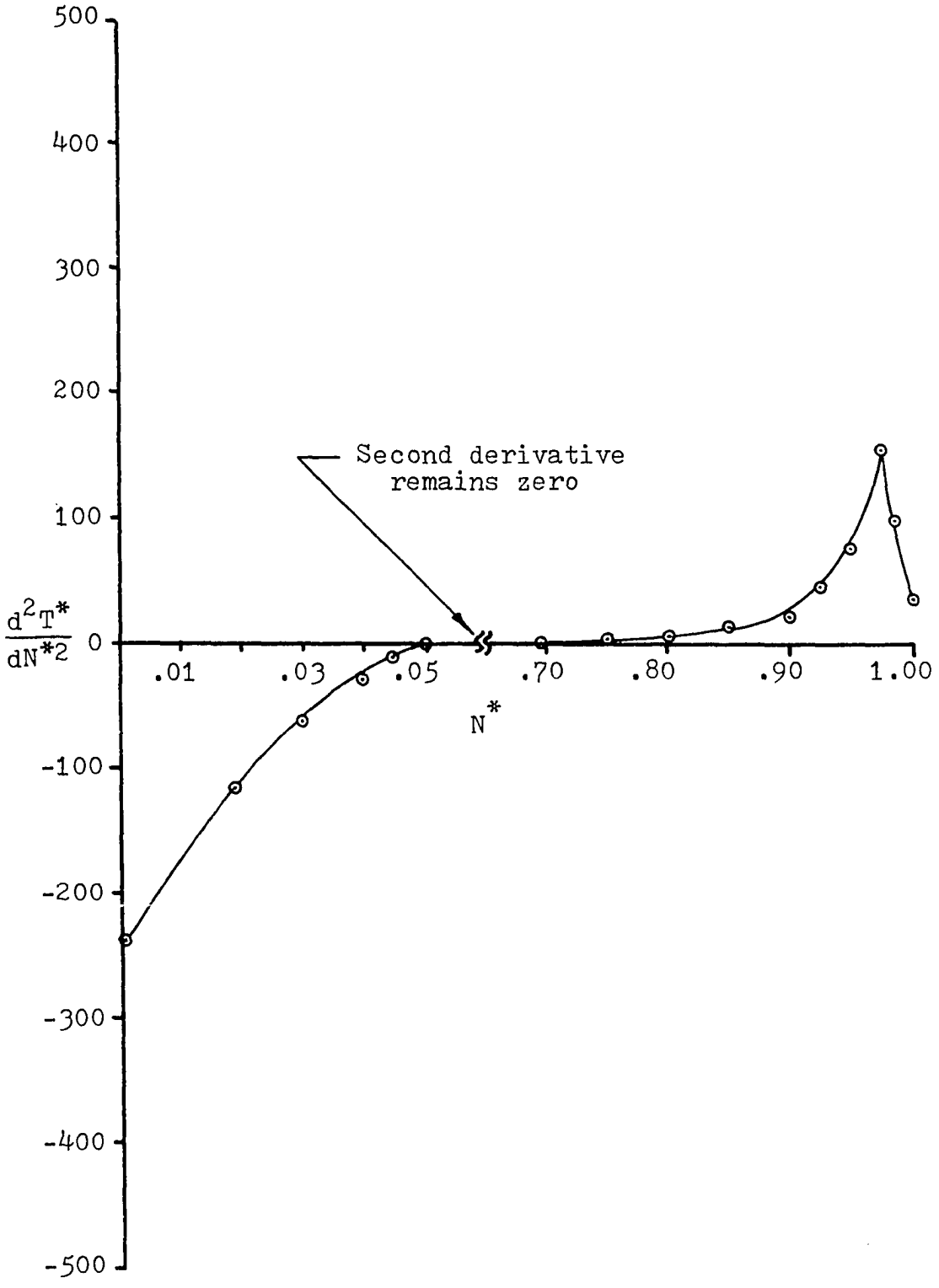

Figure 26(b). Change in slope of non-dimensional temperature-rise curve for the 5-0 series.

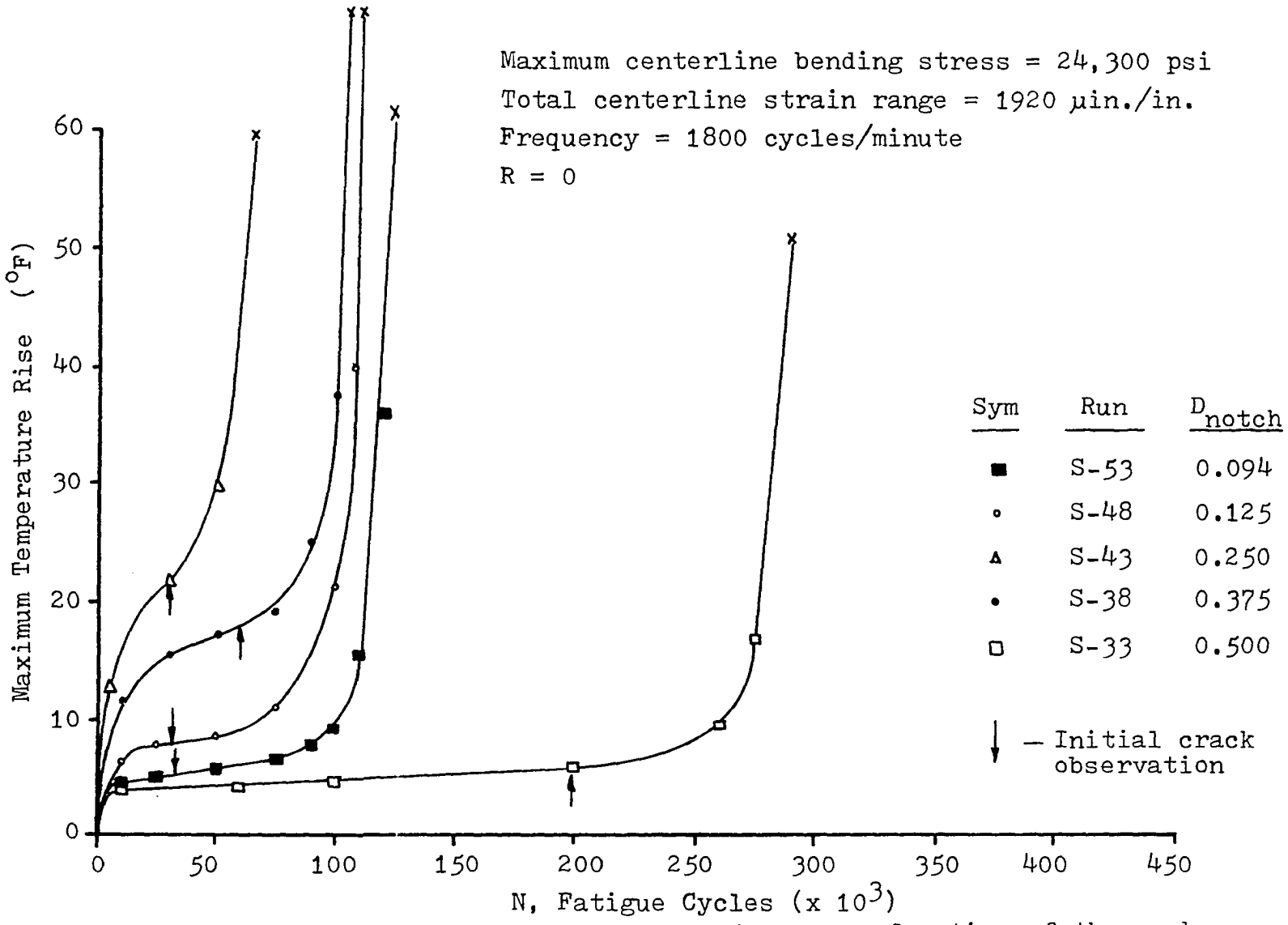

Figure 27. Maximum temperature rise on specimen as a function of the number of fatigue cycles endured for the 3-8 series.

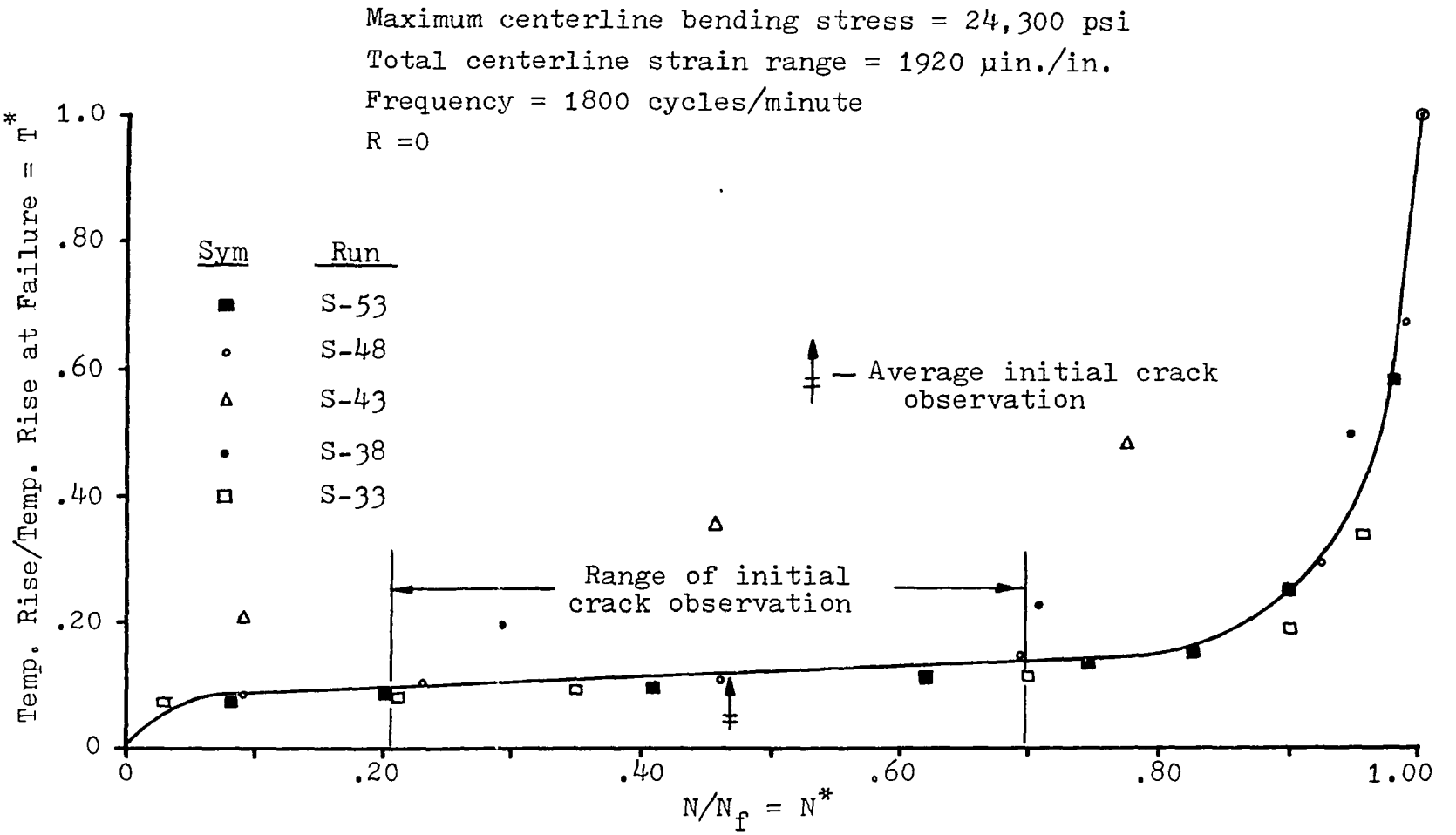

Figure 28. Non-dimensional temperature rise as a function of fraction of fatigue life for the 3-8 series.

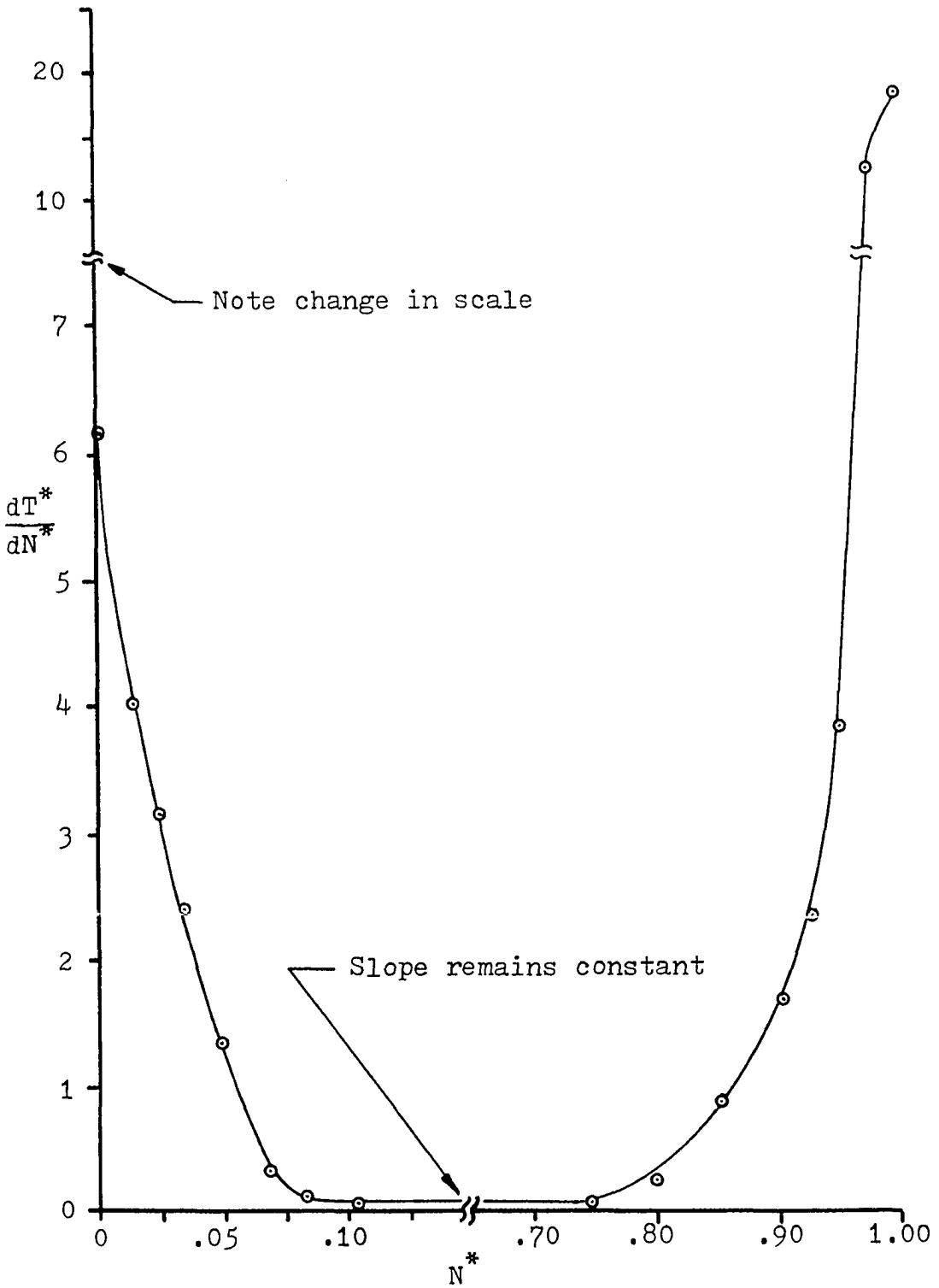

Figure 29(a). Slope of non-dimensional temperature-rise curve for the 3-8 series.

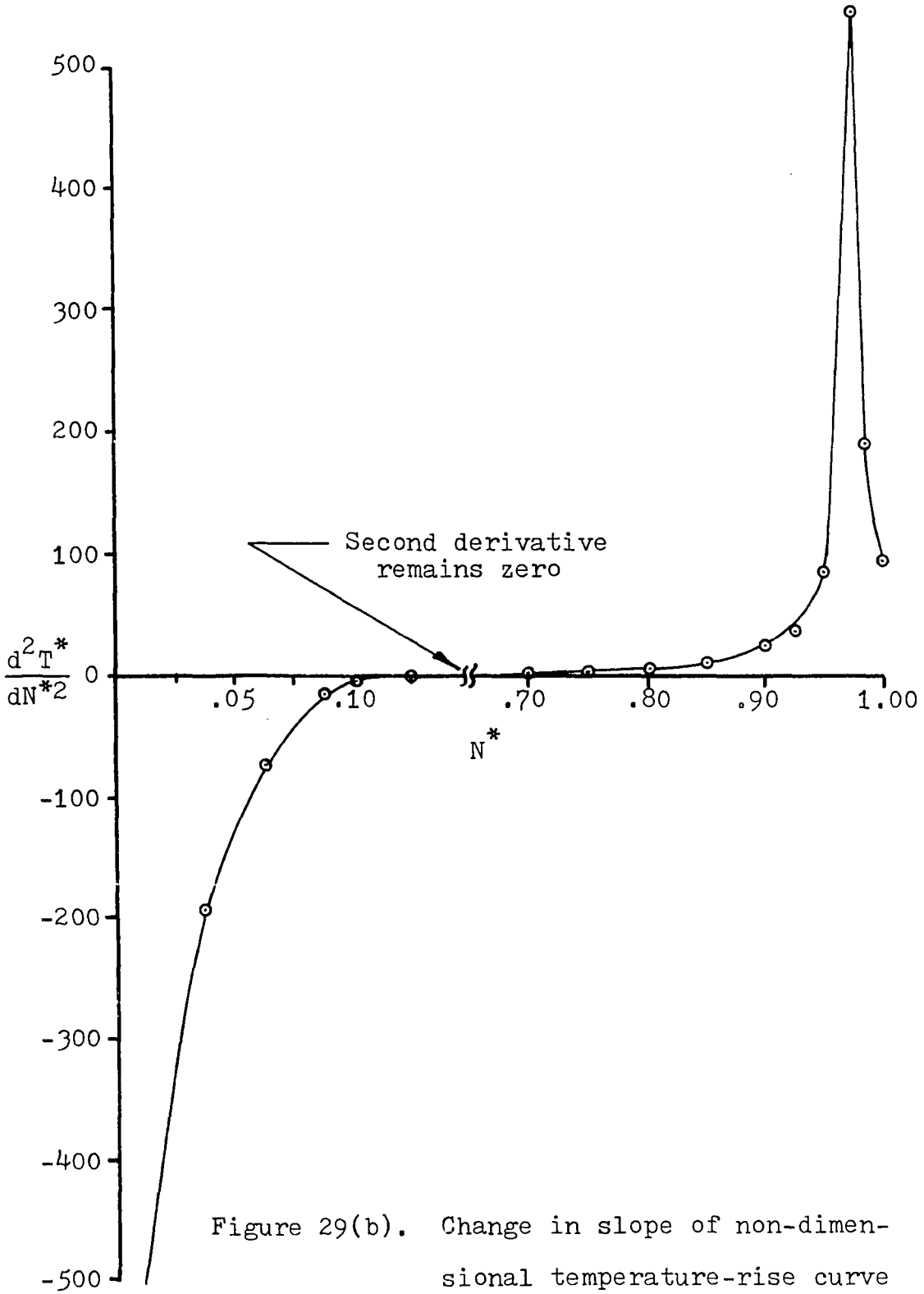

Figure 29(b). Change in slope of non-dimensional temperature-rise curve for the 3-8 series.

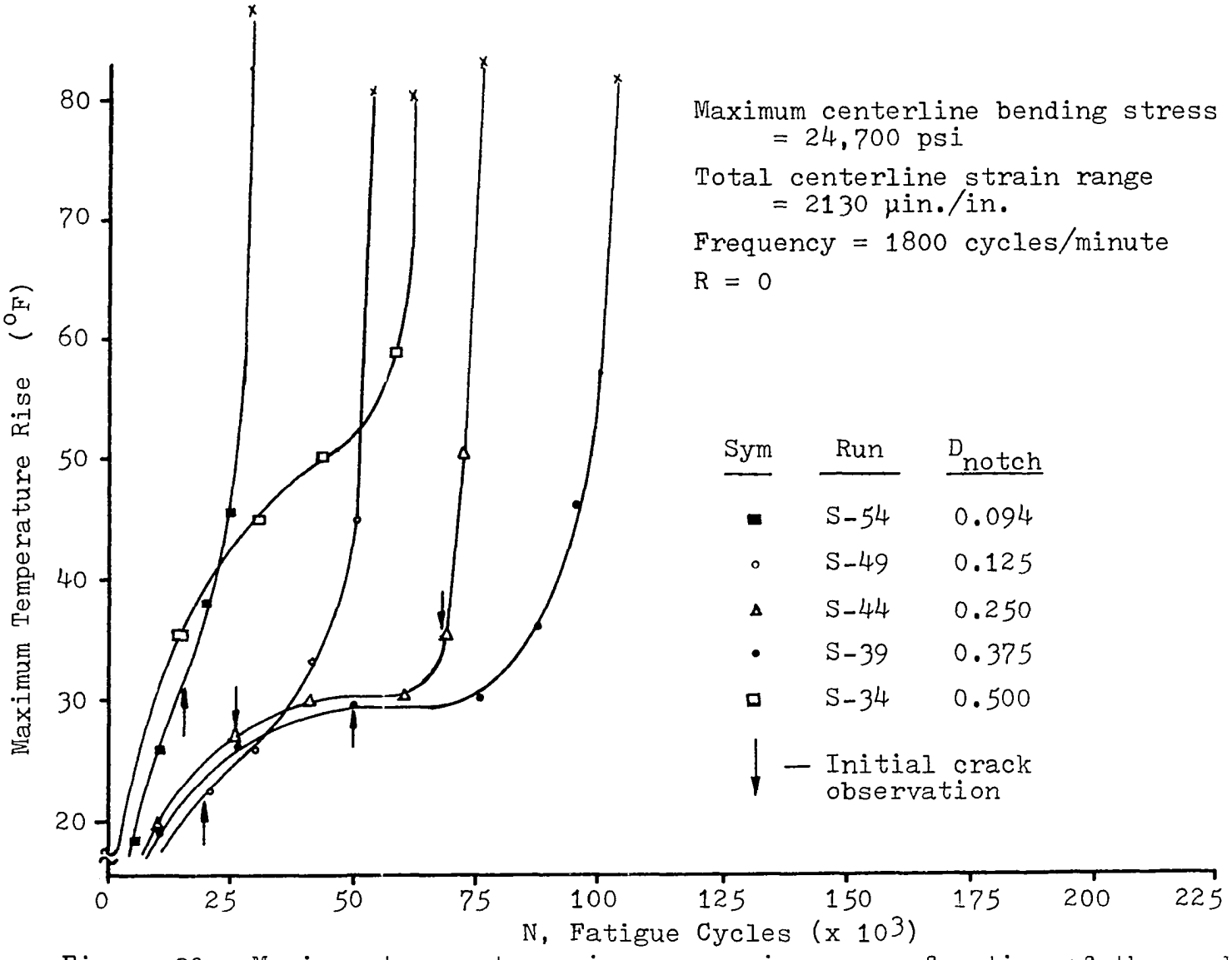

Figure 30. Maximum temperature rise on specimen as a function of the number of fatigue cycles endured for the 4-9 series.

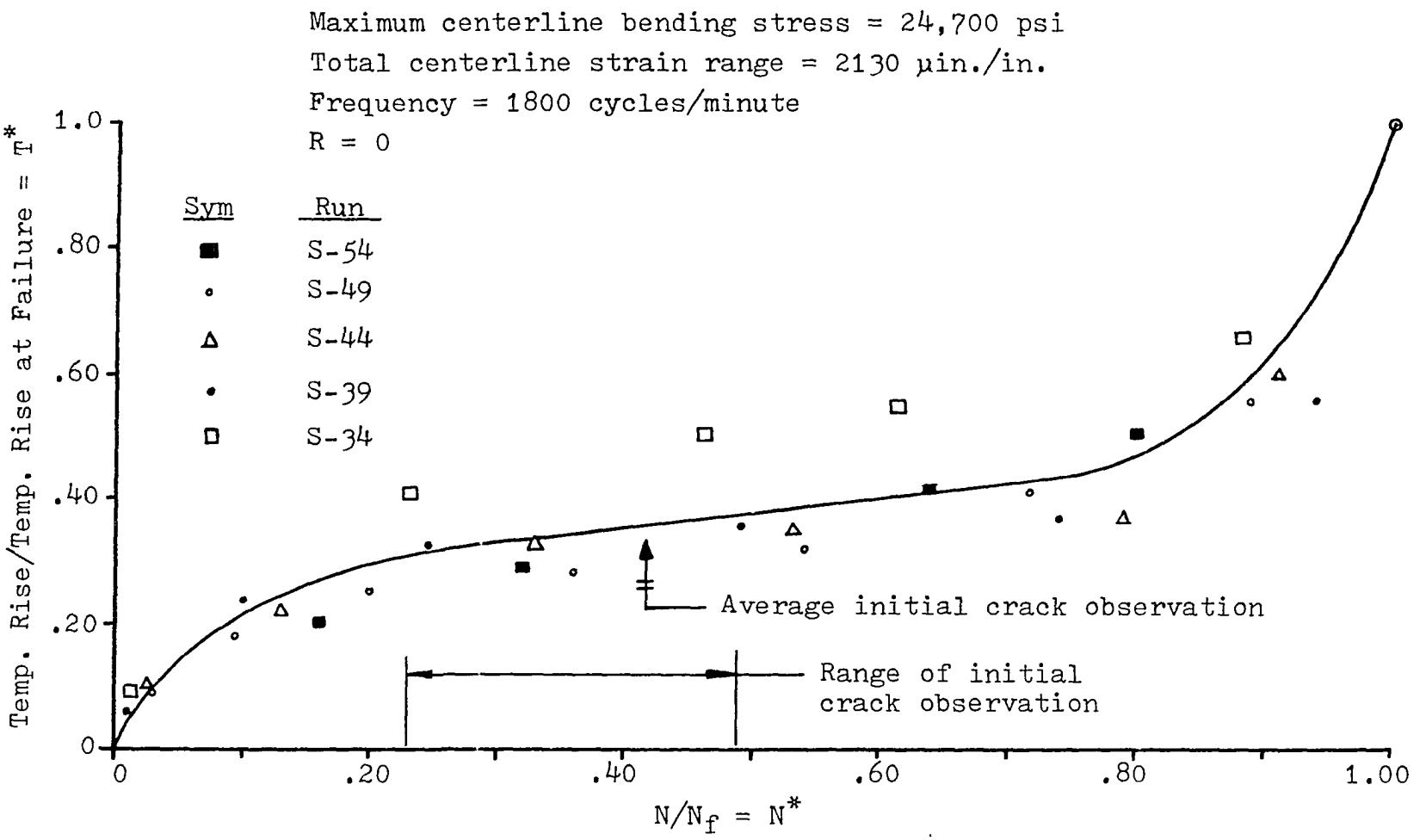

Figure 31. Non-dimensional temperature rise as a function of fraction of fatigue life for the 4-9 series.

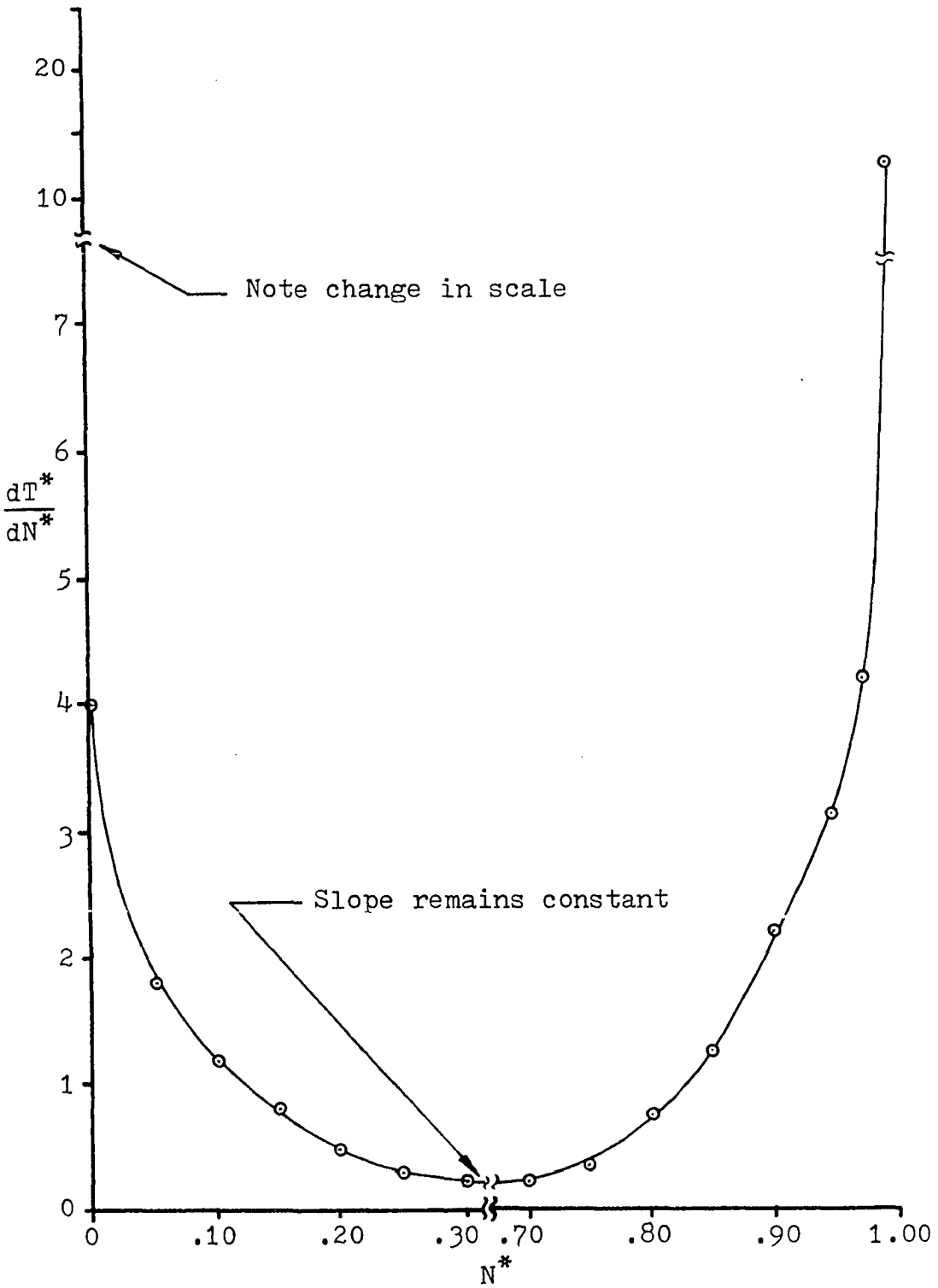

Figure 32(a). Slope of non-dimensional temperature-rise curve for the 4-9 series.

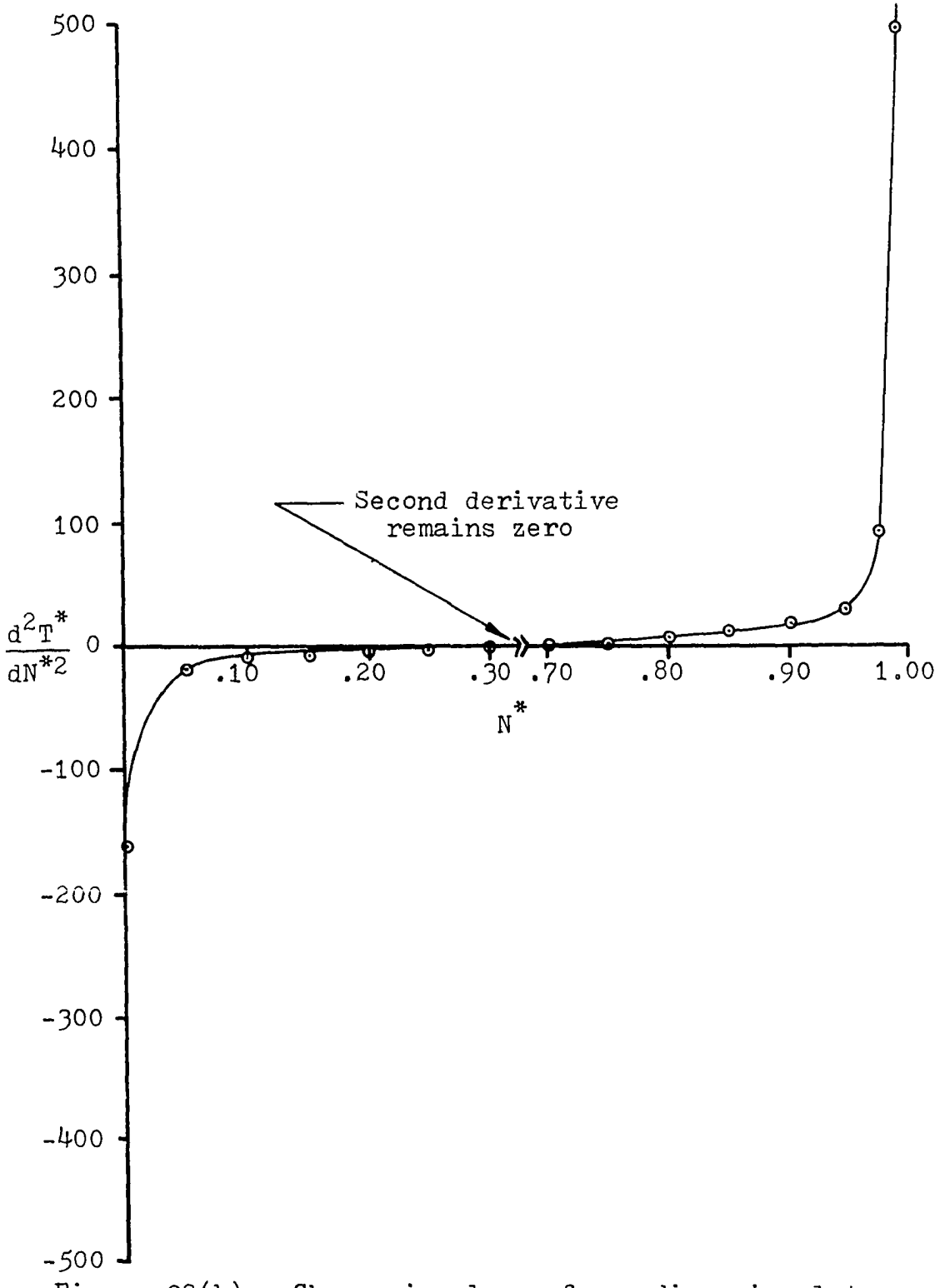

Figure 32(b). Change in slope of non-dimensional temperature-rise curve for the 4-9 series.

trends are evident throughout the data for all series. For example, as the stress level increases, the effect of the notch root diameter on the fatigue life is decreased so that at the highest level there is little difference in the lives of the different specimens. Also, as the lives become shorter, the scatter in the non-dimensional temperature-rise data is accentuated. This is somewhat apparent in the 5-0 series, but is more obvious in the 3-8 and 4-9 series, where there was one run in each which did not behave in the same manner as the other specimens. This is probably due to the very nature of fatigue studies, in which many factors (such as the precise manner in which the test is started and the loading is distributed, and the surface conditions about the notch root) can contribute to scatter in the data. In all the series, however, one can define a reasonable non-dimensional temperature rise curve through the data which displays the same three phases mentioned in connection with the 1-6 and 2-7 series.

It is also apparent from these data that although the same three phases exist in each series, the behavior in the phases changes slightly with increasing stress levels. As the stress level increases, the length of the first phase increases until it occupies a significant part of the lifetime 4-9 series. In the second phase, the slope of the temperature-rise curve (although constant) is slightly higher for higher stress levels. It also appears that the length

of the final phase becomes longer for higher stress levels. All the differences in the five series must be traceable to the differences in stress levels. The increase in length of the first phase is related to the greater amount of fatigue damage occurring, and the resulting increase in the time required for the temperature rise to reach a quasi-steady state for higher stress levels. The increase in the slope during the second phase stems from the higher crack propagation rates at higher stress levels, and hence the more rapid rise in the rate of energy release in the material. The lengthening of the last phase is likewise attributable to the rapid crack propagation and to the high stress level itself which brings about large plastic deformations leading to failure earlier in the specimen life than do other stress levels.

Other interesting results come from examining the temperature field maps which can be obtained from each thermogram. A complete series of all the possible temperature field maps from the double-notched steel tests would be impractical to present in this work. Rather, three specimens will be discussed in detail, indicating the results to be expected from any thermographic fatigue test.

The first specimen to be examined is specimen S-36. This specimen was fatigued at the lowest stress level (21,600 psi) and had two 0.375-inch diameter notches. This combination produced a fatigue life of 826,000 cycles, the sec-

ond longest test run. During the test, several thermograms were taken. Two of these are presented as Fig. 33, (a) and (b). These thermograms were taken at 400,000 cycles and 800,000 cycles, respectively. When Fig. 33(a) was taken, no sign of visible damage was found on the specimen. Small cracks were finally observed at 480,000 cycles. By the time Fig. 33(b) was taken, cracks were propagating from both notch roots toward the center of the specimen. This specimen is interesting in that the crack from the lower notch in the figure travelled much farther than that from the upper notch, as can be seen be comparing the white spots in Fig. 33(b). Note that the hot rectangular region at the top of the figures is the reference temperature source used to calibrate the results of the scanning infrared camera.

While the thermograms themselves are interesting and provide a rapid means of gaining qualitative results, far more useful data come in the form of the temperature field maps generated from the thermograms. A complete series of these temperature field maps for specimen S-36 is presented in Fig. 34, (a) through (f). Figure 34(a) was derived from the thermogram of Fig. 33(a), taken at 400,000 cycles. Whereas it is difficult to determine which notch is warmer from the thermogram, it is readily apparent from the temperature field map that the lower is displaying the greatest temperature rise. It is at this location that a fatigue crack was sighted some 80,000 cycles later. Figure 34(b),

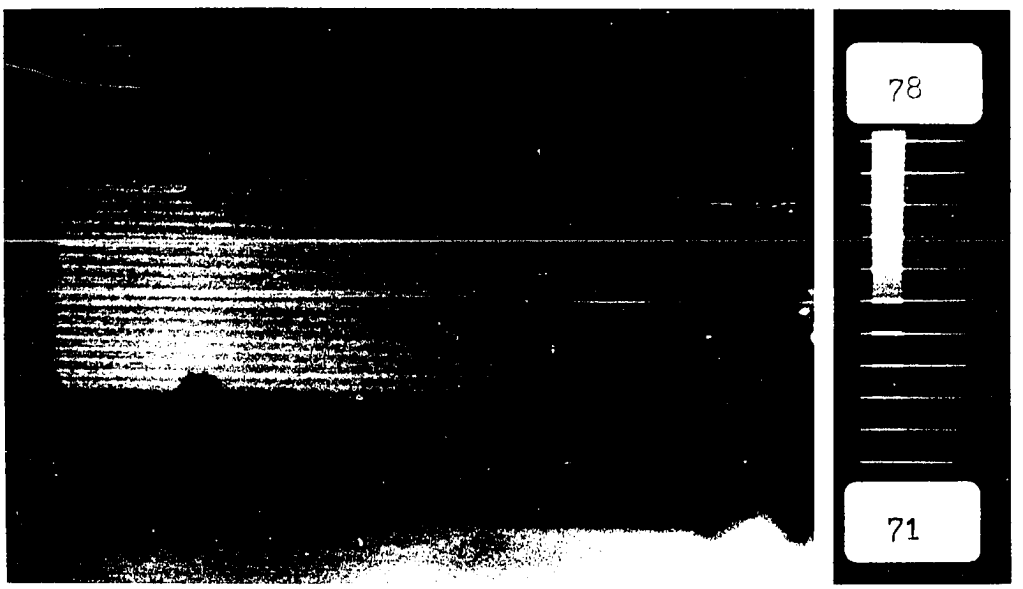

Figure 33(a). Thermogram of specimen S-36 at 400,000 cycles.

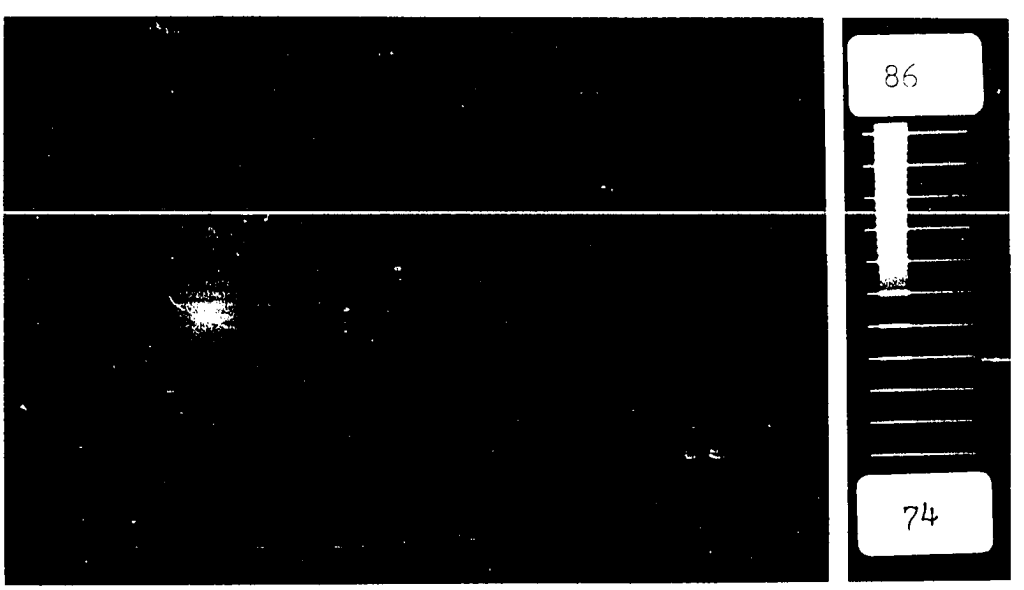

Figure 33(b). Thermogram of specimen S-36 at 800,000 cycles.

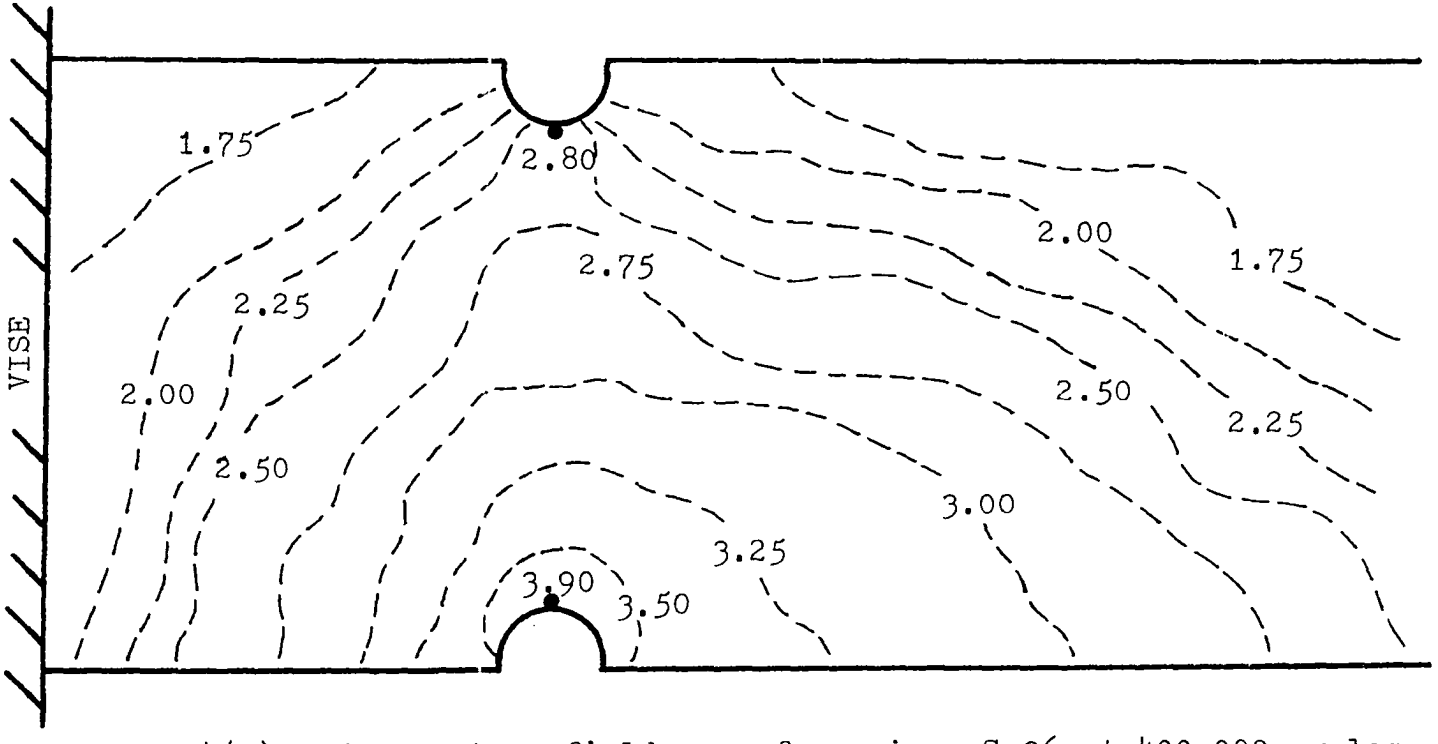

Figure 34(a). Temperature field map of specimen S-36 at 400,000 cycles (Temperatures in ^{o}F above ambient).

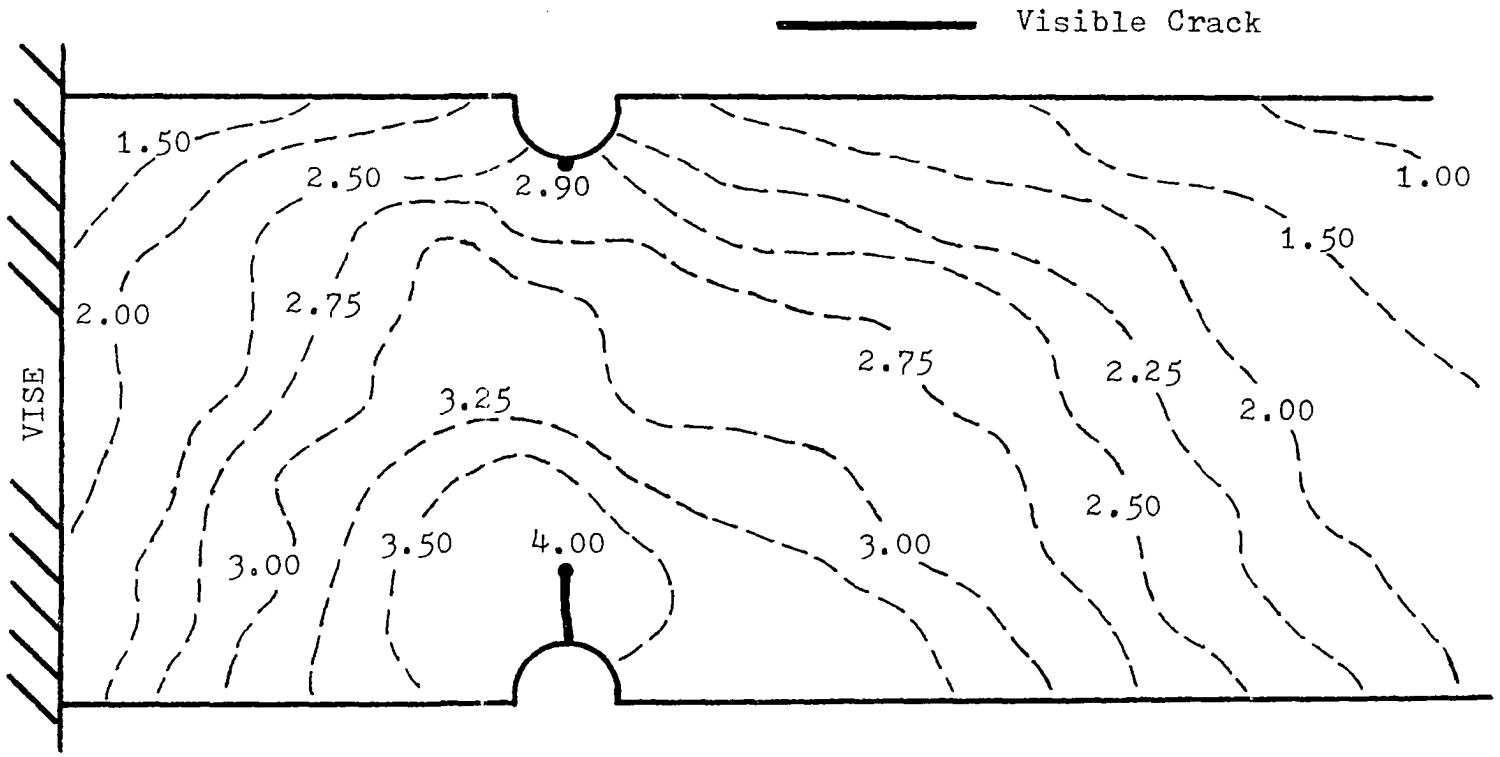

Figure 34(b). Temperature field map of specimen S-36 at 720,000 cycles (Temperatures in ^{o}F above ambient).

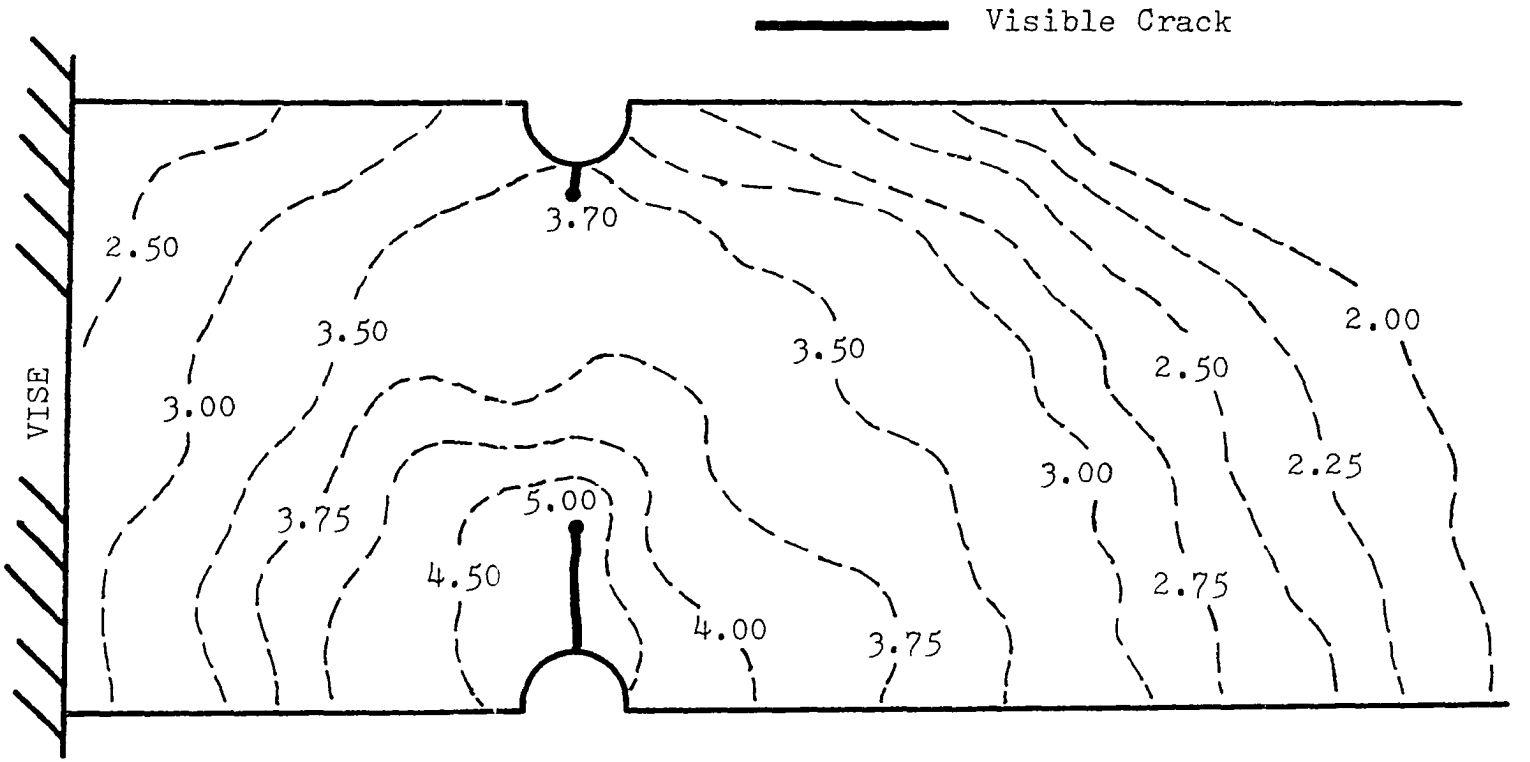

Figure 34(c). Temperature field map of specimen S-36 at 750,000 cycles (Temperatures in ^{o}F above ambient).

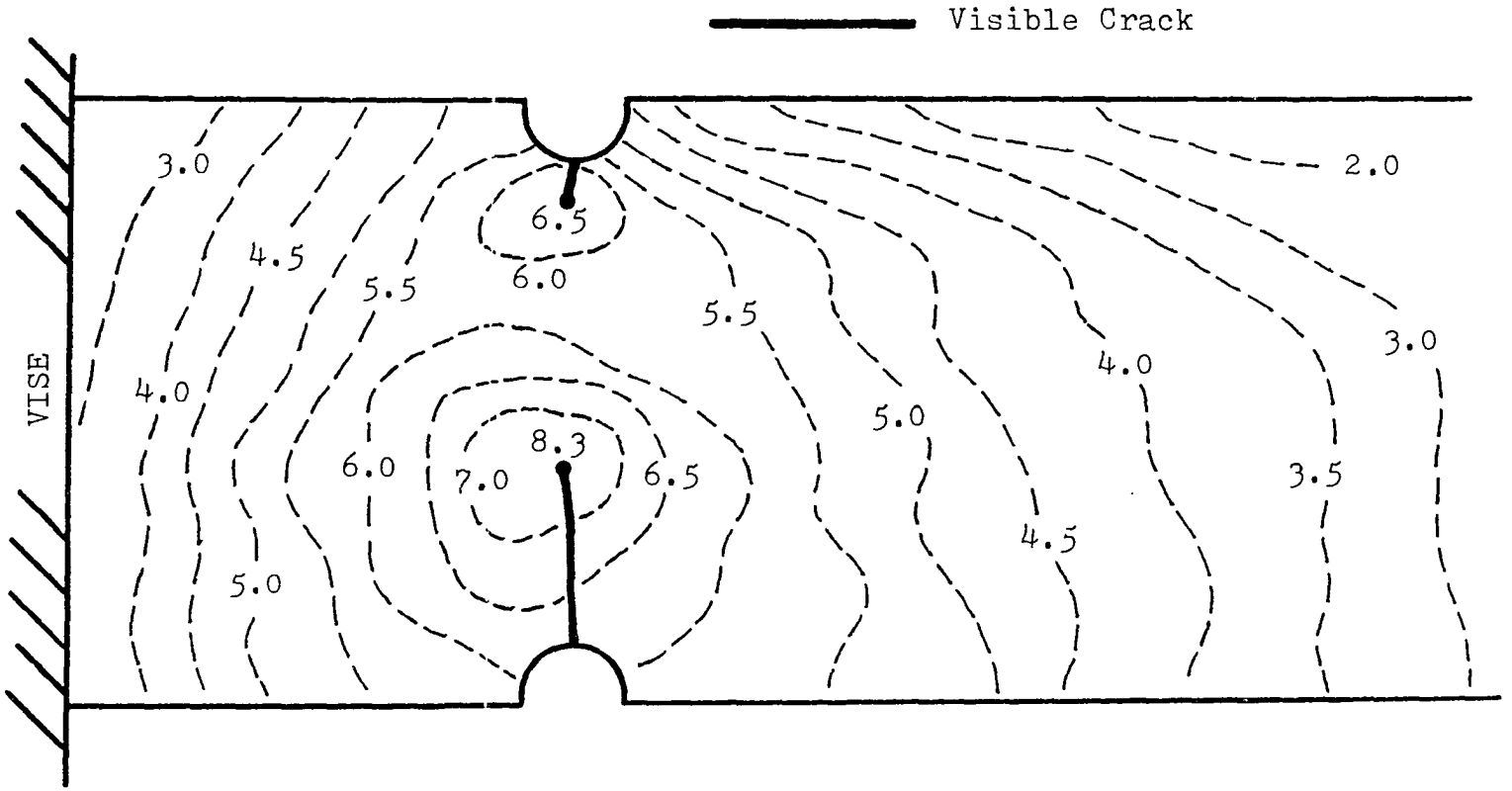

Figure 34(d). Temperature field map of specimen S-36 at 800,000 cycles. (Temperatures in ^{o}F above ambient).

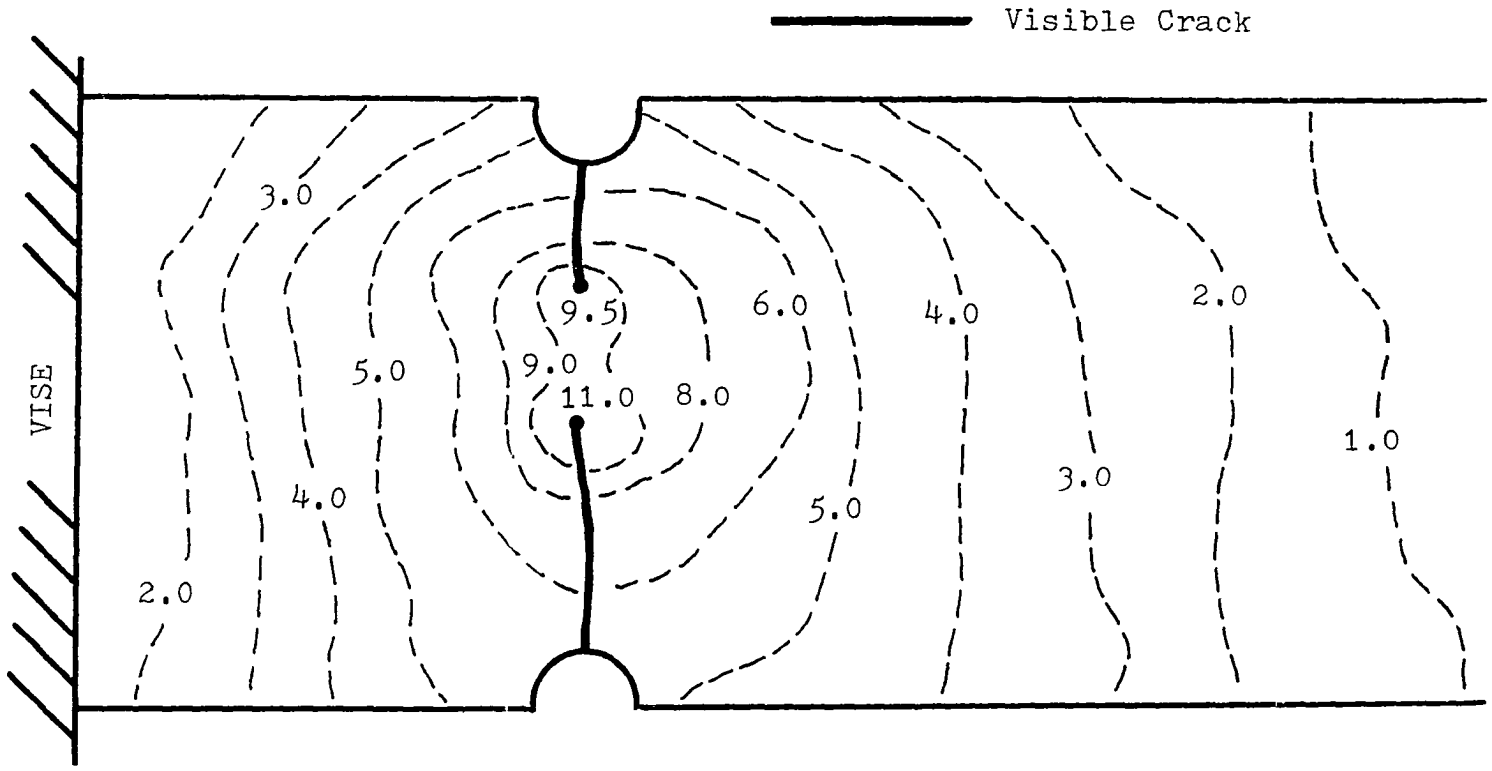

Figure 34(e). Temperature field map of specimen S-36 at 815,000 cycles (Temperatures in ^{o}F above ambient).

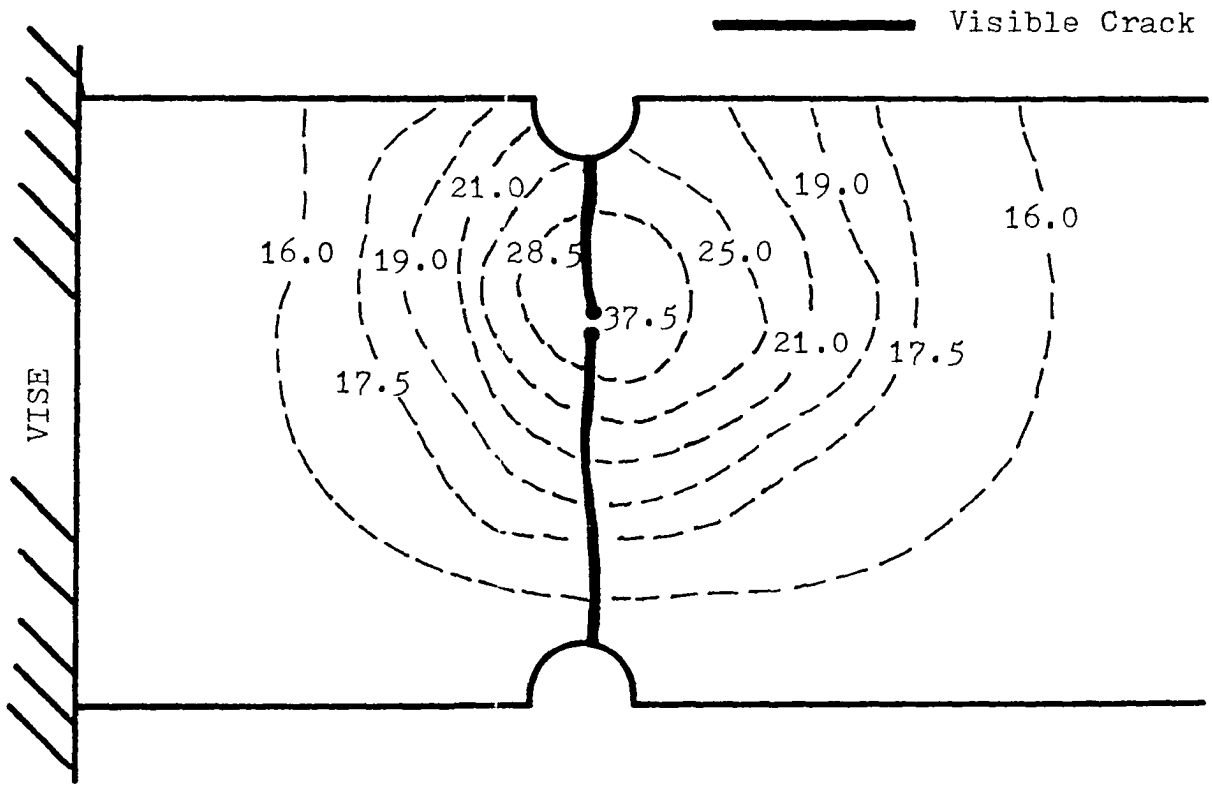

Figure 34(f). Temperature field map of specimen S-36 at 825,300 cycles (Temperatures in ^{o}F above ambient).

taken from a thermogram of the specimen at 720,000 cycles, shows the presence of the visible crack extending from the lower notch root. No crack was evident at the upper notch root. Figure 34(c) shows two cracks propagating in the specimen at 750,000 cycles. The remaining figures of S-36 follow the progress of the two cracks until just prior to failure when the last thermogram was taken. Note that Fig. 34(d) was made from the thermogram shown in Fig. 33(b), and clearly indicates the extent of both cracks in the specimen at 800,000 cycles.

The temperature field maps presented in Fig. 34 can be used to determine approximate energy dissipation rates in the material at any time. The approach used to accomplish this assumes that the temperature distribution on the specimen surface is at least quasi-steady state, and that a balance between the energy generated in the material and that removed by heat-transfer mechanisms exists at any time. This assumption is not strictly valid, especially in the final stages of the fatigue life, but will nevertheless yield reasonably accurate energy dissipation rates with little difficulty. Assuming a quasi-steady state exists, the heat transfer from the material by conduction is calculated by considering the temperature gradient at the isotherm farthest from the notches. Using the cross-sectional area of the specimen at that isotherm, and the thermal conductivity of the material, the conduction loss is derived by multiplying

the gradient, the area, and the conductivity according to Fourier's law. The losses by convection and radiation heat transfer are determined by using a combined heat transfer coefficient, as discussed in Chapter VI, and assigning areas on the surface within the outermost isotherm temperatures from the temperature field maps. Thus, the total loss of energy per unit time is found by adding the losses due to convection, conduction and radiation. This loss must be equalled by the energy generation for a quasi-steady state to exist. Using this procedure, the data in Fig. 35 were obtained. As can be seen, the heat generation rate (energy dissipation rate) follows generally the same three phases that the temperature rise itself does. By finding the area under the dissipation rate curve, one obtains the total energy dissipation in the material during the course of the fatigue test. In the case of this test, the total energy dissipation was found to be approximately 21.30 Btu, or $1.989(10^5)$ inch-pounds. If as an approximation, the volume of material dissipating this energy during the test is assumed to be a strip across the width of the specimen, 2 inches long and 0.375 inches wide, then the specific energy dissipation in the material, or the fatigue toughness of the material, is $2.267(10^6)$ in-lb/in^3. This value compares very well with the toughness for various metals reported in reference 62. In the reference, toughnesses between 10^5 and 10^7 in-lb/in^3 were reported for the life of about 800,000 cycles. It should be

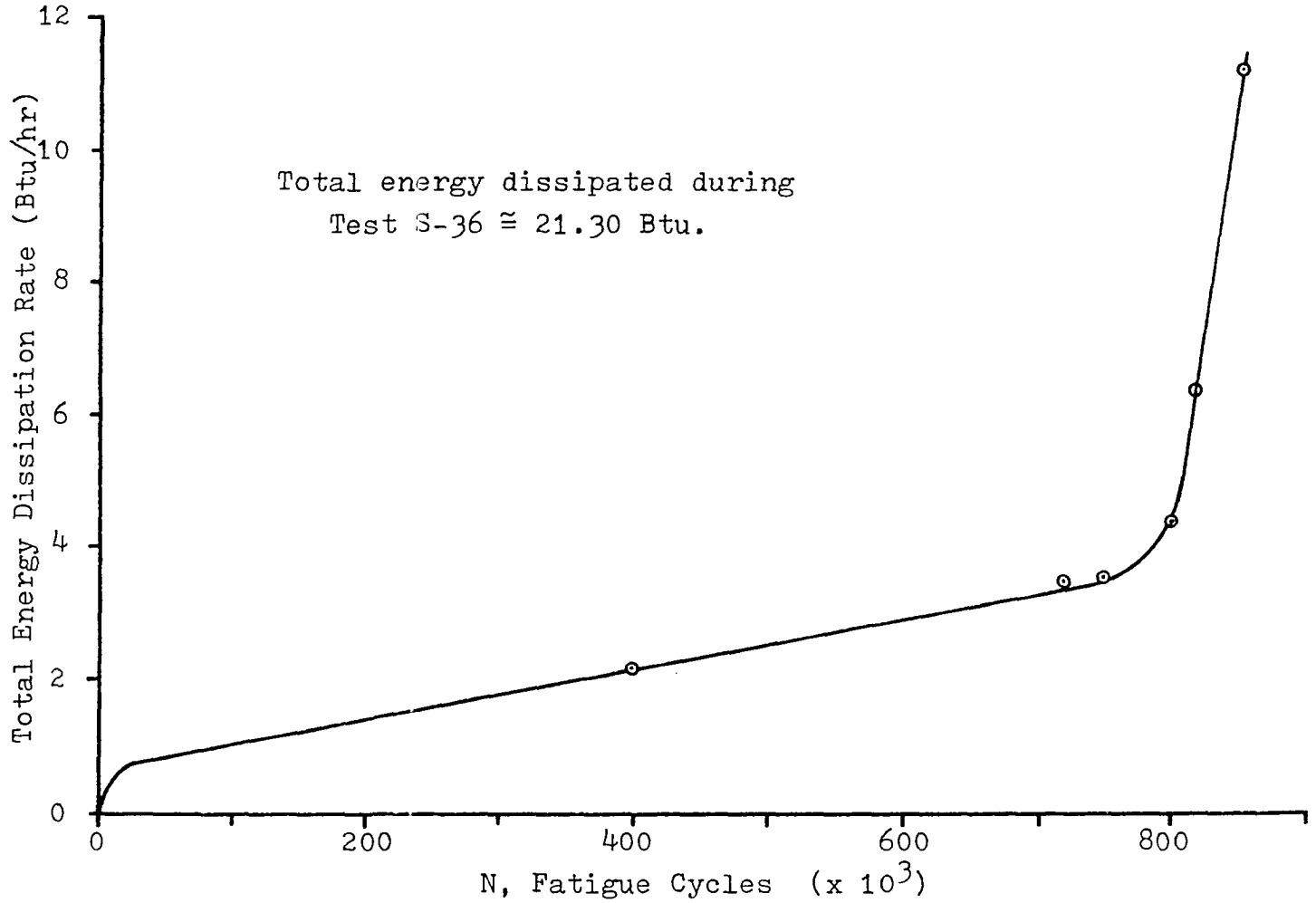

Figure 35. Energy dissipation rates for specimen S-36 during fatigue test.

noted that in determining the energy dissipation rates in the material, a heat transfer coefficient of 2.0 was assumed for both the upper and lower surfaces of the material. This assumption will be justified in the discussion accompanying Chapter VI on analytical considerations.

Specimen S-52 from the series at the next highest stress level is shown in Figures 36 and 37. Figure 36(a) shows the specimen, which had sharp 0.094-inch diameter notches and was cycled at a centerline stress of 22,700 psi, at only 10,000 cycles. The temperature rises at the notch roots are easily seen in this figure, indicating the initiating of fatigue damage mechanisms in the material. Not until 180,000 cycles was a visible crack detected, propagating from the notch at the lower side of the figure. The temperature field map of this thermogram shown in Fig. 37(a) shows that this notch root displayed the highest temperature on the surface at 10,000 cycles. Figure 36(b) shows specimen S-52 at 225,000 cycles, not long before its failure at 243,900 cycles. Compared to specimen S-36, the two cracks in Fig. 36(b), indicated by the hot spots on the surface of the specimen, are propagating more nearly symmetrically, as one would expect.

The remaining figures for this test show the temperature field maps taken from other thermograms of specimen S-52. The first thermogram to include a visible crack was that used to produce Fig. 37(d). Note that although the

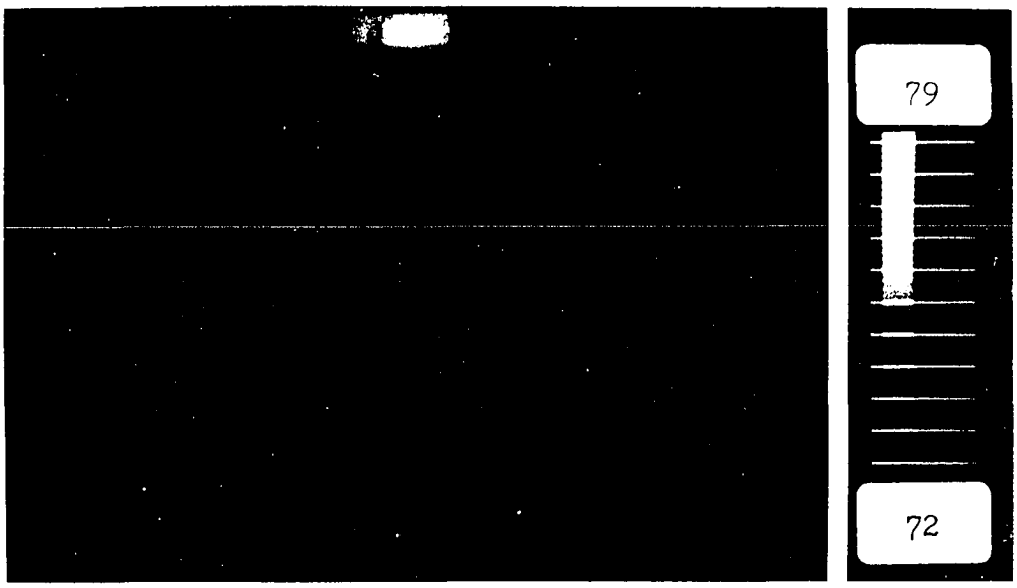

Figure 36(a). Thermogram of specimen S-52 at 10,000 cycles.

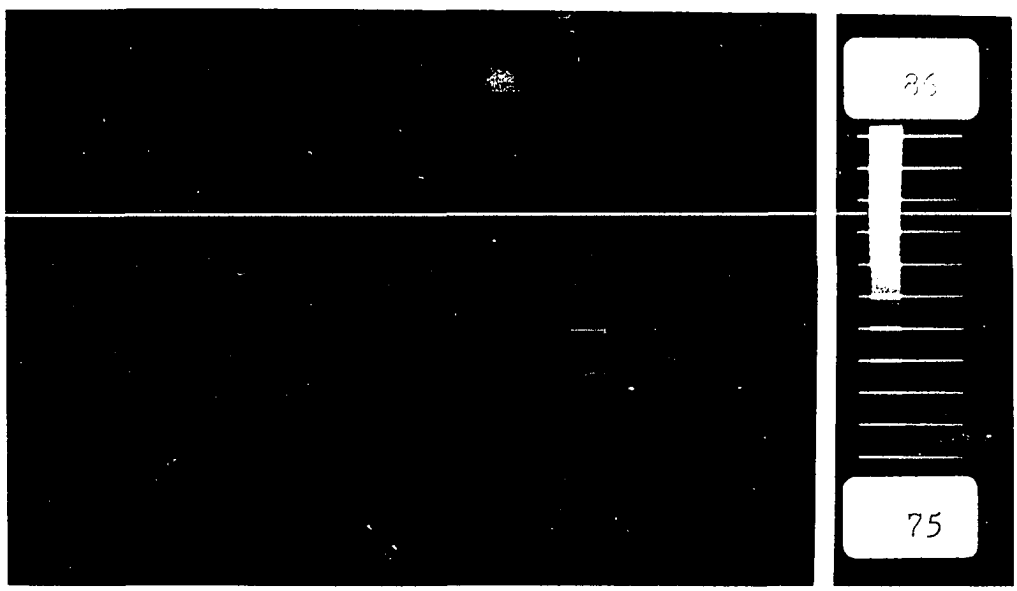

Figure 36(b). Thermogram of specimen S-52 at 225,000 cycles.

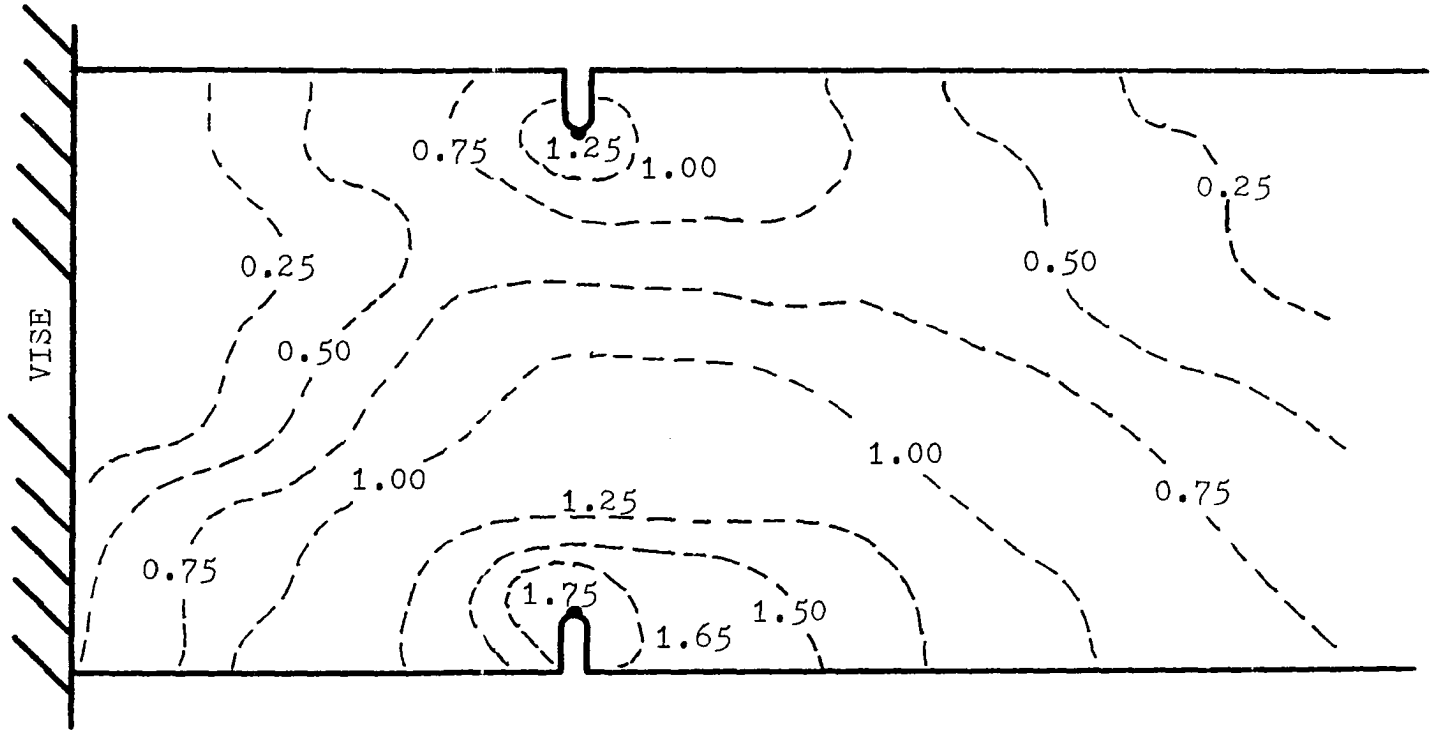

Figure 37(a). Temperature field map of specimen S-52 at 10,000 cycles (Temperatures in ^{o}F above ambient).

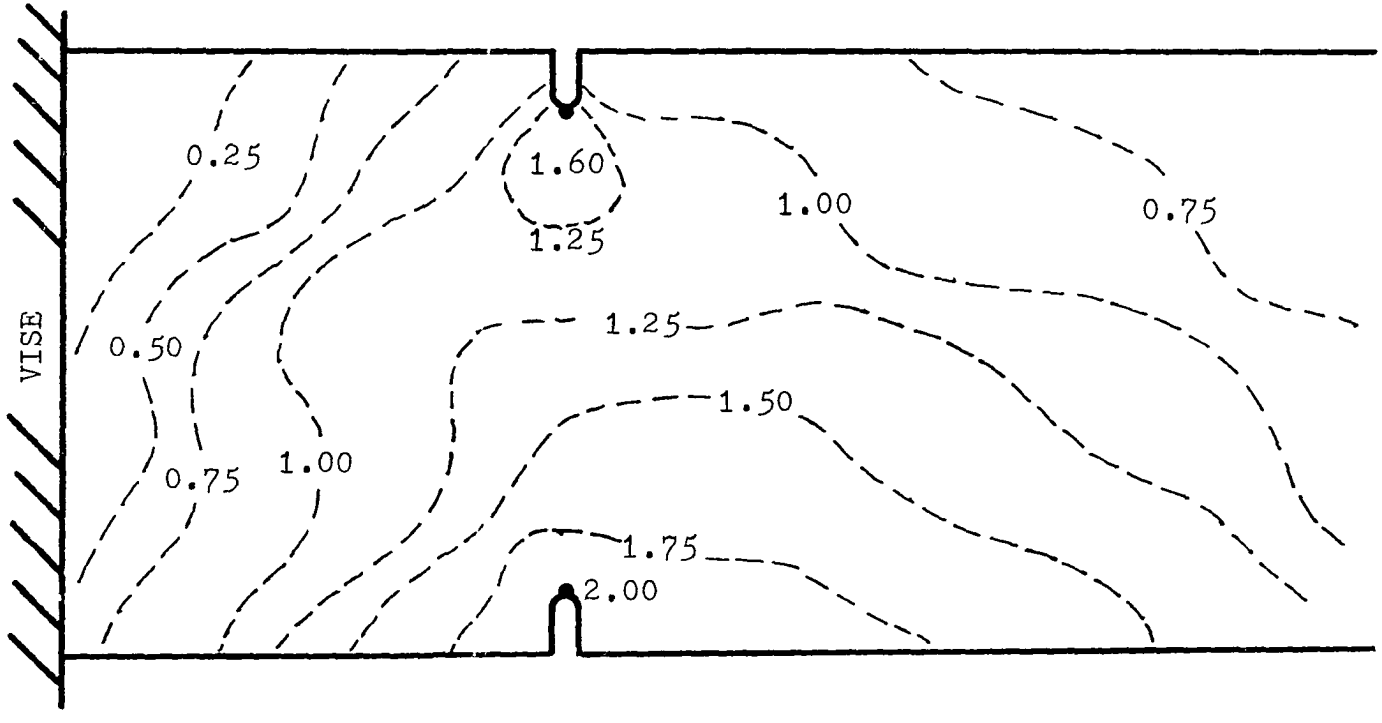

Figure 37(b). Temperature field map of specimen S-52 at 50,000 cycles (Temperatures in ^{o}F above ambient).

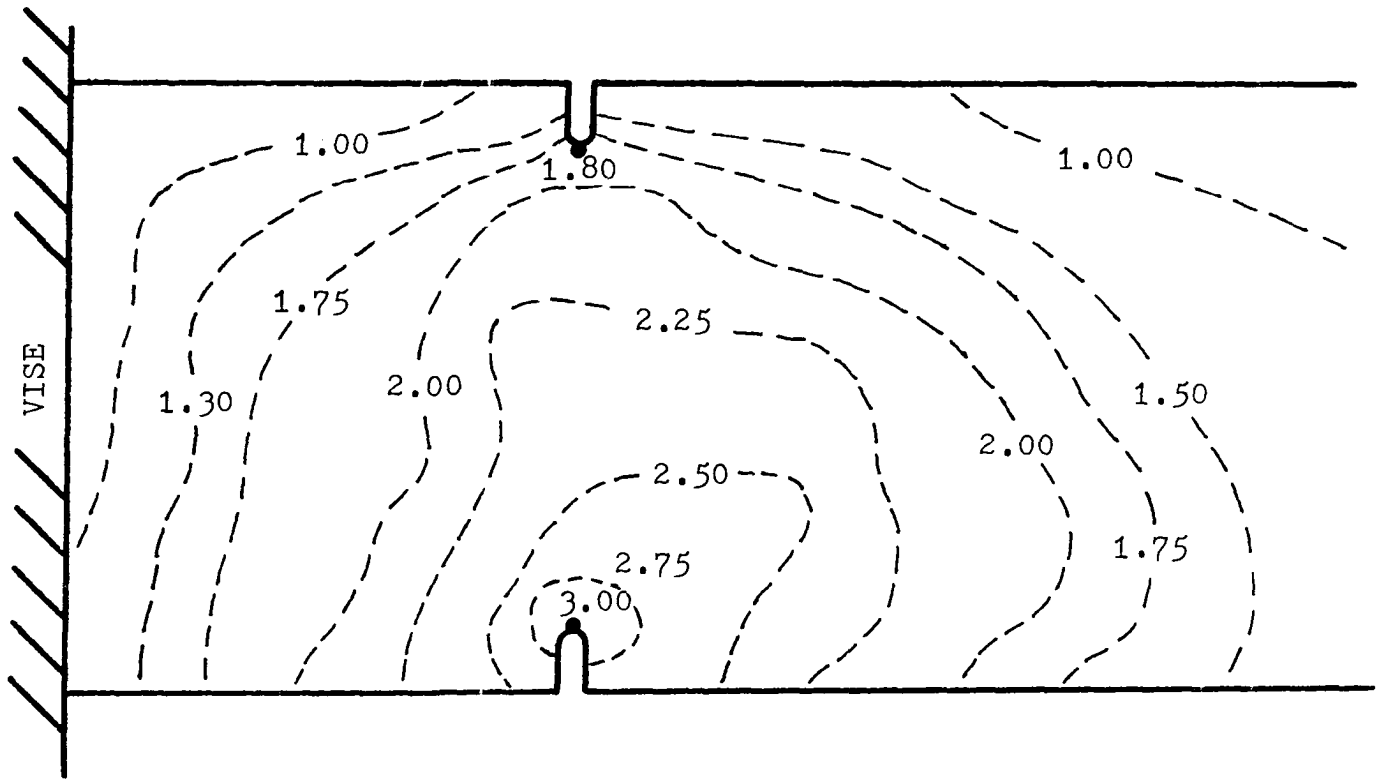

Figure 37(c). Temperature field map of specimen S-52 at 100,000 cycles (Temperatures in ^{o}F above ambient).

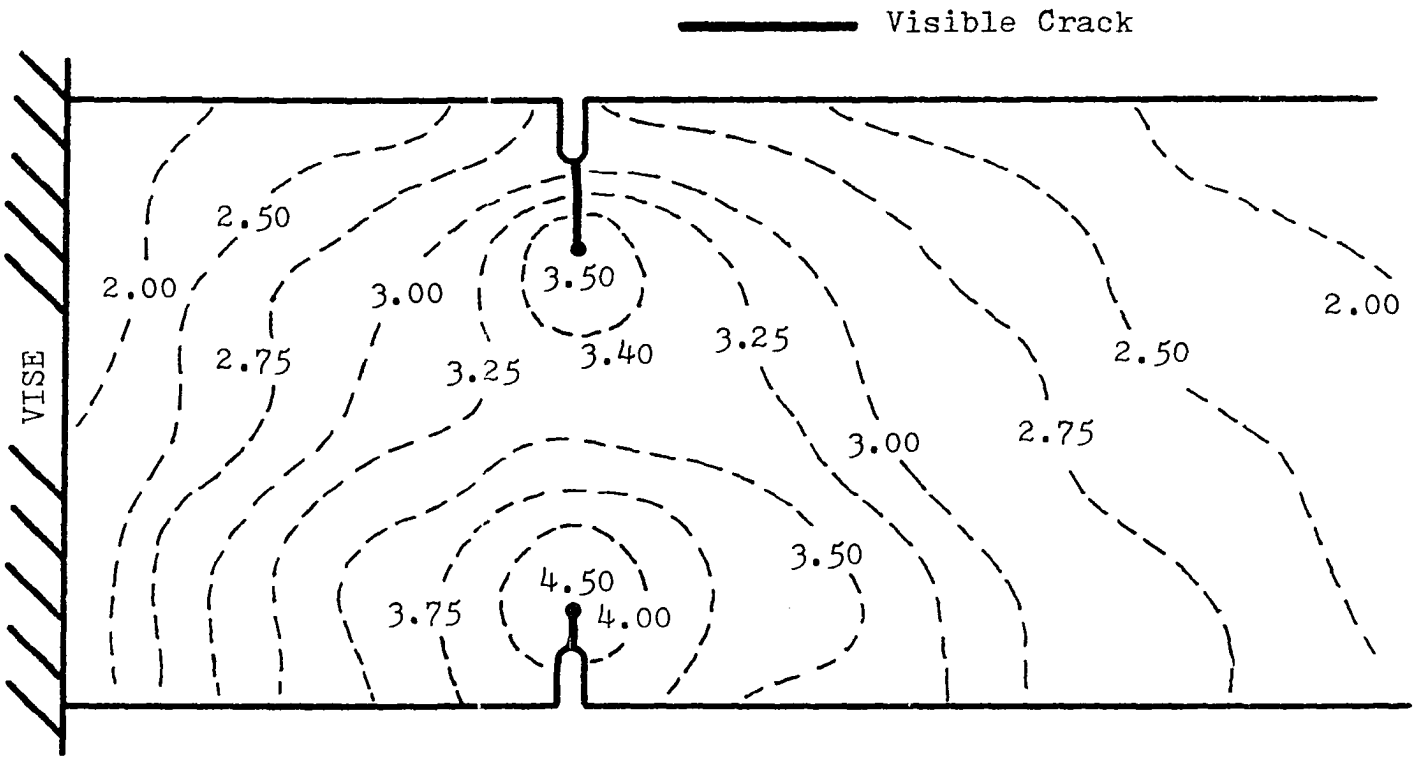

Figure 37(d). Temperature field map of specimen S-52 at 186,000 cycles (Temperatures in ^{o}F above ambient).

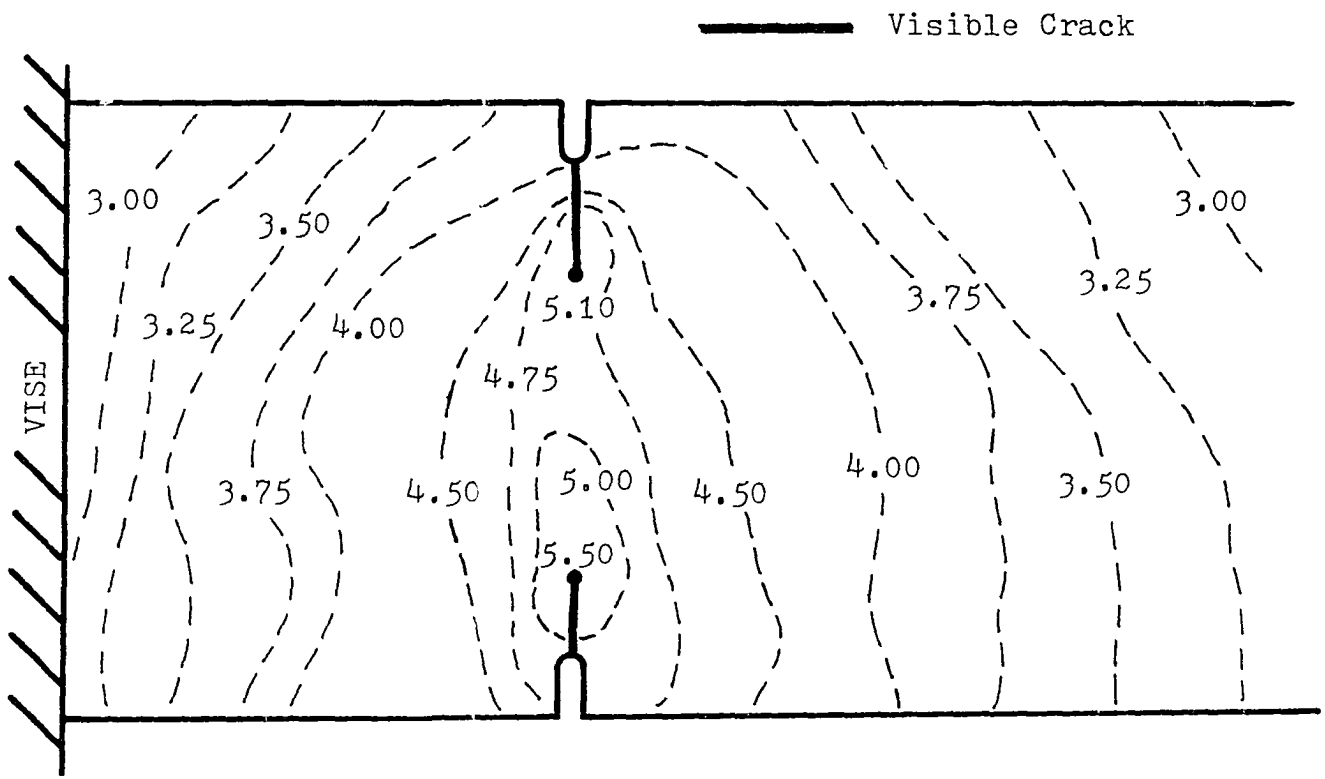

Figure 37(e). Temperature field map of specimen S-52 at 200,000 cycles (Temperatures in ^{o}F above ambient).

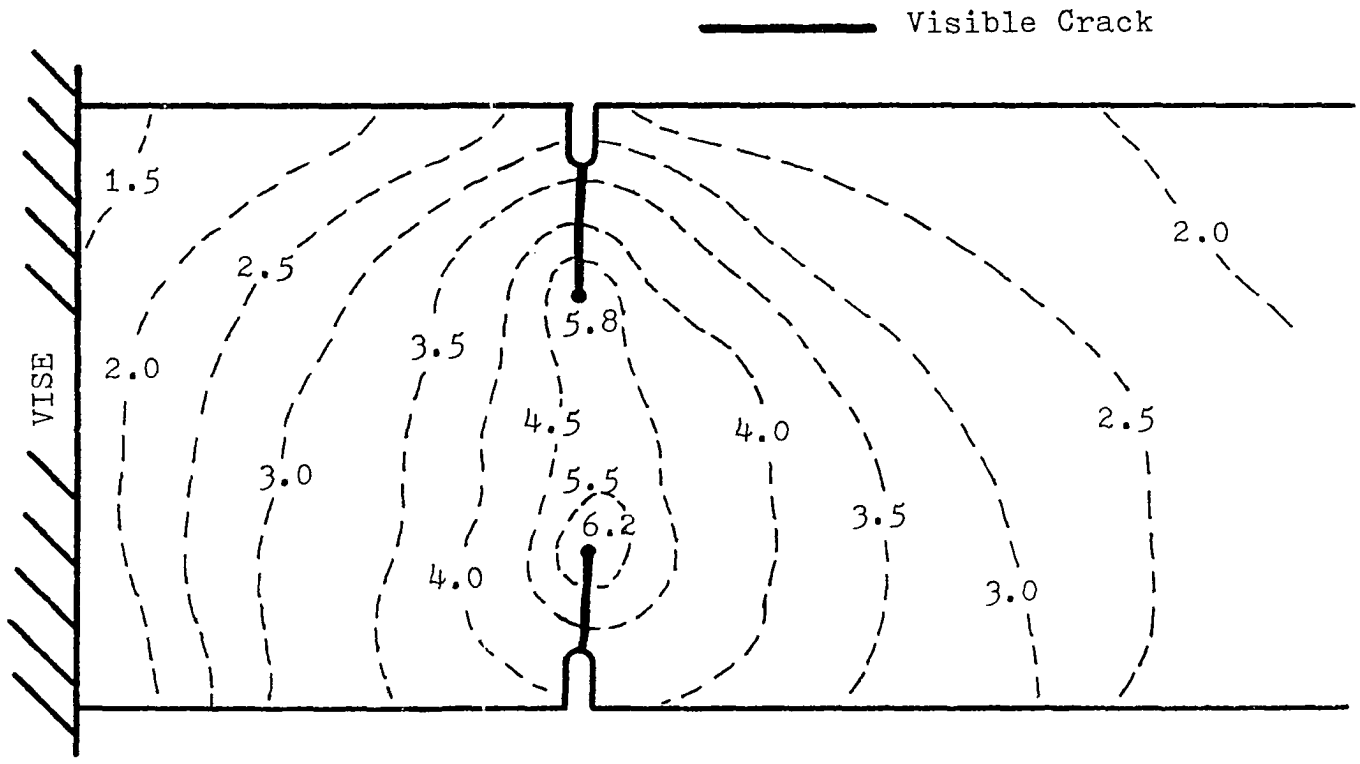

Figure 37(f). Temperature field map of specimen S-52 at 215,000 cycles (Temperatures in ^{o}F above ambient).

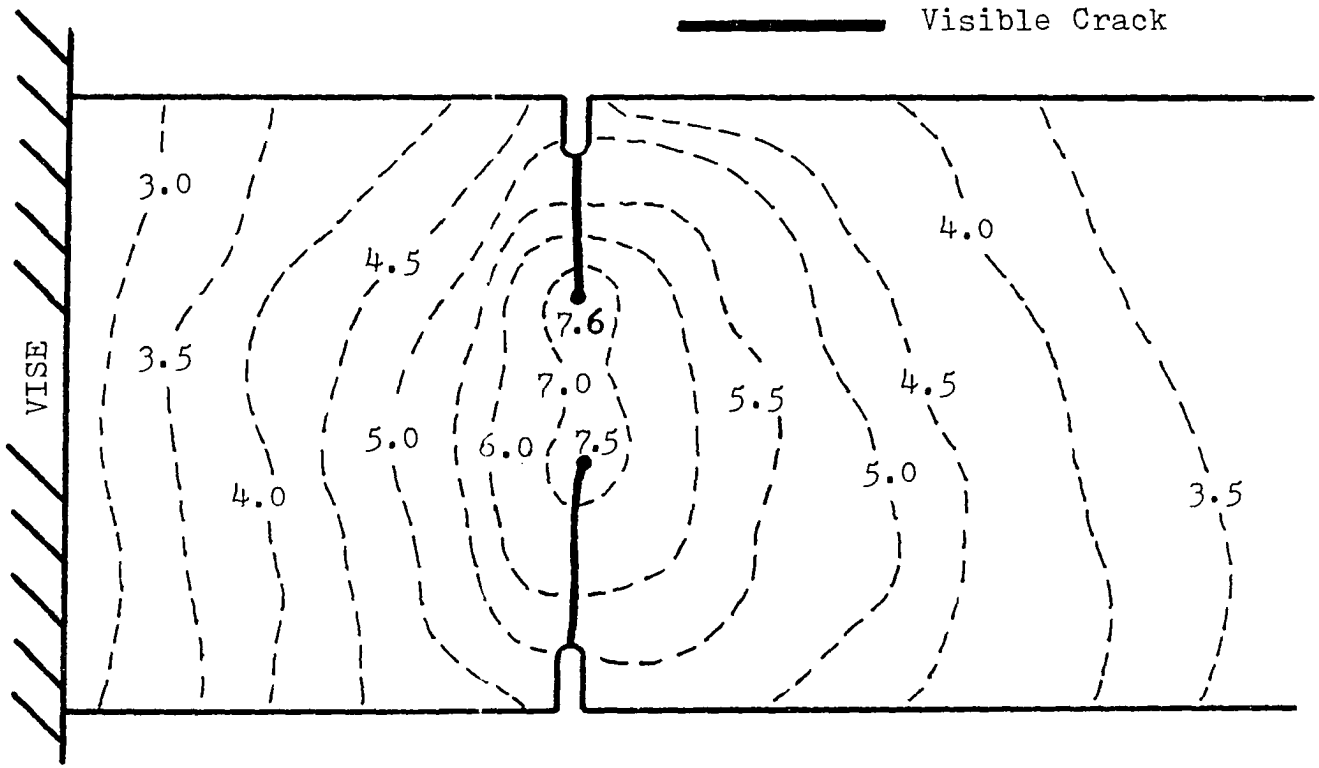

Figure 37(g). Temperature field map of specimen S-52 at 225,000 cycles (Temperatures in ^{o}F above ambient).

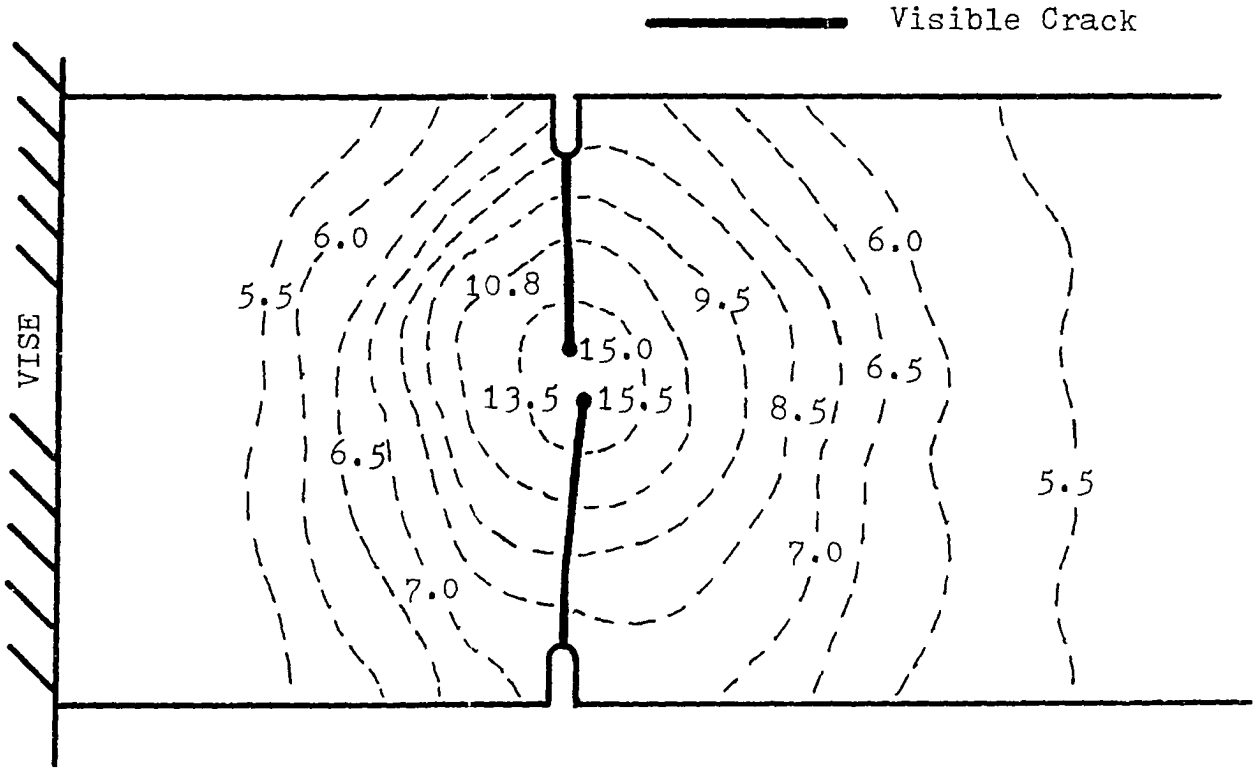

Figure 37(h). Temperature field map of specimen S-52 at 239,000 cycles (Temperatures in ^{o}F above ambient).

first crack was found at the lower notch root, in Fig. 37(d) taken at 186,000 cycles, the crack from the upper notch has become longer than that from the lower notch. By the time of the thermogram in Fig. 36(b) at 225,000 cycles, however, the crack lengths are nearly equal. This is seen in Fig. 37(g).

Figure 38 shows the results of the energy balances performed on the thermograms to obtain energy dissipation rates in the material. The total energy dissipation for this test was found to be 5.90 Btu, or $5.509(10^4)$ in-lb. Using the same approach as used for S-36, except that the width of the strip across the specimen will be assumed to be 0.094 inches, one obtains a fatigue toughness of $2.50(10^6)$ in-lb/in^3, which is again in agreement with the results in reference 62.

Similar results are also presented for the test of specimen S-55. This specimen had 0.094-inch diameter notches, and was cycled at a maximum centerline bending stress of 23,600 psi. The behavior observed form this specimen was very much like that seen in the previous two specimens. Figure 39 presents two thermograms taken during the test of specimen S-55. Figure 39(a) was taken early in the test (10,000 cycles), and Fig. 39(b) was taken toward the end of the test at 90,000 cycles. The fatigue life of the specimen was 103,300 cycles. The location of the impending fatigue damage can be predicted from Fig. 39(a). Cracks finally be-

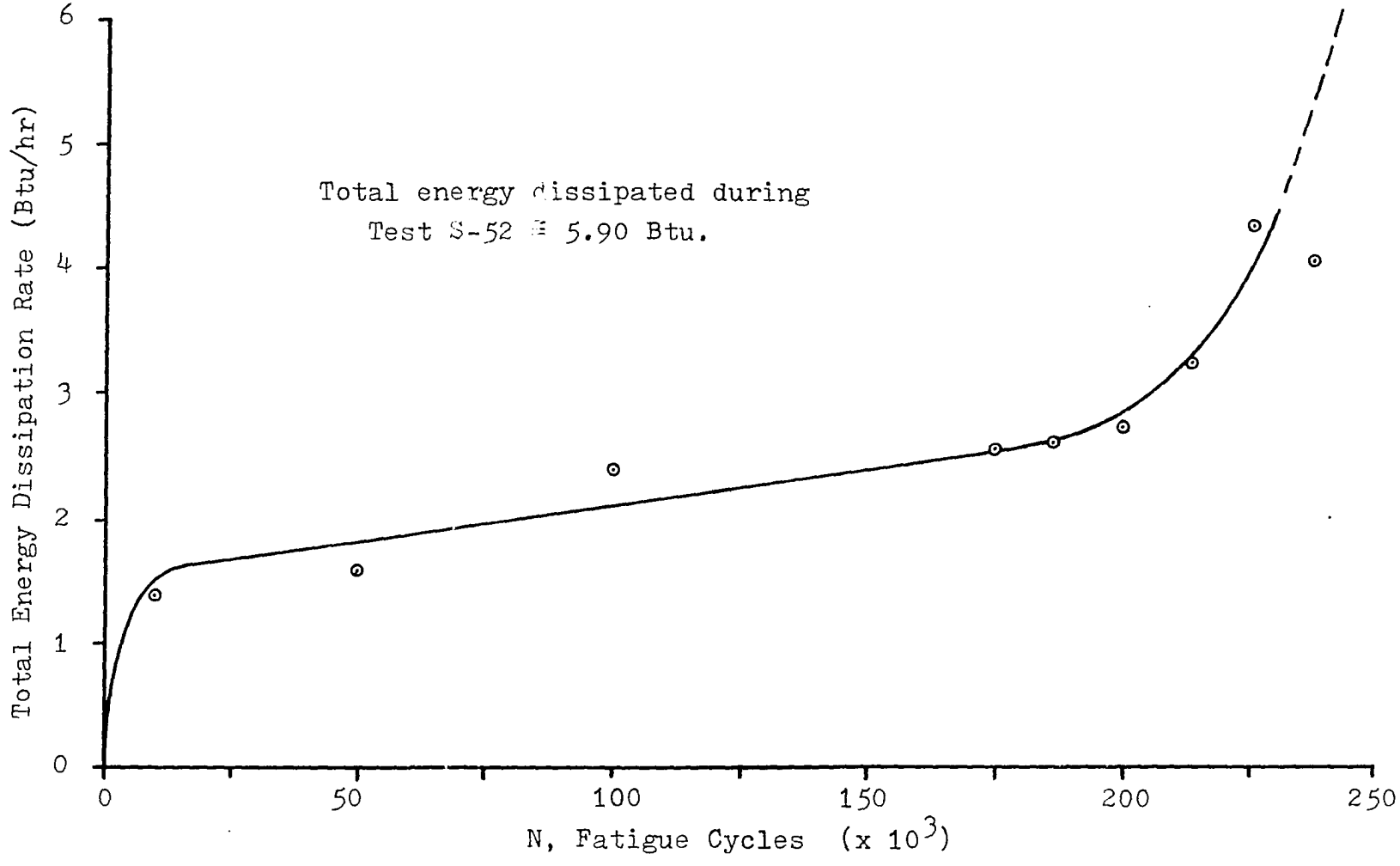

Figure 38. Energy dissipation rates for specimen S-52 during fatigue test.

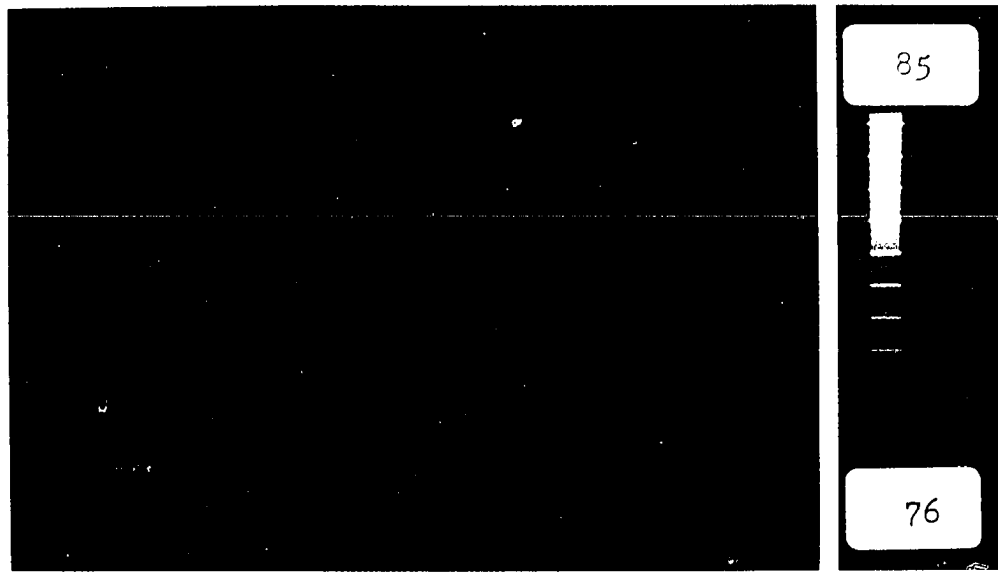

Figure 39(a). Thermogram of specimen S-55 at 10,000 cycles.

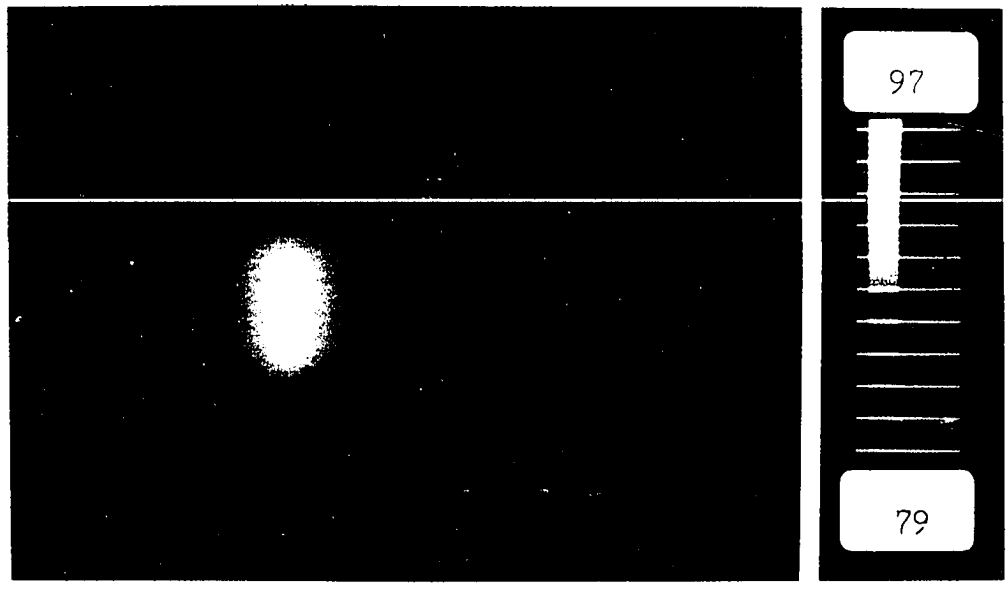

Figure 39(b). Thermogram of specimen S-55 at 90,000 cycles.

came evident at 28,000 cycles into the test, first appearing at the lower notch root as would be predicted from the thermogram. The seven temperature field maps of Fig. 40 follow the initiation of the cracks at both notches and their propagation to failure. Although the crack from the lower notch was slightly longer than that from the upper notch, they propagated nearly symmetrically throughout the test. Figure 41 shows the energy dissipation rates calculated from the temperature field maps. The distributions of thermograms taken during this test allows an energy dissipation curve to be defined more clearly than in the previous examples, and the three-phase behavior discussed already is again evident in the data.

Similar results could be obtained from any fatigue test with thermographic monitoring, provided of course that the stress levels are sufficient to produce a temperature rise on the specimen surface. In any such case, the results of this study indicate that using thermography one can predict where damage will occur, monitor the propagation of fatigue cracks, determine the temperature field map, and obtain approximate energy dissipation rates and fatigue toughness for fatigue tests of steel plate.

Fatigue Tests Using Aluminum

Another important structural material, which is used in many applications involving fatigue loading, is aluminum. A few tests were performed using aluminum fatigue

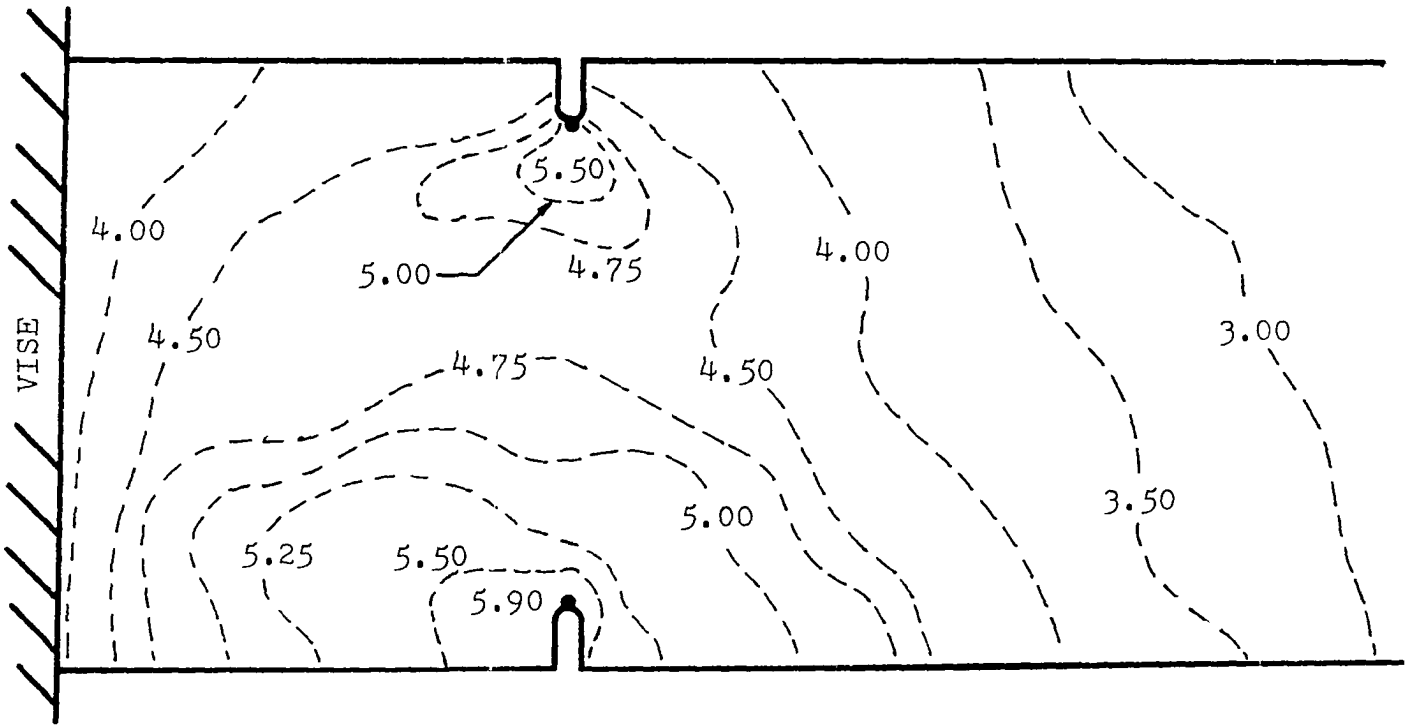

Figure 40(a). Temperature field map of specimen S-55 at 10,000 cycles (Temperatures in ^{o}F above ambient).

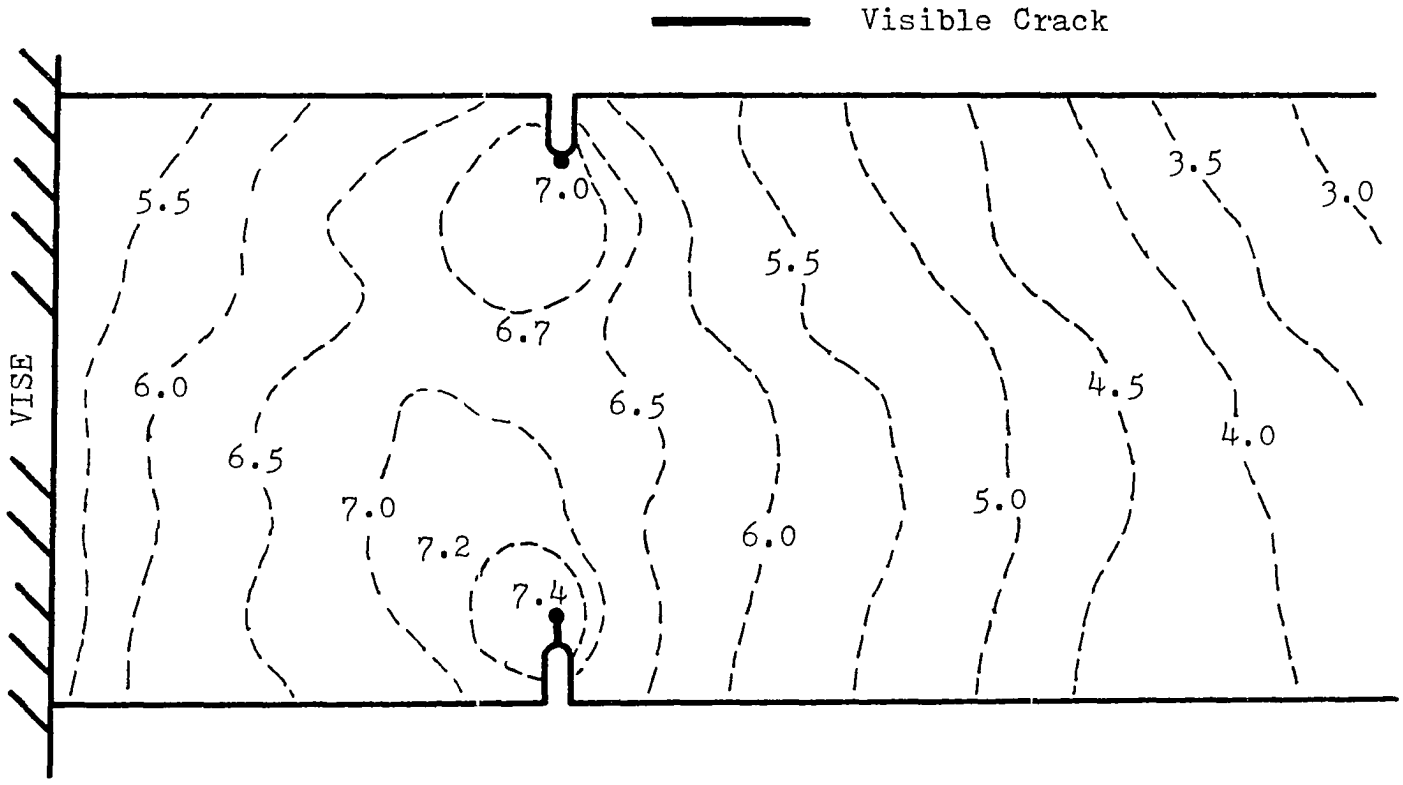

Figure 40(b). Temperature field map of specimen S-55 at 25,000 cycles (Temperatures in ^{o}F above ambient).

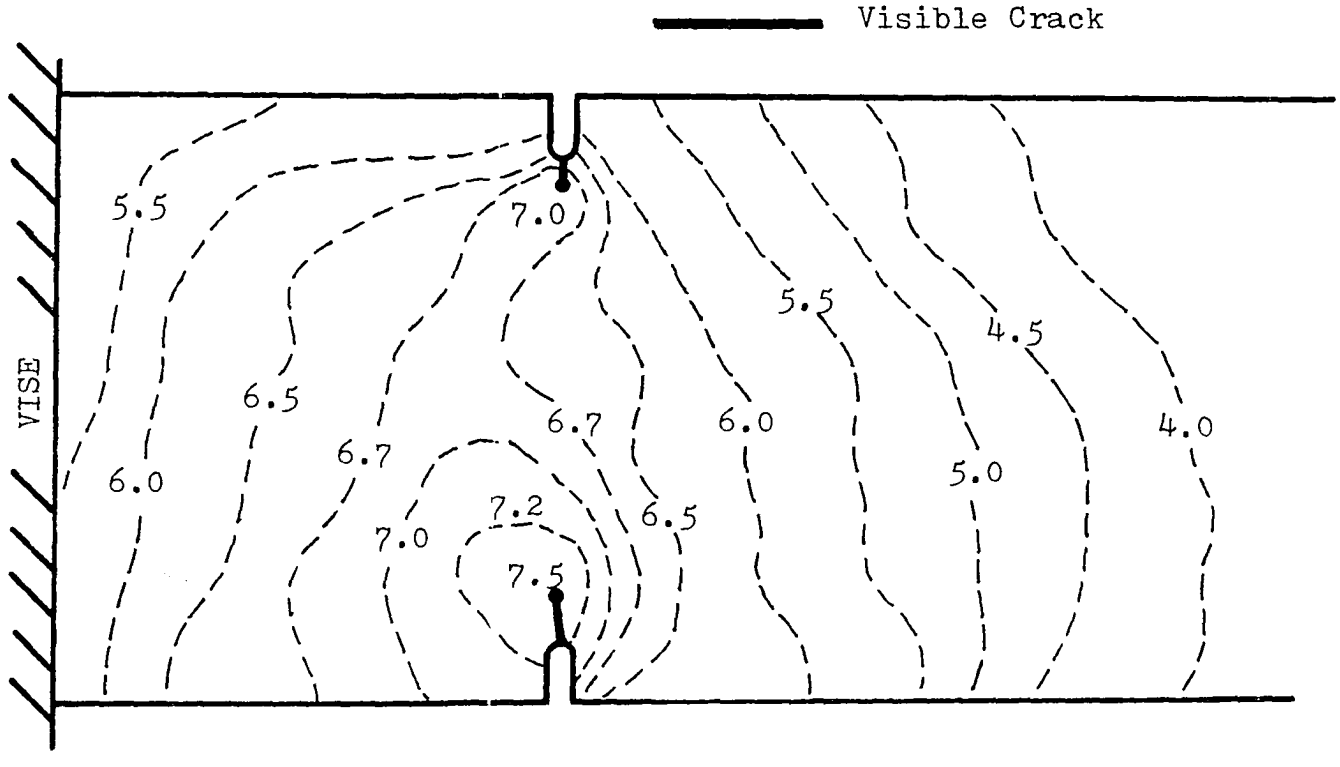

Figure 40(c). Temperature field map of specimen S-55 at 40,000 cycles (Temperatures in ^{o}F above ambient).

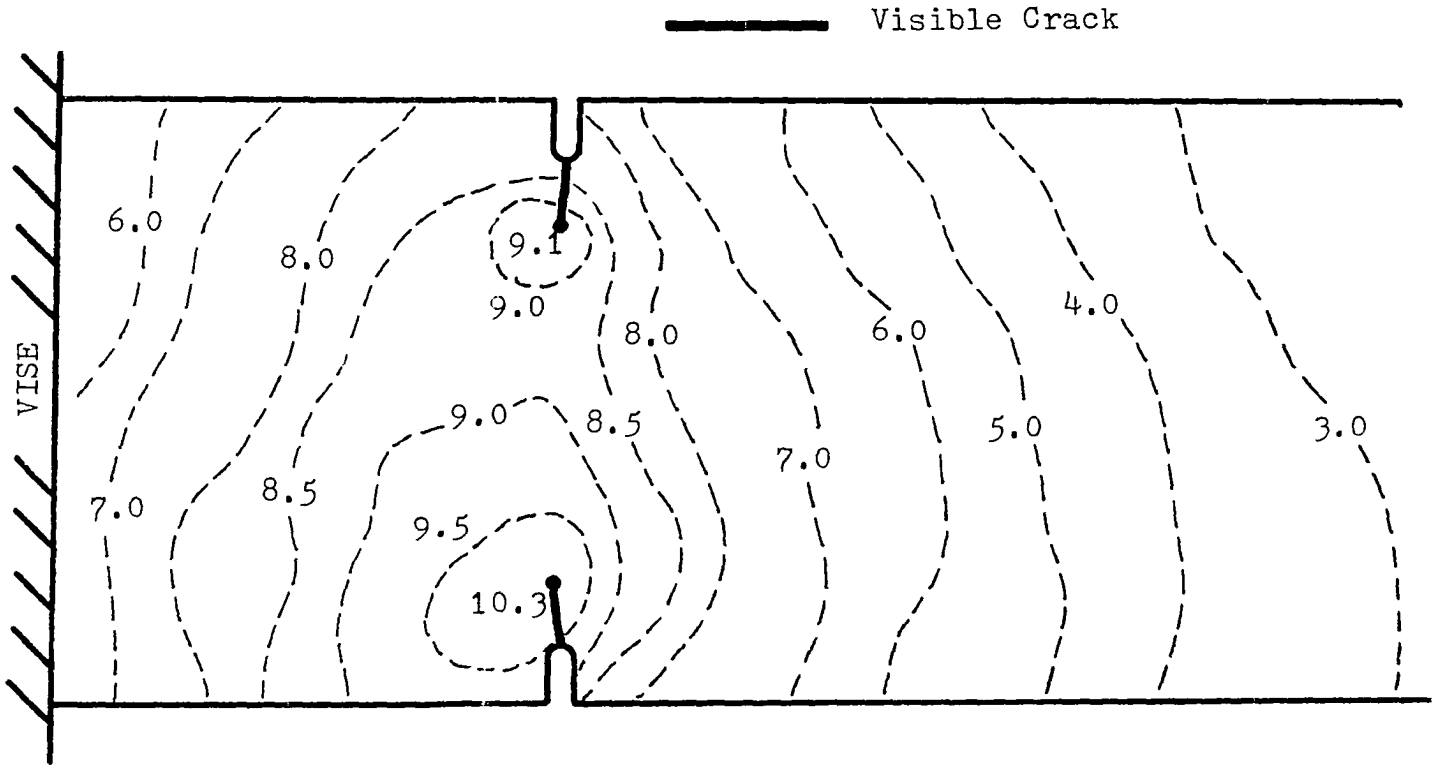

Figure 40(d). Temperature field map of specimen S-55 at 60,000 cycles (Temperatures in ^{o}F above ambient).

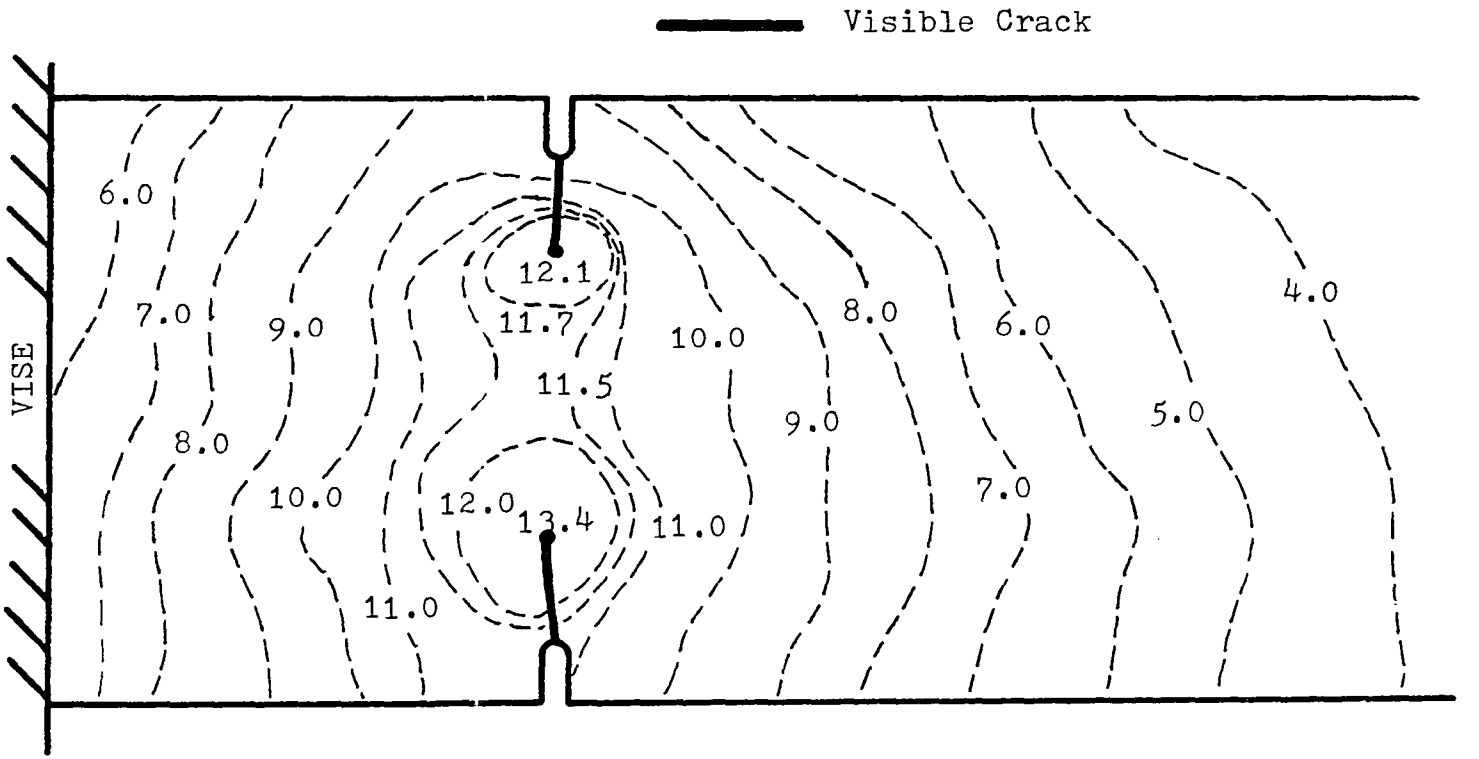

Figure 40(e). Temperature field map of specimen S-55 at 80,000 cycles (Temperatures in ^{o}F above ambient).

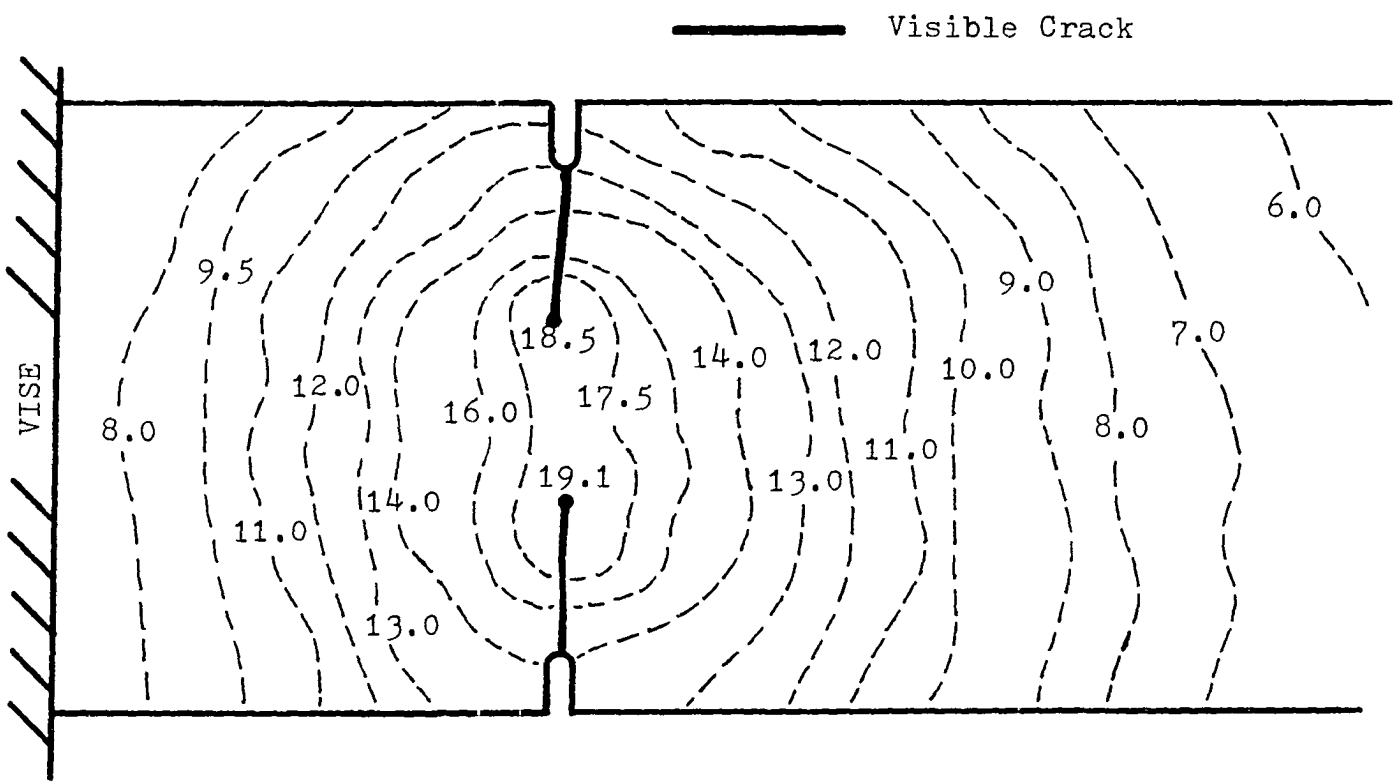

Figure 40(f). Temperature field map of specimen S-55 at 90,000 cycles (Temperatures in ^{o}F above ambient).

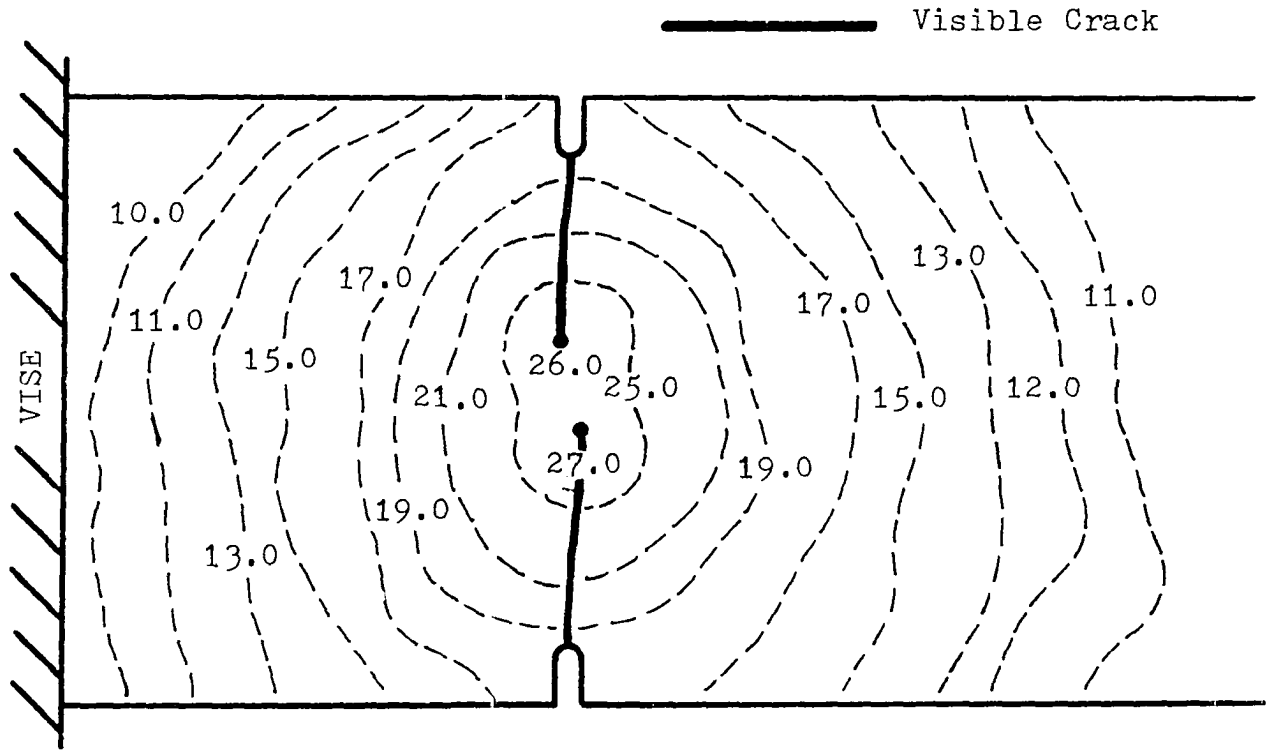

Figure 40(g). Temperature field map of specimen S-55 at 95,000 cycles (Temperatures in ^{o}F above ambient).

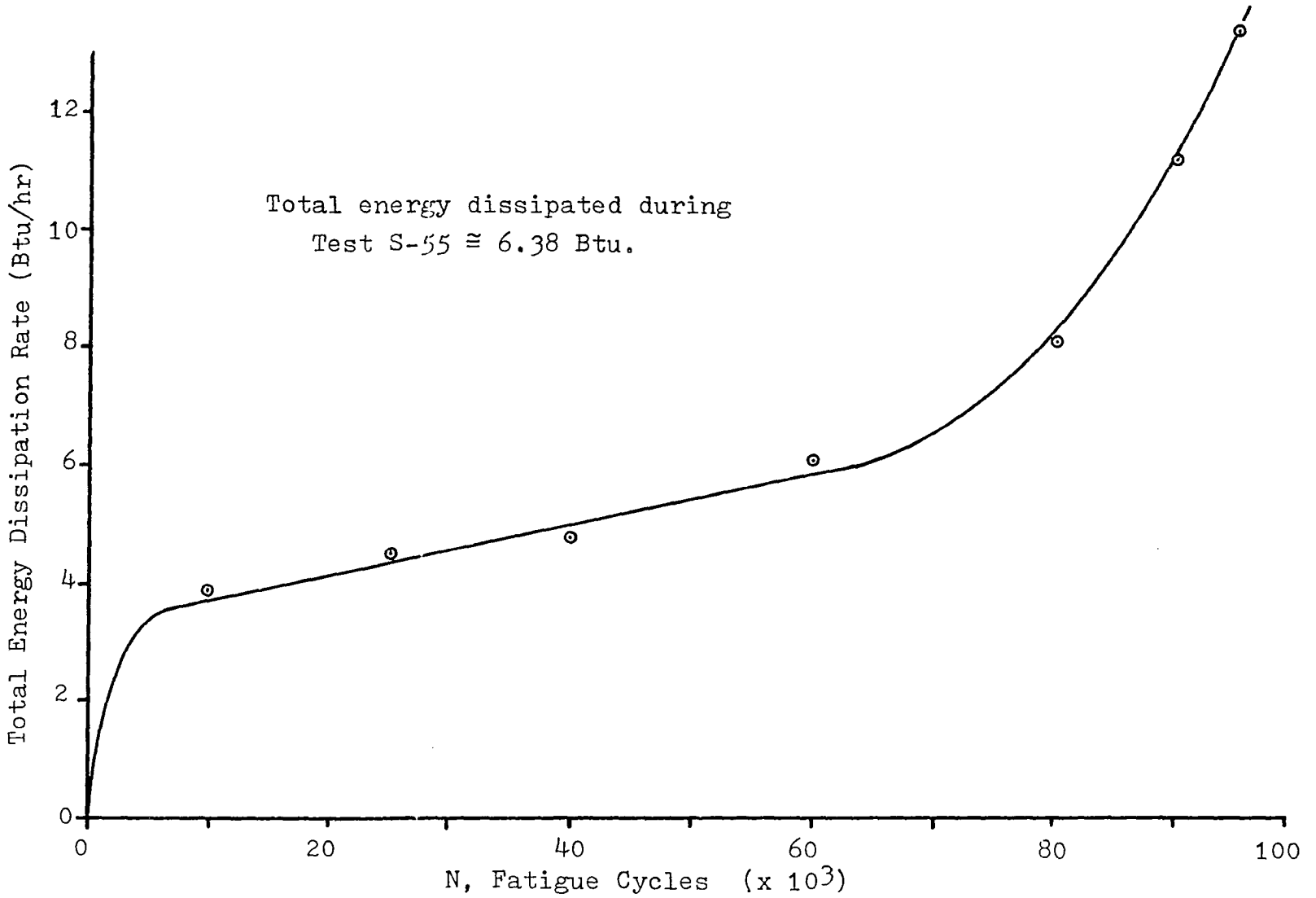

Figure 41. Energy dissipation rates for specimen S-55 during fatigue test.

specimens to determine the potential for thermographic monitoring of this material for fatigue damage. As will be seen, it was found that the thermal conductivity of aluminum, which can be four times that of steel, makes it difficult to obtain useful thermographic data during tests of aluminum.

One aluminum fatigue specimen tested is shown in Fig. 42. This specimen was 2024-T6 aluminum and was given the same black paint coating as were the steel specimens. A saw cut was made in the specimen to a depth of about 1.0 inches, or half the width of the material. Attention could then be focused at the root of the cut in making visual inspections. The aluminum specimen was cycled at a maximum nominal bending stress of 23,300 psi. Figure 43 shows a thermogram taken of this specimen at 30,000 cycles. By this time, a crack had formed at the root of the saw cut and was propagating across the uncut region of the specimen. Unlike the temperature fields observed in the tests of steel, the temperature rise caused by the high stress levels in the aluminum resulted in a very blurred image from the thermograph. This rise gave only a general indication of the location of the maximum fatigue damage in the material. The warmest region was only about $5^{\circ}F$ above room temperature. There was no easily distinguished change in the temperature field on the specimen as the crack was formed and began to propagate, as was the case with the steel specimens. The

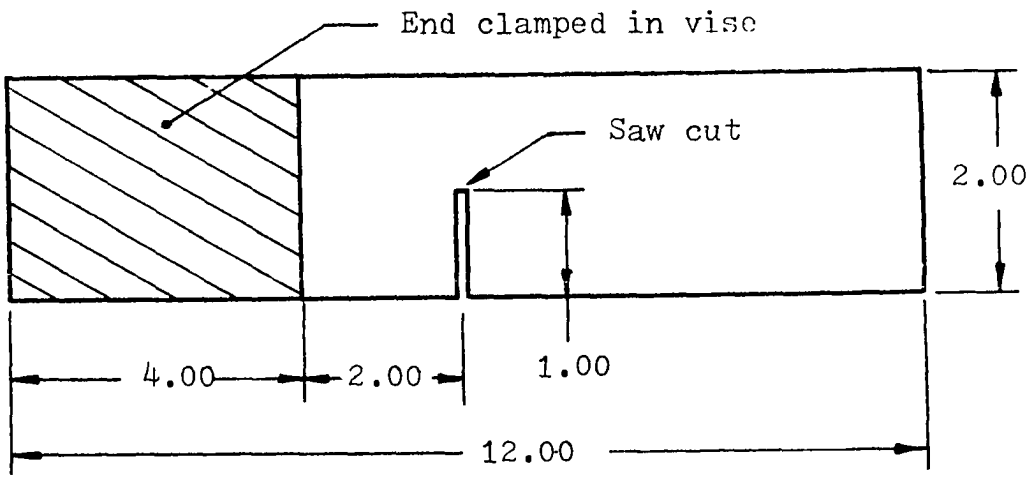

Thickness = 0.100

Figure 42. Aluminum fatigue specimen (Dimensions given in inches).

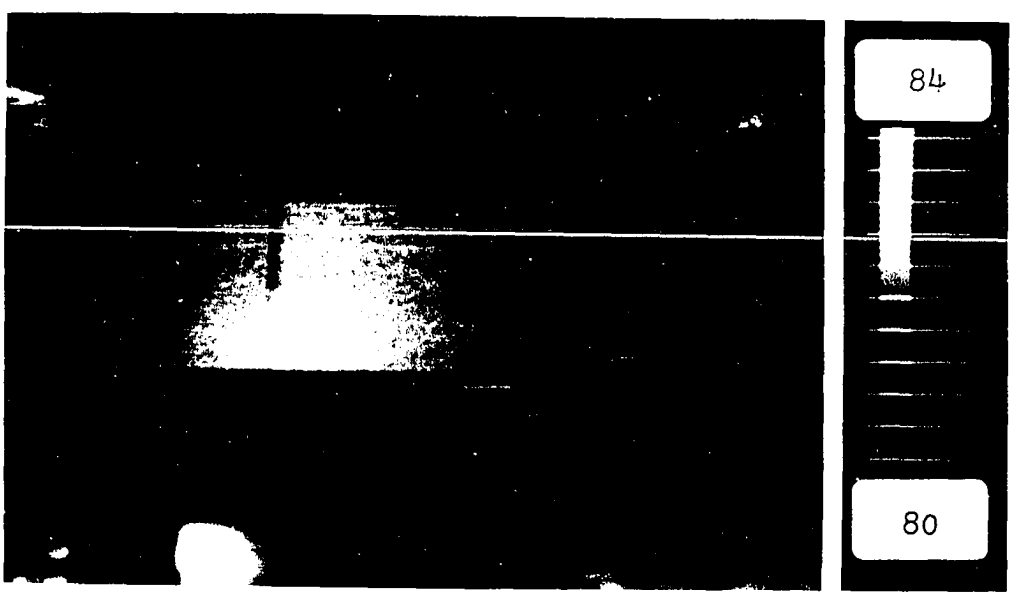

Figure 43. Thermogram of aluminum fatigue specimen at 30,000 cycles.

diffuse nature of the temperature field in Fig. 43 makes the location of the hottest point at the tip of the crack most difficult, and detracts from the accuracy of any determination. Although several other fatigue tests were attempted using both 2024-T3 and 7075-T6 aluminum, there was never a clear indication of the location of the fatigue crack, and the data obtained were generally poorer than those in the thermogram discussed.

Obviously the thermal conductivity of the aluminum acts to efficiently remove heat from the region of generation. Unless the heat generation is very high, as would be caused by undesirably high stress levels, the resulting temperature field map as obtained with thermography is of little value. As aluminum is an important structural material, it would be desirable to be able to use thermographic techniques on aluminum fatigue specimens. It may be possible to enhance the image of the thermogram by altering the environment about the specimen. Particularly, by changing the convecting heat transfer in the problem, either by blowing air over the specimen or by changing the ambient temperature, it may be possible to create a more localized temperature rise on the surface of the material. In that case, thermography would become more useful as an inspection technique for aluminum. These possibilities will be discussed further in Chapter VI.

Fatigue Tests Using Composite Materials

There is presently a great deal of interest in the use of composite materials in engineering applications. Many of these applications involve situations where fatigue loading is imposed on the material, such as in aircraft parts. An ever-increasing number of composite materials have been developed or are being developed for structural use, including fiberglass-reinforced epoxys, boron-reinforced epoxys, and graphite-reinforced epoxys. Composite materials generally behave quite well under fatigue loading, but when damage begins to occur, it can take many forms. Unlike steel or aluminum, where fatigue damage manifests itself as cracks which propagate to failure, composite materials can experience damage in the form of debonding, delamination, fiber fracture, matrix cracking, and others[28]. This certainly complicates the fatigue problem from an analytical approach, and makes a reliable testing method highly desirable for these materials. Fortunately, most composite materials exhibit a low thermal conductivity, and with sufficient heat generation due to hysteresis losses and fracture mechanisms during fatigue loading, lend themselves very well to being monitored with thermography. Furthermore, many composite materials also display a high thermal emissivity, making coating with paint unnecessary for the technique to be successful.

In this study, fatigue tests were performed using

two composite materials in several different geometries. The materials used were a fiberglass-epoxy composite and a graphite-epoxy composite, which was supplied by the Tulsa Division, Rockwell International Corporation, Tulsa, Oklahoma. The material properties of these composites were unknown, and they were used as supplied except for machining. The geometries to be discussed are shown in Fig. 44.

The graphite-epoxy material was supplied with several small saw cuts along its edges. As the material was rather narrow, it was decided not to machine the sides to remove these cuts. Instead, one cut was chosen to serve as a "primary notch", and was lengthened to a depth of 0.50 inches, as shown in Fig. 44(a). This specimen was fatigued at a rate of 1,800 cycles per minute with a total nominal strain range of 1,770μin./in., as determined from strain gage measurements. Due to the length of this fatigue test (4 million cycles) it was necessary to interrupt the test several times. The deflection range, however, was constant.

Figure 45(a) is a thermogram of the graphite-epoxy specimen taken at 1,600 cycles. At this time, a visual inspection revealed no signs of fatigue damage anywhere on the specimen. However, the thermogram shows a significant temperature rise on the specimen located at the root of the primary notch. This rise of almost 5°F is indicative of the high strain range occurring at the root of the notch, and foretells the location of the origin of the eventual

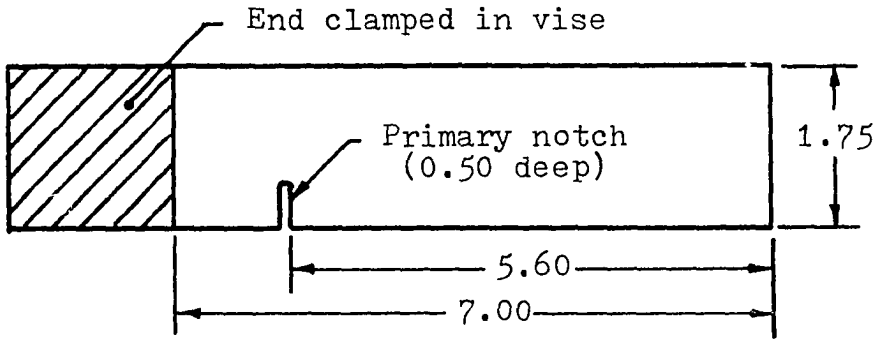

a. Graphite-epoxy specimen
(Thickness = 0.21)

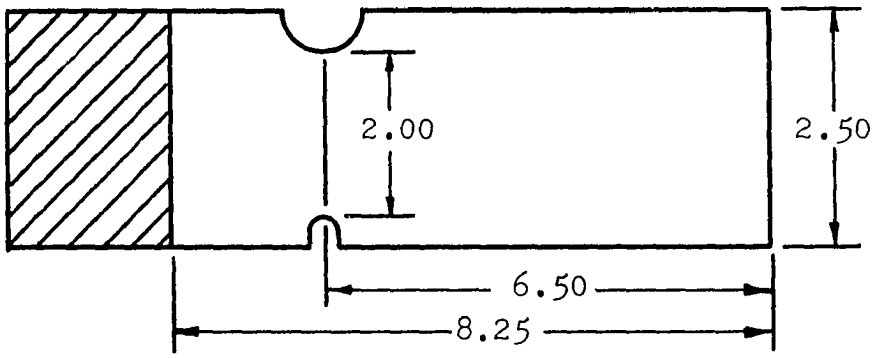

b. Notched fiberglass-epoxy
(Thickness = 0.125)

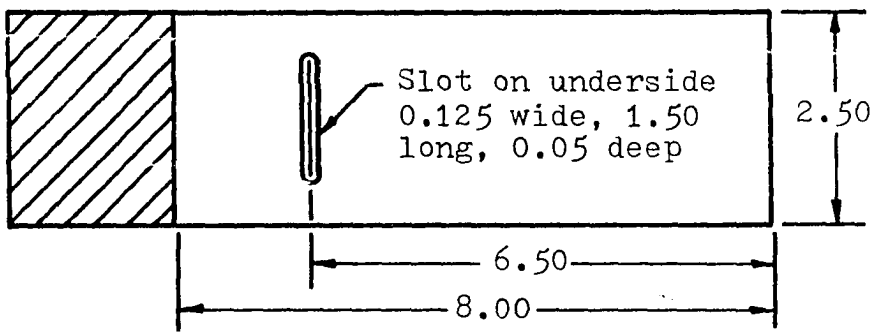

c. Slotted fiberglass-epoxy
(Thickness = 0.125)

Figure 44. Composite material fatigue specimens (Dimensions given in inches).



Figure 45(a). Thermogram of graphite-epoxy specimen at 1,600 cycles.

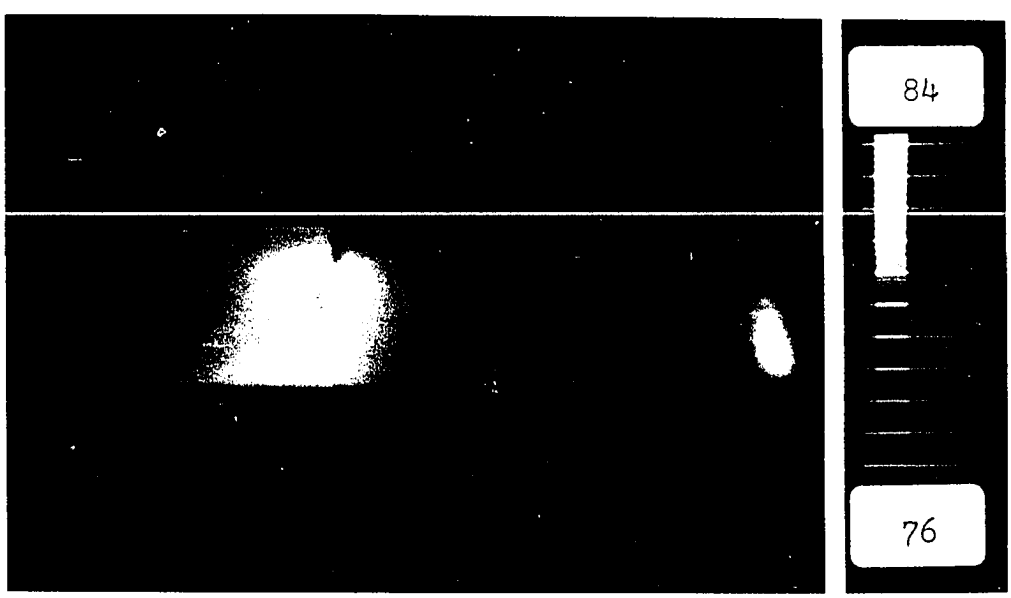

Figure 45(b). Thermogram of graphite-epoxy specimen at 4.0 million cycles.

major surface damage on the specimen. The temperature field map taken from this early thermogram is shown in Fig. 46(a). This figure indicates another temperature rise occurring at the same time opposite the primary notch. This corresponds to the location of a small saw cut, which also produces a stress concentration and thus serves as an additional site for eventual fatigue damage. The relative magnitude of the temperature rises at the two locations indicates that the most likely location for the earliest major damage is the root of the primary notch. Visual damage was observed at the root of the primary notch at about 50,000 cycles. At that time, the maximum temperature rise had increased to $7.5^{\circ}F$ at the root of the notch, and small surface cracks and some laminate slipping were observed.

The general trends of crack formation at the primary notch and temperature rises there and opposite continued throughout the test. At about 800,000 cycles small surface cracks became evident opposite the primary notch. A slight delamination appeared just to the left of the primary notch root at 1.5 million cycles, as the size and the area of the surface cracks continued to increase. The appearance of a delamination was accompanied by a slight decrease of the surface temperature at the location of the delamination. This apparent cooling is due to the decrease in the stress level in the delaminated region, and increased cooling by air circulating under the delamination. Figure

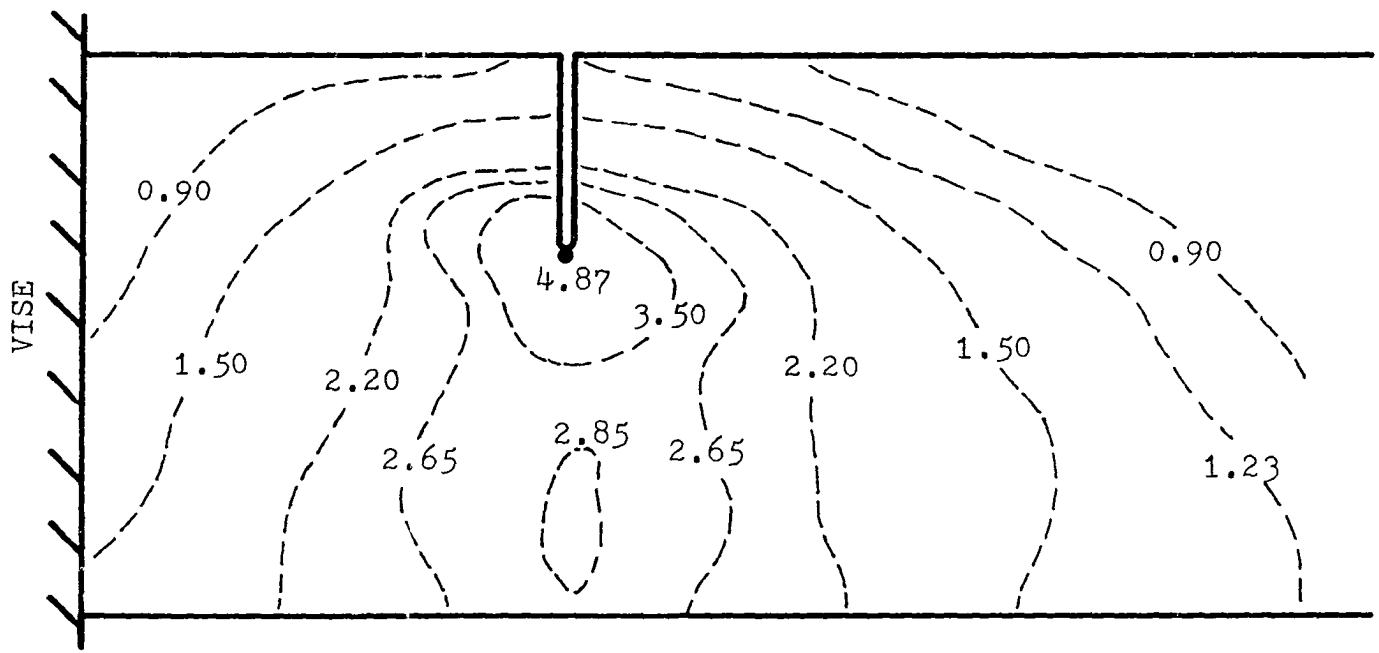

Figure 46(a). Temperature field map of graphite-epoxy specimen at 1,600 cycles (Temperatures in ^{o}F above ambient).

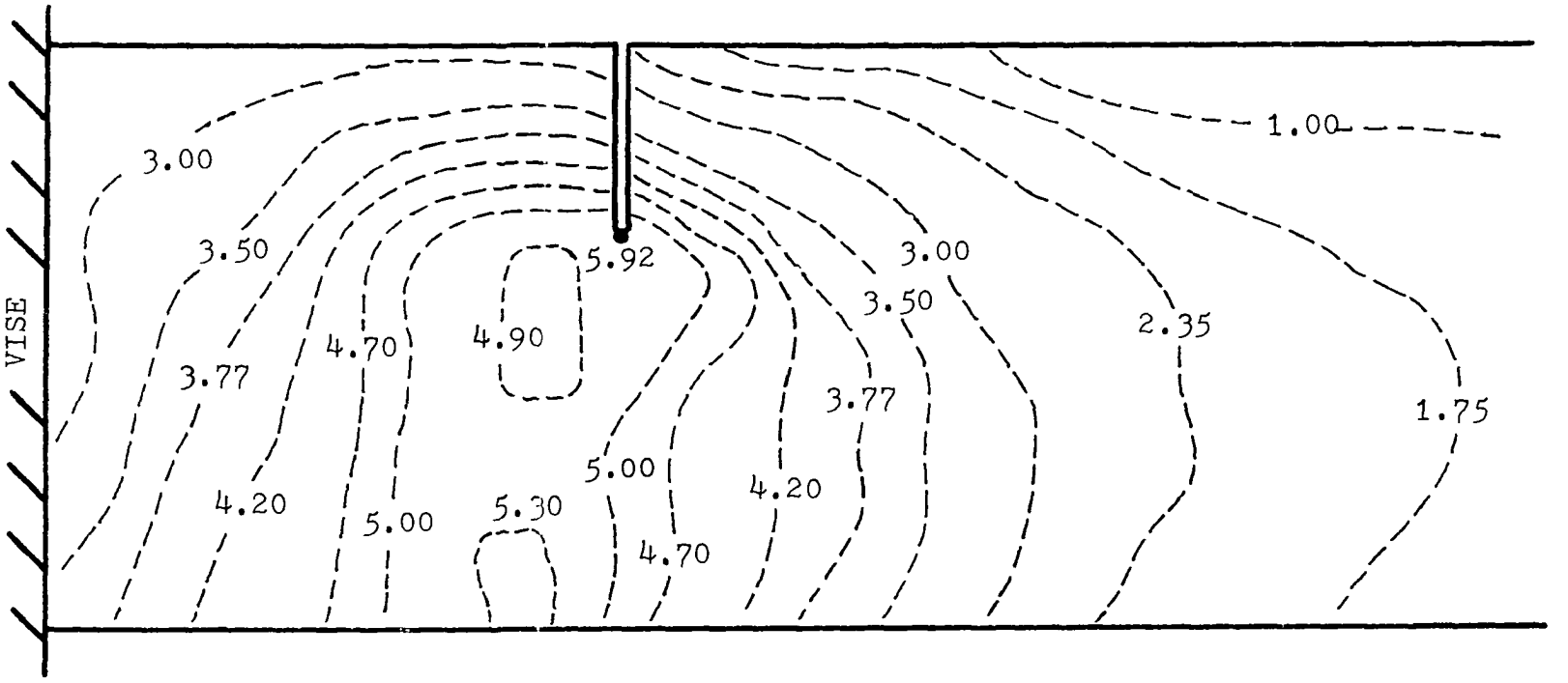

Figure 46(b). Temperature field map of graphite-epoxy specimen at 2.88 million cycles (Temperatures in ^{o}F above ambient).

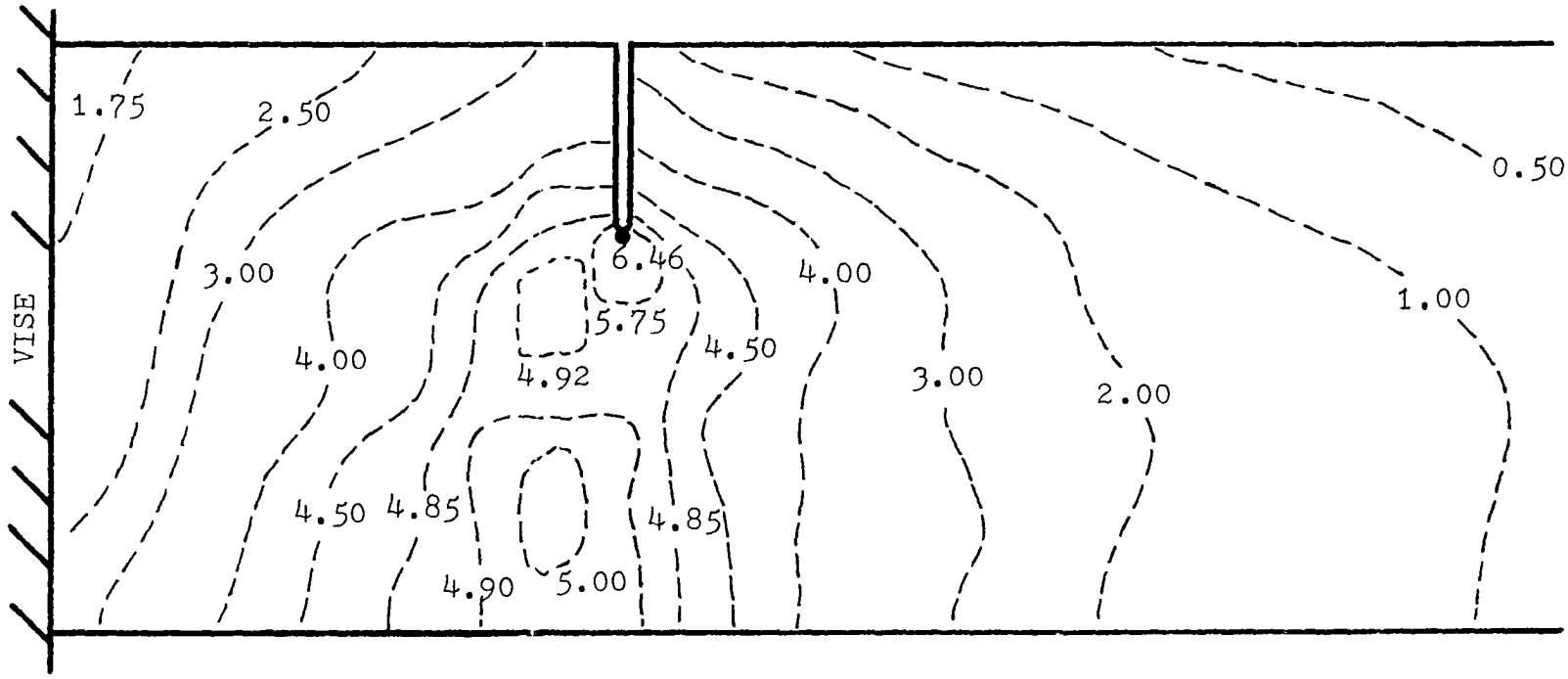

Figure 46(c). Temperature field map of graphite-epoxy specimen at 4.0 million cycles (Temperatures in ^{o}F above ambient).

46(b) shows the temperature field map taken from a thermogram of the graphite-epoxy composite at 2.88 million cycles. The delaminated region is clearly visible as the cool region to the left of the primary notch root. Although the delamination represents the major surface damage on the specimen, the maximum temperature rise continues to be at the root of the primary notch, where the stress level is highest. However, the level of the temperature rise opposite the notch has increased as the surface damage there had taken the form of a dominating surface crack about 0.4 inches long.

Prior to the termination of the test at 4 million cycles the thermogram presented in Fig. 45(b) was taken. As can be seen, the delaminated region remains cooler than the surrounding area as it continues to increase in size. The rectangular cool region in Fig. 46(c), taken from this thermogram, closely corresponds to the size and shape of the delaminated area on the specimen after the test ended. The area opposite the primary notch continued to exhibit an increasing temperature rise, indicating that further cracking or surface damage would occur in this region.

Fatigue tests were also conducted on several notched fiberglass-epoxy specimens. Each of the specimens had two different U-notches milled into its sides such that the total area removal was 20 percent in all cases. The diameters of the notch roots ranged from 0.50 inches down to a narrow saw cut. A typical specimen is shown in Fig. 44(b).

Two strain ranges were used for each of the specimens, which were cycled at 1,800 cycles per minute with R = 0. First, a total strain range of 3,375μin./in. was used for 30,000 cycles, after which the strain range was increased to 3,938μin./in. for another 30,000 cycles. The resulting temperature rises at the notch roots were observed just before termination of the loading at each strain range.

Figure 47 shows a typical thermogram for this series of tests. The specimen was being cycled at the higher strain range, and had notch diameters of 0.375 in. and 0.125 in. As would be expected, the smaller radius produces a higher stress concentration and displays a greater temperature rise than does the larger radius notch. The surface temperature field map made from Fig. 47 is shown in Fig. 48. As can be seen, the temperature rises at the two notches differ by approximately $0.9^{\circ}F$. The more localized nature of the rise about the smaller notch is also evident in this figure.

In Fig. 49, the temperature rise at the root of each notch is plotted as a function of the stress concentration factor for the notch. The stress concentration factors are those for isotropic material behavior taken from reference 63. Stress concentration factors for orthotropic materials such as this fiberglass-epoxy composite are actually slightly different[64,65], but those used in Fig. 49 could be obtained without a knowledge of the material be-

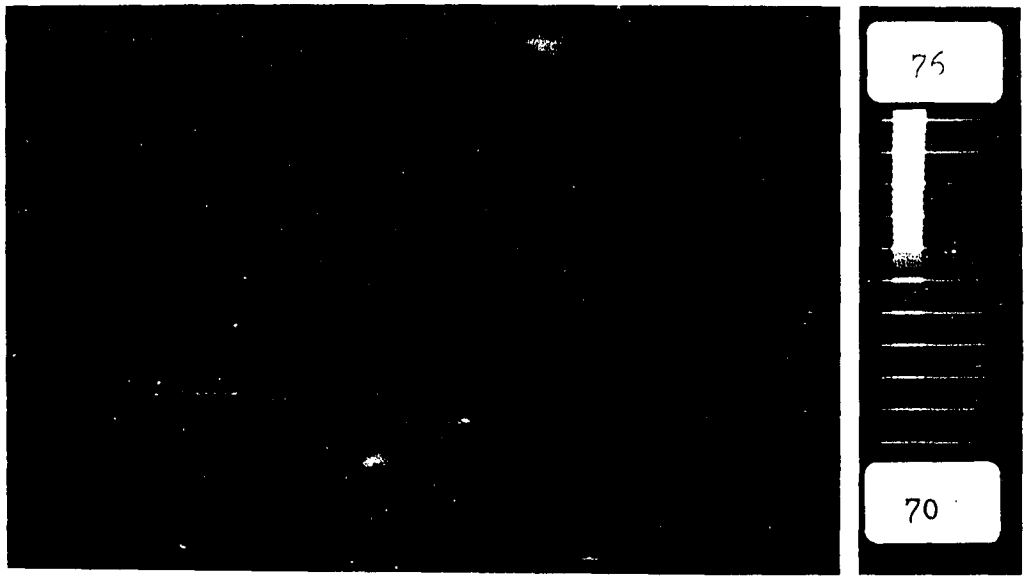

Figure 47. Thermogram of notched fiberglass-epoxy specimen at 30,000 cycles.

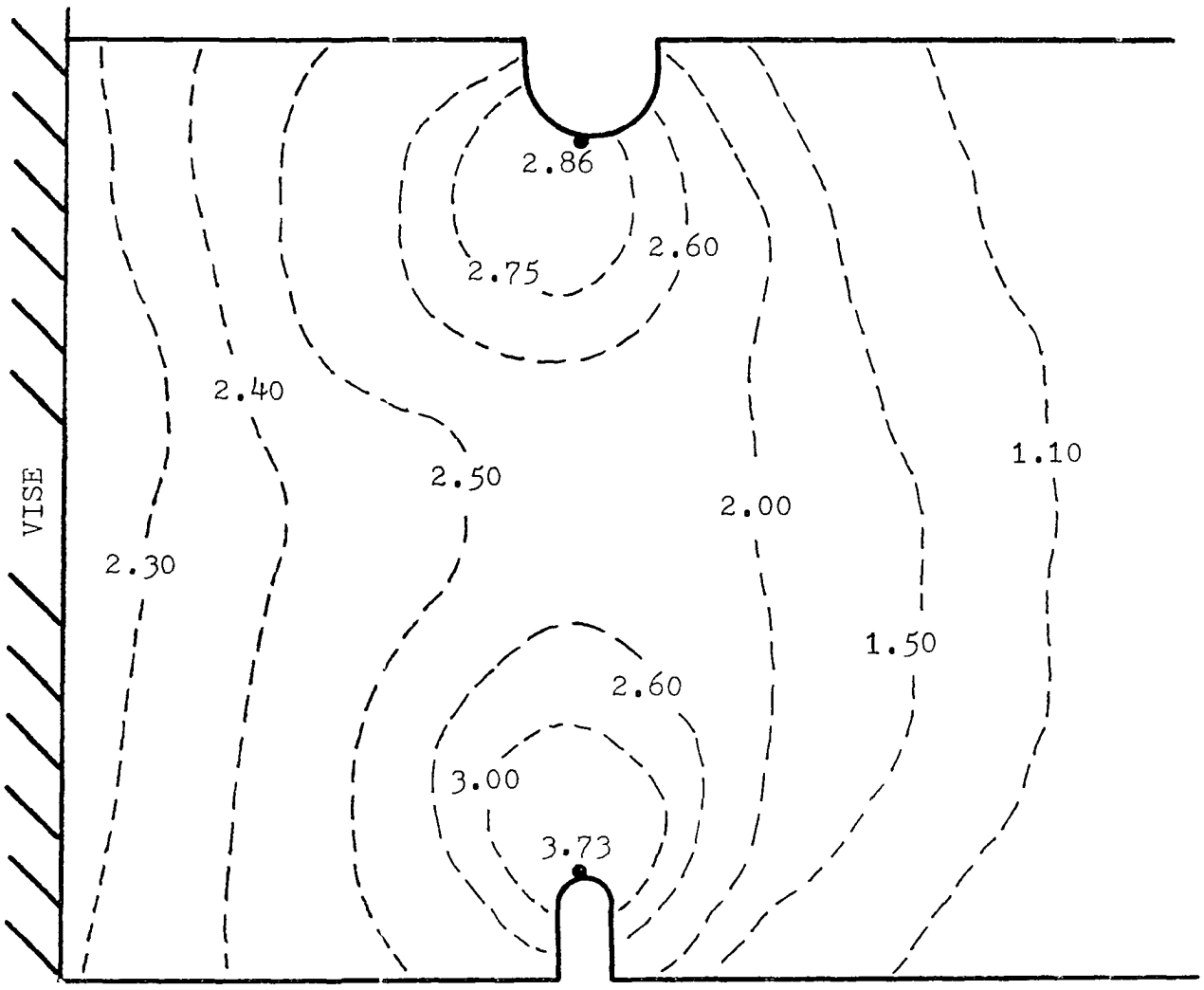

Figure 48. Temperature field map of notched fiberglass-epoxy specimen at 30,000 cycles (Temperatures in ^{o}F above ambient).

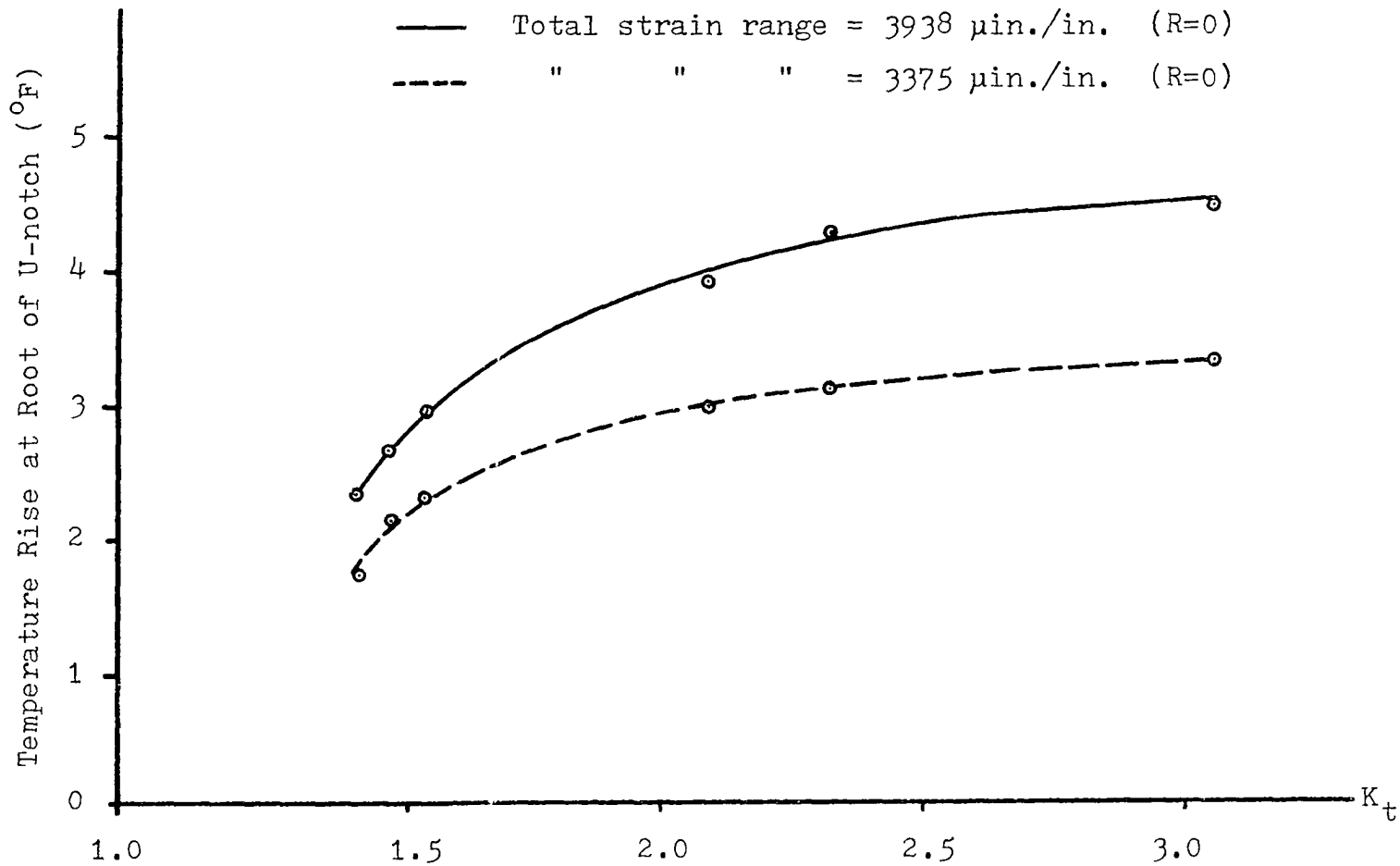

Figure 49. Temperature rise at U-notch root as a function of stress concentration factor, K_t, for fiberglass-epoxy specimens.

havior, and will serve to illustrate a possibitlty of thermographic testing. As the stress concentration factor increases, the magnitude of the temperature rise also increases, as might be expected. This behavior makes it possible for the relative intensity of stress concentrations to be determined quickly using thermography.

The location, prediction and monitoring of fatigue damage on the surface of various materials has been discussed in this work. It is also of interest to be able to locate sub-surface flaws in materials which can serve as stress concentrations and can lead to failures. This is an area where visual inspections are of little value. However, thermography can be used to locate such sub-surface flaws in composite materials undergoing cyclic loading. As an example of this ability, a fiberglass-epoxy specimen was slotted as shown in Fig. 44(c). The slot was made on the underside of the material to a depth of 0.050 inches, or slightly less than half the original thickness of the material. The specimen was then cyclically loaded at a total strain range of 6,200μin./in. (R = 0) while being monitored by the thermograph. At no time was the slot in the material visible to the eye, being on the underside of the specimen. Hence, the slot actually served as a sub-surface flaw. Figure 50 shows one thermogram made during this test at 150,000 cycles. No damage was visible on the top surface of the specimen at this time. The hot region in the center

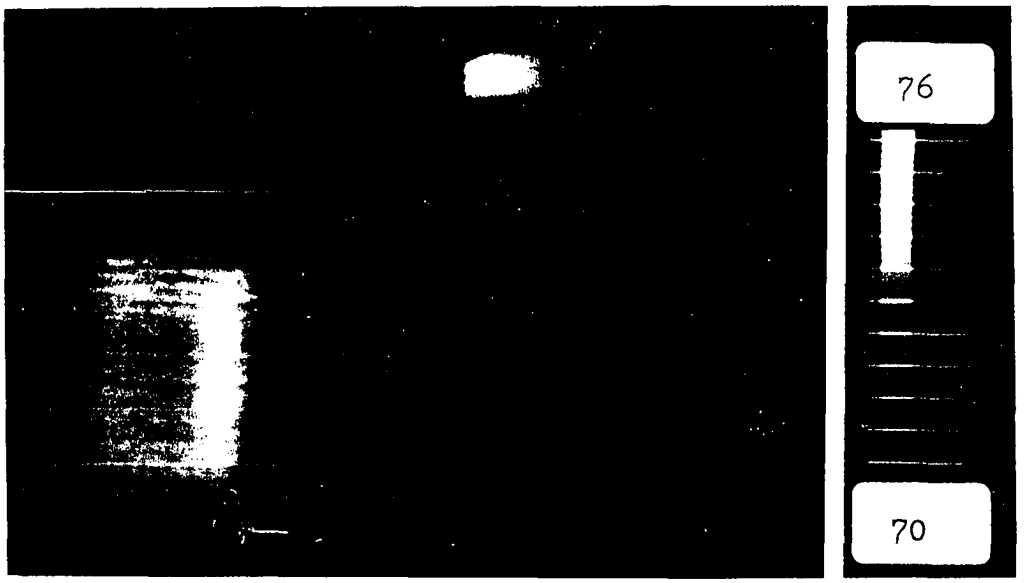

Figure 50. Thermogram of slotted fiberglass-epoxy specimen at 150,000 cycles.

of the specimen corresponds to the location of the slot on the underside of the material. The vise is at the left of the figure, and the reference source is above the specimen. Figure 51 is the temperature field map made from the thermogram and shows clearly the pattern of heating present. In this manner, thermography may be used to monitor fatigue specimens and locate regions likely to incur the greatest fatigue damage even when those regions are located below the surface of the material in question.

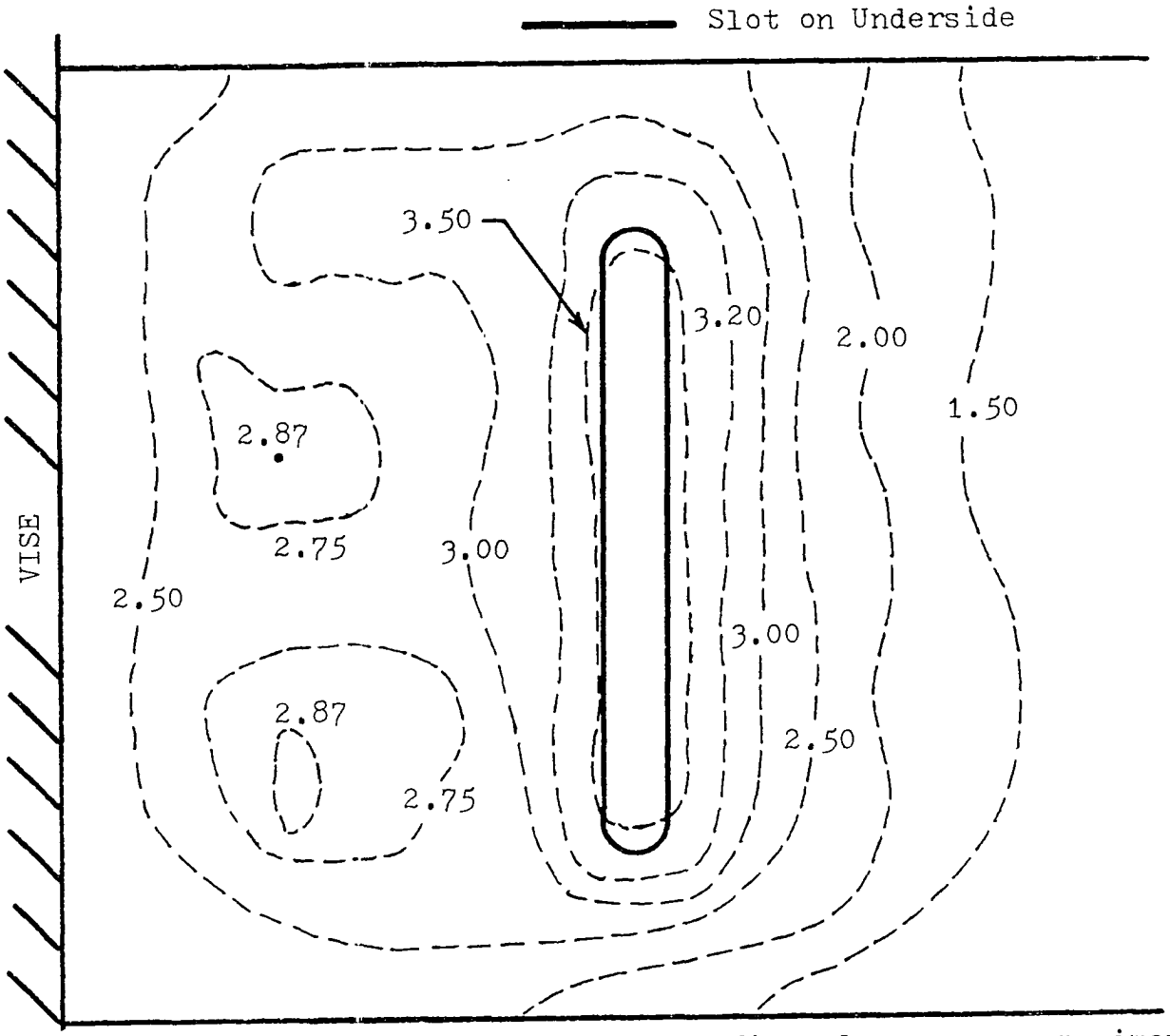

Figure 51. Temperature field map of slotted fiberglass-epoxy specimen at 150,000 cycles (temperatures in ^{o}F above ambient).

CHAPTER VI

ANALYTICAL CONSIDERATIONS

A better understanding of the experimental results given in the previous chapter can be gained through the use of several analytical models which yield temperature rises in materials assuming heat generation rates. Of necessity, these models are simplifications of a more complex situation and require restrictions to be placed on the problem, but they nevertheless provide insight into the importance of various parameters and point out some of the limitations of the use of thermography in fatigue studies.

The models to be considered can be divided into two categories. The first category includes all the models which are based on a closed-form solution to the governing heat transfer equations for each problem. The second group consists of computer-aided numerical solutions. These models are the more useful ones, since the complex geometry and convective heat transfer processes can be more accurately included. In each category described above, two basic geometries are considered. A rectangular geometry corresponds to that used most often in the experimental portion of this study, while a triangular model is used to compare with

the test of the tapered steel specimen already discussed.

Rectangular Geometry

Throughout the discussion of models with a rectangular geometry, it will be assumed that the heat generation occurs essentially at a point. Hence, the plastic zone is assumed to shrink to a point, and all the energy released in the vicinity of a notch or crack tip is assumed to be released at that point. With this assumption, it is possible to make use of some of the classical heat transfer results dealing with point generations in materials.

The first of these classical solutions is the well-known solution for a point generation occurring in an infinite slab of material under steady-state conditions. For the case of constant heat generation, q, the temperature rise above the initial temperature of the slab is given by

$$\theta = q/4\pi kr \ , \qquad (6.1)$$

where k is the thermal conductivity of the material and r is the radius of a circular isotherm from the point of generation. These circular isotherms do not compare well with the data produced early in the life of a fatigue specimen, since the effect of the edge of the specimen is important then. However, as the fatigue cracks in the specimen propagate into the interior of the material, the isotherms generated approach concentric circles and the effect of the boundary decreases. This simple approach is, however,

of little value since it ignores convective and radiative losses from the surface of the material.

Other solutions are available which deal with a source of heat as a point or line in a semi-infinite solid with a boundary kept at a specified temperature. These solutions are found using the method of images. While these solutions do show the effect of having a boundary near the generation point, the boundary condition imposed on the boundary of the solid is usually such that the model does not approximate the actual case. For example, the boundary may be kept at zero temperature rise. In this case, the isotherms generated are non-concentric circles skewed toward the interior of the solid, as shown in Fig. 52. In fact, the boundary of the fatigue specimen is not controlled in any way, being allowed to convect and radiate to the surroundings. As can be seen by the experimental results, this boundary does not remain at room temperature. It is possible to produce a model with a more elaborate boundary condition, such as a specified temperature distribution, but to do so yields a solution in terms of an infinite series, and such complexity is not warranted for the purposes of this study.

One closed-form solution which is quite important and which should be discussed is that for the temperature distribution due to a moving point source of heat in an infinite plane. The results of this model allow one to make assumptions which simplify the computer-aided numerical solutions

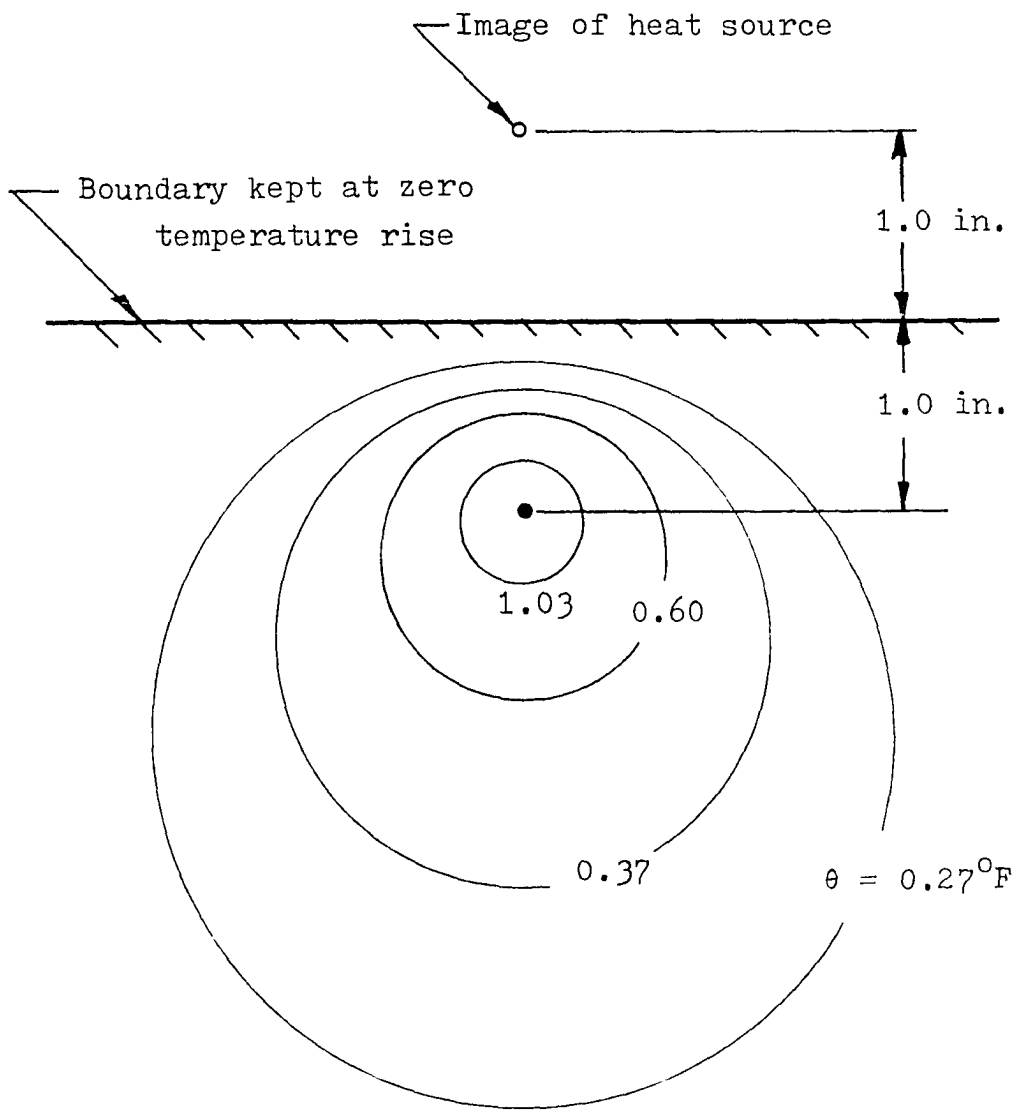

• q" = 100 Btu/hr-ft k = 30 Btu/hr-ft-F

Figure 52. Temperature field about a point heat source near an isothermal boundary.

to be discussed later. In this solution, the point source of heat is moving with a velocity v in a plate of thickness s. The model includes the effects of convection and radiation from the top and bottom of the plate in the heat transfer coefficients, h_1 and h_2, which include linearized radiative contributions. According to Jakob[66], the solution for the temperature rise above ambient at any point (x,y) is

$$\theta = \frac{q'}{2\pi k} \exp(-vc/2\alpha)\, K_o\left[\left[(v/2\alpha)^2 + m^2\right]^{\frac{1}{2}} r\right], \qquad (6.2)$$

where q' is the generation rate per unit thickness of the plate, k is the thermal conductivity of the material and α is the thermal diffusivity of the material. The remaining terms in eq. (6.2) are

$$m^2 = (h_1 + h_2)/ks \qquad (6.3)$$

$$r = (c^2 + y^2)^{\frac{1}{2}} \qquad (6.4)$$

$$c = x - vt\ . \qquad (6.5)$$

K_o is the modified Bessel function of the second kind of order zero.

The solution given in eq. (6.2) may be used to demonstrate that it is not necessary to consider the motion of the point source when modeling the heat transfer in fatigue specimens. For the shortest of the double-notched steel fatigue tests which were performed (about 30,000 cycles), the average crack tip velocity can be calculated. Assuming that each of the two crack tips propagated one inch in 30,000 cycles,

at a cycling frequency of 1,800 cycles per minute, the average tip velocity of propagation would be 0.06 in./min. In the longest tests, the crack propagation velocity averaged only 0.002 in./min. Using the solution in eq. (6.2), the isotherms shown in Fig. 53 can be determined. As can be seen from the figure, for the case of the highest propagation velocity the results are nearly what would be expected from a stationary point source. Since this is the worst case of the moving source, it must be concluded that the problem is actually a quasi-steady state one in which the source of heat moves indeed, but at any given time the motion of the source is insignificant. This conclusion allows one to produce more accurate and elaborate models of the problem without having to deal with the motion of the source. Hence, the models are far simpler than they would be if the crack propagation velocities were greater. It should be noted that for studies involving monotonic fracture, crack tip velocities can be expected to be of the order that would necessitate the use of a moving point source in any heat transfer analysis of the process.

It would be extremely difficult to produce a closed-form solution to the actual problem faced in this study. The geometry is basically simple for rectangular specimens, but the boundary conditions, generation locations, and ambient conditions combine to produce a highly complicated problem. Due to these complexities, it was necessary to seek solutions in a numerical form using a digital computer. In

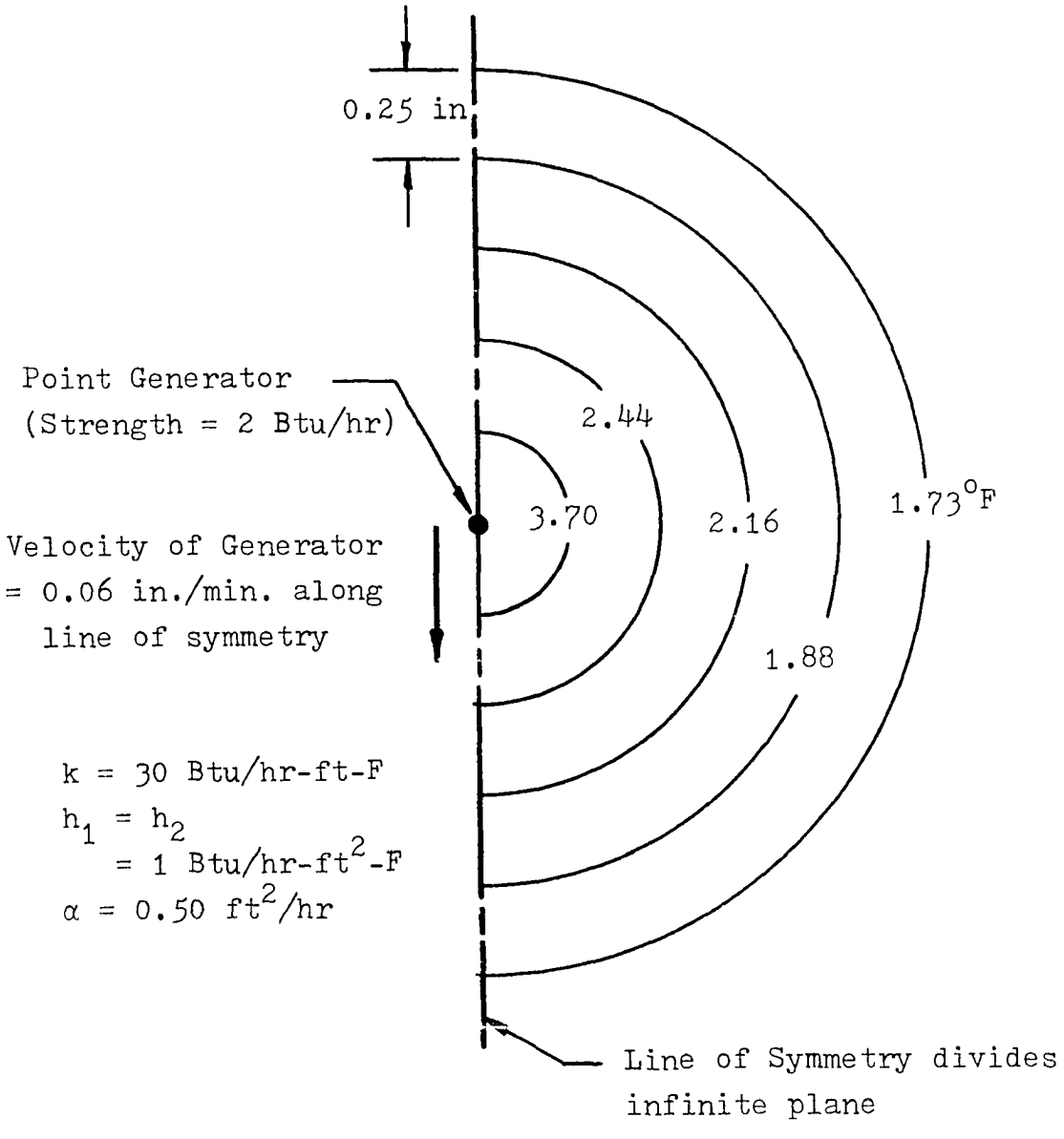

Figure 53. Exact solution for a point source of heat moving in an infinite plane.

the numerical solutions, the boundary conditions could be better approximated than otherwise, and the complex convective and radiative heat transfer behavior could be included.

For an accurate analysis of heat transfer problems including convection it is necessary to have an understanding of the heat transfer coefficient, h, on the surface of the material. In many problems, it may be assumed that the heat transfer coefficient is constant on the surface. Such was the case in the solution for the moving point source in the infinite slab of material. However, due to the type of fatigue loading used in this study, it cannot be assumed that the heat transfer coefficient is constant down the length of the specimen. In fact, near the vise, where the deflections of the specimen are nearly zero, free convection can be assumed. A far more complicated case exists near the crank, where the flow of air around the specimen is periodically stagnation flow and then the turbulent wake behind the plate. As complicated as this situation is, it is possible to gain a reasonable estimate of the distribution of the convective heat transfer coefficient on the surface by appealing to some results from heat transfer studies published in texts.

Near the vise, it will be assumed that free convection occurs at both the upper and lower surfaces of the specimen. Using well-known results for free convection of

surfaces in air, it is found that on the top surface[67],

$$h_1 = 0.27 \left(\frac{\theta}{L}\right)^{\frac{1}{4}} . \qquad (6.6)$$

In eq. (6.6), θ is the temperature rise above the ambient, and L is the width of the plate, 2.50 inches. Thus the heat transfer coefficient from the upper surface is $h_1 = 0.53$ Btu/hr-ft^2-F, based on a temperature difference of 3°, determined as an average from the experimental results. For the lower surface,

$$h_2 = 0.12 \left(\frac{\theta}{L}\right)^{\frac{1}{4}} \qquad (6.7)$$

The heat transfer coefficient h_2 is found to be 0.23 Btu/hr-ft^2-F for a temperature difference of 3°F. Thus, the average of equations (6.6) and (6.7) gives a heat transfer coefficient of about 0.38 Btu/hr-ft^2-F, to be used in the numerical models.

The situation near the crank is more complicated. Assuming a frequency of 1,800 cycles/min. and an average deflection of 1.0 inch, the average velocity of the specimen during the cycle is about 5 ft./second. For stagnation flow on a surface with a velocity v,[68]

$$Nu_L = \frac{hL}{k_\infty} = C \, (Re_L)^n , \qquad (6.8)$$

where L is the width of the plate, Nu_L is the Nusselt number based on L, and Re_L is the Reynolds number based on L. C and n are constants, which for this case are

$$C = 0.205$$
$$n = 0.731 \ . \tag{6.9}$$

Using values of the properties of air at $70^{o}F$, the Reynolds number is

$$Re_L = \frac{vL}{\nu} = 6.51 \ (10^3). \tag{6.10}$$

In eq. (6.10), ν is the viscosity of air at $70^{o}F$. Using the Reynolds number from eq. (6.10) in eq. (6.8), the average heat transfer coefficient during the stagnation flow is

$$h = 9.05 \text{ Btu/hr-ft}^2\text{-F}. \tag{6.11}$$

The heat transfer from the surface which is experiencing the wake of the flow on the opposite side is less efficient than that just determined. If one assumes that it is half as efficient as the stagnation flow, the average heat transfer coefficient for both surfaces is about 6 Btu/hr-ft^2-F. If the heat transfer in the region of the wake goes to zero, the average would be reduced to 4.5 Btu/hr-ft^2-F. Fortunately, the real region of interest is not near the crank, so the errors in determining the average heat transfer coefficient there will not be critical.

It may be of importance to know how the heat transfer coefficient varies from the vise to the crank since the average values at those locations are so different. By examining the deflection of a cantilever beam, one can determine how the coefficient varies along the fatigue

specimen. From classical strength of materials, the deflection of a cantilever beam is proportional to x^3, if x is measured from the clamped end. Hence, the average velocity of any position also varies as x^3. Since $Re_L = vL/\nu$, it can be seen that the Reynolds number at any point on the beam is proportional to x^3 also. From the argument of eq. (6.8), the Nusselt number, and therefore the heat transfer coefficient itself, varies as the Reynolds number to the 0.731 power. Hence,

$$h \alpha Re_L^{0.731} \alpha x^{2.19} . \tag{6.12}$$

Based on the result in eq. (6.12), a second order variation of the average heat transfer coefficient is the most realistic one to use. However, the effect of changing this variation will also be investigated.

The radiation heat transfer from the surface in the numerical models will be included through the use of the radiative heat transfer coefficient, h_r. Assuming that the fatigue specimen is a blackbody radiating to a black environment at the ambient temperature T_∞, one finds that[69]

$$h_r = \sigma (T^2 + T_\infty^2) (T + T_\infty). \tag{6.13}$$

This radiative heat transfer coefficient is then added to the convective heat transfer coefficient to give the total heat transfer coefficient

$$h_t = h + h_r . \tag{6.14}$$

The solution then proceeds as in a problem dealing only with convection.

The numerical investigations of the heat transfer problem related to the generation of heat in fatigue specimens were carried out using finite difference methods. It was assumed that all of the heat generation occurred within a single element and appeared at that element's nodal point. It was further assumed that the heat transfer and stress problems were uncoupled so that the temperature rises did not affect the material behavior. Attention was directed primarily toward the initial period in the life of the specimen when the temperature rises were small. The transient start-up problem was modeled separately and will be discussed later. The models to be discussed immediately deal with steady-state generation, and so are useful in analyzing the second thermal phase of the fatigue life of a specimen after the transient start-up.

The geometry and nomenclature used for the numerical models of rectangular geometry are shown in Fig. 54. Convection and radiation were allowed from the top and bottom surfaces and from the edges. The heat transfer coefficient, h, was varied according to the result of eq. (6.12) from the free convection value at the vise to the stagnation value at the crank end. As written, the finite difference program allows for various boundary conditions at the vise and crank. Commonly, it was specified that the temperature of each end

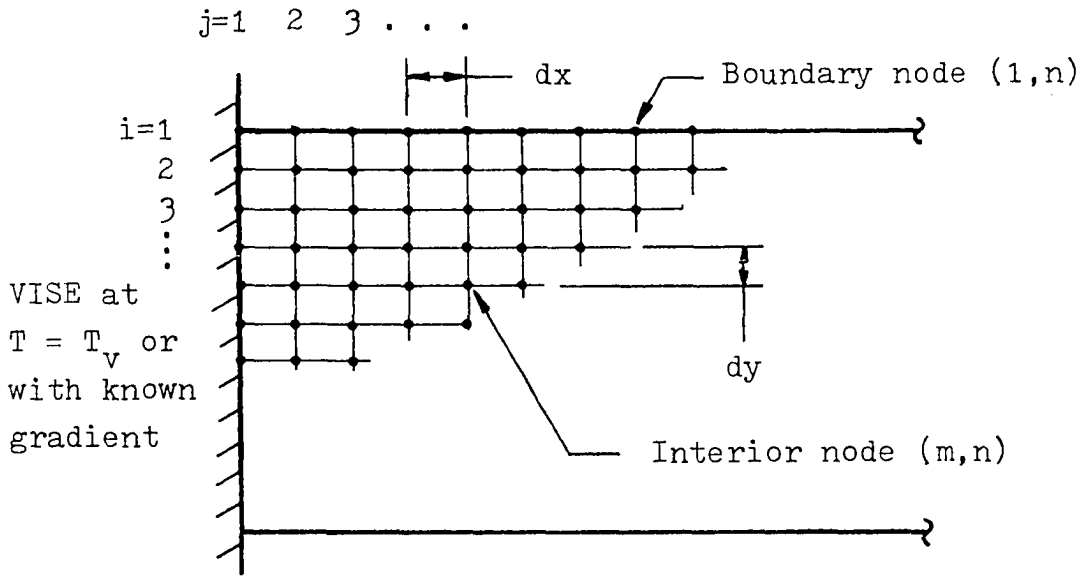

a. Geometry and nomenclature

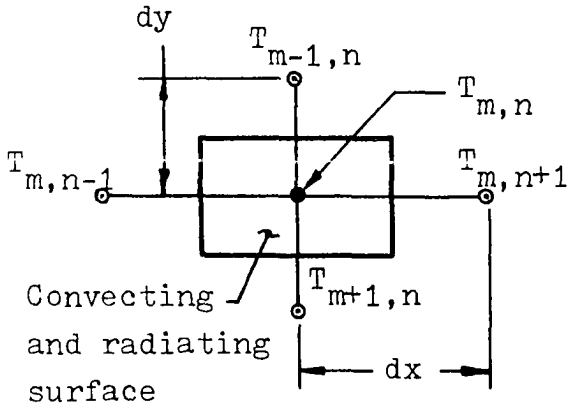

b. Typical interior node

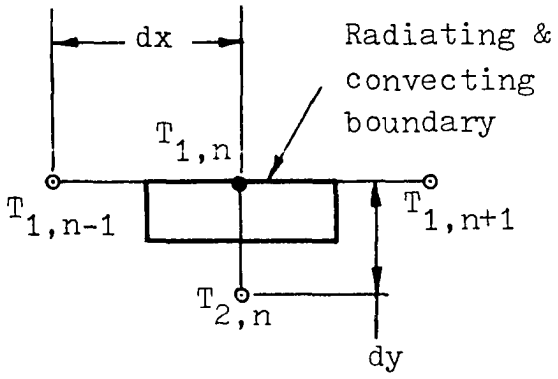

c. Typical boundary node

Figure 54. Numerical model for heat transfer in rectangular fatigue specimens.

was constant (usually T_∞), but provision for a known temperature gradient was also included. Elements on the specimen were of constant size, dx by dy, as shown in Fig. 54.

The nodal equations for each node are determined using a simple heat balance. For this steady-state case, the heat which enters the element, including that by generation in the element, must equal the heat which leaves the element. The nodes are allowed to exchange heat with all surrounding nodes and with the environment at the surfaces of the elements. Four types of nodes were needed to construct the model of rectangular geometry: an interior node, a node at the convecting boundary, and nodes for constant temperature and specified gradient boundaries. The interior node is shown in Fig. 54(b). After performing the heat balance on the node, one finds that the nodal equation is

$$T_{m,n} = \left[\frac{Q_{m,n}dxdy}{kb} + \frac{2h_t dx^2 dy^2}{kb} T_\infty + dy^2(T_{m,n-1}+T_{m,n+1}) + dx^2(T_{m-1,n}+T_{m+1,n}) \right] \Big/ \left[2h_t \frac{dx^2 dy^2}{kb} + 2(dy^2 + dx^2) \right] , \qquad (6.15)$$

where

k = thermal conductivity

b = material thickness

$Q_{m,n}$ = heat generation rate at node (m,n)

$T_{m,n}$ = temperature of node (m,n) .

A node on the convecting and radiating boundary is shown in Fig. 54(c). For this case, the nodal equation is

$$T_{m,n} = \left[\frac{2Q_{m,n}dxdy}{kb} + \frac{2dx^2dyh_t}{kb} T_\infty(dy + b) + 2dx^2T_{m-1,n} + dy^2(T_{m,n+1}+T_{m,n-1})\right] \Big/ \left[2dx^2 + 2dy^2 + \frac{2dx^2dyh_t}{kb}(dy + b)\right] . \quad (6.16)$$

For a node on a constant temperature boundary the equation is simply $T_{m,n}$ = constant, and for a node on a boundary with a specified temperature gradient, the equation is

$$T_{m,n} = G_x\, dx + T_{m,n+1} , \quad (6.17)$$

where G_x is the specified gradient in the direction of the boundary. Equation (6.17) assumes that to be the x-direction.

Several computer programs were constructed using the nodal equations defined above. One program was aimed at obtaining temperature profiles on the surfaces of specimens under various conditions. This program had additional features included to allow for locally altering the convective heat transfer coefficient in order to study the possibilities of image enhancement. A listing of this program is included in Appendix C. Another program without this feature was used to investigate the effects of the different parameters on the temperature rises on the specimens. A third program was altered to include the transient part of the problem. The

investigation of the effects of the various parameters will be discussed first.

For this study, the specimens were divided down their centerlines using a symmetry condition. Nodes along the centerline were treated as if they were on an insulated boundary. Hence, the solutions generated apply directly to the cases of a double-notched specimen with two symmetric notches or cracks. The various parameters influencing the maximum temperature rise on the specimen are the generation strength, the thickness, the material conductivity, the convective losses, changes in the boundary conditions, and the location of the generation point. Each of these effects was investigated using the program. Since the use of thermography as a fatigue test monitoring technique depends not only on the temperature rise on a surface, but also on a sufficient temperature gradient to make the location of hot spots possible, the results of these investigations include the maximum temperature gradients (along the grid pattern in Fig. 54) on the material as well as the maximum temperature rises.

The effect of the heat generation rate on the maximum temperature rise and gradient in the material can be seen in Fig. 55. Changes in the heat generation rate can occur through changes in the stress levels in the material or by altering the cycling frequency of the specimen. Both the maximum temperature rise and the gradient vary linearly

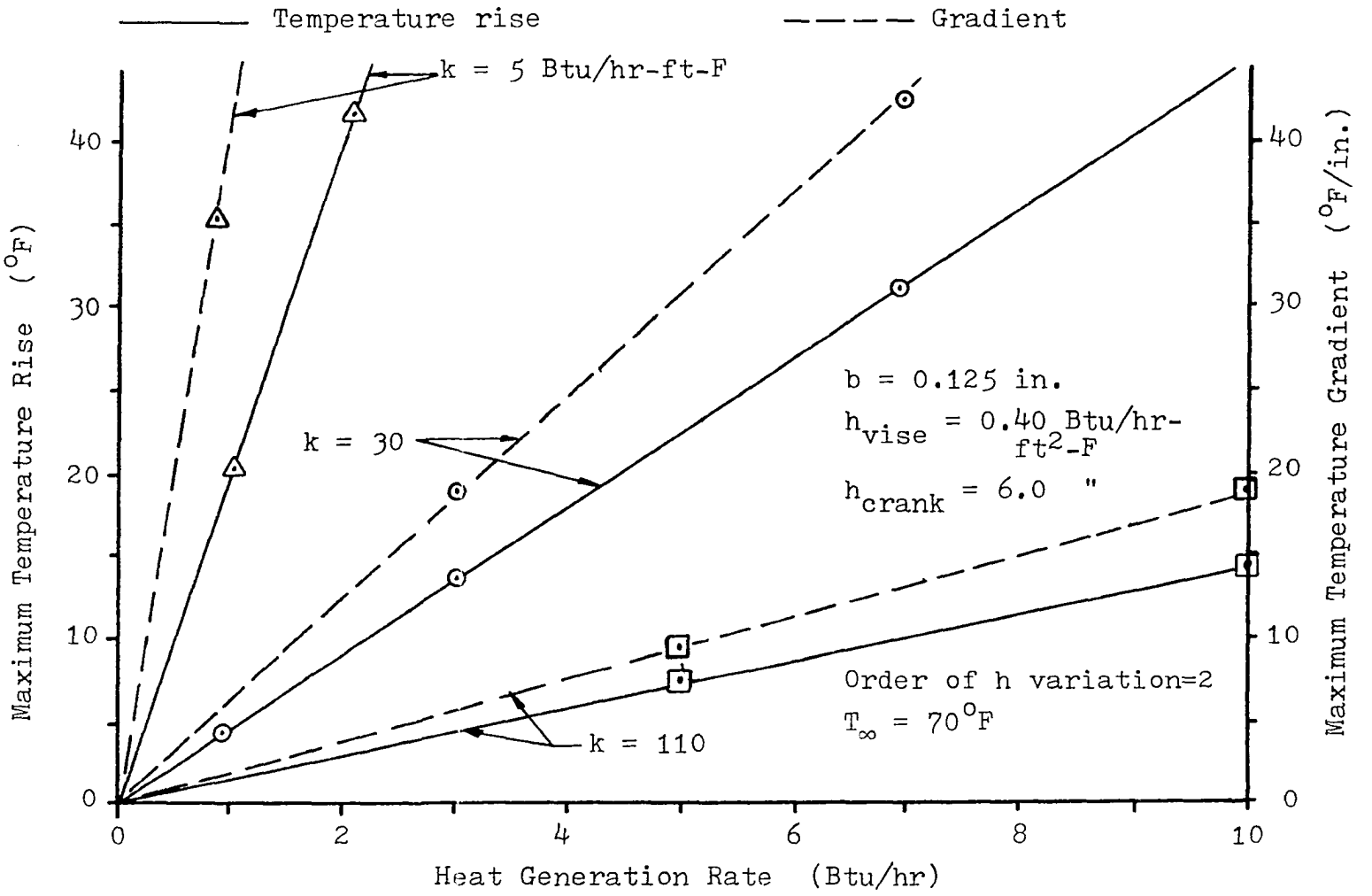

Figure 55. Maximum temperature rise and gradient as a function of heat generation rate for rectangular fatigue specimens.

with heat generation rate, as would be expected. The effect of the thermal conductivity of the material is also seen in this figure. As the thermal conductivity of the material increases, the temperature rise produced by a given generation rate becomes smaller. This effect is better illustrated in Fig. 56, which shows the temperature rise and gradient for a constant heat generation rate of 2.0 Btu/hr. From this figure, it appears that the thermal conductivity of steel (about 30 Btu/hr-ft-F) represents an important point. Below this value of conductivity, the temperature rise takes a rapid increase, while above this value, the temperature rise to be expected from a given generation rate decreases only slightly. It must be remembered that the heat generation rates in various materials can be quite different depending on the properties of the materials and the loading.

A parameter which enters into the problem in different ways is the thickness of the material. For a given heat generation rate, increases in the thickness of the material effectively change the area available to the specimen for the removal of heat from the generation point by conduction heat transfer. This effect is illustrated in Fig. 57 for steel. A more probable situation would relate the thickness to the heat generation in the material. Thicker specimens being fatigued at the same stress levels as thin ones would be dissipating energy in a greater volume of material. Hence

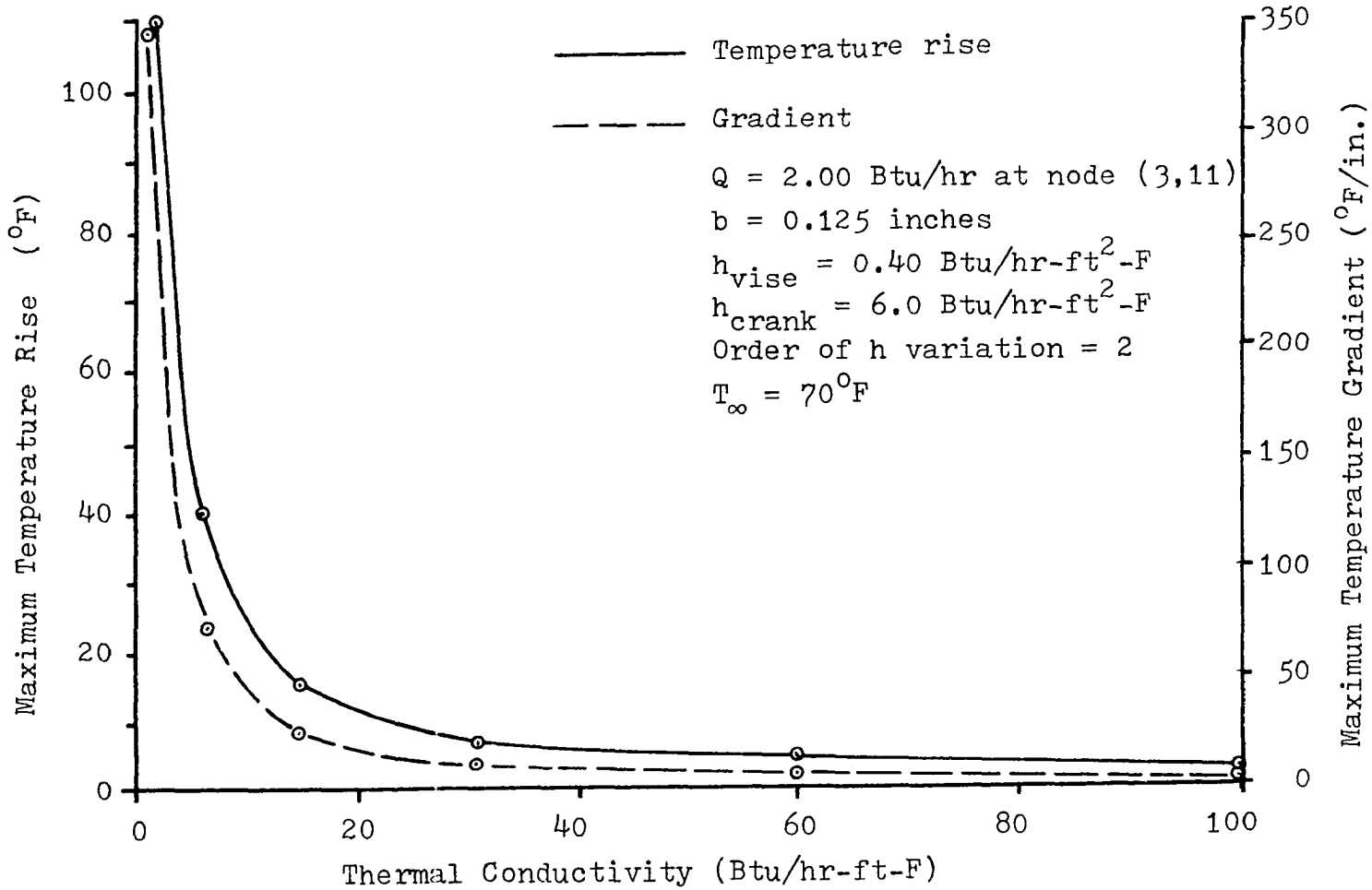

Figure 56. Maximum temperature rise and gradient as a function of thermal conductivity for rectangular fatigue specimens.

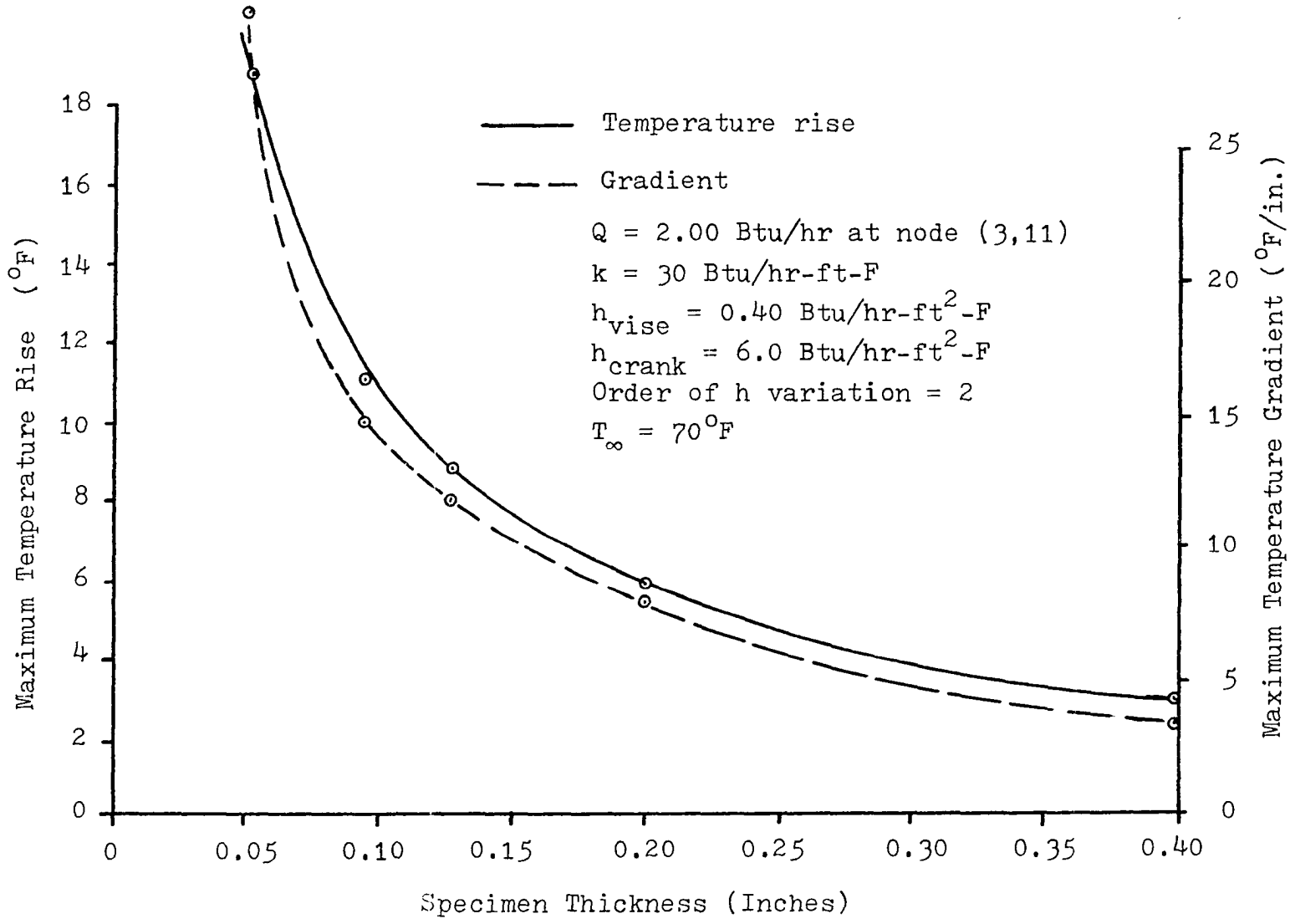

Figure 57. Maximum temperature rise and gradient as a function of specimen thickness for rectangular steel fatigue specimens.

the total heat generation rate increases as the thickness increases. The final result of this change would be a combination of Figs. 55 and 57. As an illustration of this interaction, it was assumed that in one case the heat generation rate would be linearly proportional to the thickness of the material. Using this relationship, the curves shown in Fig. 58 were produced. From this figure, it is apparent that the effect of increasing the generation rate outweighs the effect of increasing the thickness on the maximum temperature rise. As the material thickness increases, the maximum temperature increases slightly and tends to a very slowly increasing value for thick materials. This behavior is the reverse of that seen in Fig. 57. It is interesting, however, that the temperature gradient shows virtually no dependence on the combined thickness-generation rate change. Note that the scales in Fig. 58 are somewhat magnified, and that the changes in both temperature rise and gradient are small.

The difficulty of accurately specifying the convective heat transfer coefficient on the surface of the fatigue specimen has already been discussed. By using empirical results from the literature, it was possible to obtain estimates of the magnitude of the heat transfer coefficient at the vise and at the crank. By examining the deflection of the cantilevered specimen, the order of the variation in h from the vise to the crank was estimated. These figures are indeed estimates, however, and the effect of making errors in

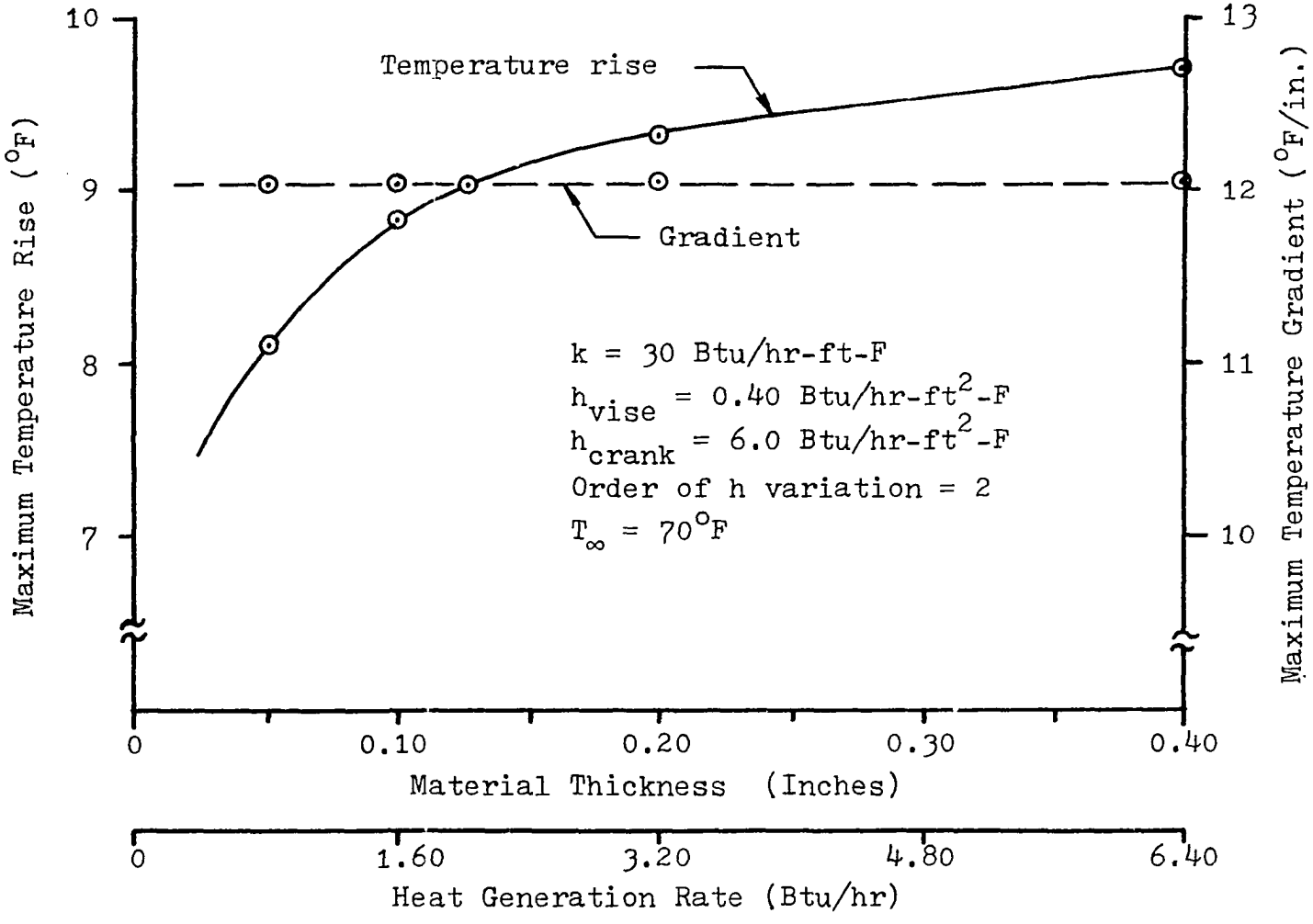

Figure 58. Maximum temperature rise and gradient as a function of thickness and heat generation rate when Q α b.

the estimates should be known before the numerical model is used extensively. In order to gain an understanding of the effects of misjudging the values of the heat transfer coefficients at the vise and crank ends, the numerical model was used while the coefficients were varied over a wide range of values. Examining the coefficient at the vise end first, where the estimate was h_{vise} = 0.40 Btu/hr-ft^2-F, the coefficient was varied from zero to 2.0 Btu/hr-ft^2-F while the other parameters in the problem were held constant. The result of this examination is given in Fig. 59. As can be seen, the maximum temperature rise on the specimen shows little variation over the range of heat transfer coefficients used for both steel and aluminum. The fact that the steel shows slightly higher dependence on h_{vise} is due to the lower efficiency of the conduction heat transfer in the steel compared to that in the aluminum. Although it is not shown in Fig. 59, the maximum temperature gradients on the specimens exhibited very little dependence on the heat transfer coefficient at the vise also.

Similar results are presented in Fig. 60 for changes in the heat transfer coefficient at the crank end of the specimens. In this case, the estimate for h_{crank} was approximately 6 Btu/hr-ft^2-F. The range considered with the model was from 1.0 to 15.0 Btu/hr-ft^2-F. The results in Fig. 60 show that there is also very little effect on the maximum temperature rise due to changes in h_{crank}. Again, the rise

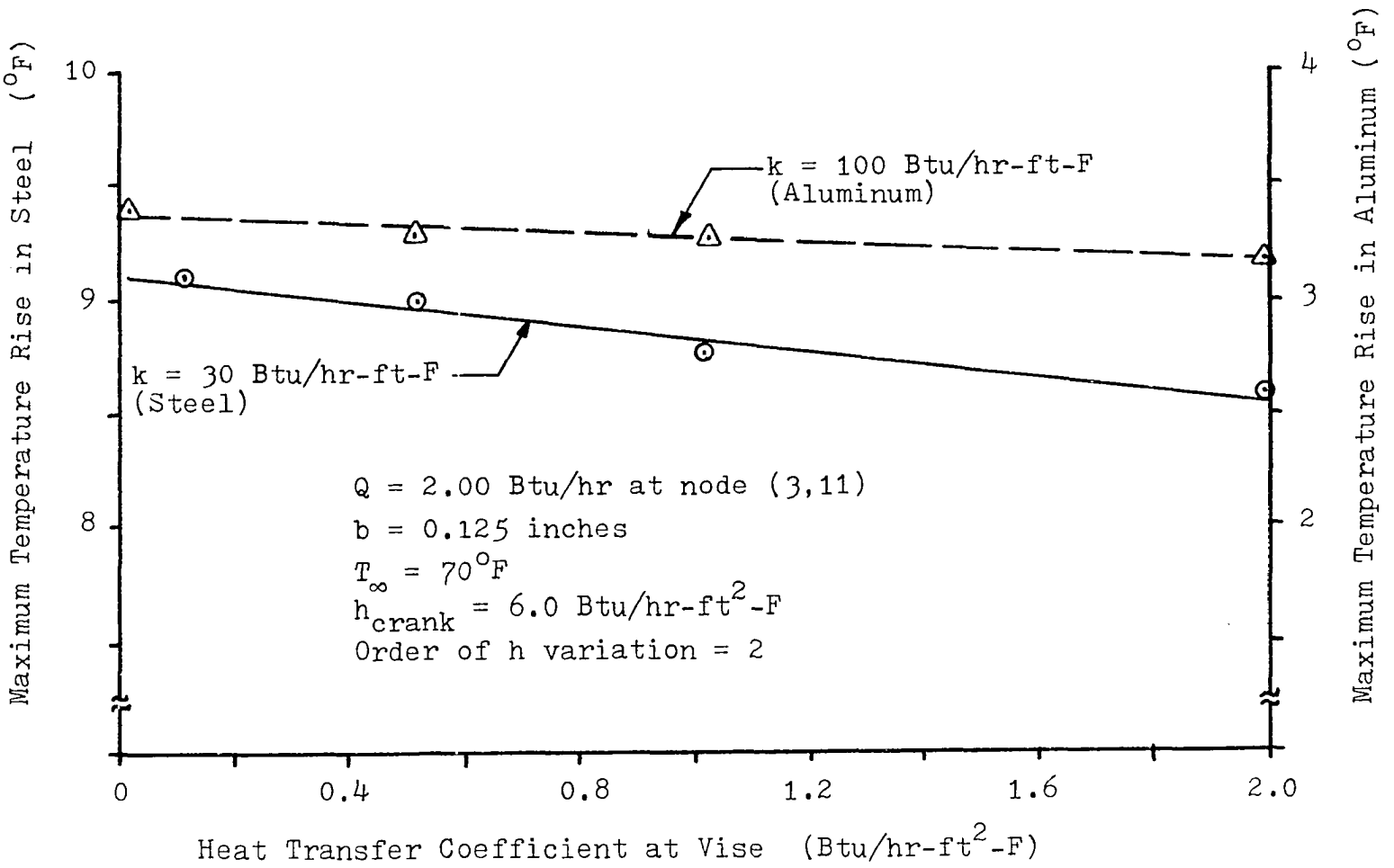

Figure 59. Maximum temperature rise as a function of h_{vise} for rectangular fatigue specimens.

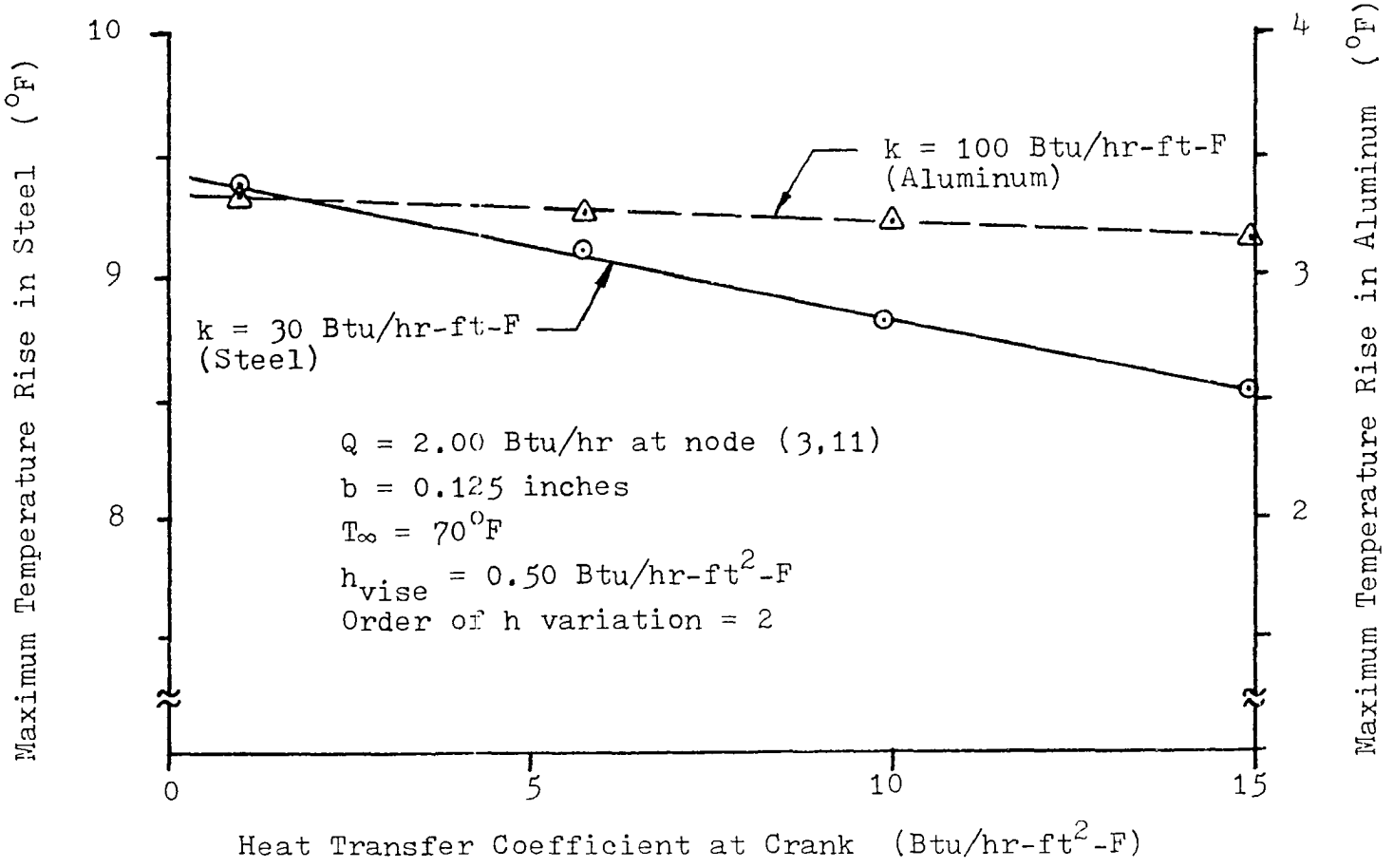

Figure 60. Maximum temperature rise as a function of h_{crank} for rectangular fatigue specimens.

in the steel shows slightly greater dependence than in the aluminum, but is small nonetheless. (Note the expanded scales for temperature rise in Fig. 60.) It would be expected that a fairly large variation in h_{crank} would have only a slight effect on the maximum temperature rise since the real region of interest lies closer to the vise. Nevertheless, the results of Figs. 59 and 60 indicate that it is sufficient to use the numerical model with only a good estimate of the heat transfer coefficients on the specimens for steel and aluminum. This is a significant result since accurate values of the heat transfer coefficients are indeed difficult to obtain.

The effect of changing the order of the variation of h from h_{vise} to h_{crank} on the maximum temperature rises to be expected in aluminum and steel is shown in Fig. 61. Noting the expanded scale for temperature rise in this figure, one can conclude that the order assumed for the h variation from one end of the specimen to the other is unimportant.

It is to be expected that for a given heat generation rate, the maximum temperature rise on the specimen will depend on the location of the generation point. This will be particularly true for the rectangular specimens which were considered, since they have convecting and radiating edges and ends with fixed temperatures or gradients. To observe this effect, a fixed generation rate of 2.00 Btu/hr was considered at several locations on the rectangular specimen. Figure 62 shows the maximum temperature rise obtained at each

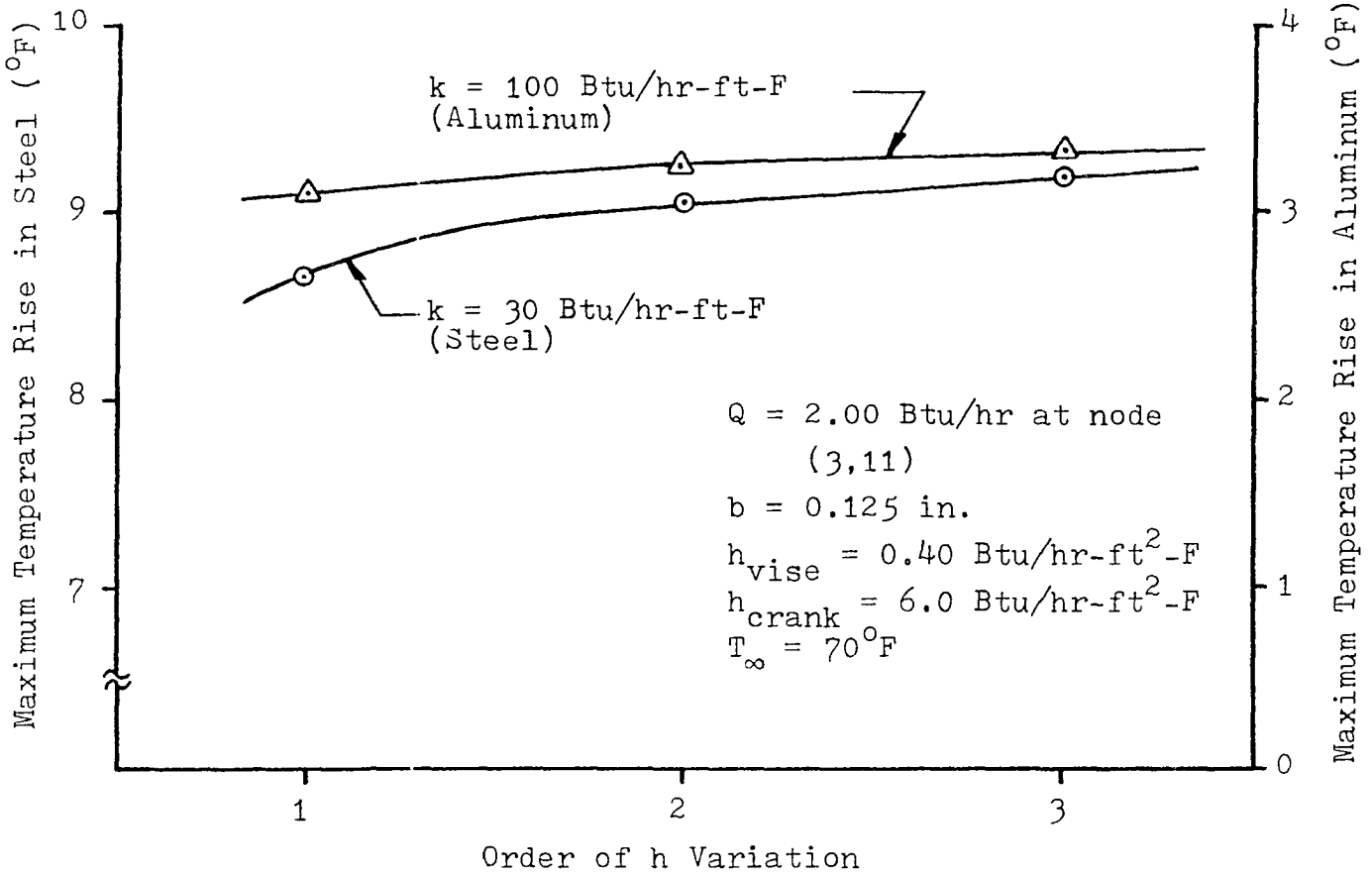

Figure 61. Maximum temperature rise as a function of the order of the heat transfer coefficient variation for rectangular fatigue specimens.

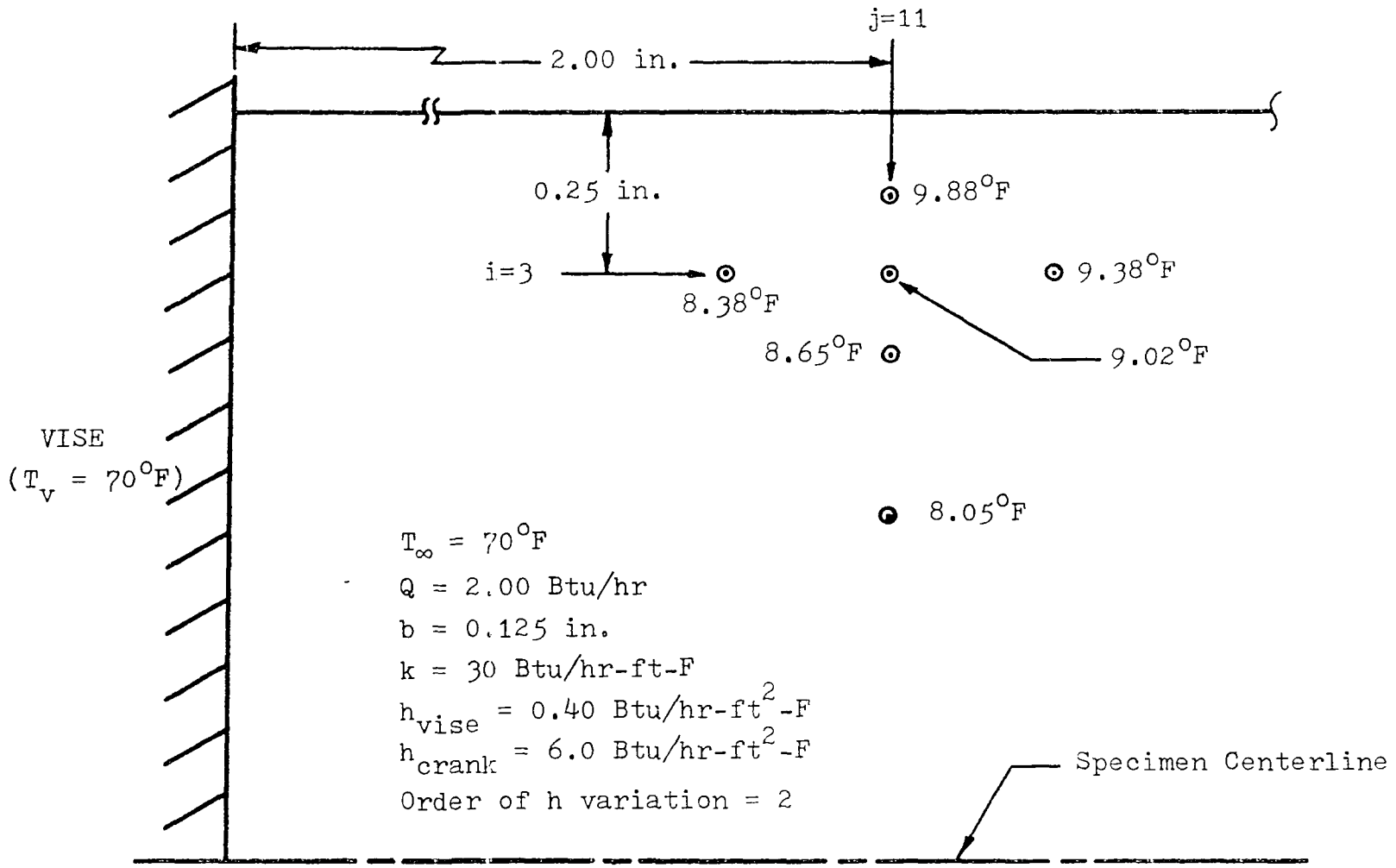

Figure 62. Maximum temperature rise for constant generation rate at different positions in rectangular steel fatigue specimens.

position on the specimen. It should be remembered that the specimens were divided by their centerlines using symmetry, and that there is a second generation point on the mirror image of the figure for each point shown. It is apparent that the location of the generation point has a marked effect on the levels of the temperature rises obtained on the specimen. As the generation point moves toward the centerline, as if a crack tip were propagating, the temperature rise decreases. This result is in keeping with the results found experimentally for the double-notched steel specimens. It was found that as the crack moved toward the centerline of the specimen the temperature rise above ambient increased slightly. It was also found that the heat generation rate in the material increased, but more rapidly than did the temperature rise. (Compare, for example, Figs. 21 and 38 for specimen S-52.) The increase in the generation rate did not produce an equal increase in the maximum temperature rise on the specimen because the point of generation was moving toward the centerline of the specimen. At the more interior positions, more heat was required to produce the temperature rise than early in the fatigue life.

From these investigations of the effects of various parameters on the maximum temperature rise on the specimen, it can be concluded that the important parameters are the heat generation rate, the thermal conductivity of the material, the thickness of the material, and the location of the

generation point. It can also be concluded that the heat transfer coefficient on the surface of the specimen need only be estimated with marginal accuracy to gain useful results from the numerical model.

A slightly more elaborate computer model was produced to generate typical isotherm maps on rectangular specimens and to investigate the possibilities of enhancing the image of the surface temperatures by altering the ambient conditions on the surfaces of the specimens. In this model, the specimens were not divided using symmetry, so non-symmetrical cases could be considered. An additional provision in the model was the ability to locally alter the value of the convective heat transfer coefficient anywhere on the surface of the specimen. This would produce the same effect as blowing a stream of cool air over the specimen to try to enhance the image. The results of this investigation indicate that enhancement may prove useful in improving the quality of thermographic data in some cases.

The first use of this new numerical model is to produce several temperature field maps for comparison to those found experimentally for the double-notched steel fatigue specimens. Figure 63 shows the isotherms found for a steel specimen with unequal heat generations at two points. The locations of the generation points correspond to that for the temperature field map of Fig. 34(a), which was taken from a thermogram of specimen S-36 at 400,000 cycles.

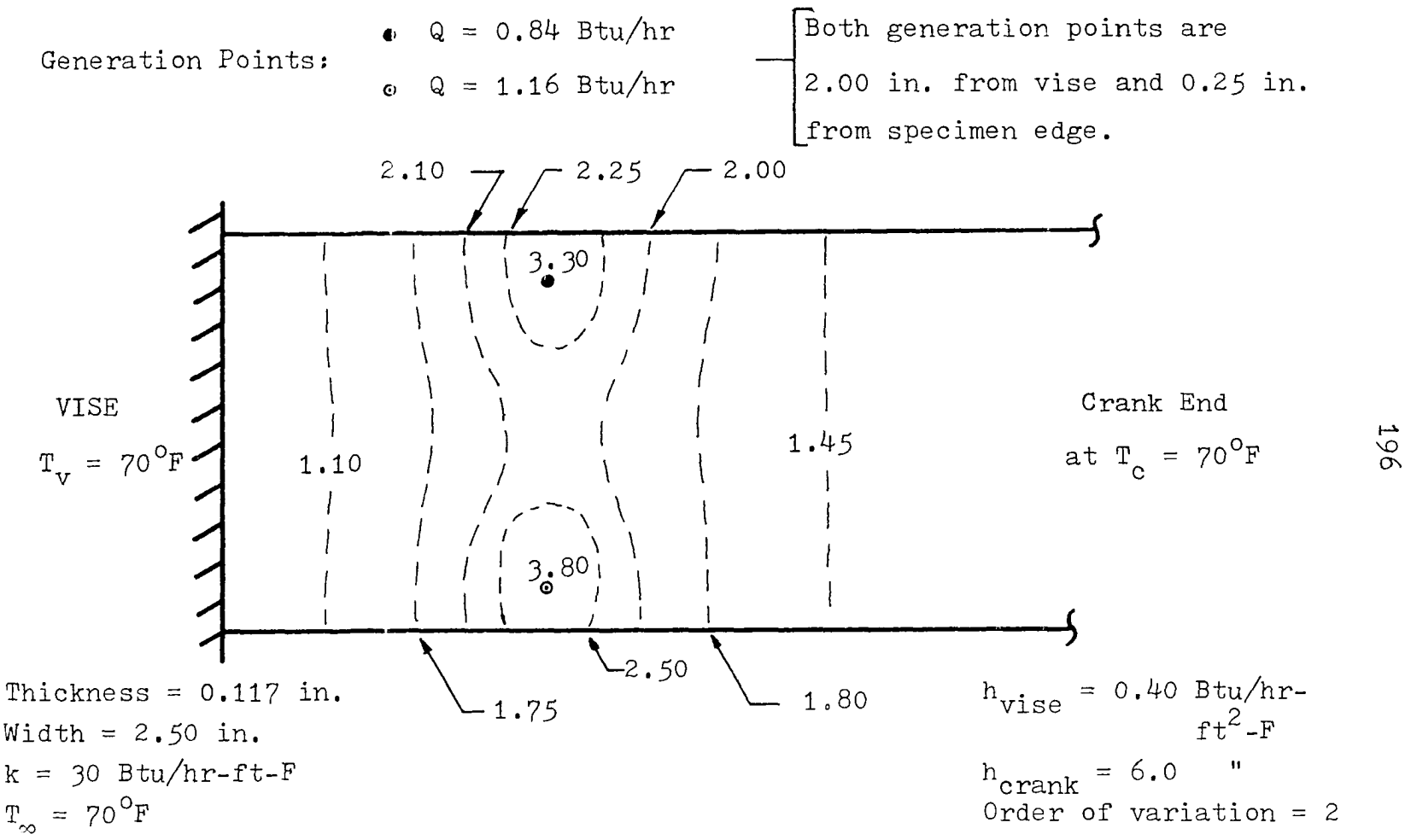

Figure 63. Temperature field map for numerical model of steel fatigue specimen.

The generation strengths chosen for the numerical model were proportioned according to the temperatures at the notch roots that are seen in Fig. 34(a), and their sum equals that found in Fig. 35 (generation rate vs. cycles) for S-36. Comparing the isotherms of Fig. 63 with those from Fig. 34(a), one finds rather poor agreement. The maximum temperature rises found numerically, however, are not far from those found experimentally. It is perhaps unreasonable to expect to match very well the isotherms of the experimental case with a somewhat idealistic model. But the agreement of the temperature rises is encouraging.

Several other cases were attempted. In each, it was possible to predict with reasonable accuracy the maximum temperature rises on the specimens, but more difficult to produce very good agreement on isotherm shapes. As the points of heat generation moved into the center of the specimen, the agreement of the model with the experimental results improved. Figure 64 shows isotherms for a steel specimen near the end of its fatigue life. This case corresponds to that for specimen S-36 at 825,000 cycles. Experimentally determined isotherms for this specimen are given in Fig. 34(f). The strength of the heat generators for Fig. 64 came from the data of Fig. 35 also. As can be seen by comparing the two figures, the agreement of the isotherms is much better than it was earlier in the life of the specimen. However, the level of the temperature rise on the specimen is in poorer

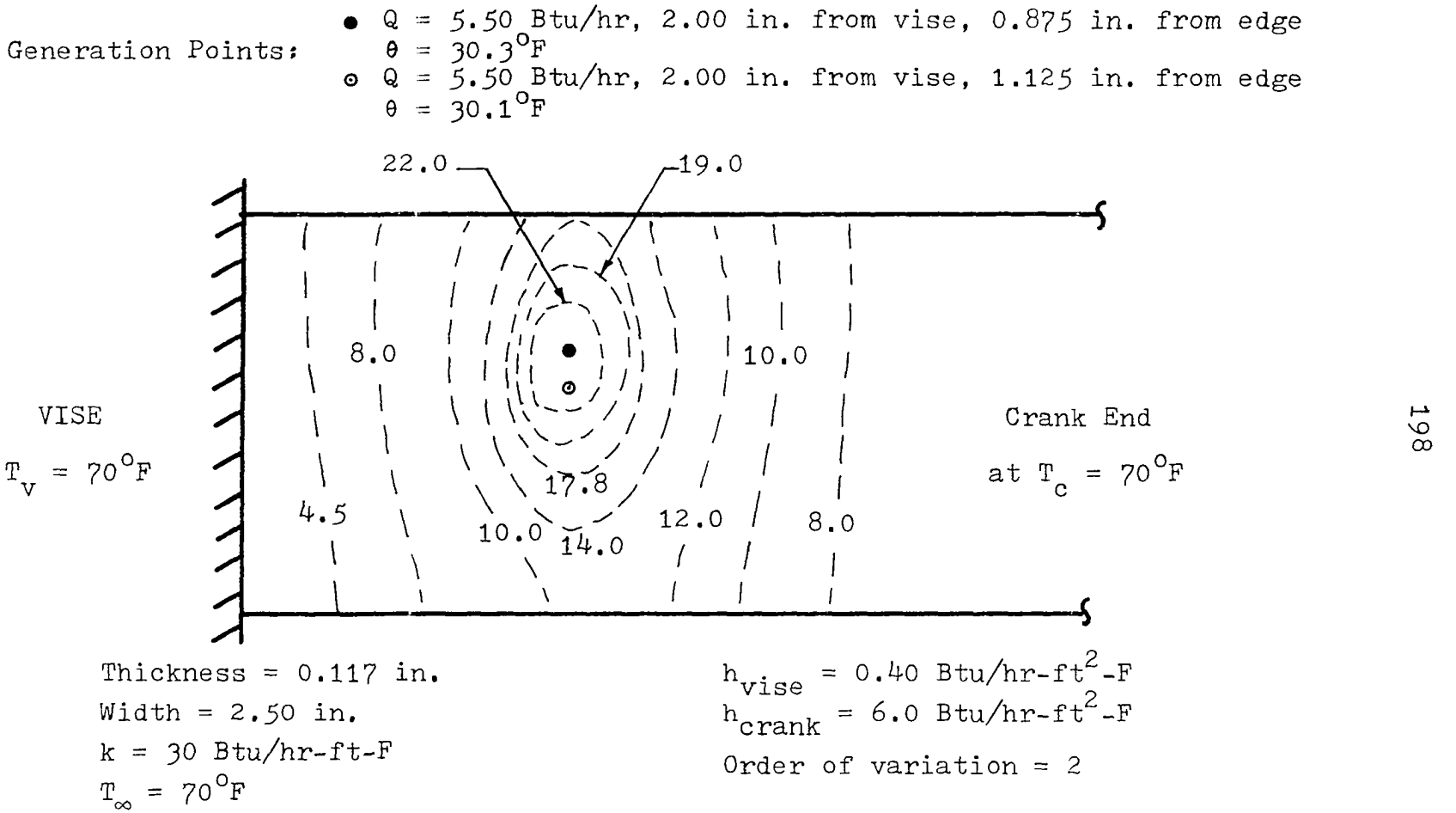

Figure 64. Temperature field map for numerical model of steel fatigue specimen near end of fatigue life.

agreement than previously. There exists more than a $7^{o}F$ difference in the two figures. This discrepancy could easily be due to an error in determining the heat generation rate in the material experimentally. If the generation at each point were 6.5 Btu/hr rather than the 5.5 used, the temperature rises would match quite well again. The reasonable agreement which can be obtained in the experimental and numerical data lends credence to the results obtained from the numerical model, even if it cannot exactly match the shapes of the isotherms for some cases.

A more useful application of this numerical model is in studying the possibilities of enhancement of the thermographic image to obtain better spatial data from thermography with materials of high thermal conductivity. Particularly, the experimental results obtained with the notched aluminum specimens gave no "early warning" of where the fatigue damage was going to occur. Nor did they provide good pictures of the propagating fatigue cracks in the aluminum. The lack of good results can be traced to the high thermal conductivity of the aluminum, which effectively removes heat from the region of the heat generation. The effect of the conductivity of the material has already been discussed and is illustrated in Figs. 55 and 56. In order to enhance the image of the region incurring the fatigue damage in aluminum, it may be possible to change the relative processes of convection and conduction by changing the ambient conditions

around the specimen. Specifically, by blowing a stream of air either cool or at room temperature over a portion, one can increase the convective heat transfer on that part of the specimen. Hopefully, this would remove heat from the specimen before it could be conducted away, and the lower conduction would result in a steeper temperature gradient near the generation point.

In order to study this possibility, the numerical model was used with the capability of changing the heat transfer coefficient in a strip running from the top to the bottom of the specimen. The particular geometry and region of altered convective heat transfer coefficient is shown in Fig. 65. The convective coefficient was altered in the indicated strip by the addition of a coefficient h_{add}. This approximates the condition to be expected if a stream of air were blown over the specimen in this strip. Various values of h_{add} were used in the study, ranging from zero to 100 Btu/hr-ft^2-F. The air stream necessary to produce such a high heat transfer coefficient would have to be cool air at quite a high velocity. The study considered both aluminum and steel, although enhancement techniques may not be required for steel. As seen in Fig. 65, the strip for the enhanced h value was 0.50 in. wide and included both generation points. The generation strengths (1.00 Btu/hr) were assumed small to approximate the case where enhancement is most desirable.

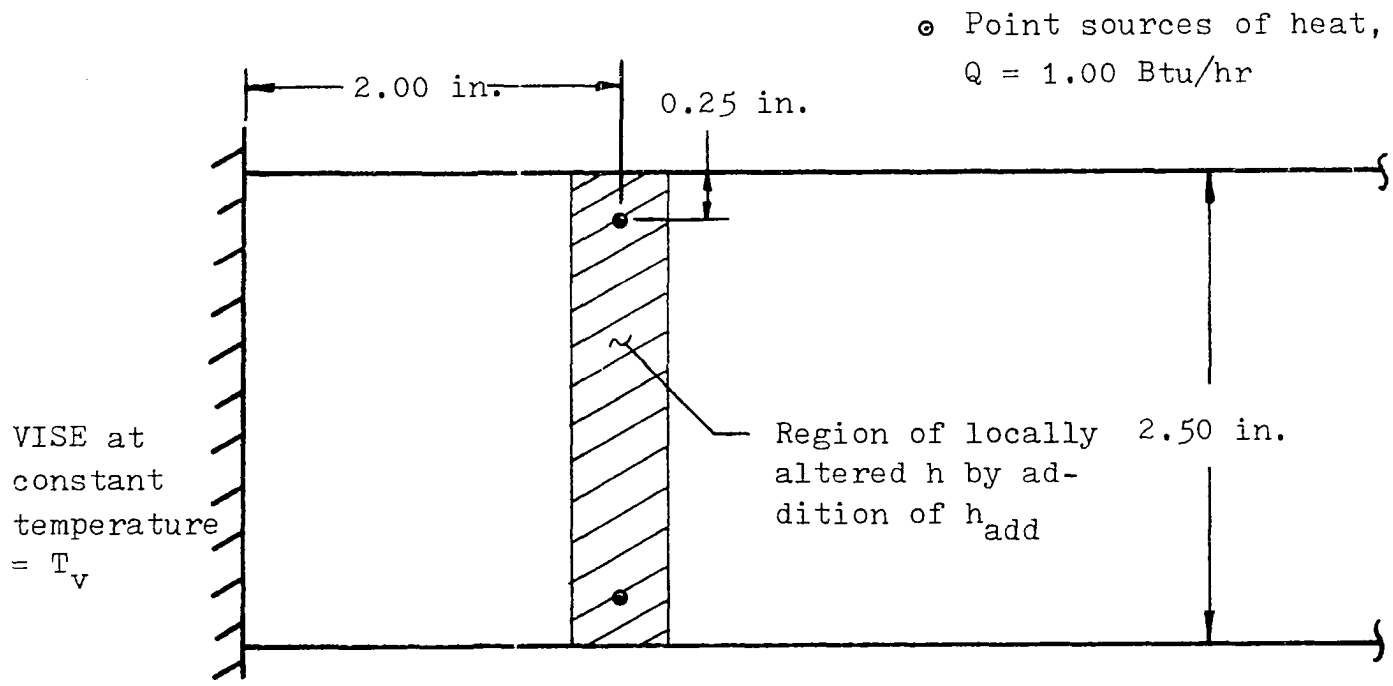

Figure 65. Geometry and nomenclature for enhancement study by blowing air.

The results of the enhancement study are shown in Figs. 66 and 67. Figure 66 considers the temperature rise and maximum temperature gradient at one of the heat generation points. As can be seen in the figure, over the wide range of h_{add} considered, no improvement in the temperature gradient occurred at the generation point. This result would be expected for a steady-state case. In addition, the maximum temperature rise on the specimen decreased with increasing h_{add}. A more appropriate choice of location on which to focus attention might be some point a small distance from the generation point. At any such point, the action of h_{add} would result in a decrease in the temperature rise compared to the unaltered case. However, as Fig. 67 shows, the behavior of the temperature gradient is changed more significantly by the increased convection. Figure 67 considers the temperature gradients at various distances from the generation point toward the vise. At any distance from the generator, the gradient is found to become smaller with increasing h_{add}. This result would be expected, since the specimen is in a steady state, and the increased loss of heat by convection must be accompanied by a decrease in the heat transfer by conduction. The important feature of Fig. 67 is that the gradient itself changes more rapidly (moving away from the generation point) as h_{add} increases. Hence, if the heat generation rate is sufficient to make a temperature rise visible with the convective coef-

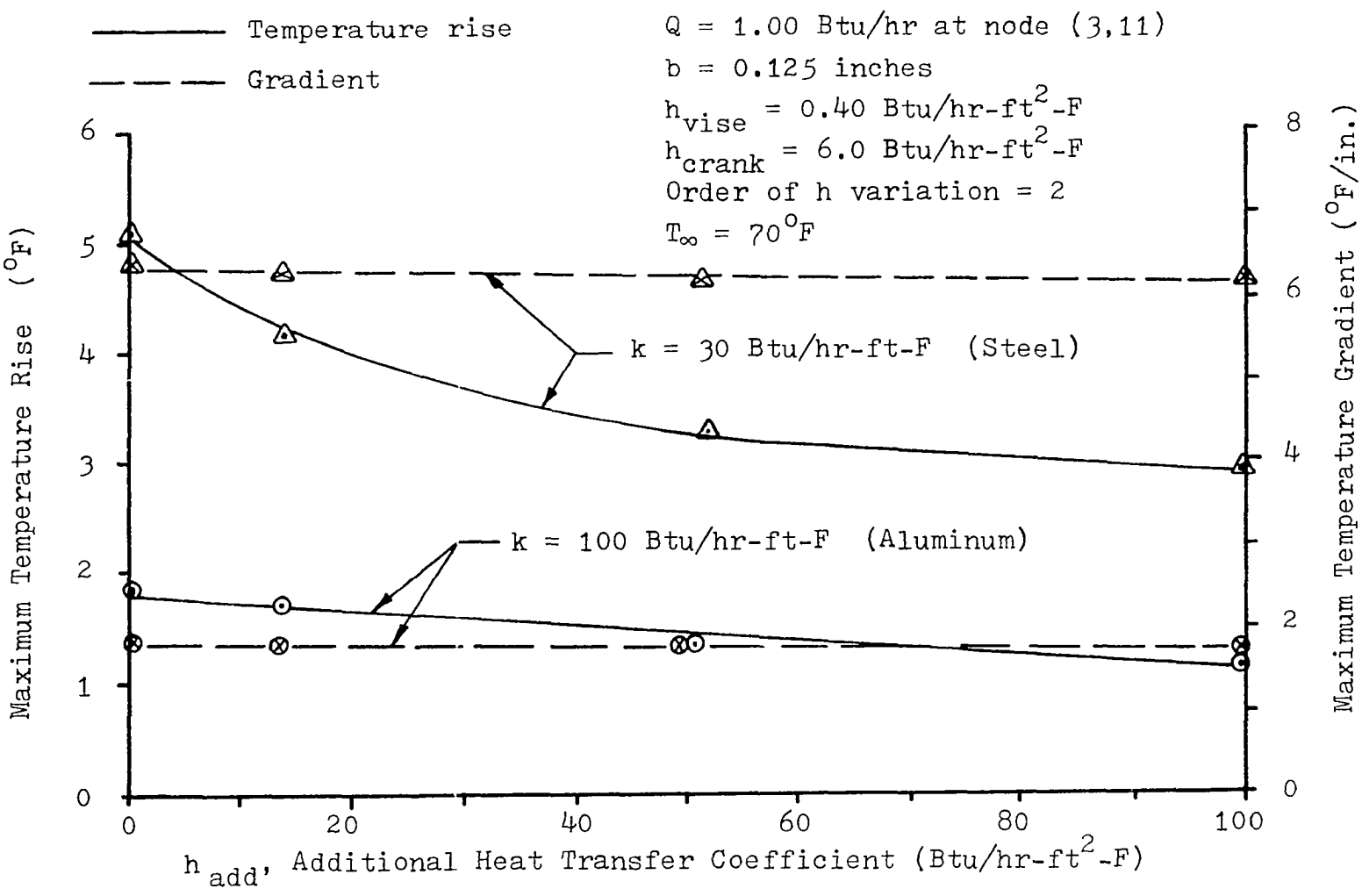

Figure 66. Temperature rise and gradient at generation point with enhancement.

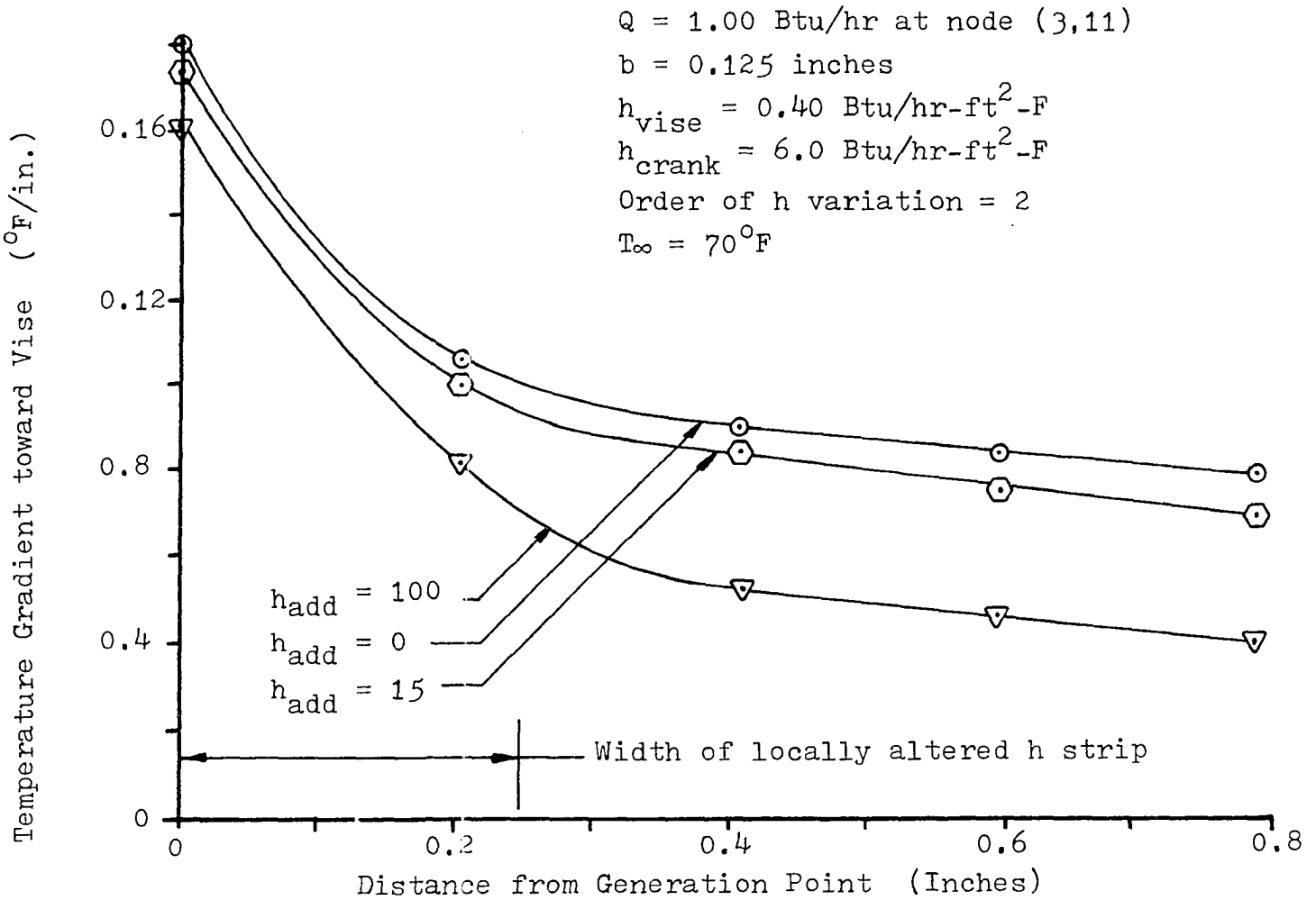

Figure 67. Effect of h_{add} on temperature gradient in aluminum.

ficient increased to a high value, it may be possible to obtain a more localized thermographic image of the regions sustaining fatigue damage with enhancement than is found under unaltered conditions. The results of the enhancement study are based on a limited number of cases using the numerical model described, but they are encouraging enough to warrant further investigation.

The transient response of the maximum temperature rise on the material is quite important during the early stage of the fatigue life of the specimen. In examining the non-dimensional curves for temperature rise as a function of fatigue cycles for the double-notched steel specimens, it was found that the specimens have three stages in their lives based on the thermal data. These stages were divided according to the sign of the second derivative of the non-dimensional curve with respect to time (see Fig. 20(b), for example). The first stage was defined as that in which the second derivative was negative. During this stage, the fatigue damage accumulates and forms slip bands which eventually lead to cracks in the material. Of course, if a test were stopped and the specimen allowed to cool to a uniform temperature before being restarted, a region of negative second derivative would result even if a crack had already been formed. This region of negative change in the slope of the temperature rise curve would be due to the simple transient start-up period for a uniform heat generation at the tip

of the crack, as opposed to the initial stage of the fatigue life, in which the damage processes change with cycles. Therefore, in order to correctly define from thermographic data the stage in which a specimen is being fatigued, there must be a way to distinguish the transient problem due to the changes in the damage of the material from that due to a uniform generation rate.

This problem was investigated using a transient finite difference approach to the rectangular geometry already used. In this case, the heat transfer coefficient was kept constant on the specimen based on the results of the parametric study. The nodal equations derived for the transient problem were based on a square grid of size dx by dx, and employed the forward-differencing technique. For interior nodes, a heat balance on the element produced the following equation for the temperature of the node (i,j):

$$\theta_{i,j}^{t+i} = \frac{dt\ k}{\rho C dx^2}\left[\theta_{i-1,j}^{t} + \theta_{i\ 1,j}^{t} + \theta_{i,j-1}^{t} + \theta_{i,j\ 1}^{t}\right] + \left[1 - \frac{4k\ dt}{\rho C dx^2} - \frac{2h_t dt}{\rho C b}\right]\theta_{i,j}^{t} . \qquad (6.18)$$

In eq. (6.18), $\theta_{i,j}^{t+1}$ is the temperature of node (i,j) at time t+dt, and $\theta_{i,j}^{t}$ is the temperature rise at node (i,j) at time t. C is the specific heat of the material and ρ is its density. The terms k, b, and h_t are still the conductivity, thickness, and total heat transfer coefficient (including

radiation) for the problem. The time increment dt is governed by the stability criterion that the last term in eq. (6.18) cannot become negative. Therefore,

$$dt \leq \rho C / \left[4k/dx^2 + 2h_t/b \right] . \qquad (6.19)$$

If eq. (6.19) is made an equality, then the last term in eq. (6.18) drops out and the nodal equations are simplified. Making this assumption, one obtains time increments of approximately 0.80 seconds for the steel studies run. The nodal equations of interior nodes do not include generation of heat. This was included in the equations only at the points where the generator would be placed. The nodal equation for a generating node is identical to eq. (6.18), except for the additional term $q''dt/\rho C$, where q" is the heat generation rate per unit volume. For simplicity, it was decided to neglect the convection and radiation from the edges of the specimen for this study, so the edges were treated as insulated boundaries. The nodal equation for a node on the boundary is

$$\theta_{i,j}^{t+1} = \frac{k\ dt}{\rho C dx^2} \left[\theta_{i,j-1}^{t} + \theta_{i,j\ 1}^{t} + 2\theta_{i\ 1,j}^{t} \right] + \left[1 - \frac{4k\ dt}{\rho C dx^2} - \frac{2h_t dt}{\rho C b} \right] \theta_{i,j}^{t} . \qquad (6.20)$$

The ends of the specimen were assumed to be at room temperature at all times, and the entire specimen was initially

at room temperature.

The results of the transient numerical model for a constant heat generation rate are given in Fig. 68. The maximum temperature rise on the specimen displays the classical asymptotic increase to a steady value for all values of heat generation rate. Note that the heat generation rate is given as the total rate rather than a specific rate. The effect of choosing various heat transfer coefficients is also indicated on the figure. As in the steady case, the value of h does not seriously change the results.

Experimental data were taken from several strip-chart recordings of the temperature at the notch root for various double-notched steel specimens. These data were obtained with a thermistor since the response in time was too rapid for the scanning infrared camera to be used. Some of these data are presented in Fig. 69. Note that each of the specimens included in Fig. 69 reaches a condition of constant temperature rise with cycles. Thus, each case includes all of the initial stage of the fatigue life of the specimen.

A comparison of the numerical data with the experimental data is shown in Fig. 70. As can be seen, the final temperature rise at the end of the initial stage can be predicted, but the behavior of the temperature rise with time is not predicted well. It must be concluded from the shape of the experimental data curve that the heat generation is

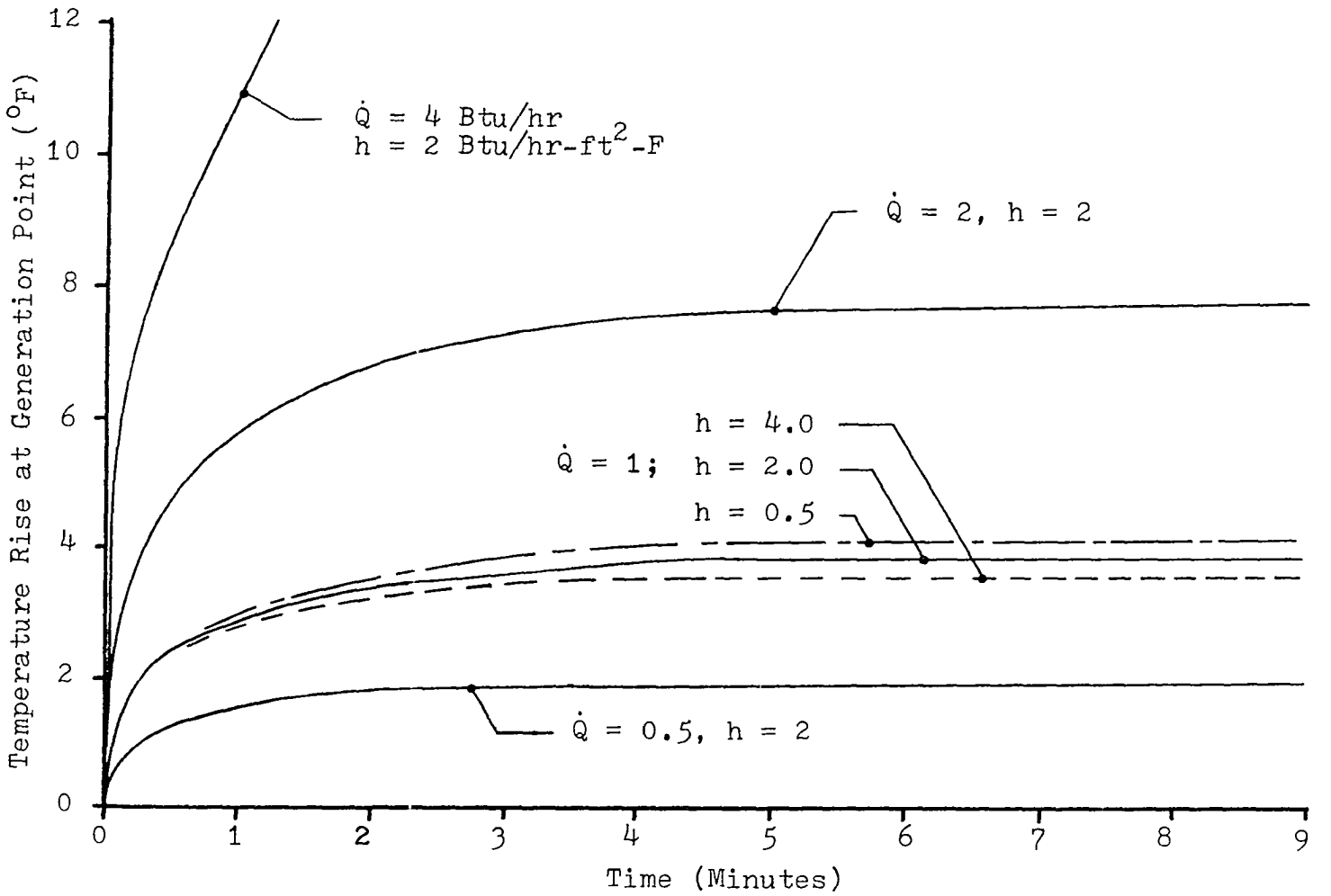

Figure 68. Results of transient numerical model for constant heat generation rate in rectangular fatigue specimens.

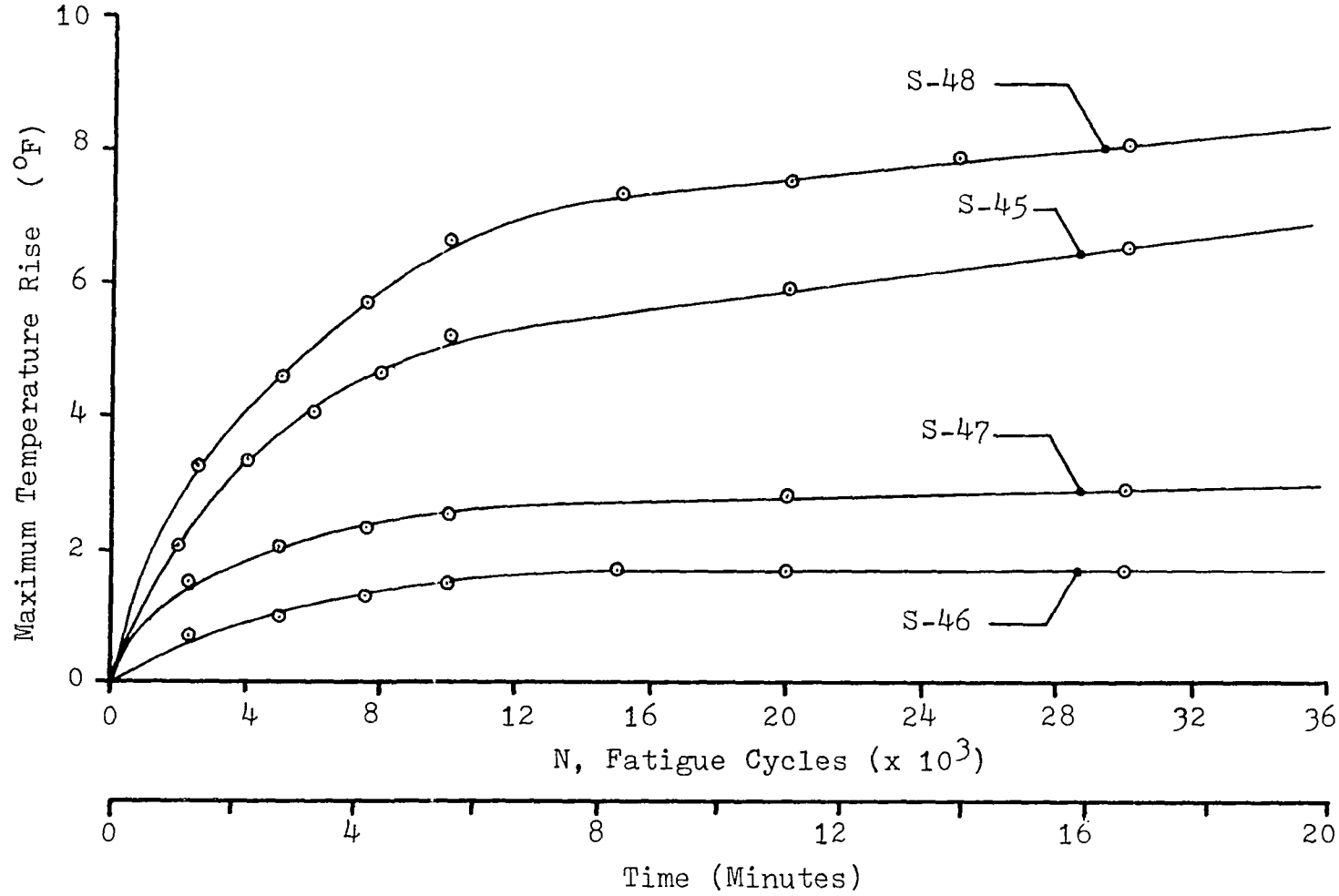

Figure 69. Experimental data for temperature rise during initial stage of life.

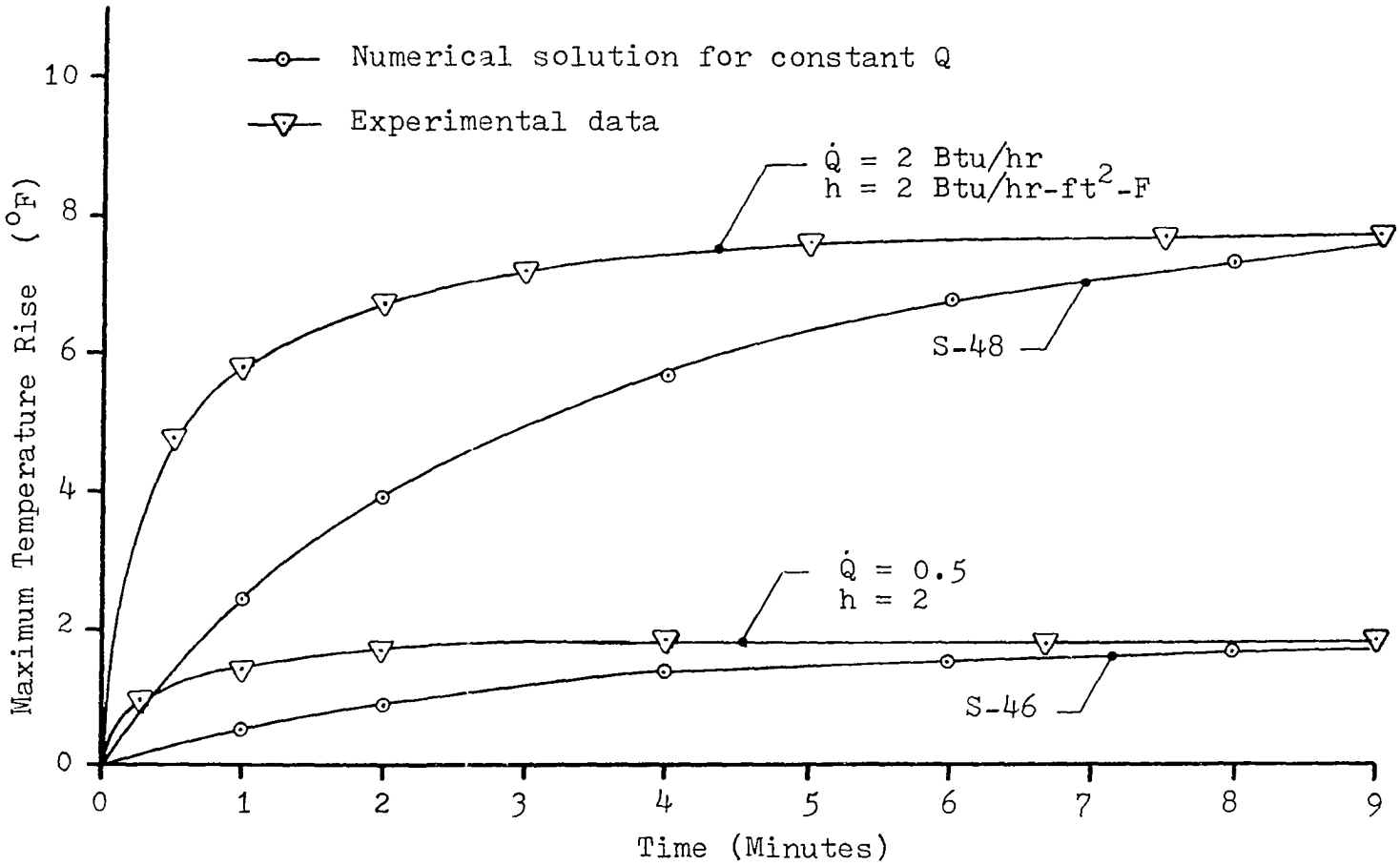

Figure 70. Comparison of numerical and experimental results for temperature rise with time for constant heat generation rate.

not constant in time. This conclusion goes well with the physical explanation of the fatigue mechanisms during the initial period of the specimen's life. It might be expected that during this time, more and more slip bands are formed and the total amount of fatigue damage occurring increases in time. Thus, the amount of heat generated in the material should also increase in time.

Based on the results of Fig. 70, the computer program for the transient model was altered to include a heat generation which varies in time. The variation was taken from zero initially to a value of $\dot{Q}_s$ at time $t = t_s$. $\dot{Q}_s$ was determined from the results of the steady-state analysis previously discussed, and was based on the temperature rises observed on the specimens experimentally after the initial phase of their lives. The order of the variation was first, second or third order, to be specified with the input data. This approach to the time-variable nature of the heat generation rate is somewhat simpler than is the actual case, since the actual case includes a period of work hardening where the hysteresis loss in the material is large. However, this period lasts only a few thousand cycles, after which the approximation made here is probably good. The length of the work-hardening period can be expected to be only about one minute or less, which occupies only a fraction of the initial stage of interest. Results of the new approximation to the generation rate are shown

for one case in Fig. 71. By varying the order of the time dependence of $\dot{Q}$, the temperature rise curve takes on quite distinct shapes. By comparing these curves to the experimental ones in Fig. 69, it can be concluded that the linear variation is not the correct one to use to match the experimental data. The slow initial rise and the inflection point at about t = 3 minutes make the linear variation curve unacceptable. However, both the second and third order curves show the proper shape.

Figure 72 shows the final attempt to describe the experimental data from one specimen, S-46, with the numerical model. The agreement is remarkably good, using a third order variation of $\dot{Q}$ from zero to 0.46 Btu/hr at t_s = 6 min. or t_s = 8 min. It is possible, through the proper choice of parameters in the problem, to accurately match other cases using models of second or third order. The linear case does not match well in any case attempted, regardless of the values of the parameters chosen.

The results just obtained provide the key to identifying whether a specimen is being started for the first time or whether it is actually in the second or third stage of its life and simply experiencing the transient response due to a sudden application of a heat generation at a point. As shown, the case for the true initial stage is best described by a model in which the heat generation rate builds up in time. For a specimen being started after already experi-

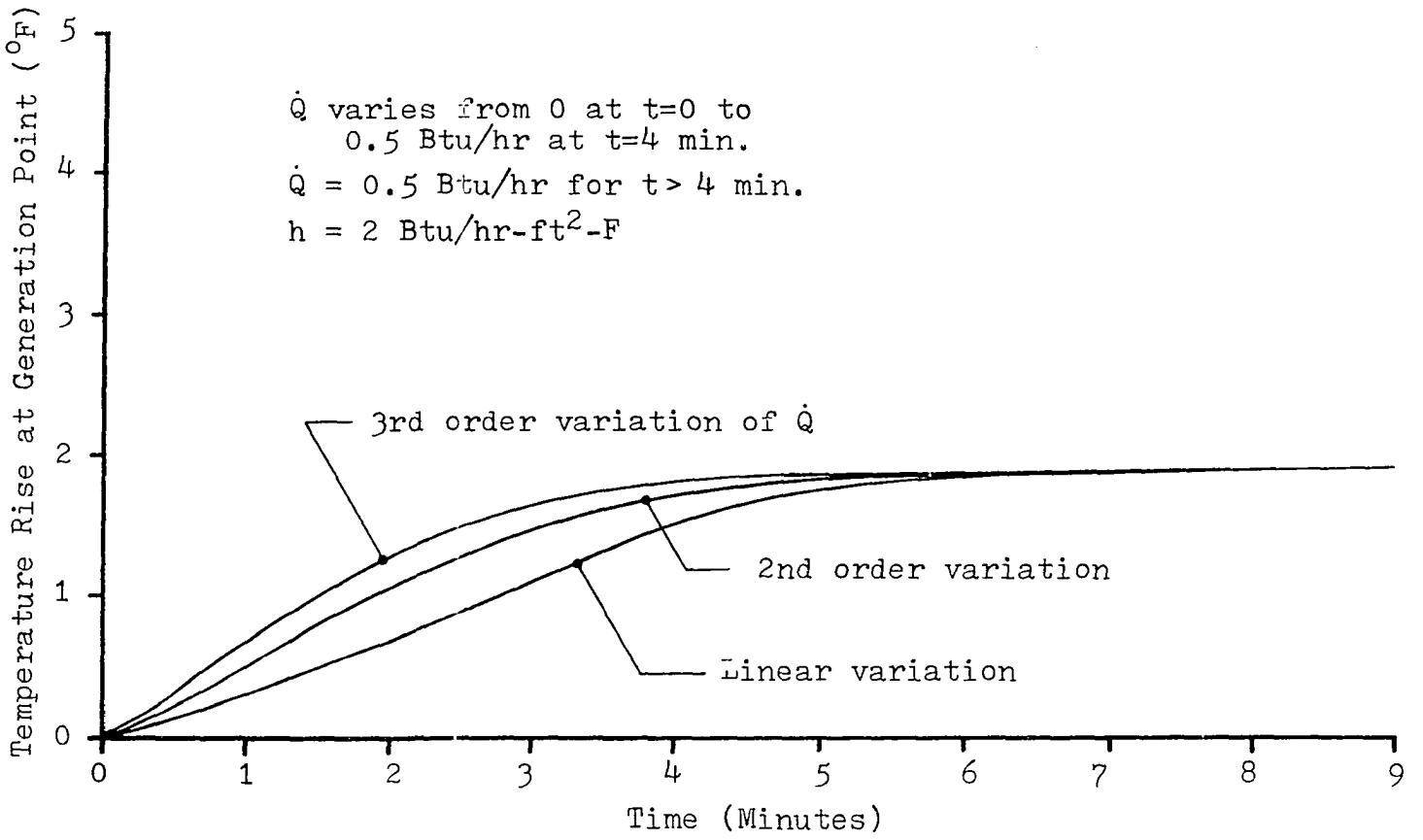

Figure 71. Results of numerical model with time-variable heat generation rate.

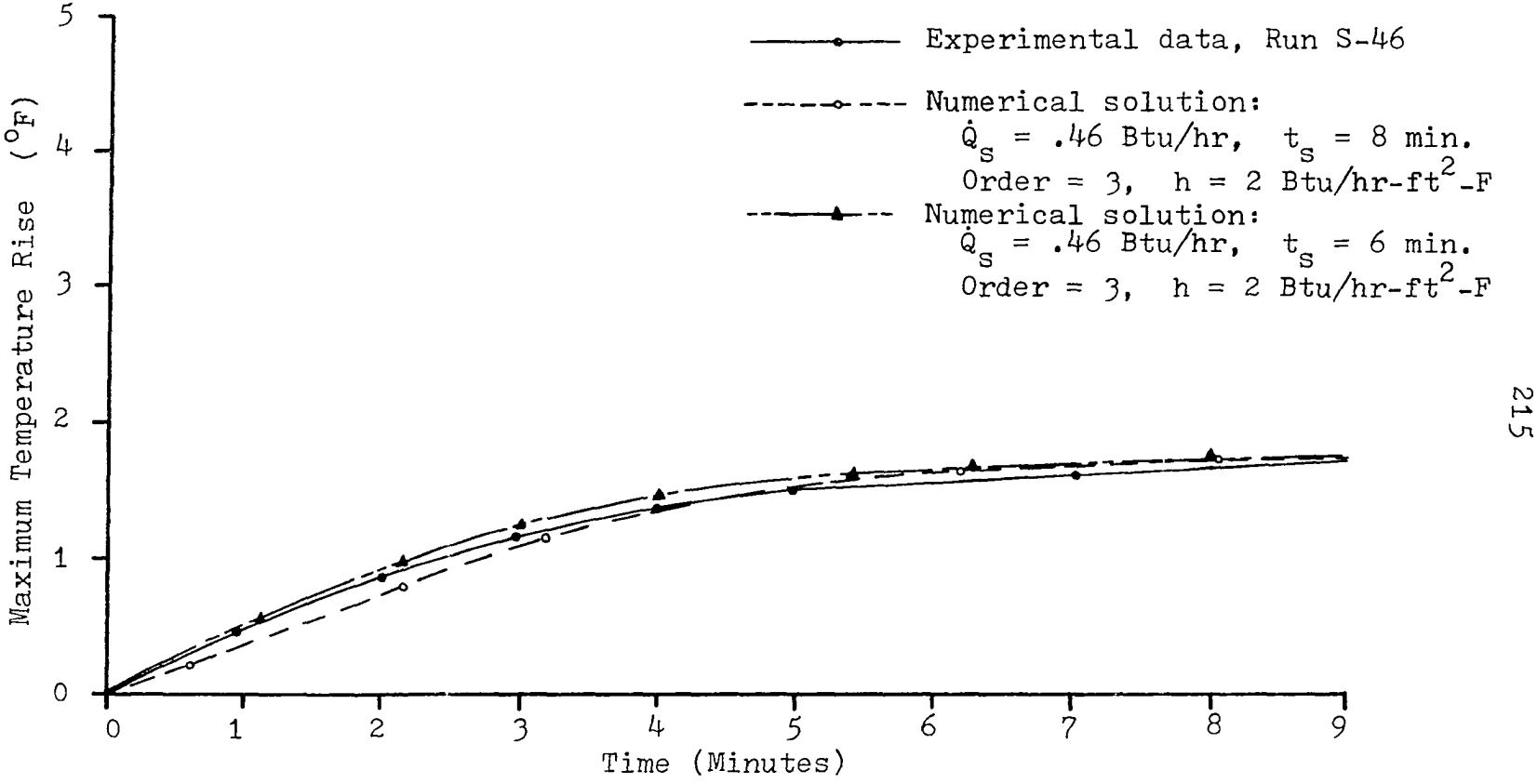

Figure 72. Comparison of experimental and numerical data for time-variable heat generation rate.

encing a portion of its fatigue life, one would expect that the heat generation rate would not increase gradually, but would have a high value immediately, in effect "picking up where it left off" before being interrupted. To illustrate this effect, a double-notched steel specimen was fatigued and stopped several times while the temperature at the notch root was monitored with a thermistor. For each period of cycling, the specimen accumulated 10,000 cycles at a frequency of 1,800 cycles per minute. After being cycled, the specimen was allowed to return to a uniform temperature before being cycled again. The results of this procedure are shown in Fig. 73. The initial start-up curve displays the behavior familiar from the numerical model with a variable heat generation rate. The temperature rise approaches a value which indicates that the final heat generation rate should be 0.395 Btu/hr. The curve for the first restart shows a more rapid initial rise, but results in the same final steady temperature rise. The second restart curve shows even more pronounced behavior of this manner. When compared to the numerical solution for a constant heat generation rate, it is seen that as the fatigue specimen accumulates more and more cycles, and initiates more damage, the start-up curves approach the case for a constant heat generation rate. Using this result, it is possible to distinguish between the early start-up periods during the first stage of the fatigue life and subsequent start-ups which may

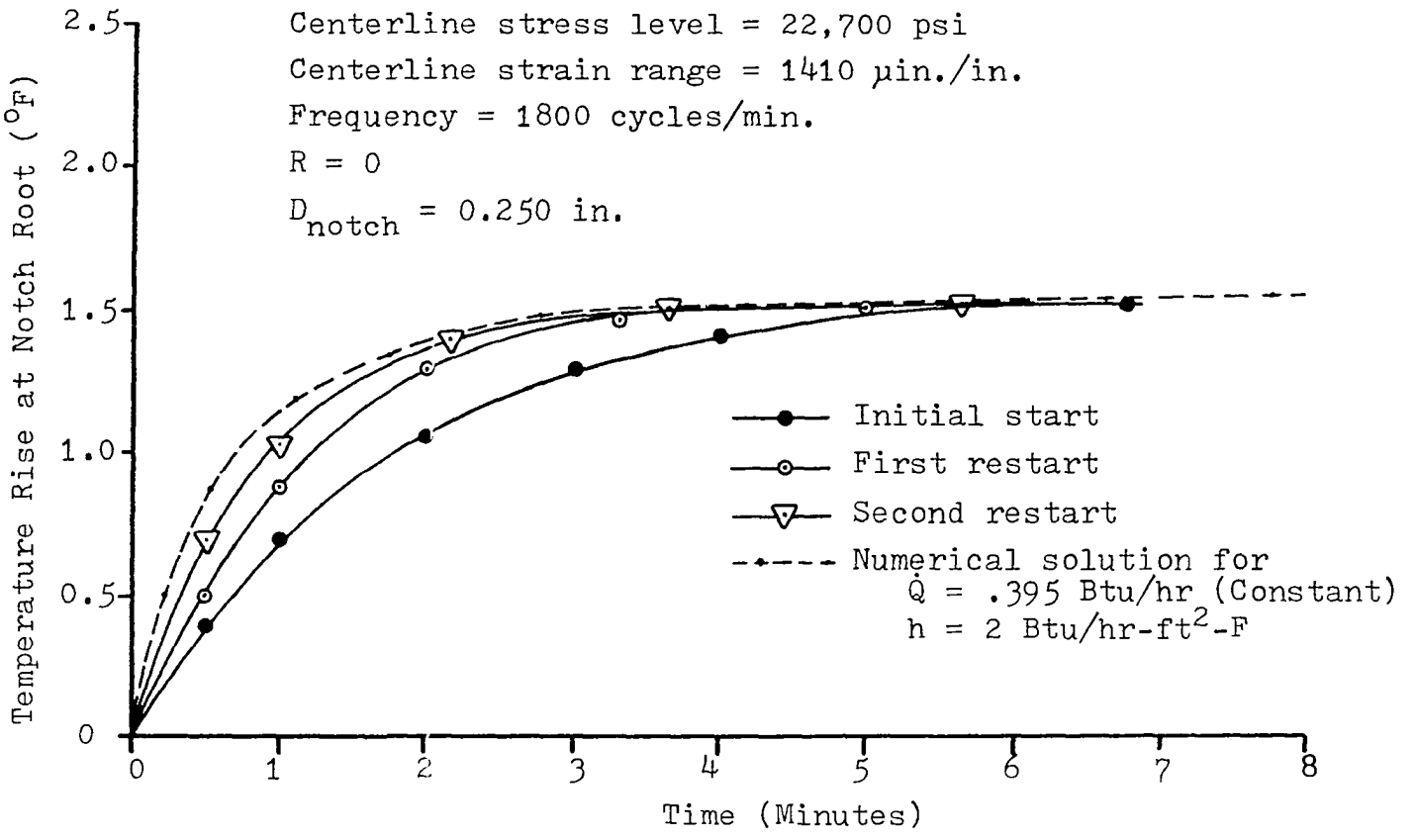

Figure 73. Effect of numerous restarts on maximum temperature rise with time.

occur in later stages. Hence, one can identify the stage of the life in which a specimen is being used without having a knowledge of the specimen's history.

Triangular Geometry

The great majority of the fatigue tests performed during the course of this study dealt with rectangular geometries. However, a few tests were conducted using specimens of triangular geometry such as that shown in Fig.12. Triangular specimens are used often in bending fatigue tests since they produce a uniform bending stress throughout the tapered section at any distance from the neutral axis of bending. These triangular specimens are being used less now than in the past, primarily due to the current popularity of tension-type fatigue testing machines, so an analysis of the heat transfer problem in these specimens is not as useful as that in the rectangular specimens. However, the problem in the triangular geometry has several interesting facets which produce difficulty in dealing with thermographic monitoring of fatigue tests for triangular specimens. Because of these facets, both an analytical and a numerical solution for the heat transfer problem in these specimens were sought.

It is possible to obtain an exact solution for the case of a triangular specimen of uniform thickness when the stress levels are assumed constant at any plane parallel to the neutral surface. In such a case, the hysteresis losses

in the material should be uniformly distributed throughout the specimen and may be represented by a uniform heat generation rate per unit volume of material of $\dot{q}$. The problem then appears as a fin of varying cross-sectional area with a uniform internal heat generation rate. The governing differential equation for this case in terms of $\theta = T - T_\infty$ is

$$\frac{d}{dx}\left(kA\frac{d\theta}{dx}\right) - hP\theta + \dot{q}A = 0 \ . \tag{6.21}$$

In eq. (6.21), k is the thermal conductivity of the material, A is the cross-sectional area at any location, and P is the perimeter around the surface at any position. The geometry used for this formulation is shown in Fig. 74. Expanding eq. (6.21), one obtains the form

$$Ak\frac{d^2\theta}{dx^2} + k\,\frac{dA}{dx}\,\frac{d\theta}{dx} - hP\theta + \dot{q}A = 0 \ . \tag{6.22}$$

The functions A(x) and P(x) can be determined from the geometry in Fig. 74:

$$A(x) = 2axt, \quad \text{where } a = b/2L_2 \ , \tag{6.23}$$

$$P(x) = 2t + 4ax = 2(t + 2ax) \ . \tag{6.24}$$

Thus, we have

$$\frac{dA}{dx} = 2at \tag{6.25}$$

and

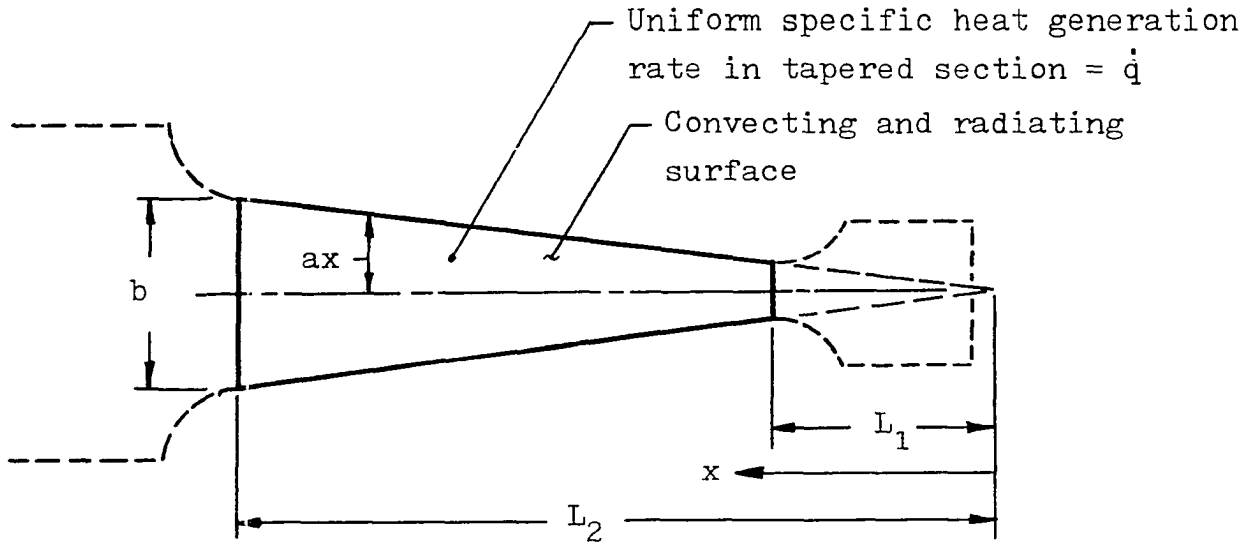

Figure 74. Geometry and nomenclature for triangular specimen with uniform heat generation.

$$\frac{P}{A} = \frac{(t + 2ax)}{axt} \cong \frac{2}{t} . \tag{6.26}$$

The differential equation of eq. (6.22) can be further reduced to give

$$\frac{d^2\theta}{dx^2} + \frac{1}{A}\frac{dA}{dx}\frac{d\theta}{dx} - \frac{hP}{kA}\theta + \frac{\dot{q}}{k} = 0 . \tag{6.27}$$

Using the results of equations (6.23) through (6.26), this equation can be written as

$$\frac{d^2\theta}{dx^2} + \frac{1}{x}\frac{d\theta}{dx} - \frac{2h}{kt}\theta + \frac{\dot{q}}{k} = 0 . \tag{6.28}$$

Assume that the solution of eq. (6.28) consists of a particular solution and a homogeneous solution:

$$\theta = \theta_H + \theta_P . \tag{6.29}$$

The particular solution which satisfies the differential equation is

$$\theta_P = \frac{\dot{q}t}{2h} . \tag{6.30}$$

The homogeneous equation to be solved then is

$$\frac{d^2\theta}{dx^2} + \frac{1}{x}\frac{d\theta}{dx} - \frac{2h}{kt}\theta = 0, \tag{6.31}$$

which can be rearranged to give a form of Bessel's equation,

$$x^2\frac{d^2\theta}{dx^2} + x\frac{d\theta}{dx} - m^2x^2\theta = 0, \tag{6.32}$$

where $m^2 = 2h/kt$. The solution of this equation is

$$\theta_H = C_1 I_o(mx) + C_2 K_o(mx) , \tag{6.33}$$

where I_o and K_o are the zeroth order Bessel functions. Combining equations (6.33) and (6.30), the total solution to the problem is

$$\theta = C_1 I_o(mx) + C_2 K_o(mx) + \frac{\dot{q}t}{2h} . \tag{6.34}$$

C_1 and C_2 are the constants of integration and depend on the boundary conditions imposed at $x = L_1$ and $x = L_2$. If the boundary conditions are that the vise (wide) end and the crank end are at known constant temperatures, θ_1 and θ_2 respectively, then it can be shown that

$$C_1 = \frac{\theta_1 - C_2 K_o(mL_1) - \dot{q}t/2h}{I_o(mL_1)} \tag{6.35}$$

and

$$C_2 = \left[\frac{\theta_2 I_o(mL_1)}{I_o(mL_2)} - \theta_1 + \frac{\dot{q}t}{2h} \left[1 - I_o(mL_1)/I_o(mL_2)\right] \right] \Big/ \left[K_o(mL_2) \frac{I_o(mL_1)}{I_o(mL_2)} - K_o(mL_1) \right] . \tag{6.36}$$

Alternately, heat fluxes q_1 and q_2 may be specified at the vise and crank ends, in which case the constants are

$$C_1 = \frac{q_2 - q_1 \cdot \dfrac{K_1(mL_2)}{K_1(mL_1)}}{km\left[\dfrac{K_1(mL_2)\ I_1(mL_1)}{K_1(mL_1)} - I_1(mL_2)\right]} \tag{6.37}$$

and

$$C_2 = \frac{q_1 + kC_1 mI_1(mL_1)}{km\ K_1(mL_1)} \ . \tag{6.38}$$

An interesting and troublesome characteristic of the solution just determined is that with uniform heat generation, triangular fatigue specimens display a band of maximum temperature rise that is not related to any particularly severe fatigue damage. This behavior was noted in a few tests of triangular fatigue specimens in which a temperature rise occurred but did not correspond to the location of the final fatigue failure of the specimen. To examine this aspect of the solution, one need only seek the maximum of $\theta(x)$ from eq. (6.34). For θ to be a maximum,

$$\frac{d\theta}{dx} = C_1\ m\ I_1(mx) - C_2\ m\ K_1(mx) = 0 \ , \tag{6.39}$$

or,

$$\frac{C_1}{C_2} = \frac{K_1(mx)}{I_1(mx)} \ . \tag{6.40}$$

Using asymptotic expansions of Bessel functions, and omitting all but the first terms in the infinite series expressions,

the condition for a maximum can be reduced to

$$\frac{C_1}{C_2} \cdot \frac{1}{\pi} = e^{-2mx} . \qquad (6.41)$$

This expression serves mainly as an approximation to the location of the maximum temperature rise, but does indeed indicate that a maximum exists since eq. (6.41) has a unique root for given values of C_1 and C_2. For the specific case of a steel specimen, 0.125 inches thick, with L_1 = 1.20 in., and L_2 = 9.0 in., it can be found from eq. (6.40) that the maximum temperature rise occurs at x = 0.433 ft., or at approximately 58 percent of the length. It must be noted that the simplified expression in eq. (6.41) gives an answer which is too low for this case, and since the expression was based on expansions of the Bessel functions for large arguments, results of eq. (6.41) cannot be used to predict the location of the maximum temperature rise accurately.

Using the exact solution in eq. (6.34) and boundary conditions of both the constant temperature and gradient types, the solid curves of Fig. 75 were determined. These curves are for steel with a uniform specific heat generation of 1.75 Btu/hr-in^3. Their purpose is mainly to provide an accurate comparison case for the data generated with the numerical model of triangular geometry to be discussed. As can be seen in this figure, the location of the maximum temperature rise on the specimen can be changed by specifying different boundary conditions.

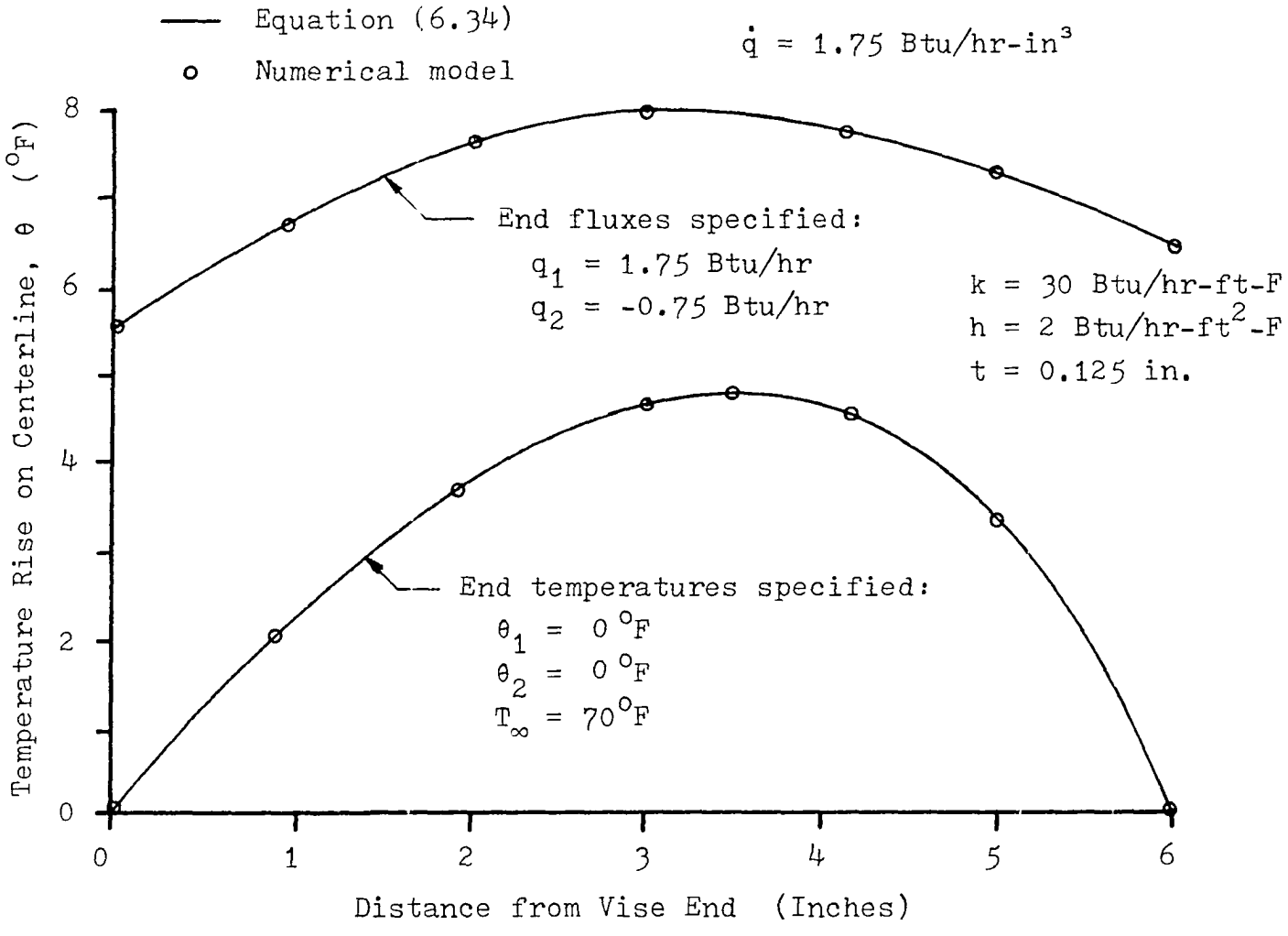

Figure 75. Centerline temperature rise for triangular fatigue specimen by exact and numerical solutions.

The numerical model developed for use in more realistic cases is based on a steady-state finite-difference approximation to the problem, as were the major models for the rectangular geometry. However, in the case of the triangular geometry, the nodal equations are complicated by the non-rectangular shape of the elements along the boundary. Because of the strong and complicated dependence of the equations on the geometry, the model was developed for a specific tapered size, which is shown in Fig.76. (Note that the scales in Fig. 76 are different in the horizontal and vertical directions by a factor of 2.) The model is composed of nodes on a rectangular grid except on the boundary along the tapered side. The specimen was divided down its centerline using symmetry as was done for the rectangular model. The nodal equations for the interior nodes and those along the centerline of the specimen are the same as those given in equations (6.15) and (6.16) for the rectangular case, except that $Q_{m,n}$ is replaced by its specific equivalent, $\dot{q}b(dx)(dy)$. This is necessary for the specific heat generation rate to be constant in the specimen when some of the elements are not of size dx by dy by b, as are the interior elements. The nodal equations for the end conditions also are similar to those for the rectangular case.

The nodes which present the difficulty are those which are on the tapered boundary of the specimen. Here,

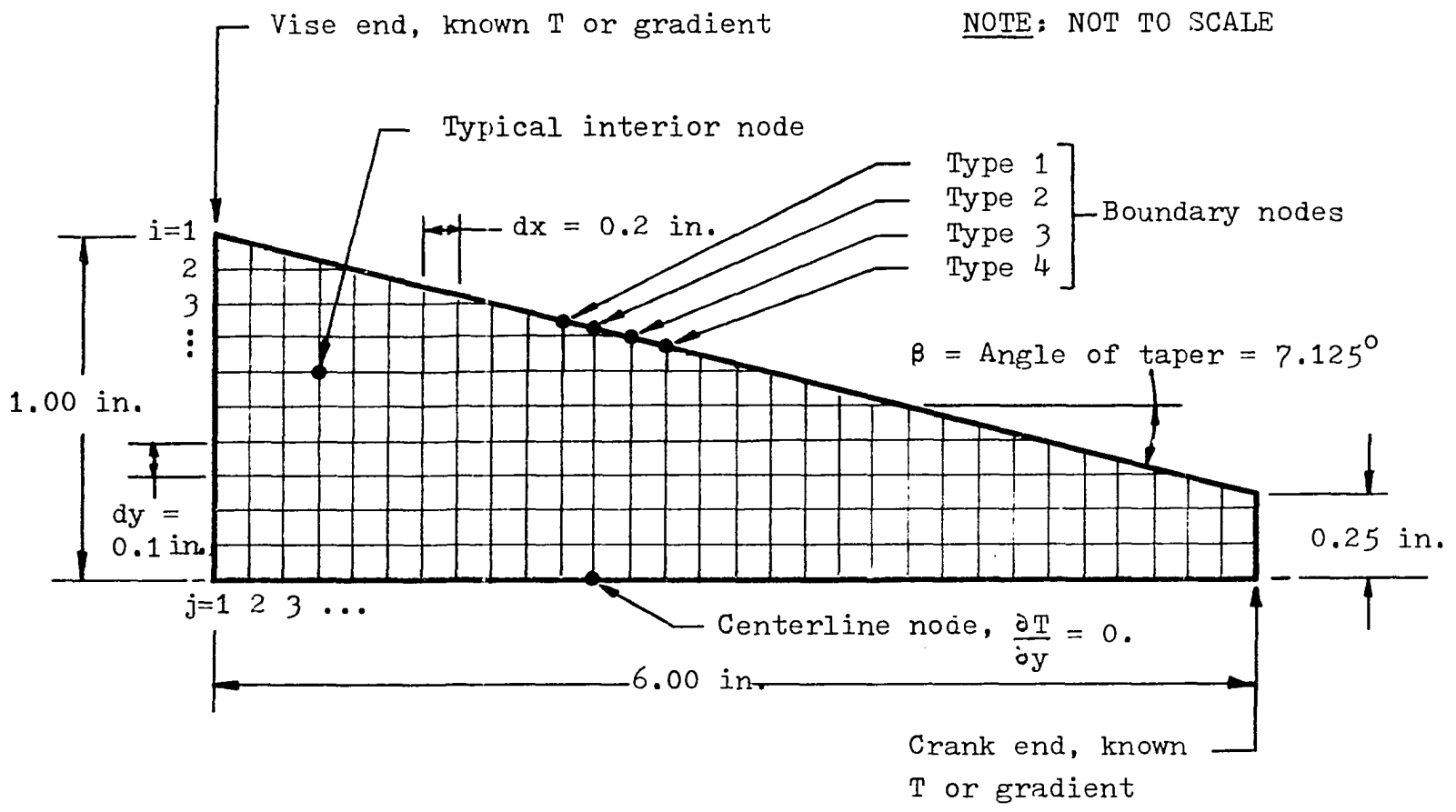

Figure 76. Geometry and nomenclature for triangular numerical model of fatigue specimen with uniform heat generation.

there are patterns of four kinds of nodes (based on the size of the elements associated with them) which repeat from the vise to the crank. These nodes are designated nodes of type 1, 2, 3, or 4, as indicated on Fig. 76. The nodal equations for any of these nodes may be written as one equation through the use of the parameter n = type number of any node. For the geometry under consideration, the general equation for a boundary node is then

$$T_{m,n} = \left[\frac{2\dot{q}ndx^2}{k} + \frac{2hdx}{kt} T_\infty (t\cos\beta + 2ndx) + \frac{2T_{m+1,n}}{(n+\frac{1}{2})} + \right.$$
$$\left. + \frac{(n-\sin\beta)}{2\cos\beta} T_{m,n+1} + \frac{(n+\sin\beta)}{2\cos\beta} T_{m,n-1} \right] \Bigg/$$
$$\left[\frac{2hdx}{kt} (t\cos\beta + 2ndx) + \frac{n}{\cos\beta} + \frac{2}{(n+\frac{1}{2})} \right] \quad (6.42)$$

where β is the angle of taper of the specimen, shown in Fig. 76. By letting n = 1, 2, 3 or 4, one obtains the proper nodal equation for each type node.

Using the interior and centerline nodal equations with the boundary nodal equations (6.42), a computer program was written to determine the temperatures on the surface of any triangular fatigue specimen. This program is listed in Appendix C. As a check on the accuracy of the numerical solution, cases corresponding to the exact solutions obtained for Fig. 75 were tried. The numerical results are plotted on Fig. 75 with the exact solutions, showing excel-

lent agreement between the two methods. Hence, the computer model could be used with confidence to examine more difficult cases.

The provision for varying the heat transfer coefficient along the specimen was included in the triangular model, as it was in the rectangular case. The heat transfer by radiation was also handled in the same manner. A few cases were run to examine the effects of different heat generation rates on the results and to illustrate the effect of varying the thermal conductivity of the material. All cases were of known end temperatures, equal to the ambient temperature. Figure 77 shows that the magnitude of the temperature rise along the triangular specimen is a strong function of the heat generation rate, but that the general shape of the centerline temperature rise curve does not change with $\dot{q}$. Thus, the location of the maximum rise does not change with changes in heat generation rate. Figure 78 displays the same behavior as that which is seen in Fig.77, but the maximum temperature rise does not seem to be very dependent on thermal conductivity, a result of the uniform heat generation in the specimen.

Of greater interest than the perfectly uniform heat generation case in the triangular geometry is that in which a more active heat generation region or point is superimposed on the uniform generation. Such would in fact be the case if a fatigue crack propagated across the triangular

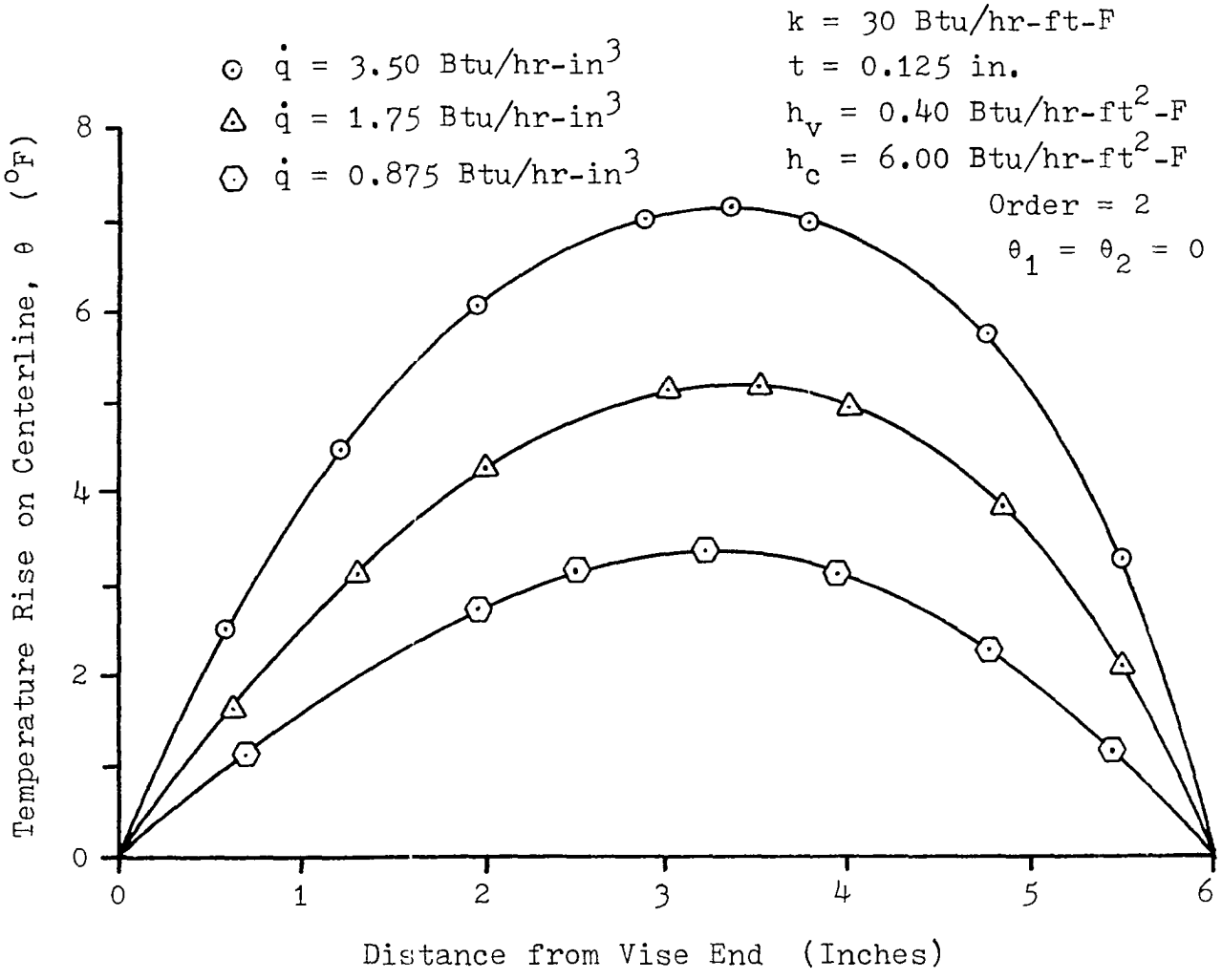

Figure 77. Centerline temperature rise as a function of specific heat generation rate in triangular fatigue specimens.

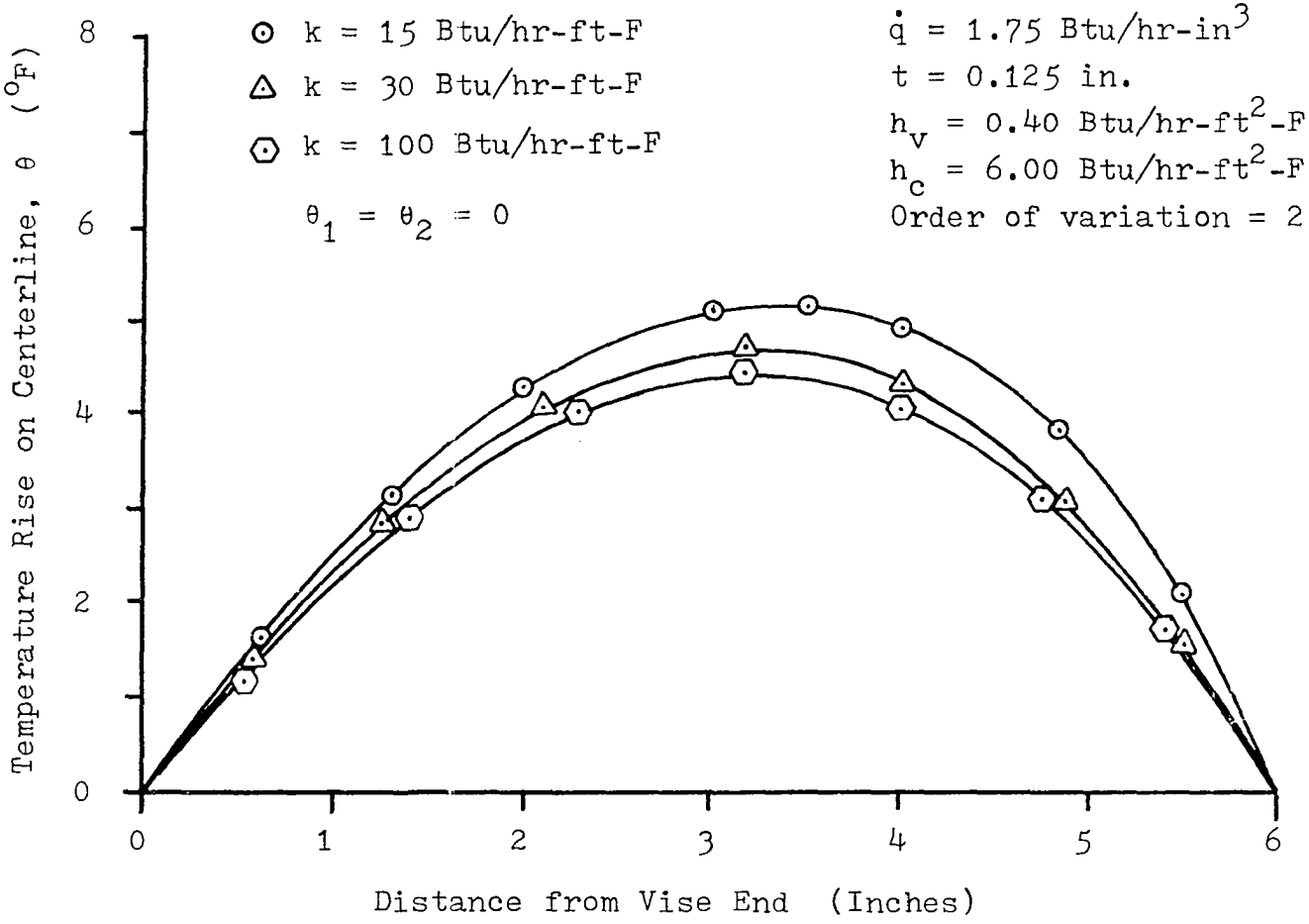

Figure 78. Centerline temperature rise as a function of thermal conductivity in triangular fatigue specimens.

specimen. The mechanisms leading to the initiation of a fatigue crack also produce this effect, although the added heat generation will in general be much lower than that for a propagating crack. It is the latter case which is actully the more important one, since it is during this period when an early indication of the location of the initiation would be desirable. In order to investigate these problems, the numerical model of the triangular specimen was modified to accept additional heat generation rates specified at any nodes. The uniform heat generation in the remainder of the specimen is left unchanged.

In the case of a fatigue crack propagating across a tapered fatigue specimen, a strong additional heat source would be superimposed on the uniform generation field in the specimen. Such a case is illustrated in Fig. 79 for a steel specimen 0.125 inches thick. The strength of the additional generation was chosen to be 1.00 Btu/hr based on the results of the experimental study with rectangular specimens. This extra generation was specified as 400 Btu/hr-in^3 in the input data for the computer program. As can be seen, the location of the extra generation point (or the crack tip in the actual case) is readily apparent in the temperature field. This behavior was also observed experimentally in some tests of tapered specimens. Once a crack forms, it is relatively easy to follow the propagation to failure, since the level of heat generation at the crack tip

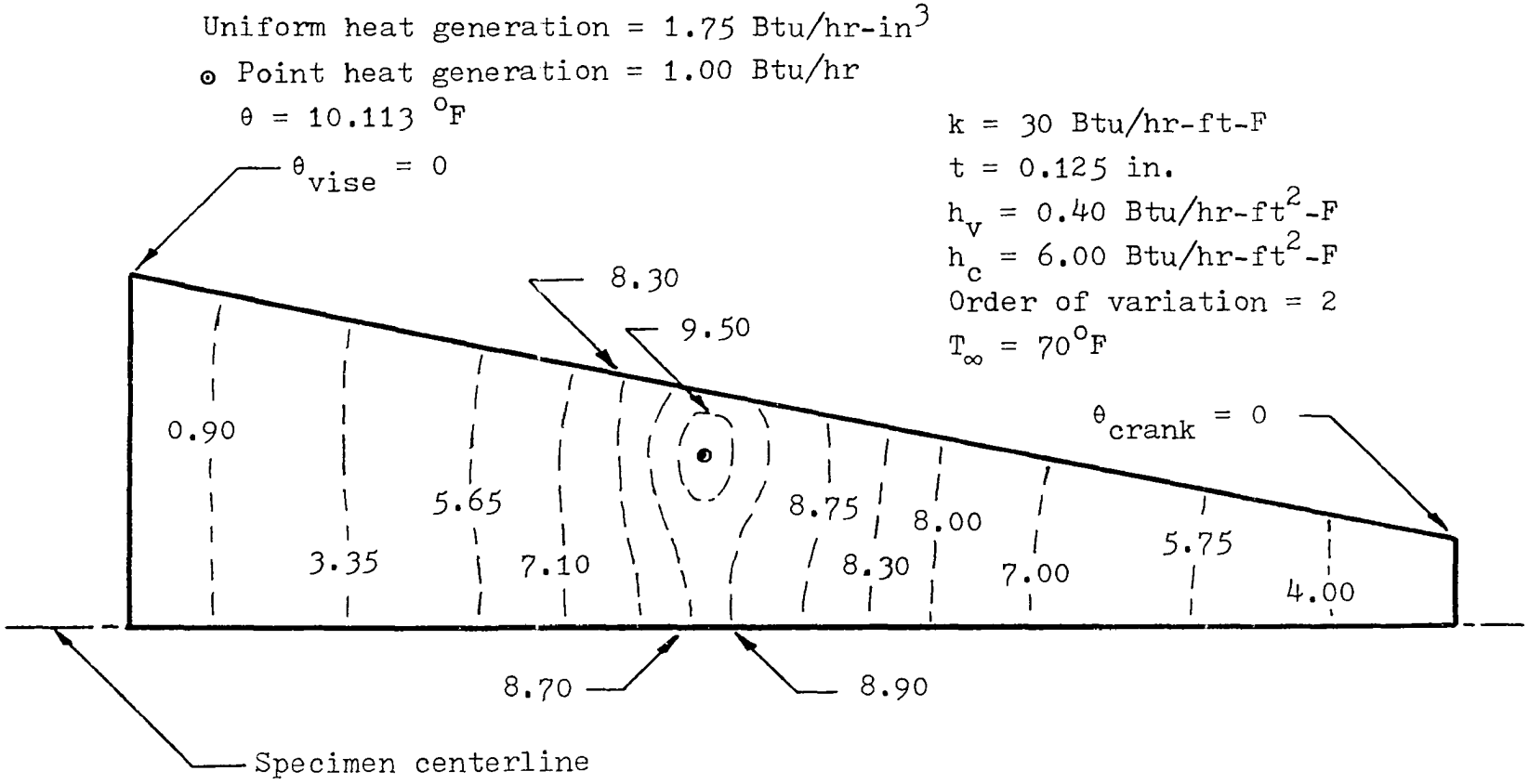

Figure 79. Numerical model results for tapered specimen with strong extra heat generation point superimposed on uniform generation.

supersedes the effects of the uniform generation. Hence, the problem approaches that for the rectangular geometry.

The case in which the triangular geometry presents the major difficulty is that in which the fatigue crack is not yet propagating but rather is just being initiated in the material. This case is of prime importance, since it is desirable to predict early in the life of the fatigue specimen where the fatigue damage will first appear. In a tapered specimen, one area will begin to experience more fatigue damage than the surrounding areas due to the presence of some flaw in the material, either metallurgical or geometric. The fatigue damage usually becomes severe at the edge of the specimen first. The strength of the heat generation at the real point of interest will be only slightly higher than that in the rest of the specimen at first. As the damage progresses until it resembles Fig. 79, the heat generation rate grows steadily. For low values of the extra heat generation rate, the effect of the uniform heat generation in the specimen dominates the resulting temperature field on the specimen and it is impossible to locate the region of major fatigue damage. For a given case of uniform generation in a specific material, there will be a lower limit to the value of the extra heat generation rate which allows one to determine thermographically where the major fatigue damage is occurring. This limit was determined for one case using the numerical model.

To determine the lowest extra heat generation which is detectable in the specimen, a uniform heat generation of 1.50 Btu/hr-in^3 was chosen in a 0.125-inch thick steel specimen. Using trial and error, different values of an extra heat generation were selected until the effect of the heat generation was barely discernable on the temperature field on the surface of the specimen. It was found that an extra generation strength of 30 Btu/hr-in^3 was necessary at a point on the edge about 20 percent of the length from the vise to make the effect visible in the temperature field. This represents a strength twenty times that in the surrounding material. The temperature field map for this case is shown in Fig. 80. Obviously, the requirement that the extra heat generation due to local fatigue damage mechanisms be twenty times that for the rest of the specimen imposes a limitation on the effectiveness of thermography for use with tapered specimens. It actually precludes the ability to locate important points early in the fatigue life of a specimen. However, once the damage reaches a given state, it is again possible to monitor further development and propagation of cracks. The behavior of the temperature field with uniform heat generation may also be of importance in on-compression testing of rectangular fatigue specimens, where a uniform heat generation in a reduced section would lead to the same difficultles discussed above.

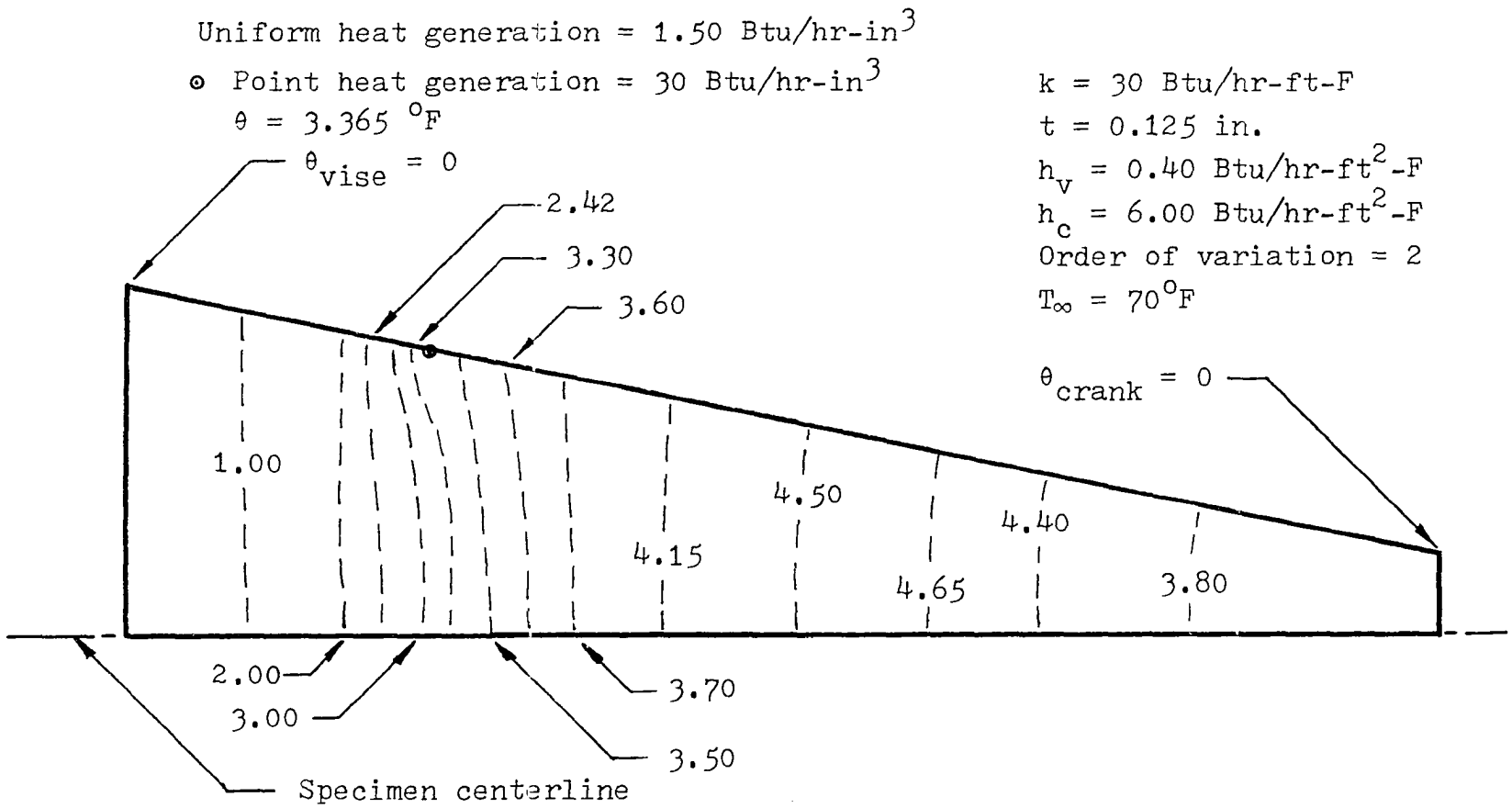

Figure 80. Numerical model results for tapered specimen with weak edge heat generation point superimposed on uniform generation.

Heat Generation and Plastic Zones

The analysis to this point has been aimed entirely at determining the thermal response of a fatigue specimen to a given heat generation. The mechanisms of fatigue through which the heat is generated have been discussed in Chapter II. It would be desirable to extend the analysis of this problem to include a method of determining the heat generation rate to be expected from a given geometry and loading. Such an extension requires considerable information concerning the stress field surrounding the notch or crack and a means to determine the volume of material in which energy is being dissipated. Hence, one must know the size of the plastic zone and its variation with the thickness of the material.

A useful variation of the problem above would be to be able to effectively measure the size of the plastic zone given thermographic data and stress data for a specimen. As has been seen in the experimental results, the temperature field on the surface of the specimen is a smoothly continuous one reaching a maximum temperature rise at the tip of the crack. There is no indication from the thermal data where the outer boundary of the plastic zone lies. Thus, an analysis of the plastic zone size must begin with the heat generation rate found from the temperature field map. Working backwards from this point, it may be possible to determine the size of the plastic zone, given enough other information

about the particular problem.

In order to demonstrate how the two problems above might be attacked, a brief analysis of the heat generation problem in general will be given. There are several assumptions necessary in the analysis, and therein lies the difficulty in using the results. The first assumption is that the heat generation takes place in a definable region about the tip of a crack or notch root called the plastic zone. It is assumed that outside the plastic zone no energy dissipation occurs. In such a case, the total energy dissipation rate, Q, is the integral effect of the distributed specific heat generations throughout the plastic zone:

$$Q = \iiint_{V_{pz}} \dot{q} \, dV \ . \tag{6.43}$$

The specific energy dissipation rate, $\dot{q}$, in the plastic zone is represented by the area under the hysteresis loop at any point as shown in Fig. 2(c). For the loading used in this study, the area under the hysteresis loop may be loosely defined as a fraction of the specific strain energy in the material at the point,

$$\dot{q} = \gamma \, uw \ , \tag{6.44}$$

where γ is a fraction less than one, and w is the cyclic frequency. The specific strain energy, u, can be written as

$$u = \int_0^{\epsilon_1} \sigma d\epsilon \ , \tag{6.45}$$

where ϵ_1 is the strain range at the point of interest. Using this expression, the specific energy dissipation rate will be

$$\dot{q} = \gamma\, w \int_0^{\epsilon_1} \sigma d\epsilon \ , \tag{6.46}$$

and the total energy generation rate in the material is

$$Q = \iiint_{V_{pz}} \gamma\, w \int_0^{\epsilon_1} \sigma d\epsilon \, dV \ . \tag{6.47}$$

The specific energy dissipation rate, $\dot{q}$, is most difficult to determine since it requires a thorough knowledge of the strains in the plastic zone and the stress distribution there. Even if it were possible to obtain an expression for $\dot{q}$, further assumptions would have to be made in order to integrate that expression to obtain Q. In particular, the factor γ is unknown, and might have to be determined empirically. It is even possible that γ will depend on the strain distribution in the plastic zone, further complicating the problem.

Due to the number of assumptions necessary in this analysis, it is not possible to work backwards given the heat generation rate to determine the plastic zone size. The discussion presented above is intended as a definition of the problems to be solved before such techniques for finding the plastic zone size can be used with confidence. However, it is possible that with sufficient additional information and research, the thermographic determination of plastic zone sizes will be a useful technique.

CHAPTER VII

CONCLUSIONS

This study has dealt with both the experimental and analytical aspects of the use of thermography in fatigue studies. The results of the study indicate that thermography is a potent technique for monitoring fatigue tests and predicting likely locations of damage in a specimen.

Early experimental investigations established the use of thermography in bending fatigue tests as a viable nondestructive means of locating areas likely to incur the greatest fatigue damage during a test. The heat generation due to hysteresis effects in the material provided a local area of elevated temperature from which one could predict where fatigue cracks would form. The early tests were conducted with several materials, and indicated that the use of thermography with aluminum specimens would be less successful than that with steel due to the high thermal conductivity of the aluminum. Composite materials worked quite well due to their low conductivity.

The lengthy series of double-notched steel fatigue tests provided a great quantity of data which supports several conclusions. The area most likely to incur the first fatigue

damage during a test was consistently and easily determined by searching for the warmest point on the surface of the specimen. Visually-observed crack locations confirm the accuracy of the thermographic technique. Once fatigue damage takes the form of a visible crack, its progress as it propagates in the material can be monitored with thermography. Crack velocities can easily be calculated using the locations of the crack tip found with thermography.

By presenting the data from this series as temperature rises on the specimens as functions of the number of fatigue cycles, other important conclusions can be drawn. The curves of temperature rise versus cycles have three basic regions in all the cases of the series. The first region is one in which the second derivative of the temperature rise with respect to cycles is negative. It is during this stage that the fatigue damage begins to accumulate on a microscopic scale. Combined with this stage is the change in temperature rise in time due to the transient heat transfer problem. Analytical considerations using numerical models show that it is possible to discern the original first stage of the fatigue life from subsequent transient behavior by observing closely how the temperature rise varies in time. The first stage itself does not experience a constant energy dissipation rate, but rather one which changes in time. Restarts of the fatigue test leading to transient behavior show responses which approach that of a constant heat gen-

eration rate.

The second stage can be characterized as the period over which the second derivative of the temperature rise curve is zero. It is during this stage that the fatigue damage coalesces into a propagating fatigue crack. In this stage, the heat generation rate changes linearly with time at a low rate. Analytical considerations in this case showed that part of this change is necessary to keep the temperature rise at even a steady level. It is important to observe that in all cases, the formation of a microscopically visible fatigue crack took place during the second stage, but in no instance was that formation accompanied by a marked change in either the temperature rise curve or the temperature. The implication, therefore, is that in order to determine exactly when a crack begins to propagate, one must continuously monitor the location of the maximum temperature rise.

The third stage in the fatigue life of a specimen is marked by a positive second derivative of the temperature rise versus cycles curve. During this period just prior to failure, the heat generation and temperature rise increase rapidly due to large plastic deformations in the material accompanying rapid crack growth.

The temperature rise curves were also shown in non-dimensional form as T^* vs. N^* for each nominal stress level. For these curves it was seen that the length of the first stage changed with stress level, but was fixed for a given

level. However, the length of the third stage was found to be less sensitive to changes in stress level. This stage usually occupied the last 30 percent of the life of the specimens. Using this conclusion, it may be determined whether or not a fatigue specimen is in a dangerous stage of its life by determining the second derivative of the temperature rise on the surface of the specimen.

Other useful conclusions can be drawn from the temperature field maps produced from thermograms taken during fatigue tests. Using an energy balance technique, the heat generation in the material can be determined from any temperature field map. Graphs of dissipation rate as functions of fatigue cycles were then used to determine the total energy dissipation in a specimen in a fatigue test. The results of this technique compare well with results in the literature.

Several tests using composite materials were performed, and led to additional useful conclusions. As was the case with the steel tests, the most probable regions to incur fatigue damage were easily located early in the fatigue life of a specimen. The propagation of damage was monitored. The damage in composite materials takes different forms from that in metals, but was still easily detected. It was shown that relative stress concentration intensities can be determined using thermography. An important conclusion is that thermography can be used to locate areas incurring the greatest fatigue damage even when those areas are below the surface of the material being monitored. In this manner,

thermography provides information at an early stage which would not be obtainable with any visual inspection technique until the material actually began to fail.

The results of the analytical considerations have a bearing on the directions future research should take. It was shown that given a heat generation rate in a specimen it is possible to predict the maximum temperature rise on the material. The rises determined using the heat generation rates obtained experimentally agreed reasonably well with those seen thermographically. The problems associated with determining the heat generation rate to be expected from a given loading were discussed and a possible method of attacking the problem was presented. A useful conclusion of the analytical study is that the temperature rises and gradients on the material are quite insensitive to changes in the heat transfer by convection. This result is important since it is most difficult to obtain a very accurate value for the heat transfer coefficient for the type of testing performed here.

The results of this study are very encouraging regarding the use of thermography in fatigue studies. However, much more research on the subject is necessary in order to fully realize the potential of the technique. Several suggestions for further research in different areas of the method can be made. First, due to the current popularity of tension-compression fatigue testing, an experimental study

using this loading would be highly desirable. By using tension-compression loading, several of the problems associated with this work could be avoided. The data in the literature are almost entirely devoted to axial loading tests, so much better comparisons of techniques and results could be obtained. The variation of stress through the material would be greatly simplified, perhaps allowing a determination of the plastic zone size. Specimens with long sections of reduced area could be used to investigate more closely the possibilities of determining where fatigue damage will occur when there are an infinite number of statistically equal initiation sites. Finally, the convective heat transfer problem would be simplified since the end of the specimen would not be deflected in the manner that it was in the bending tests.

Other experimental investigations could deal directly with the effects of geometry, material, and loading. As the technique of using thermography in fatigue studies is further developed, attention could be turned toward possible application of the technique to practical material or parts testing. The major obstacles to be dealt with in this case are the need for the part to be cycled at a rapid rate during thermographic inspection, and the difficulty presented by certain geometries (cylindrical, for example) and material finishes (as a polished surface).

Further analytical studies could be used to better

establish the heat generation as a function of stress levels in a specimen. Particularly, a combined stress analysis and heat transfer analysis conducted by using the finite element technique could yield not only the generation rate, but also the surface temperatures to be expected on the material. Such a model would be rather involved, and would have to include strain-hardening plastic effects, but in the final form could be used to determine the usefulness of thermography for any number of loadings or geometries.

With further development, thermography may become a prominent detection and measurement technique in connection with fatigue tests of materials and structures. The results of the study presented here show that the technique works well for the cases investigated, and has promise for other cases as well.

REFERENCES

1. Avery, D.H. and Backofen, W.A., "Nucleation and Growth of Fatigue Cracks", Fracture of Solids, Interscience Publishers, New York, 1963, pp. 339-382.

2. McGannon, H.E., ed., The Making, Shaping and Treating of Steel, United States Steel Corporation, 1964, pp. 1171-1176.

3. Leven, M.M., "The Interaction of Creep and Fatigue for a Rotor Steel", Experimental Mechanics, 13(9), pp. 353-372, (Sept. 1973).

4. Lamble, J.H., Principles and Practice of Non-destructive Testing, Wiley and Sons, New York, 1963, pp. 69-104.

5. Hinsley, J.F., Non-destructive Testing, MacDonald and Evans, Ltd., London, 1959, pp. 259-326.

6. McMaster, R.C., ed., Nondestructive Testing Handbook, Ronald Press, New York, 1959, pp. 43.1-43.50.

7. "Predicting Metallic Fracture", Mechanical Engineering, 94(5), p. 49, (May 1972).

8. Acoustic Emission, ASTM STP 505, American Society for Testing and Materials, Philadelphia, Pa., 1972.

9. Gericke, O.R. and Vogel, P.E.J., "Infrared Bond Defect Detection System", Materials Evaluation, 22(2), pp. 65-68, (Feb. 1964).

10. Lewis, R.K. and Norton, J.T., "Infrared Detection of Weld Defects", Advanced Metals Research Corporation, Tech. Report No. WAL 550/1, January 1961.

11. Green, D.R., "Emissivity Independent Infrared Thermal Testing Method", Materials Evaluation, 23(2), pp. 79-84, (Feb. 1965).

12. Karpman, H.L., "Current Status of Thermography", Angiology, 21, pp. 103-109, (Feb. 1970).

13. Leftwich, R.F. and Ordway, G.B., "Optical Thermal Testing - A State of the Art Review", International Journal of Nondestructive Testing, 2, pp. 129-170, (1970).

14. Pontello, A.P., "A Test Method for Nondestructive Testing of Fuel Equipment Using Thermography", Naval Air Propulsion Test Center, Trenton, New Jersey, NAPTC-AED-1963, (Dec. 1971).

15. Lee, R.E. and Pasman, J.S., "Infrared Scanning of Honeycomb Structures and Phenolic Surfaces for Bonding Defects", Picatinny Arsenal, Dover, New Jersey, AD-746 975, (Nov. 1970).

16. Yokobori, T., The Strength, Fracture, and Fatigue of Materials, Noordhoff, Groningen, the Netherlands, 1965, p. 199.

17. Attermo, R. and Ostberg, G., "Measurements of the Temperature Rise Ahead of a Fatigue Crack", International Journal of Fracture Mechanics, 7(1), pp. 122-124, (March 1971).

18. Reifsnider, K.L. and Williams, R.S., "Determination of Fatigue-related Heat Emission in Composite Materials", Experimental Mechanics, 14(12), pp. 479-485, (Dec. 1974).

19. Marcus, L.A. and Stinchcomb, W.W., "Measurement of Fatigue Damage in Composite Materials", Experimental Mechanics, 15(2), pp. 55-60, (Feb. 1975).

20. Nevedunsky, J.J., Lucas, J.J. and Salkind, M.J., "Early Fatigue Damage Detection in Composite Materials", Journal of Composite Materials, 9(4), pp. 394-408, (Oct. 1975).

21. Charles, J.A., Appl, F.J. and Francis, J.E., "The Detection of Local Heating Due to Cyclic Loading Using Thermography", Proceedings of the Oklahoma Academy of Science, 54, pp. 52-59, (1974).

22. Charles, J.A., "The Use of Thermography in Experimental Fatigue Studies", Proceedings of the Fifth Graduate Research Conference on Applied Mechanics, Texas A&M University, pp. 19-25, (March 1974).

23. Charles, J.A., Appl, F.J. and Francis, J.E., "Using the Scanning Infrared Camera in Experimental Fatigue Studies", Experimental Mechanics, 15(4), pp. 133-138, (April 1975).

24. Charles, J.A., Appl, F.J. and Francis, J.E., "Fatigue Testing Composites Using Thermography", Proceedings of the 12th Annual Meeting of the Society of Engineering Science, Austin, Tex., pp. 819-828, (Oct. 1975).

25. Charles, J.A., Appl, F.J. and Francis, J.E., "Fatigue Damage Determination by Thermography", to be presented at the Second International Conference on the Mechanical Behavior of Materials, Boston, Mass., August 1976.

26. Sandor, B.I., Fundamentals of Cyclic Stress and Strain, University of Wisconsin Press, Madison, Wis., 1972, pp. 64-84.

27. Drucker, D.C., "A Continuum Approach to the Fracture of Metals", Fracture of Solids, Interscience Publishers, New York, 1963, pp. 3-50.

28. Salkind, M.J., "Fatigue of Composites", Composite Materials: Testing and Design (2nd Conf.), STP 497, ASTM, Philadelphia, Pa., 1972, pp. 143-169.

29. Yokobori, T., The Strength, Fracture, and Fatigue of Materials, Noordhoff, Groningen, the Netherlands, 1965, pp. 237-265.

30. Gruntfest, I.J., "A Note on Thermal Feedback and the Fracture of Solids", Fracture of Solids, Interscience Publishers, New York, 1963, pp. 189-196.

31. Yokobori, T., The Strength, Fracture, and Fatigue of Materials, Noordhoff, Groningen, the Netherlands, 1965, pp. 281-330.

32. Ibid., pp. 218-220.

33. Raju, K.N., "On the Calculation of Plastic Energy Dissipation Rate During Stable Crack Growth", International Journal of Fracture Mechanics, 5(2), pp. 101-112, (1969).

34. Gough, H.J., "Crystalline Structures in Relation to Failure in Metals - Especially by Fatigue", Proceedings of ASTM, 33(pt. II), pp. 3-114, (1933).

35. Wood, W.A. and Davies, R.B., "Effects of Alternating Strain on the Structure of Metal", Proceedings of the Royal Society of London, A220, pp. 255-266, (1953).

36. Gough, H.J. and Wood, W.A., "A New Attack on the Problem of Fatigue in Metals, Using X-ray Methods of Precision", Proc. Royal Soc. of London, A154, pp. 510-527, (1936).

37. "Plastic Deformations of Metals", Nature, 172, pp. 572-573, (Sept. 1953).

38. Bullen, F.P., Head, A.K. and Wood, W.A., "Structural Changes During the Fatigue of Metals", Proc. Royal Soc. of London, A216, pp. 332-343, (1953).

39. Yokobori, T., The Strength, Fracture, and Fatigue of Materials, Noordhoff, Groningen, the Netherlands, 1965, p. 205.

40. Ibid., p. 203.

41. Sandor, B.I., op. cit., pp. 54-63.

42. Ibid., p. 75.

43. Raju, K.N., "An Energy Balance Criterion for Crack Growth under Fatigue Loading from Considerations of Energy of Plastic Deformation", International Journal of Fracture Mechanics, 8(1), pp. 1-15, (March 1972).

44. Weichert, R. and Schonert, K., "On the Temperature Rise at the Tip of a Fast Running Crack", Journal of Mechanics and Physics of Solids, 22, pp. 127-133, (1974).

45. Levy, N. and Rice, J.R., "Local Heating by Plastic Deformation at a Crack Tip", Div. of Engineering, Brown University, Contract N00014-67-A-0191-0003, Tech. Report No. 1, (April 1968).

46. Dugdale, D.S., "Yielding of Steel Sheets Containing Slits", Journal of Mechanics and Physics of Solids, 8, pp. 100-104, (1960).

47. Yokobori, T. and Masabumi, T., "A Note on the Plastic Zone Size Ahead of the Propagating Fatigue Crack", Internation Journal of Fracture Mechanics, 2(3), pp. 564-566, (Sept. 1966).

48. Yokobori, T., Tachikawa, K. and Kamei, A., "On the Macroscopic and Microscopic Plastic Zones Ahead of Propagating Fatigue Cracks and Their Relation to the Propagation", Repcrts of the Research Institue of Strength and Fracture of Materials, Tohoku University, 6, pp. 1-17, (1970).

49. Tetleman, A.S. and McEvily, A.J., Fracture of Structural Materials, Wiley and Sons, New York, 1967.

50. Carslaw, H.S. and Jaeger, J.C., Conduction of Heat in Solids, Oxford University, London, 2nd Ed., 1959.

51. Adams, J.A. and Rogers, D.F., Computer-Aided Heat Transfer Analysis, McGraw-Hill, New York, 1973.

52. Kreith, F., Principles of Heat Transfer, Intext Educational Publishers, New York, 1973, pp. 219-231.

53. Love, T.J., Radiative Heat Transfer, Merrill, Columbus, Ohio, 1968, pp. 64-78.

54. Siegel, R. and Howell, J.R., Thermal Radiation Heat Transfer, McGraw-Hill, New York, 1972, pp. 170-228.

55. Hottel, H.C. and Sarofim, A.F., Radiative Transfer, McGraw-Hill, New York, 1967.

56. Lawson, W.D. and Sabey, J.W., "Infrared Techniques", Research Techniques in Nondestructive Testing, Academic Press, New York, 1970, pp. 443-479.

57. Manual on Fatigue Testing, ASTM STP 91, American Society for Testing Materials, Philadelphia, Pa., 1949.

58. Gubareff, G.G., Janssen, J.E. and Torborg, R.H., Thermal Radiation Properties Survey, Honeywell Research Center, Minneapolis, Minn., 1960, pp. 20-190.

59. Lerner, E.N., "Measurement of the Reflectivity of Human Skin in the 8 to 14 Micrometer Region Using a Rapid Scanning Infrared Camera", report in the School of Aerospace, Mechanical, and Nuclear Engineering, University of Oklahoma, (May 1971).

60. Hall, W.M., "Effect of Low Temperature on the Thermal Emittance of Three Black Paints; Comparison of Normal and Hemispherical Emittances", JPL Space Programs Summary, IV (37-31), Jet Propulsion Laboratory, California Institue of Technology, Pasadena, Calif.

61. Marin, J., Mechanical Behavior of Engineering Materials, Prentice-Hall, Englewood Cliffs, N.J., 1962.

62. Grover, H.J., "The Energy Required for Fatigue", Journal of Materials, 1(1), pp. 3-18, (March 1966).

63. Peterson, R.E., Stress Concentration Factors, Wiley and Sons, New York, 1974, p. 66.

64. Savin, G.N., Stress Concentration Around Holes, Pergamon Press, London, 1961.

65. Daniel, I.M. and Rowlands, R.E., "Determination of Strain Concentrations in Composites by Moire Techniques", Journal of Composite Materials, 5(2), pp. 250-254, (April 1971).

66. Jakob, M., Heat Transfer, vol. 1, Wiley and Sons, New York, 1950, p. 350.

67. Parker, J.D., Boggs, J.H. and Blick, E.F., Introduction to Fluid Mechanics and Heat Transfer, Addison-Wesley, Reading, Mass. 1970, p.292.

68. Gebhart, B., Heat Transfer, McGraw-Hill, New York, 1971, pp. 273-274

69. Holman, J.P., Heat Transfer, McGraw-Hill, New York, 1963, p. 264.

APPENDICES

APPENDIX A

CALIBRATION PROCEDURE

In order to obtain accurate temperatures from the information presented in a typical thermogram, it is necessary to calibrate the reference system used. In the Texas Instruments "ThermIscope" scanning infrared camera, an internally-generated gray scale provides the information required to convert shades of gray in the field of the thermogram to temperatures (^{o}F). However, it was found in using this instrument that there were two persistent sources of error in finding the temperatures directly from the scale. First, the temperatures indicated on the gray scale as the high and low temperatures covered in a thermogram were found to be incorrect. Second, once the correct temperatures were determined, the shades of gray corresponding to known temperatures were found to be slightly out of calibration.

In this study, a single heated resistor was used as a calibration temperature source to correct the errors above. By setting the thermograph on a low range ($1^{o}F$) it was possible to determine to what degree the indicated temperatures were incorrect. For example, if the indicated high temperature was $80^{o}F$, the reference source was set to be at

80°F also. Then, with the range of the thermograph set at 1°, the indicated temperature of the source was determined. If the indicated temperature were found now to be 78°F, it was concluded that the temperatures indicated were approximately 2° too low at that time. As a correction, the high and low temperatures were increased by 2° when finding temperatures from the gray scale.

The density of the reference source was later used to correct the densities on the gray scale also. Linear interpolation was used to determine the density of any temperature between the limits on the gray scale after the limits had been corrected. For example, if the corrected high temperature were 82°F and the low temperature 72°F, and the optical densities of the high and low indications were 1.00 and 0.0 respectively, the optical density of 77° would be 0.50. If the reference source were at 77° also, and its density measured 0.45, a correction of -0.05 would have to be added to the densities of the gray scale in order to obtain true temperatures from the thermogram.

It was found by comparing this procedure to other reference sources that the scale was generally out of calibration by the same amount at both the high and low extremes of the range in a given thermogram. Thus, correction of the entire scale using the data from one point was possible. It was also found, however, that the miscalibration changed from one thermogram to the next even without changing the settings

on the thermograph. Hence, it was necessary to use this calibration procedure on each thermogram evaluated for temperatures using the densitometer.

Other methods of calibration are available. All include a known temperature or temperatures in the field of the thermogram. The primary advantages of the procedure developed for use in this study are that the single reference source could be adjusted to fall within the range of any thermogram in this study, and the reference responded to changes rather quickly. The latter point was important in keeping up with the rapid changes in maximum temperature which occurred on the fatigue specimens near the end of a test.

APPENDIX B

STRESS-STRAIN DATA FOR MILD STEEL

The material used for the double-notched steel fatigue specimens discussed in Chapter V displayed unusual material behavior in the initial tension tests performed to determine the material properties. The yield stress was low, no double yield point was evident, and the modulus of elasticity was lower than normally observed for mild steel. In light of these results, a number of additional tension tests were performed at various times and with various equipment in order to establish whether the material properties were indeed those first determined.

A Riehle testing machine was used for most of the tests. Specimens of different widths and reduced-section lengths were used. Strain data were obtained using both strain gages and a mechanical extensometer to give values throughout the range of interest in this study. The data obtained from these tests are plotted in Fig. 81. Data from strain gages and extensometers are identified separately. As can be seen in the figure, these data complement each other quite well in the overlapping region.

Since the data still indicated low mechanical properties for the material, further tests were conducted using an Instron tension testing machine. Data were available from these tests in the form of strain gage readings and strain readings reduced from an extensometer. These data are also plotted in Fig. 81. As can be seen, the agreement in the data is again excellent.

The absence of upper and lower yield points in a steel loaded uniaxially suggests that it is not virgin material, but has been subjected to some prior stressing.

Based on the large number of tests, performed on different equipment, it must be concluded that the mechanical properties for the mild steel which were originally determined were in fact accurate. These properties are then used with confidence in Chapter V.

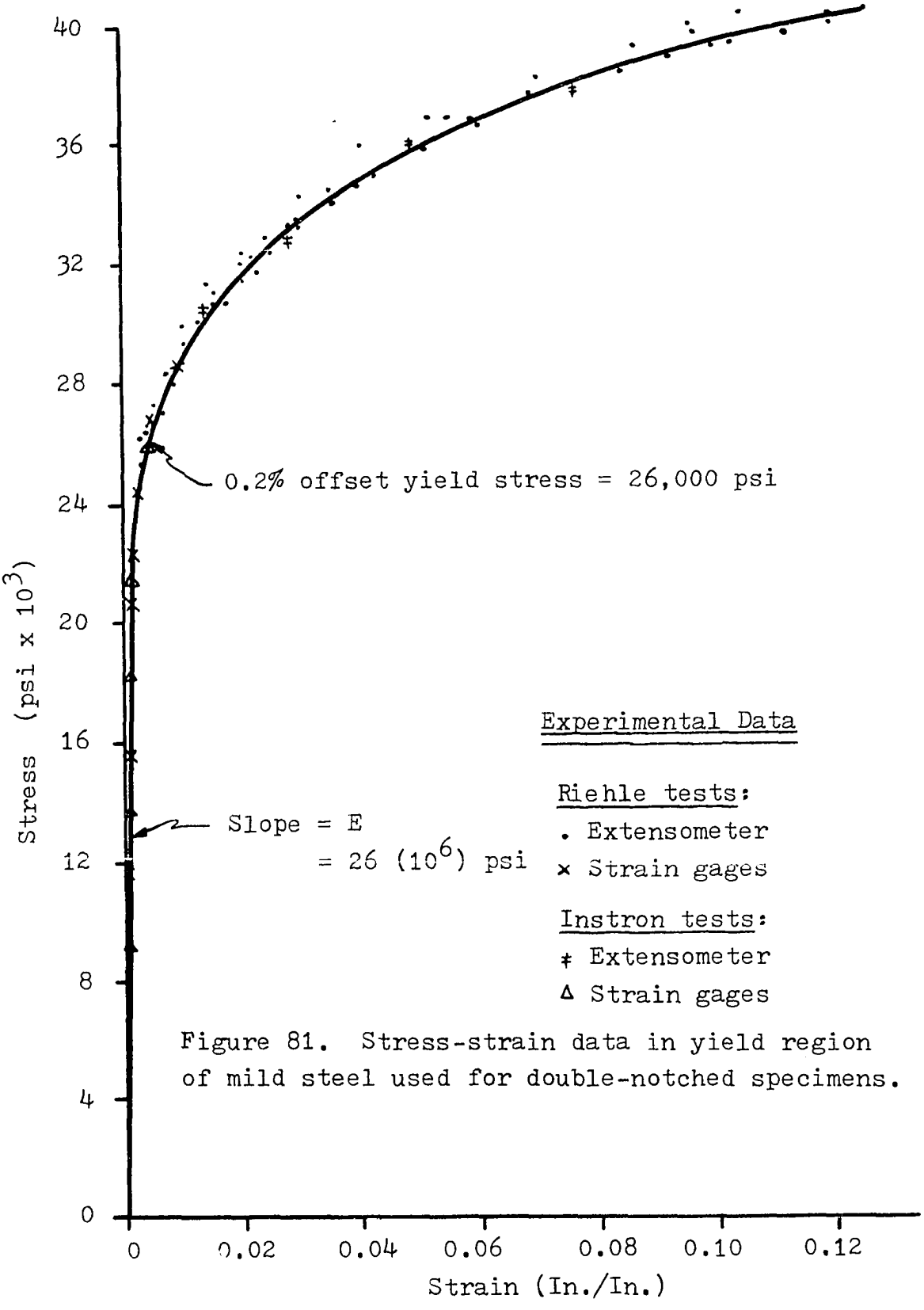

Figure 81. Stress-strain data in yield region of mild steel used for double-notched specimens.

APPENDIX C

COMPUTER PROGRAMS

Included in this appendix are listings of three computer programs used in the analysis of the heat transfer problems associated with energy dissipation in fatigue specimens. The programs are listed as used on an IBM 370 digital computer.

The first program listed (TEMPROF) utilizes a finite difference approach to find steady-state temperature rises on the surface of rectangular fatigue specimens. Heat generations Q(I,J) are allowed at any nodes in the grid for the specimen. Options included in the program include variable heat transfer coefficients from the vise (HV) to the crank (HC) with any order of variation specified (KONVOP), variable boundary conditions (NDOP), and the addition of extra convective heat loss (HAD) for the study of enhancement possibilities. The nodal equations used for the model are given in Chapter VI. Comment statements in the listing indicate the structure of the program.

The second program listed is based on TEMPROF but includes the transient behavior as noted in Chapter VI. This program (TRANTEMP) omits several of the options inclu-

ded in the steady-state program. Only one heat generation is used and boundary conditions are constant temperature ends. The time interval for the forward-stepping solution is governed by the convergence criterion established in Chapter IV. As can be seen from the listing, the lack of several options in the program results in a much shorter program than TEMPROF.

Finally, TRIPROF is a program using finite difference methods to determine the steady-state response of the surface temperatures on a triangular fatigue specimen. The specimen experiences a uniform heat generation throughout (QI), but includes the option of specifying different rates of heat generation at other nodes (QG at IG,JG). Also included in this program are options for the convective heat transfer coefficient distribution (KONVOP) and boundary conditions (NDOP) as were seen in TEMPROF previously. The nodal equations for the specimen and the specimen geometry are discussed in Chapter VI. A plotting routine is included which gives a printed graph of the centerline temperatures on the specimen for each case. Numerous comment statements in the program explain the structure of the program.

```
      $JOB
      C
      C    TEMPROF PROGRAM FOR COMPUTING THE TEMPERATURE DISTRIBUTION ON A
      C    RECTANGULAR FATIGUE SAMPLE.   GENERATIONS ARE INPUT AT ANY NODES.
      C    BOTH CONVECTIVE AND RADIATIVE LOSSES ARE INCLUDED.  THE CONVECTIVE
      C    COEFFICIENT CAN VARY FROM VISE TO CRANK ON THE SAMPLE.
      C    MAXIMUM SIZE OF ARRAY IS 21 BY 50 NODES OF SIZE DY BY DX.
      C
 1          DIMENSION T(21,50),TOLD(21,50),U(21,50),THETA(21,50)
 2          DIMENSION Q(21,50),HT(21,50),H(21,50),GRAD(4),TITLE(50)
      C
      C    INPUT DATA IS AS FOLLOWS...
      C       NCASE = NO. OF CASE TO BE RUN
      C       TITLE = 50 SPACES FOR TITLE OF CASE
      C       CON = THERMAL CONDUCTIVITY OF MATERIAL
      C       B = MATERIAL THICKNESS
      C       RT = ROOM TEMPERATURE IN DEG. F
      C       ACC = ACCURACY REQUIRED FOR CONVERGENCE
      C       TMAX = ESTIMATION OF MAXIMUM TEMPERATURE ON THE MATERIAL
      C       IMAX,JMAX = LOCATION OF TMAX IN ARRAY
      C       KONVOP = ORDER OF VARIATION OF CONVECTIVE COEFFICIENT
      C                FROM VISE TO CRANK (1,2, OR 3)
      C       HV,HC = CONVECTIVE COEFFICIENTS AT VISE AND CRANK ENDS
      C       NDOP = TYPE OF BOUNDARY CONDITION TO USE...
      C            1 = BOTH END TEMPERATURES (DEG. F) ARE KNOWN
      C            2 = BOTH END GRADIENTS KNOWN (DEG. F/IN)
      C            3 = VISE TEMPERATURE KNOWN, CRANK GRAD KNOWN
      C            4 = CRANK END TEMP KNOWN, VISE GRAD KNOWN
      C       TV,TC = END CONDITIONS AS LISTED ABOVE FOR ANY NDOP
      C       IN,JN = SIZE OF ARRAY DESIRED
      C       DX,DY = DIMENSIONS (IN) OF ELEMENTS IN ARRAY
      C       NOGENS = NUMBER OF GENERATION POINTS USED
      C       I,J = LOCATION OF GENERATION POINT
      C       Q(I,J) = STRENGTH OF GENERATION (BTU/HR) AT I,J
      C       NOCEL = OPTION FOR DELETING CELSIUS OUTPUT (0 = DELETE)
      C       NOFAR = OPTION FOR DELETING FARENHEIT OUTPUT (0 = DELETE)
      C       NDJ = WIDTH OF STRIP OF LOCALLY ALTERED H'S
      C       JCEN = CENTER OF ALTERED COEFFICIENT STRIP
      C       IMAXH = MAXIMUM VALUE OF I FOR ALTERED H'S
      C       HAD = LOCAL VALUE OF CONVECTIVE COEFFICIENT SPECIFIED
 3          READ (5,400) NCASE
 4      400 FORMAT (I2)
 5          DO 410 NCT=1,NCASE
 6          READ (5,990) (TITLE(I),I=1,50)
 7      990 FORMAT (50A1)
 8          READ (5,900) CON,B,RT,ACC,TMAX,IMAX,JMAX
 9      900 FORMAT (5E10.0,2I5)
10          READ (5,910) KONVOP,HV,HC
11      910 FORMAT (I1,9X,2E10.0)
12          READ (5,910) NDOP,TV,TC
13          READ (5,915) IN,JN,DX,DY
14      915 FORMAT (2I5,2E10.0)
15          INP=IN+1
16          INM=IN-1
17          JNM=JN-1
18          SJNM=JNM
19          WINM=INM
20          WIDTH=DY*WINM
21          SLEN=DX*SJNM
22          BETA=B/12.
```

```
      X=DX/12.
      Y=DY/12.
      SIGMA=5.1714E-08
      GV=TV*DX
      GC=TC*DX
      RTR=RT+460.
      TMAXR=TMAX+RTR
      TVR=TV+460.
      TCR=TC+460.
      R= X*Y
      S=CON*RFT
      K1=JMAX-1
      CD=K1
      K3=JN-JMAX
      CC=K3
C
C   ALL TEMPERATURE ARRAYS AND THE Q ARRAY ARE INITIALIZED
C   THE TEMPERATURE IS ASSUMED LINEAR FROM EACH END TO TMAX AT JMAX.
C
      DO 2 J=1,JN
      K=J-1
      C=K
      DO 4 I=1,IN
      Q(I,J)=0.
      IF (J.GT.JMAX) GO TO 6
      T(I,J)=TMAX*(C/CD)+RTR
      GO TO 8
    6 T(I,J)=TMAXR-((C-CD)/CC)*TMAX
    8 U(I,J)=T(I,J)
      TOLD(I,J)=T(I,J)
    4 H(I,J)=HV+((C/SJNM)**KONVOP)*(HC-HV)
    2 CONTINUE
C
C   LOCALLY CHANGE CONVECTIVE COEFFICIENT IF DESIRED.
C
      READ (5,3) NOJ, IMAXH,JCEN
    3 FORMAT (I2,8X,I2,8X,I2)
      IF (NOJ.LT. 1) GO TO 9
      DO 1 K=1,NOJ
      READ (5,5) J, HAD
    5 FORMAT (I2,8X,F10.0)
      DO 1 I=1,IMAXH
    1 H(I,J)=HAD
    9 CONTINUE
C
C   READ IN THE GENERATION POINTS AND STRENGTHS
C
      READ (5,920) NOGENS
      DO 10 K=1,NOGENS
   10 READ (5,925) I,J,Q(I,J)
  925 FORMAT (2I5,F10.0)
      READ (5,920) NOCEL,NOFAR
  920 FORMAT (I1,4X,I1)
      L=0
C
C   BEGIN ITERATIONS.   USE LIEBMANN METHOD.
C
   12 L=L+1
C
C   THE RADIATIVE COEFFICIENT IS CALCULATED AND USED TO GET THE
```

```
      C   TOTAL H.T. COEFFICIENT AT EACH NODE.
      C
   68       DO 14 I=1,IN
   69       DO 15 J=1,JN
   70       HRAD=SIGMA*(T(I,J)**2+RTR**2)*(T(I,J)+RTR)
   71    15 HT(I,J)=HRAD + H(I,J)
   72    14 CONTINUE
      C
      C   CALCULATE NEW TEMPERATURES AT THE ENDS USING GIVEN B.C'S.
      C
   73       IF (NOOP-2) 16,18,20
   74    16 DO 22 I=1,IN
   75       U(I,1)=TVR
   76    22 U(I,JN)=TCR
   77       GO TO 30
   78    18 DO 24 I=1,IN
   79       U(I,1)=T(I,2)-GV
   80    24 U(I,JN)=T(I,JNM)+GC
   81       GO TO 30
   82    20 IF (NOOP.GT.3) GO TO 28
   83       DO 26 I=1,IN
   84       U(I,1)=TVR
   85    26 U(I,JN)=T(I,JNM)+GC
   86       GO TO 30
   87    28 DO 29 I=1,IN
   88       U(I,1)=T(I,2)-GV
   89    29 U(I,JN)=TCR
   90    30 DO 32 I=1,IN
   91       T(I,1)=U(I,1)
   92    32 T(I,JN)=U(I,JN)
      C
      C   CALCULATE NEW TEMPERATURES AT EDGE NODES.
      C
   93       DO 34 J=2,JNM
   94       U(1,J)=(Q(1,J)*P/S +HT(1,J)*P*X/S*RTR*2.*(Y/2.+BFT)+4.*X*X*T(2,J)
           1 +Y*Y*(T(1,J+1)+T(1,J-1)))/(4.*X*X+2.*Y*Y+2.*P*X/S*HT(1,J)*
           2 (Y/2.+BFT))
   95       U(IN,J)=(Q(IN,J)*P/S+HT(IN,J)*P*X/S*RTR*2.*(Y/2.+BFT)+4.*X*X*
           1 T(INM,J)+Y*Y*(T(IN,J+1)+T(IN,J-1)))/(4.*X*X+2.*Y*Y+
           2 2.*P*X/S*HT(IN,J)*(Y/2.+BFT))
   96       T(IN,J)=U(IN,J)
   97       T(1,J)=U(1,J)
      C
      C   CALCULATE NEW TEMPERATURES AT ALL INTERIOR NODES.
      C
   98       DO 36 I=2,INM
   99       U(I,J)=(Q(I,J)*P/S+HT(I,J)*P*P/S*RTR+Y*Y*(T(I,J-1)+T(I,J+1))+
           1 X*X*(T(I-1,J)+T(I+1,J)))/(HT(I,J)*P*P/S+2.*(X*X + Y*Y))
  100    36 T(I,J)=U(I,J)
  101    34 CONTINUE
      C
      C   FIND MAXIMUM DIFFERENCE
      C
  102       D=0.
  103       DO 38 I=1,IN
  104       DO 40 J=1,JN
  105       DU = ABS(U(I,J)-TOLD(I,J))
  106       IF (DU.LT.D) GO TO 40
  107       D=DU
  108    40 CONTINUE
```

```
      39 CONTINUE
C
C   CHECK AGAINST INPUT ACCURACY.   IF OK, GO TO OUTPUT.  IF NOT,
C   GO BACK AND TRY AGAIN.
C
        IF (D.LT.ACC) GO TO 42
        DO 44 I=1,IN
        DO 46 J=1,JN
   46 TOLD(I,J)=U(I,J)
   44 CONTINUE
        GO TO 12
   42 DO 48 I=1,IN
        DO 50 J=1,JN
        THETA(I,J)=U(I,J)-RTR
        T(I,J)=U(I,J)-460.
   50 U(I,J)=(T(I,J)-32.)*5./9.
   48 CONTINUE
C
C   OUTPUT DATA CONSISTS OF INPUT PLUS TEMPERATURES.  BOTH
C   FAHRENHEIT AND CELSIUS OUTPUT MAY BE BLANKED IF DESIRED (NOCEL,
C   NOFAR = 0).
        WRITE (6,940) (TITLE(I),I=1,50)
  940 FORMAT (1H1,5X,'FINITE DIFFERENCE RESULTS FOR ',50A1)
        WRITE (6,941)
  941 FORMAT (1X,'**************************************************
     1**********************************',//)
        WRITE (6,945)
  945 FORMAT (5X,'GENERATION POINTS AND STRENGTHS.....')
        WRITE (6,950)
  950 FORMAT (10X,'I',9X,'J',9X,'Q(I,J)')
        DO 190 I=1,IN
        DO 200 J=1,JN
        IF (Q(I,J)) 200,200,210
  210 WRITE (6,955) I,J,Q(I,J)
  955 FORMAT (9X,I2,8X,I2,8X,F6.2)
  200 CONTINUE
  190 CONTINUE
        WRITE (6,942)
  942 FORMAT (1X,/)
        WRITE (6,570) CON,HV,HC
  570 FORMAT (5X,'CONDUCTIVITY = ',F6.1,5X,'H(VISE) = ',F6.2,5X,
     1'H(CRANK) = ',F6.2,/)
        IF (KONVOP-2)  412,413,414
  412 WRITE (6,584)
  584 FORMAT (9X,'A LINEAR DISTRIBUTION OF H WAS ASSUMED.',/)
        GO TO 587
  413 WRITE (6,588)
  588 FORMAT (9X,'A SECOND ORDER DISTRIBUTION FOR H WAS ASSUMED.',/)
        GO TO 587
  414 WRITE (6,586)
  586 FORMAT (9X,'A THIRD ORDER DISTRIBUTION FOR H WAS ASSUMED.',/)
  587 IF (NOJ.LT.1) GO TO 589
        WRITE (6,61) IMAX,JCEN
   61 FORMAT (9X,'CONVECTIVE COEFFICIENT LOCALLY INCREASED FROM I=1 TO '
     1,I3,/,9X,'CENTERED ABOUT J=',I3,'.',/)
        WRITE (6,62) NOJ,H(IMAX,JCEN)
   62 FORMAT (9X,'WIDTH OF STRIP = ',I2,'.  H(CENTER) =',F6.2,/)
  589 WRITE (6,583) B,RT
  583 FORMAT (5X,'MAT. THICKNESS = ',F6.3,' IN',5X,'ROOM T = ',F6.1,/)
        WRITE (6,590)
```

```
      590 FORMAT (20X,'...END CONDITIONS...')
          WRITE (6,596)
      596 FORMAT (8X,'T(V)',8X,'T(C)',6X,'GRAD(V)',6X,'GRAD(C)',/)
          IF (NDOP-2) 380,381,382
      380 WRITE (6,591) TV,TC
      591 FORMAT (5X,F7.2,5X,F7.2,/)
          GO TO 389
      381 WRITE (6,592) TV,TC
      592 FORMAT (20X,F8.2,5X,F8.2,/)
          GO TO 389
      382 IF (NDOP-4) 383,384,384
      383 WRITE (6,593) TV,TC
      593 FORMAT (4X,F7.2,29X,F8.2,/)
          GO TO 389
      384 WRITE (6,594) TC,TV
      594 FORMAT (17X,F7.2,5X,F8.2,/)
      389 WRITE (6,972) WID, SLEN
      972 FORMAT (5X,'SPECIMEN WIDTH =',F6.2,' IN     LENGTH =',F7.2,' IN',
         1/)
          WRITE (6,100) DX,DY
      100 FORMAT (5X,'ELEMENT SIZE = ',F6.3,' BY ',F6.3,' INCHES.',/)
          WRITE (6,942)
          WRITE (6,990)
          WRITE (6,942)
      990 FORMAT (/,5X,'TEMPERATURE ABOVE ROOM TEMPERATURE (DEG F)...')
          WRITE (6,941)
          DO 230 J=1,JN
          WRITE (6,985) (THETA(INP-I,J),I=1,IN)
      230 CONTINUE
      985 FORMAT (////,1X,21F6.2)
          WRITE (6,942)
          WRITE (6,975) ACC, L
      975 FORMAT (///,5X,'ACCURACY WITHIN ',F7.4,' DEGREES REQUIRED ',
         1I4,' ITERATIONS.',/)
          IF (NOFAR.LT.1) GO TO 110
          WRITE (6,940) (TITLE(I),I=1,50)
          WRITE (6,980) RT
      980 FORMAT (//,5X,'FAHRENHEIT TEMPERATURES...',10X,'ROOM TEMP. =',
         1F6.2,' F',/)
          WRITE (6,941)
          DO 220 J=1,JN
          WRITE (6,985) ( T(INP-I,J),I=1,IN)
      220 CONTINUE
      110 IF (NOCEL.LT.1) GO TO 120
          WRITE (6,940) (TITLE(I),I=1,50)
          RC = (RT-32.)*5./9.
          WRITE (6,1000) RC
     1000 FORMAT (//,5X,'CELSIUS TEMPERATURES...',10X,'ROOM TEMP=',F6.2,
         1' C',/)
          WRITE (6,941)
          DO 122 J=1,JN
          WRITE (6,985) (U(INP-I,J),I=1,IN)
      122 CONTINUE
C
C   CALCULATE TEMPERATURE GRADIENTS AT ALL POINTS OF HEAT GENERATION.
C   IF POINT IS ON EDGE, LET THE OUTWARD GRADIENT BE ZERO.
C
      120 WRITE (6,655)
      655 FORMAT (1H1,//,5X,'TEMPERATURE GRADIENTS AT GENERATION POINTS  (DE
         1G/IN.) ...',//)
```

```
      WRITE (6,941)
      WRITE (6,660)
  660 FORMAT (3X,'I',5X,'J',10X,'N',10X,'E',10X,'S',10X,'W',8X,'THETA(I,
     1J)',/)
      DO 600 I=1,IN
      DO 610 J=1,JN
      IF (O(I,J)) 610,610,630
  630 IF(I-1) 300,300,310
  300 GRAD(1)=0.0
      GRAD(2)=(T(I,J)-T(I,J+1))/DX
      GRAD(3)=(T(I,J)-T(I+1,J))/DY
      GRAD(4)=(T(I,J)-T(I,J-1))/DX
      GO TO 350
  310 IF (I-IN) 320,330,330
  330 GRAD(3)=0.0
      GRAD(4)=(T(I,J)-T(I,J-1))/DX
      GRAD(1)=(T(I,J)-T(I-1,J))/DY
      GRAD(2)=(T(I,J)-T(I,J+1))/DX
      GO TO 350
  320 GRAD(1)=(T(I,J)-T(I-1,J))/DY
      GRAD(2)=(T(I,J)-T(I,J+1))/DX
      GRAD(3)=(T(I,J)-T(I+1,J))/DY
      GRAD(4)=(T(I,J)-T(I,J-1))/DX
  350 WRITE (6,650) I,J,(GRAD(K),K=1,4),THETA(I,J)
  650 FORMAT (2X,I2,4X,I2,3X,4F11.3,5X,F7.2)
  610 CONTINUE
  600 CONTINUE
      WRITE (6,942)
      WRITE (6,941)
  410 CONTINUE
      STOP
      END

C$/
C$/
```

```
      $JOB
1           DIMENSION TO(8,20),TN(8,20),TITLE(50)
      C
      C     "TRANTMP2" - JOHN A. CHARLES, JANUARY 22, 1976.
      C
      C     TRANTMP2 UTILIZES THE SCHEME OF "TRANTEMP", BUT ALLOWS
      C     FOR THE HEAT GENERATION RATE TO VARY IN TIME.  THE
      C     ORDER OF THE VARIATION IS SPECIFIED BY THE USER.
      C     SOLUTION IS BY FINITE DIFFERENCE, FORWARD STEP, WITH THE TIME
      C     INTERVAL GOVERNED BY THE CONVERGENCE CRITERION.
      C     PRESENTLY SET UP FOR A 6 BY 19 SQUARE GRID,WITH HEAT GENERATION
      C     AT NODE (2,9), INSULATED AT SIDES I=1 AND I=6, AND CONSTANT
      C     THETA (=ZERO) AT J=1 AND J=18.
      C       INPUT VARIABLES...
      C       TITLE = 50 SPACES FOR TITLE
      C       CON = THERMAL CONDUCTIVITY OF MATERIAL (BTU/H-FT-F)
      C       B = THICKNESS OF SLAB (IN)
      C       RHO = DENSITY OF MATERIAL (LBM/FT**3)
      C       C = SPECIFIC HEAT OF MATERIAL (BTU/LBM-F)
      C       DX = SQUARE GRID SIZE (IN)
      C       HT = TOTAL HEAT TRANSFER COEFFICIENT (BTU/H-FT**2-F)
      C       QT = TOTAL HEAT GENERATION RATE (BTU/HR)
      C       TLIM = LIMIT OF TIME FOR PROGRAM TO COMPUTE (MIN)
      C       NOSTP = NUMBER OF ITERATIONS BETWEEN EACH LINE OF OUTPUT
      C       TSTDY = TIME AT WHICH GENERATION IS TO REACH FINAL VALUE
      C                (GENERATION IS MAINTAINED CONSTANT THEREAFTER)
      C       ORD = ORDER OF GENERATION VARIATION IN TIME
      C     READ INPUT DATA, COMPUTE PARAMETERS, WRITE VARIABLES.
      C
2           READ  (5,1) (TITLE(I),I=1,50)
3         1 FORMAT (50A1)
4           READ (5,2) CON,B,RHO,C
5         2 FORMAT (4F10.0)
6           READ (5,3) DX,HT,QT
7         3 FORMAT (3F10.0)
8           READ (5,4) TLIM, NOSTP
9         4 FORMAT (F10.0,I2)
10          READ (5,17) TSTDY, ORD
11       17 FORMAT (2F10.0)
12          QT=(RHO*C)/(4.*CON/(DX/12.)**2+2.*HT/(B/12.))
13          VOL=((DX**2)*B)/(12.**3)
14          Q=QT/VOL
15          DTS=QT*3600.
16          A=DT*CON/(RHO*C*(DX**2))*144.
17          WRITE (6,940) (TITLE(I),I=1,50)
18      940 FORMAT (1H1,2X,50A1)
19          WRITE (6,950) CON, RHO, C
20      950 FORMAT (//,2X,'K=',F6.1,'  RHO=',F7.2,'  C=',F6.2,/)
21          WRITE (6,960) QT, HT
22      960 FORMAT (2X,'QDOT =',F6.2,5X,'H(TOTAL) =',F5.1,/)
23          WRITE (6,970) DX,DTS
24      970 FORMAT (2X,'DX=DY=',F6.3,5X,'DT =',F7.4,' SEC.',/ )
25          WRITE (6,977) TSTDY
26      977 FORMAT (2X,'TIME FOR CONST. Q =',F4.1,/)
27          WRITE (6,975) ORD
28      975 FORMAT (2X,'ORDER OF Q VARIATION =',F4.1,//)
29          WRITE (6,980)
30      980 FORMAT  (5X,'TIME(MIN.)',5X,'Q(TOTAL)',5X,'THETA(MAX)',/)
      C
      C     INITIALIZE TIME AND TO MATRIX BOTH TO ZERO.
```

```
      C
   31         T=0.
   32         DO 5 I=1,6
   33         DO 6 J=1,18
   34       6 TO(I,J)=0.0
   35       5 CONTINUE
      C
      C    BEGIN ITERATIONS.  K COUNTS ITERATIONS BETWEEN
      C    EACH LINE OF OUTPUT.  COMPUTE MATRIX TN OF NEW
      C    TEMPERATURES FOR ALL NODES USING FINITE DIFFERENCE
      C    SCHEME.
      C    HEAT GENERATION RATE IS CHANGED AT EACH INTERVAL
      C    UNTIL TSTDY IS REACHED
      C
   36       7 K=1
   37       8 T=T+DT
   38         DO 9 I=1,6
   39         TN(I,1)=TO(I,1)
   40       9 TN(I,18)=TO(I,18)
   41         TMIN=T*60.
   42         IF (TMIN.GT.TSTDY) GO TO 27
   43         QTIME=Q*(1.-(1.-(T*60.)/TSTDY)**PRD)
   44         GO TO 25
   45      27 QTIME = Q
   46      25 TN(2,9)=A*(TO(2,8)+TO(2,10)+TO(1,9)+TO(3,9))+QTIME*DT/(RHO*C)
   47         DO 10 J=2,17
   48         TN(1,J)=A*(TO(1,J-1)+TO(1,J+1)+2.*TO(2,J))
   49      10 TN(6,J)=A*(TO(6,J-1)+TO(6,J+1)+2.*TO(5,J))
   50         DO 11 I=2,5
   51         DO 12 J=2,8
   52      12 TN(I,J)=A*(TO(I-1,J)+TO(I+1,J)+TO(I,J-1)+TO(I,J+1))
   53         DO 23 J=10,17
   54      23 TN(I,J)=A*(TO(I-1,J)+TO(I+1,J)+TO(I,J-1)+TO(I,J+1))
   55         IF (I.EQ.2) GO TO 11
   56         TN(I,9)=A*(TO(I,8)+TO(I,10)+TO(I-1,9)+TO(I+1,9))
   57      11 CONTINUE
      C
      C    RESET TO MATRIX FOR NEXT ITERATION.
      C
   58         DO 13 I=1,6
   59         DO 14 J=1,18
   60      14 TO(I,J)=TN(I,J)
   61      13 CONTINUE
      C
      C    CHECK IF TIME TO PRINT, AND IF LIMIT OF PROBLEM
      C    HAS BEEN REACHED.  PRINT IF NECESSARY.  RETURN
      C    FOR NEXT ITERATION IF TIME LIMIT NOT EXCEEDED.
      C    IF OVER TIME LIMIT, STOP EXECUTION.
      C
   62         IF(K.LT.NOSTP) GO TO 15
   63         QTT=QTIME*VOL
   64         WRITE (6,999) TMIN,QTT,TN(2,9)
   65     999 FORMAT (5X,F7.3,8X,F8.5,5X,F8.3)
   66         GO TO 7
   67      15 IF (TMIN.GT.TLIM) GO TO 16
   68         K=K+1
   69         GO TO 8
   70      16 WRITE (6,990) TMIN,QTT,TN(2,9)
   71         STOP
   72         END
```

```
      C   TRIPROF PROGRAM FOR TEMPERATURE DISTRIBUTION ON SURFACE OF TRIANGULAR
      C   FATIGUE SPECIMEN.   SPECIMEN HAS BEEN DIVIDED DOWN CENTERLINE
      C   USING SYMMETRY CONDITIONS.  SOLUTION IS BY FINITE DIFFERENCES.
      C   LIEBMANN ITERATION TECHNIQUE IS USED FOR THE SOLUTION.
      C
    1       DIMENSION IG(100),JG(100),QG(100),A(4),TITLE(50),T(11,31),U(11,31)
    2       DIMENSION H(11,31),HT(11,31),THETA(11,31),Q(11,31),TOLD(11,31)
    3       DIMENSION AA(70)
      C
      C   INPUT DATA IS AS FOLLOWS...
      C     NTRI = NUMBER OF TRIANGULAR CASES TO BE RUN
      C     TITLE = 50 SPACES FOR TITLE OF CASE
      C     CON = CONDUCTIVITY OF SPECIMEN
      C     B = MATERIAL THICKNESS (IN.)
      C     QI = UNIFORM SPECIFIC GENERATION ON SPECIMEN (BTU/HR-FT**3)
      C     RT = ROOM TEMPERATURE (FARENHEIT)
      C     ACC = DESIRED ACCURACY CRITERION
      C     TMAX = GUESS AT MAXIMUM TEMP ON SPECIMEN
      C     JMAX = LOCATION ALONG LENGTH OF TMAX
      C     KONVOP = ORDER OF H VARIATION FROM VISE TO CRANK (1, 2, OR 3)
      C     HV,HC = CONVECTIVE COEFFICIENTS AT VISE AND CRANK ENDS
      C     NOOP = B.C. OPTION...1 = END TEMPS KNOWN, 2 = GRADIENTS KNOWN,
      C        3 = VISE TEMP AND CRANK GRAD, 4 = OPPOSITE OF 3
      C     TV,TC = VISE AND CRANK END CONDITIONS FOR ANY NOOP
      C     IPLOT = OPTION TO CALL PLOT SUBROUTINE FOR CENTERLINE
      C        TEMPERATURES (1 = YES, 2 = NO)
      C     NOCASE = CASE NUMBER (TO BE PUT AT TOP OF PLOT)
      C     NOGENS = NUMBER OF POINTS WHERE GENERATION OTHER THAN QI SPECIFIED
      C     IG,JG = LOCATION OF SPECIAL GENERATION
      C     QG = STRENGTH OF SPECIAL GENERATOR
      C
    4       READ (5,520) NTRI
    5       DO 370 NCTY=1,NTRI
      C
      C   READ IN TITLE, PROPERTIES, AMBIENT CONDITIONS, DESIRED ACCURACY
      C   SET GEOMETRIC VARIABLES
      C
    6       READ (5,500) (TITLE(I),I=1,50)
    7   500 FORMAT (50A1)
    8       READ (5,510) CON,B,QI,RT,ACC,TMAX,JMAX
    9   510 FORMAT (6E12.0,I2)
   10       READ (5,550) KONVOP,HV,HC
   11       READ (5,550) NOOP,TV,TC
   12   550 FORMAT (I1,9X,2E10.0)
   13       READ (5,501) IPLOT,NOCASE
   14       IWIDE=70
   15   501 FORMAT (I1,4X,I3)
   16       DL=0.1/12.
   17       TVR=TV+460.
   18       TCR=TC+460.
   19       RTR = RT +460.
   20       SIGMA = 0.1714E-08
   21       DET =B/12.
   22       Y=CON*DET
   23       Z=DL**2/Y
   24       X=2*DET
   25       TR = .125
   26       CR=.992277877
   27       A(1)=1.0
```

```
      A(2)=.75
      A(3)=.50
      A(4)=.25
      HD =(HC-HV)/30.
      GV=TV*.20
      GC=TC*.20
      TMAXR=RTR+TMAX
      K1=JMAX-1
      CD=K1
      K3=31-JMAX
      CC=K3
C
C   INITIALIZE Q, T AND U ARRAYS.  USE A LINEAR APPROXIMATION TO THE
C   POSSIBLE TEMPERATURE DISTRIBUTION BETWEEN ZERO AT THE ENDS,
C   AND TMAX (GUESSED) AT JMAX.
C   THE CONVECTIVE COEFFICIENT IS TAKEN AS A LINEAR VARIATION
C   BETWEEN THE WISE AND CRANK COEFFICIENTS IF KONVOP = 1.
C   PARABOLIC VARIATIONS ARE ASSUMED IF KONVOP = 2 , AND A THIRD ORDER
C   VARIATION IF KONVOP = 3.
C
      DO 10 J=1,31
      K=J-1
      C=K
      DO 30 I=1,11
      Q(I,J)=QI
      IF (J-JMAX) 1000,1000,1050
 1000 T(I,J)=TMAX*(C/CD)+RTR
      GO TO 1100
 1050 T(I,J)=TMAXR-((C-CD)/CC)*TMAX
 1100 U(I,J)=T(I,J)
      TOLD(I,J)=T(I,J)
      IF (KONVOP-2) 21,22,23
   21 H(I,J)=HV+(C*HD)
      GO TO 30
   22 H(I,J)=HV+((C/30.)**2.)*(HC-HV)
      GO TO 30
   23 H(I,J)=HV+((C/30.)**3.)*(HC-HV)
   30 CONTINUE
   10 CONTINUE
C
C   READ IN THE NUMBER OF EXTRA GENERATORS, FOLLOWED BY THE
C   POINTS AND THE GENERATION AT THOSE POINTS
C   THE EXTRA GENERATION IS INSTEAD OF THE QI UNIFORM GENERATION.
C   IF NOGENS=0, THEN GENERATION WILL BE UNIFORM.
C
      READ (5,520) NOGENS
  520 FORMAT (I2)
      IF (NOGENS) 30,30,40
   40 DO 50 N=1,NOGENS
      READ (5,530) IG(N),JG(N),QG(N)
  530 FORMAT (2I5,F10.0)
      I=IG(N)
      J=JG(N)
   50 Q(I,J)=QG(N)
   30 L=0
C
C   BEGIN ITERATION ON NODAL EQUATIONS TO FIND TEMPERATURE
C   DISTRIBUTION.  L IS THE NUMBER OF THE ITERATION.
C   THE T ARRAY IS THE OLD TEMPS, U ARE THE NEW ONES.
C
```

```
      60 L=L+1
C
C   THE RADIATIVE H.T. COEFFICIENT IS COMPUTED FOR THE OLD ARRAY,
C   AND USED TO FIND THE TOTAL H.T. COEFFICIENT, HT(I,J).
C
         DO 90 I=1,11
         DO 100 J=1,31
         HRAD=SIGMA*(T(I,J)**2+RTR**2)*(T(I,J)+RTR)
  100 HT(I,J)=H(I,J)+HRAD
   90 CONTINUE
C
C   END CONDITIONS MAY BE SPECIFIED TO BE CONSTANT TEMPERATURES (NDOP=1),
C   KNOWN TEMPERATURE GRADIENTS (NDOP=2), OR COMBINATIONS OF THE TWO
C   (NDOP=3 HAS LEFT TEMP KNOWN AND RIGHT GRADIENT, NDOP=4 IS THE OPPOSITE).
C
         IF (NDOP-2) 61,62,63
   61 DO 65 I=1,11
   65 U(I,1)=TVP
         U(9,31)=TCP
         U(10,31)=TCR
         U(11,31)=TCR
         GO TO 71
   62 DO 64 I=1,11
   64 U(I,1)=T(I,2)-GV
         U(9,31)=GC+T(9,30)
         U(10,31)=GC+T(10,30)
         U(11,31)=GC+T(11,30)
         GO TO 70
   63 IF (NDOP-3) 67,67,66
   67 DO 68 I=1,11
   68 U(I,1)=TVP
         U(9,31)=GC+T(9,30)
         U(10,31)=GC+T(10,30)
         U(11,31)=GC+T(11,30)
         GO TO 70
   66 DO 69 I=1,11
   69 U(I,1)=T(I,2)-GV
         U(9,31)=TCP
         U(10,31)=TCR
         U(11,31)=TCR
   70 DO 1020 I=1,11
 1020 T(I,1)=U(I,1)
         DO 1030 I=9,11
 1030 T(I,31)=U(I,31)
C
C   COMPUTE NEW TEMPERATURES AT INTERIOR NODES.
C
         DO 111 I=3,10
  110 U(I,2)=(T(I,1)+T(I,3)+4.*(T(I-1,2)+T(I+1,2))+8.*HT(I,2)*Z*RTR+
        10.*Q(I,2)*X)/(10.+8.*HT(I,2)*Z)
  111 T(I,2)=U(I,2)
         K=2
         DO 120 I=4,10
         K=K+4
         LL=1
         DO 130 J=3,30
         U(I,J)=(T(I,J-1)+T(I,J+1)+4.*(T(I-1,J)+T(I+1,J))+8.*HT(I,J)*Z
        1*RTR+4.*Q(I,J)*X)/(10.+8.*HT(I,J)*Z)
         T(I,J)=U(I,J)
         IF (LL-K) 130,120,120
```

```
      130 LL=LL+1
      120 CONTINUE
C
C   COMPUTE NEW CENTERLINE TEMPERATURES ASSUMING THAT THE CENTERLINE
C   IS AN INSULATED BOUNDARY.
C
        DO 80 J=2,30
        U(11,J)=(T(11,J-1)+T(11,J+1)+8.*HT(11,J)*Z*RTR+4.*Q(11,J)*X+8.*T(1
       10,J))/(10.+8.*HT(11,J)*Z)
   80 T(11,J)=U(11,J)
C
C   COMPUTE NEW TEMPERATURES AT SPECIAL EDGE NODES AND
C   THEIR ASSOCIATED INTERIOR NODES
C
        D12=2.*HT(1,2)*DL/Y*(BFT/CB+A(4)*DL*2.)+2.91666667
        U(1,2)=(Q(1,2)*.5*X+2.*HT(1,2)*DL/Y*RTR*(BFT/CB+.50*DL)+2.56667*
       1T(2,2)+.062500*T(2,3)+.187500*T(1,1))/D12
        T(1,2)=U(1,2)
        U(2,2)=(T(2,1)+T(2,3)+4.*(T(1,2)/.75+T(3,2))+8.*HT(2,2)*Z*RTR
       1+4.*Q(2,2)*X)/(11.333+8.*HT(2,2)*Z)
        T(2,2)=U(2,2)
        JJ=3
        DO 140 I=2,9
        K=1
        JP3=JJ+3
        DO 150 J=JJ,JP3
        IF (K-1) 144,144,145
   145 DEN=2.*HT(I,J)*DL/Y*(BFT/CB+A(K)*DL*2.)+A(K)*CB*2./(A(K)+.50)
        IF (K-4) 141,142,142
   141 U(I,J)=(2.*Q(I,J)*A(K)*X+2.*HT(I,J)*DL/Y*RTR*(BFT/CB+A(K)*DL*2.)+
       12.*T(I+1,J)/(A(K)+.5)+(A(K)-1.*TB)*CB/2.*T(I,J+1)+(A(K)+1.*TB)*
       2CB/2.*T(I,J-1))/DEN
        T(I,J)=U(I,J)
        GO TO 143
   142 U(I,J)=(2.*Q(I,J)*A(K)*X+2.*HT(I,J)*DL/Y*RTR*(BFT/CB+A(K)*DL*2.)+
       12.*T(I+1,J)/(A(K)+.5)+(A(K)-1.*TB)*CB/2.*T(I+1,J+1)+(A(K)+TB)*
       2CB/2.*T(I,J-1))/DEN
        T(I,J)=U(I,J)
        GO TO 143
   144 DEN1=2.*HT(I,J)*DL/Y*(2.*DL+BFT/CB)+2.31453
        U(I,J)=(2.*Q(I,J)*X+2.*HT(I,J)*DL/Y*RTR*(2.*DL+BFT/CB)+.43412*
       1T(I,J+1)+1.33333*T(I+1,J)+.06202*T(I-1,J-1)+.48606*T(I,J-1))/DEN1
        T(I,J)=U(I,J)
   143 U(I+1,J)=(T(I+1,J-1)+T(I+1,J+1)+4.*(T(I,J)/(.5+A(K))+T(I+2,J))+
       18.*HT(I+1,J)*Z*RTR+4.*Q(I+1,J)*X)/(6.+4./(.5+A(K))+8.*HT(I+1,J)*Z)
        T(I+1,J)=U(I+1,J)
   150 K=K+1
   140 JJ=JJ+4
C
C   DETERMINE THE MAXIMUM DIFFERENCE BETWEEN THE OLD AND NEW
C   ARRAYS OF TEMPS.  IF GREATER THAN ACCURACY NEEDED, GO BACK
C   AND TRY AGAIN.  IF GOOD ENOUGH, GO ON TO PRINT
C
        D=0.
        DO 160 M=1,11
        DO 170 N=1,31
        DU=ABS(U(M,N)-TOLD(M,N))
        IF (DU-D) 170,170,180
   180 D=DU
        KX=M
```

```
152           KY=N
153       170 CONTINUE
154       160 CONTINUE
155           IF (L.LT.100) GO TO 200
156           IF(D-ACC) 190,190,200
157       200 DO 210 I=1,11
158           DO 220 J=1,31
159       220 TOLD(I,J)=U(I,J)
160       210 CONTINUE
161           IF (L.GT.2500) GO TO 360
162           GO TO 60
163       190 DO 230 I=1,11
164           DO 240 J=1,31
165       240 THETA(I,J)=U(I,J)-RTR
166       230 CONTINUE
      C
      C   OUTPUT CALLS FOR TITLE, PERTAINENT DATA AND FINAL TEMPERATURES
      C
167           WRITE (6,555) (TITLE(I),I=1,50)
168       555 FORMAT (1H1,///,5X,'FINITE DIFFERENCE RESULTS FOR ',50A1)
169           WRITE (6,560)
170       560 FORMAT (5X,'**********************************************************
             1**************************',//)
171           WRITE (6,570) CON,HV,HC
172       570 FORMAT (5X,'CONDUCTIVITY = ',F6.1,5X,'H(VISE) = ',F6.2,5X,
             1'H(CRANK) = ',F6.2,/)
173           IF (KONVOP-2)  412,413,414
174       412 WRITE (6,584)
175       584 FORMAT (5X,'A LINEAR DISTRIBUTION OF H WAS ASSUMED.',/)
176           GO TO 587
177       413 WRITE (6,588)
178       588 FORMAT (5X,'A SECOND ORDER DISTRIBUTION FOR H WAS ASSUMED.',/)
179           GO TO 587
180       414 WRITE (6,586)
181       586 FORMAT (5X,'A THIRD ORDER DISTRIBUTION FOR H WAS ASSUMED.',/)
182       587 WRITE (6,583) B,RT
183           WRITE (6,590)
184       583 FORMAT (5X,'MAT. THICKNESS = ',F6.3,' IN',5X,'ROOM T = ',F6.1,/)
185       590 FORMAT (20X,'...END CONDITIONS...')
186           WRITE (6,596)
187       596 FORMAT (8X,'T(V)',8X,'T(C)',6X,'GRAD(V)',6X,'GRAD(C)',/)
188           IF (NOOP-2) 380,381,382
189       380 WRITE (6,591) TV,TC
190       591 FORMAT (4X,F7.2,5X,F7.2,/)
191           GO TO 389
192       381 WRITE (6,592) TV,TC
193       592 FORMAT (20X,F8.2,5X,F8.2,/)
194           GO TO 389
195       382 IF (NOOP-4) 383,384,384
196       383 WRITE (6,593) TV,TC
197       593 FORMAT (4X,F7.2,20X,F8.2,/)
198           GO TO 389
199       384 WRITE (6,594) TC,TV
200       594 FORMAT (17X,F7.2,5X,F8.2,/)
201       389 IF (NOGENS) 250,250,260
202       250 WRITE (6,600) QI
203       600 FORMAT (5X,'HEAT GENERATION IS UNIFORM AT ',F9.0,' BTU/HR-CUFT.',
             1/)
204           GO TO 270
205       260 WRITE (6,610) QI
```

```
      610 FORMAT (6X,'UNIFORM GENERATION OF ',F9.0,' BTU/HR-CUFT EXCEPT AS N
     1OTED BELOW...',/)
          WRITE (6,620)
      620 FORMAT (10X,'I',9X,'J',9X,'Q(I,J)')
          DO 630 N=1,NOGENS
      630 WRITE (6,640) IG(N),JG(N),QG(N)
      640 FORMAT (9X,I2,9X,I2,8X,F8.1)
      650 WRITE (6,660)
          WRITE (6,670)
      660 FORMAT (2X,'J',7X,'I=11',6X,'10',7X,'9',7X,'8',7X,'7',7X,'6',7X,
     1'5',7X,'4',7X,'3',7X,'2',7X,'1')
          DO 690 J=1,9
      690 WRITE (6,680) J,(THETA(12-I,J),I=1,11)
      680 FORMAT (////,1X,I2,5X,12F8.3)
          KK=10
          J=3
      750 K=0
      740 K=K+1
          WRITE (6,680) J,(THETA(12-I,J),I=1,KK)
          J=J+1
          IF (J-31) 290,290,310
      290 IF (K-4) 320,330,330
      320 GO TO 340
      330 KK=KK-1
          GO TO 750
      310 WRITE (6,710) ACC,L
      710 FORMAT (////,2X,'ACCURACY OF ',F6.3,' REQUIRED ',I5,' ITERATIONS')
          IF (IPLOT) 370,370,1150
     1150 TLO = 100.
          THIGH = 0.
          DO 1200 I=1,31
          IF (THETA(11,I).LT.THIGH) GO TO 1200
          THIGH = THETA(11,I)
     1200 CONTINUE
          DO 1210 I=1,31
          IF (THETA(11,I).GT.TLO) GO TO 1210
          TLO = THETA (11,I)
     1210 CONTINUE
          TMID=(THIGH-TLO)/2.
          WRITE (6,1240) NOCASE
     1240 FORMAT (1H1,35X,'CENTERLINE TEMPERATURE RISE - CASE',I3,/)
          WRITE (6,1250) TLO,TMID,THIGH
     1250 FORMAT (4X,'J',7X,'THETA',4X,F6.2,26X,F6.2,26X,F6.2)
          DO 1220 I=1,31
          Y=(THETA(11,I)-TLO)/(THIGH-TLO)
          CALL BPLOT (Y,AA,IWIDE)
     1220 WRITE (6,1230)I,THETA(11,I),(AA(J),J=1,IWIDE)
     1230 FORMAT (/,5X,I2,5X,F7.2,5X,70A1)
          GO TO 370
      360 WRITE (6,700)
      700 FORMAT (10X,'EXECUTION STOPPED SINCE ITERATIONS EXCEEDED 2500.')
          WRITE (6,701) Q
      701 FORMAT (10X,'MAX DIFF = ',E12.3)
          WRITE (6,702) KX,KY,U(KX,KY)
      702 FORMAT (10X,'OCCURS AT NODE ',I2,',',I2,' WHERE U = ',E10.2)
          WRITE (6,703) (TITLE(I),I=1,50)
      703 FORMAT (10X,'THIS WAS FOR ',50A1)
      370 CONTINUE
          STOP
          END
```

```
      SUBROUTINE BPLOT (Y,AA,IWIDE)
      DIMENSION AA(IWIDE)
      DATA ASTR/'*'/,BLNK/' '/
      DO 1 I=1,IWIDE
    1 AA(I)=BLNK
      N= ABS(Y)*(IWIDE-1)+.50
      IF (N.GT.IWIDE) GO TO 4
      DO 3 I=1,N
    3 AA(I)=ASTR
    4 RETURN
      END

C*/
C*/
```